Springer Tracts in Modern Physics 241

Koichi M.T. Yamada
Gisbert Winnewisser *Editors*

Interstellar Molecules

Their Laboratory and Interstellar Habitat

Springer

Springer Tracts in Modern Physics

Volume 241

For further volumes:
http://www.springer.com/series/426

Springer Tracts in Modern Physics

Springer Tracts in Modern Physics provides comprehensive and critical reviews of topics of current interest in physics. The following fields are emphasized: elementary particle physics, solid-state physics, complex systems, and fundamental astrophysics.

Suitable reviews of other fields can also be accepted. The editors encourage prospective authors to correspond with them in advance of submitting an article. For reviews of topics belonging to the above mentioned fields, they should address the responsible editor, otherwise the managing editor.

See also springer.com

Koichi M. T. Yamada · Gisbert Winnewisser
Editors

Interstellar Molecules

Their Laboratory and Interstellar Habitat

Springer

Editors
Dr. Koichi M. T. Yamada
National Institute of Advanced Industrial Science & Technology (AIST)
EMTech
Onogawa 16-1
305-8569 Tsukuba
Ibaraki, Japan
e-mail: kmt.yamada@aist.go.jp

Prof. Dr. Gisbert Winnewisser
Alte Str. 8a
79249 Merzhausen
Germany

ISSN 0081-3869 e-ISSN 1615-0430

ISBN 978-3-642-16267-1 e-ISBN 978-3-642-16268-8

DOI 10.1007/978-3-642-16268-8

Springer Heidelberg Dordrecht London New York

Cover design: eStudio Calamar, Berlin/Figueres

Printed on acid-free paper

Springer is part of Springer Science+Business Media (www.springer.com)

Preface

About 30 years ago, the Cologne laboratories were founded with a design such that laboratory spectroscopy and appropriate interstellar observations would support each other by supplying new results. From the very early stage, the Terahertz spectroscopy has been one of the most important subjects of the laboratory, but it has remained to be one of the most poorly explored areas of the entire electromagnetic spectrum. It was our dream to have a space observatory, with which we can observe the spectra in Terahertz region without the strong attenuation of the radiation by the Earth's atmosphere.

It is a great pleasure of us to publish this textbook for the students who are learning molecular astrophysics at the occasion when the tremendous amount of new results for the interstellar molecules in the Terahertz region are reported successively from the Herschel space observatory.

In the first chapter of this book, the history from ancient days to now is briefly presented by Gisbert Winnewisser with the editorial help of Koichi M. T. Yamada.

In the second chapter, the molecules observed in the interstellar medium and circumstellar envelops are reviewed by Karl M. Menten and Friedrich Wyrowski. Quite large number, more than 150, of molecular species have been detected up to today, and thus it is impossible to describe all of those molecules. We have limited ourselves to present only the selected molecules: molecules detected in the early stage, prototypical molecules, and those detected most recently.

The third chapter accounts for the molecular spectroscopy, which is the irreplaceable tool for the astrophysics. The basic theory for the spectroscopy of atoms, diatomic molecules, and polyatomic molecules are briefly presented in Sects. 3.1–3.3; Sects. 3.1 and 3.2 are contributions of K. M. T. Yamada, and 3.3 of Per Jensen with the appendix by K. M. T. Yamada. Since many text books have been published concerning to the molecular spectroscopy, the descriptions are limited to the very fundamental level.

The number of molecules with internal rotation observed in the interstellar space is increasing steadily. The spectra of such molecules are rather complicated and are of interest not only for astrophysics but also for molecular spectroscopy. Section 3.4 is a contribution of Nobukimi Ohashi, which accounts for the internal

rotation problems with one- and two-methyl tops. Various methods for the energy calculation for such molecules are described in detail. The symmetry labeling of the energy levels are also discussed on the basis of permutation-inversion group. We wish to acknowledge Prof. Kaori Kobayashi's assistance to produce many of the figures in Sects. 3.4.

In the fourth chapter, the most recent progress in the laboratory spectroscopy in Cologne is presented by Thomas F. Giesen, and the development of heterodyne mixers, the essential device for the radio observation, is reviewed by Karl Jacobs.

In the last chapter, the molecules observed in the interstellar space are listed on the basis of the Cologne Database for Molecular Spectroscopy (CDMS).

We would like to thank the Cologne students, post doctoral fellows, and all collaborators, whose enthusiastic and untiring efforts are essential for many of the beautiful results presented in this book. We would like to express special thanks to Helga Winnewisser, who has supported Gisbert mentally and physically during the preparation of this book.

On behalf of the contributors

August, 2010 Koichi M. T. Yamada

Contents

Chapter 1
History

Koichi M. T. Yamada and Gisbert Winnewisser

1.1 Prelude

1.1.1 The Ancient Mechanical Universe

Claudius Ptolemaeus who lived in the second century (83–161 AD) was an ancient mathematician, geographer, astronomer, and astrologer in Roman Egypt.[1] Ptolemy, as he is known in English, was the last great and dominating figure before the dawn of the renaissance of science during the years 1500–1700. During the lifespan of Ptolemy, arithmetical techniques were developed for calculating astronomical phenomena. Greek astronomers, e.g., Hipparchus, had produced geometric models for calculating celestial motions. Ptolemy himself contributed to the fitting of the astronomical data. He had developed elaborate arithmetical techniques for calculating celestial motions. Ptolemy, however, claimed to have derived his geometrical models from selected astronomical observations by his predecessors spanning more than 800 years, though astronomers have for centuries suspected that his models' parameters were adopted independently of

K. M. T. Yamada (✉)
National Institute of Advanced, Industrial Science and Technology (AIST), EMTech,
Onogawa 16-1, Tsukuba,
Ibaraki 305-8569, Japan
e-mail: kmt.yamada@aist.go.jp

G. Winnewisser
Alte Str. 8a, 79249 Merzhausen, Germany

[1] See, e.g., Encyclopedia Britannica: http://www.britannica.com/.

K. M. T. Yamada and G. Winnewisser (eds.), *Interstellar Molecules*,
Springer Tracts in Modern Physics 241, DOI: 10.1007/978-3-642-16268-8_1,

observations. Ptolemy presented his astronomical observations in a convenient form of tables, which could be used directly to compute the past or future position of the planets. The Almagest ("The Great Treatise," originally written by Ptolemy) also contains a star catalog, which is an appropriate version of the catalog created by Hipparchus.

Since ancient times, astronomers of the heavens had noted that from night to night the stars moved across the sky in a regular procession, trailing from east to west, following the motions of the sun and the moon. In this night time procession, the stars maintained their heavenly order. If one inspects the movement of the Big Dipper, one notices in a short time that the five planets move across. Today, we find that, with the exception of five stars, the rest would hold their relative positions. The five stars looped forward and backward from these, west to east, and then from east to west. The Greeks, observing this remarkable fact repeatedly, called each of these five celestial bodies *asteres planetai*, the Greek word for wandering stars. But today, we call them the planets, i.e., Mercury, Venus, Mars, Jupiter, and Saturn. The looping motion of each planet could be duplicated if the planet were anchored to the outer rim of a wheel that was located on a track moving across the sky. When the observed positions of the planets were plotted, they agreed fairly well with this description of the twelve wheels rolling across the sky. But if the ancient astronomers tried to make the calculated motions of the planets fit the observations accurately, then the system became very complicated and cumbersome. It had to be assumed that some of the wheels themselves rolled on the rims of other wheels. The best job of fitting was done by Ptolemy. He and his followers found that 80 wheels within wheels were needed for just the five planets known at that time. Some planets required wheels within wheels within wheels.

To account for departures of heavenly bodies from uniform circular motion, early astronomers devised an elaborate system, based on mechanical or mathematical models. In its simplest form, the system employs an earth-centered circle called a deferent. The second circle, called an epicycle, has a center Q which lies on the deferent and revolves uniformly counter-clockwise around the earth from west to east. The point Q was said to be "immaterial," since it did not contain matter. The celestial body, meanwhile, revolves uniformly around Q on the epicycle circle. The second motion can be either clockwise or counter-clockwise. The apparent motion of the body relative to the earth is the combined motion in the two circles.

Ptolemy was the author of 13 scientific treatises in astronomy: three of which were of continuing importance to later Islamic and European science. The first book he published is an astronomical treatise now known as the *Almagest* (in Greek or "The Great Treatise"). Discussion of the geographic knowledge is the content of a second treatise the Geography, which boils down to a thorough discussion of the geographic knowledge of the Greco-Roman world. The third one is the astrological treatise known as the *tetrabiblos* ("Four books") in which he attempted to adapt horoscopic astrology to the Aristotelian natural philosophy: the first actual star catalog in the second century.

This catalog appeared in the book known later as Almagest (which is a Latin corruption of the name of the Arabic translation, Al-mijisti). It had 1,025 entries; the positions of these bright stars had been measured by Hipparchus 250 years earlier. Ptolemy's catalog was the only widely used one before to the seventeenth century, i.e., the renaissance of science. His collected works, amounted to 13 books of the mathematical composition, were written in Alexandria, and these books comprise the best guide to Ptolemy's ideas and to the contributions of those who preceded him. Out of careful observation, logical deduction, and the application of basic geometrical principles, without telescopes and with only primitive measuring devices at hand, the Greeks compiled a tremendous amount of observational data concerning the motions of the planets with respect to the stars.

Although beclouded here and there with vague philosophical ideas and superstitions, the Greek concept of the universe was the prod. The geocentric world of Ptolemy had as the basic assumption that the Earth is situated at the center of an un-movable universe. The movement of the moon and the sun on the other hand, were still described with relative ease as a fairly simple circular motion problem.

1.1.2 The Dark Ages

Peace and prosperity continued to reign until about the end of the second century AD. Then, a series of catastrophes dissolved the Roman Empire and all but destroyed civilization itself. Decadent political and social systems collapsed. The exhaustion of gold and silver coins, as the Spanish mine ran out of the precious minerals, paralyzed commerce. A horrible pestilence brought back from Asia by the military, struck down the population at the rate of 2,000–3,000 persons per day, rendering wide areas of being completely depopulated. Barbarian tribes pressed in, conquering and devastating southern Europe. The centuries that followed were sad times for science. Deprived of comfort in this world, people looked forward to solace in a better world thereafter, and turned away from the science of the past. Christianity, the major force during the Middle Ages, brought with it a growing desire to reconcile science in general and concepts of the universe in particular with the literal statements of the Scriptures. Lactantius ridiculed the concept of a spherical earth. Most people came to believe that the earth was flat, square, and supported by four pillars, one at each corner. Under such circumstance, contributions to science were few. The "meteors" became signs in the sky prophetic of events, evil or good, about to happen on the earth. Superstition and fear were the motivating forces in astronomical thought for many centuries.

For some time, the torch of learning passed into hands of the Arabs. They made few advances, but at least they preserved in the *Almagest* the writings of Ptolemy and they continued to make a few observations of the motions of the heavenly bodies. The *Koran*, fortunately, was silent on questions that related to concepts of the earth and the universe. By the end of the twelfth century, interest was rekindled in learning, in agriculture, craft, commerce, and in science. But an aura of

superstition, mysticism, and magic continued to obstruct the development of the sciences, especially astronomy and chemistry.

The pseudoscience of alchemy burgeoned, bearing a relationship to chemistry similar to that of astrology to astronomy. There was a widespread belief that with the use of magic, potions, and incantations, one could turn base metal into gold or silver. Failure did not discourage the alchemists and magicians. From time to time, they even made, by accident, some useful chemical discovery. In such an atmosphere, it is not surprising that astrology flourished. The idea that God, through the stars, could influence mankind was not unacceptable to the church fathers. And so, with the full approval of the church, astrologers continued to cast horoscopes as they did in the ancient world.

1.1.3 The Renaissance of Science

Without any obvious or logical reason the fifteenth century undergoes decisive changes in the lifestyle particularly the way science was handled. This trend started in Italy, and soon it spread out to the north. As an example of changing, the mood and the way it can be traced was demonstrated by looking at the setup and behavior of the imperial court of the Emperor Karl IV (Charles IV) who laid down in the year 1348, the foundation of Charles University at Prague. Charles IV did recognize the importance of liberal arts and science at large and in particular for his fellow country men. By about 1600, the development of modern science started, which has rendered such a large number of results that we are proud to use still today. At his residence in Prague, Emperor Karl IV employed two outstanding experts in the field of astronomy, or as you would nowadays call them, scientists: Tycho de Brahe (1546–1601), who provided superb quality of the astronomical measurement, and his successor Johannes Kepler (1571–1630).

Galileo Galilei (1563–1642) and Johannes Kepler, who lived in the same period but geometrically separated by a large distance, reached to a common conclusion of the heliocentric movement of the planets, which had been proposed much earlier by the great pioneer, Nicolaus Copernicus (1473–1543).

The harvest out of their high quality measurements was reaped by Isaac Newton (1643–1727). Today, the complicated movements of planets, against which Ptolemy and his successors fought desperately, can be explained by simple principles: Newton's equations of motion and gravitation theory. Newton's equations of motion form the beginning of classical mechanics. The observed continuous nature of macroscopic motion in space and time can be explained by applying integral and differential calculus to the solution of dynamic problems. The principal ideas embodied in the deterministic formulation of classical mechanics. It consists of the following:

1. The system in question is observationally accessible at all times, and observations can be executed without disturbing the system under investigation.

2. By defining the state of a system in time, all the mechanical variables of the system at that particular time can be determined.
3. Combining the specification of the state in statement 2 with the laws of mechanics allows for a complete description of the system as a function of time.

1.1.4 Discovery of Dark Nebulae

Dark nebulae, or dark dust clouds, as we designate them nowadays, have been noticed early on as huge voids in an otherwise star-filled heaven. Clearly, it must have been an utter nuisance for star counters, like Sir F. W. Herschel, who were hampered in getting reliable numbers for their star-counting business. If Herschel would have been able to use his scrutinizing eyes, then he probably would have got great satisfaction out of the fact that the cold dark clouds also take part in star formation, more so individually, i.e., as single stars. In contrast to the cold clouds, with temperatures of around 10 K, the warm dark clouds having temperatures well over 15 K are heated by external sources or by embedded stars. By choosing the proper molecules or class of molecules, like symmetric top molecules, the kinetic temperature can be estimated rather quickly from the level-populations.

Therefore, Herschel investigated all astrophysically interesting phenomena, stars, nebulae, and star clusters. He discovered something like 2,000–3,000 nebulae and clusters. In his article on the "Construction of the Heavens," he presented speculation on the evolution of matter by successive steps from the nebulous material to the final planetary state.

As it has turned out over the years and very recently with the advent of molecular spectroscopic investigation of the dark clouds, one is not surprised to find out that one of the earliest references in the literature addresses the Taurus Cloud Complex. It is mentioned explicitly in an important publication by Herschel (1784), entitled: "Account of some observations tending to investigate the construction of the Heavens." In his description of the nebulae, he noted that "the spaces preceding them were generally quite deprived of their stars, so as often to afford many fields without a single star in it." Here, he clearly refers to the task of star counting. He found himself, as figuratively expressed it "... on nebulous ground." He refers in this early publication to those regions in the sky, where no stars are observable, or where the number and the brightness of background stars is drastically reduced relative to the surrounding areas. A particularly beautiful example of these conspicuous dust clouds are the dark dust clouds in Taurus region, with the truly remarkable sources, like TMC 1, TMC 2, ..., very cold ($T_{\mathrm{kin}} \approx 8-10\,\mathrm{K}$), very quiet sources with almost no turbulences within the sources themselves, and therefore with no indication of any start of star-formation. In Fig. 1.1, which is an excellent "historic" reproduction of Barnard's plate No. 5 of the nebulous region in Taurus [1]. In his description of this region, Barnard comments that "very few regions of the sky are so remarkable as this one ..." and

Fig. 1.1 This is the Taurus region with the famous dark clouds which are for the Terahertz frequencies such an important dark region, see, e.g., Winnewisser and Kramer [46]. The photograph image is reproduced with the permission of copyright holder, Carnegie Institution

he continues "... and bears strongest proof of the existence of obscuring matter in space."

1.1.5 Dawn of Spectroscopy

The very gifted young Joseph von Fraunhofer succeeded in manufacturing high-quality lenses and constructed one of the finest refractory telescopes ever built. He invented a heliometer and a diffraction grating for measuring the wavelength of light precisely. In addition, he acquired great skill in the manufacture of homogenous glass prisms, which reached unparalleled quality. These technical achievements, in particular, his uniquely homogeneous glass prisms, gave him the edge over all his contemporaries working on similar project in dispersing light. Pointing his refracting telescope together with his "self-built spectrograph" toward the sun and some of the close-by stars, he discovered that the sun's spectrum, when sufficiently dispersed, was punctuated by a large number of fine dark absorption lines, about 700 of which he studied in great detail. He collected an atlas of these lines, naming the strongest features consecutively as A, B, C, D, ...

Currently, a few of these cataloged lines are still known to spectroscopists by the famous Fraunhofer notation, such as the two sodium D-lines, which he named D_1 and D_2. We now know that the 3p level of sodium (Na) displays an observable fine structure, so closely spaced doublet. Thus, the two Fraunhofer lines correspond to the following transitions: $D_1 = {}^2P_{1/2} - {}^2S_{1/2} = 589.5940\,\text{nm}$, and $D_2 = {}^2P_{3/2} - {}^2S_{1/2} = 588.9973\,\text{nm}$.

About the time when Joseph von Fraunhofer found a large number of fine dark absorption lines in the solar spectrum, he published his thorough and extensive research study on the solar spectrum in form of a catalog. This monumental work

on the solar spectrum was followed in 1823 by a second catalog, summarizing stellar lines discovered in different stars close to the sun. It may be justified to state that the beginning of spectroscopy was set by the very professional level of J. v. Fraunhofer in presenting his results.

The optical window was traditionally always used to carry through the observational program and check out new observational part of the electromagnetic spectrum to be used in the quest for recording weaker and ever weaker signals from distances well beyond the sun. The construction of a telescope is a considerably demanding task during the last century to record absorption lines in the spectrum of the sun and other stars. Around the year 1860, Kirchhoff and Bunsen marked the beginnings of what we now call modern astrophysics. Their contribution was the recognition that every chemical element exhibits a characteristic spectrum which can be used to detect it in the laboratory and in far distant cosmic objects.

The first molecules in space were discovered in cometary spectra, as early as 1864, and a spirit of science. They were studied for the first time visually by Donati in comet Temple [2]. The spectral features he saw were presumably the 474.0, 516.5, and 563.0 nm band groups of C_2. But at the time, they were not in a position to identify the lines as such, because the knowledge of comparing spectra with each other was just not yet known. This step would have provided the important final check. In this context, we note that Huggins [3] in 1882 first observed the 405.0-nm group of lines, which was identified only in 1951 by Douglas [4] as due to the C_3 molecule. In the meantime, C_3 has been studied extensively in the laboratory employing optimized spectrometers, covering the microwave region almost continuously to the ultraviolet. The C_3 molecule has recently been found in interstellar space.

1.2 Interstellar Medium (ISM)

The enormously vast spaces between the stars in our Galaxy and in between the stars of the extragalactic domain are by no means void. On the contrary, they contain an interesting and highly surprising, but totally unexpected composition of a rarefied gas and dust, which is very in homogeneously distributed.

The study of ISM started about the turn of the century (about 1904), when Hartmann noticed that matter must be dispersed among the stars. At that time, he was checking in great detail the Doppler velocities of stellar absorption lines in the gas associated with the close binary system δ-Orionis. He noticed that some of the CaII resonance absorption lines did not participate in the system's periodic Doppler shift, whereas others did. Subsequently, "stationary" Na-D lines (Fraunhofer notation) were also discovered in δ-Orionis and in other stars.

The main components/constituents of interstellar medium, ISM, consist of molecular particles and interstellar dust, with a % ratio of gas to dust of about 99–1. The interstellar particles are predominantly in the gas phase in neutral form and consist of atoms, molecules, free radicals, whereas interstellar dust consists

of μm-particles of rather uncertain chemical composition. A smaller fraction of the gas, ca. 3% is found to be ionized.

Hydrogen, H, is with about 70% by mass, the most abundant element in the universe and it is followed in abundance by helium (28% by mass). Hydrogen, helium, and deuterium are considered to be primordial in nature. The available evidence indicates that these three elements were created during the earliest evolutionary phases of the universe, i.e., the Big Bang. All elements, heavier than helium may have been synthesized more slowly by thermonuclear reactions in the various stellar burning stages involving intensive mass loss from stars in their late burning stages which include supernovae, novae, and planetary nebula. However, the details of the processes which led to the present chemical composition of the Galaxy and the Universe are far from being understood. The composition of the interstellar dust on the other hand is unknown.

Atoms, both neutral and ionized, exhibit spectral features throughout most of the electromagnetic spectrum. These spectral lines—in emission and/or absorption—carry detailed and rather specific information on the physical and chemical conditions of the sources from which they emanate. In fact, the heights of the energy levels of the observed transitions together with the degree of their population furnish a reliable measure of the excitation conditions and thus the temperature of the source itself. The relative intensities of various transitions of a molecule, in conjunction with the principle of statistical equilibrium, can be used to derive the gaseous number-density of the source. The widely different line profiles observed can be analyzed to provide information on the sources' dynamical states, i.e., whether the line widths are thermal, broadened by turbulence, or by pressure.

Atomic spectral features have played, and still play a crucial role in the study of stellar atmospheres. The classification of stars by their atomic optical transitions has been an important field of astronomy since the turn of the century. In addition to standard dipole-allowed spectral transitions, atomic lines are found in the radio, infrared, and optical regions in the form of recombination lines, fine-structure lines and hyperfine-structure lines.

1.2.1 Atomic and Molecular Hydrogen

H_2 molecule forms on the surfaces of dust grains, in the ISM. The dust exerts, because of its large opacity, a strong influence on the diffuse interstellar radiation field and undoubtedly it has a fundamental effect on the processes whereby interstellar clouds collapse to form stars. Energy generated in the stars is absorbed and re-emitted by the ISM. Molecular hydrogen, H_2, stands out to be the most abundant interstellar molecule. As shown by Spitzer and Zweibel [5, 6], it will be synthesized rather efficiently on the surface of interstellar dust grains. The dust contains a significant fraction of the interstellar heavy elements and thereby ties up important atomic species that can cool the interstellar gas throughout and causes increasingly excited fine-structure transitions.

Progress in characterizing the nature of interstellar dust will therefore not only provide important information to secure knowledge about the chemical composition of significant constituent of the universe forming stars, which in turn undoubtedly has a fundamental effect to introduce very significant uncertainties in the energy distributions of astronomical sources located behind dust clouds.

The influence of high mass stars on the ISM is tremendous: during their formation process, they assume various stages of luminosity. Important new results were obtained within the last 40–50 years. In fact, the early construction of a radio telescope in the 1930s by K. G. Jansky made him discover with his home-built telescope in his backyard a completely new era of physics by investigating the Milky Way in different wavelength regions. The free–free radiation was discovered from a plasma, HII regions were seen for the first time, and most important, the discovery of the 21-cm line of atomic hydrogen, predicted on account of theoretical calculations by H. C. van de Hulst in 1944.

1.2.2 The 21-cm Line of Neutral Hydrogen

Approximately 5–10% of the mass of the Milky Way is in the form of interstellar atomic hydrogen. The study of the physical properties of this matter is possible only because the atomic ground state $\left({}^2S_{1/2}\right)$ can undergo a hyperfine transition giving rise to the radio emission at the wavelength of 21.1 cm. The transition occurs when the electron reverses its spin relative to that of the proton. The higher energy state is the one in which the two spins are parallel to each other. The lower state is the one where the two spins are anti-parallel. The prediction that this should be an observable transition was made by van de Hulst in 1944 just before the end of the Second World War; neutral hydrogen line should emit at a wavelength about 21 cm, although it is a highly forbidden transition with a spontaneous transition probability with every twelve million years, because of extremely low changes in energy when the relative spins of the proton and electron in a hydrogen atom change. The Doppler effect of the neutral hydrogen line was readily observable, displayed, and recorded, by producing a frequency shift of the neutral 21 cm atomic hydrogen line.

The use of the 21-cm line of atomic hydrogen for mapping the distribution of low temperature regions opened new vistas on the structure and dynamics of galaxies. Since then, additional lines were discovered in the cm- and dm-spectroscopic areas and assigned to high quantum numbers of hydrogen and helium lines. Furthermore, a fair number of diatomic and polyatomic molecular lines have been assigned. They came as a certain surprise, and they are a signature of the low density interstellar clouds.

This famous and fundamental transition ($^2S_{1/2}$, $F = 1 - 0$; 1420.405 751 786(1) MHz) was originally detected in space by Ewen and Purcell [7] and by Muller and Oort [8]. It has since been used to map out neutral diffuse interstellar

gas in large regions of our galaxy and others. Despite the low transition rate for spontaneous emission $\left(A_{21\,\mathrm{cm}} = 2.86 \times 10^{-15}\,\mathrm{s}^{-1}\right)$, this line is very easily detectable in space because of the large column densities of atomic hydrogen. The frequency of transition was accurately determined in the laboratory $\nu_{\mathrm{mn}} = 1420.405751767\,\mathrm{MHz}$ [9].

1.2.3 Recombination Lines

Recombination lines are emitted during the (free → bound) capture of an electron by ions such as H^+, He^{++}, C^+, ..., or during the ensuing bound–bound cascade processes. These processes typically occur with $\Delta n = 1, 2, 3$, where n is the principal quantum number, and are referred to as alpha, beta, gamma, ..., transitions, respectively. According to the Rydberg formula, the position of these transitions are (in cm^{-1})

$$\tilde{\nu}_{ji} = R_{\mathrm{a}}\left[\frac{1}{n_i^2} - \frac{1}{n_j^2}\right] \tag{1.2.1}$$

where the quantum numbers are given by $n_i > n_j$, and $R_{\mathrm{a}} = 1.097 \times 10^5(1 - m_{\mathrm{e}}/m_{\mathrm{a}})$ is the atomic Rydberg constant in cm^{-1}, m_{e} is the electron mass $(5.586 \times 10^{-4}\,\mathrm{amu})$, and m_{a} is the atomic mass. While low-n transitions appear in the UV (Lyman lines, lower level $n = 1$; $L_\alpha, L_\beta, \ldots$, with the suffix $\alpha, \beta, \ldots$ denoting $\Delta n = 1, 2, \ldots$), in the optical (Balmer series, $n = 2$; $H_\alpha, H_\beta, \ldots$), and the adjoining near-infrared region, high-n (main quantum number ~ 50 and larger) recombination lines are found throughout the radio region. Transitions with $n > 110$ appear at frequencies lower than 5 GHz. Hydrogen recombination lines have been used in the last 30 years; see, e.g., Wilson and Filges [10] and Verschuur and Kellermann [11] for detailed studies of ionized regions called H^+ or HII regions. These ionized regions are always associated with young O- and B-stars which have recently formed from cool interstellar matter. Thus, recombination lines, in conjunction with atomic fine–hyperfine-structure lines, as well as molecular transitions (see below), are now among the tools of astrophysicists used to study star formation and the interactions of ionized plasma with dense molecular clouds.

1.2.4 Atomic Fine- and Hyperfine-Structure Lines

Atoms and molecular ions with unpaired outer electrons can possess a non-zero electronic orbital angular momentum $\boldsymbol{L}$ and a spin angular momentum $\boldsymbol{S}$. The total angular momentum $\boldsymbol{J} = \boldsymbol{L} + \boldsymbol{S}$ in Russel–Saunders coupling scheme.

The configuration of the atoms outer electron shell determines $\boldsymbol{J}$ and thus the multiplicity of the fine-structure levels, which arise from the magnetic spin–orbit coupling. The magnitude of the fine-structure splitting is approximately of the order of the square of the fine-structure constant $\alpha \sim (1/137)^2$ times the electronic energy (10–100 eV) and is largest for low n levels. Fine-structure transitions are found predominantly in the far-infrared region.

Since the first detection of the forbidden far-infrared lines of neutral oxygen (O, OI) at 63.2 μm [12, 13], and ionized carbon (C^+, CII) at 157.7 μm [14], fine-structure lines have become important tools in probing the atomic and ionized portions of interstellar matter. Neutral carbon C (CI), neutral O (OI), and ionized carbon, C^+ (CII), are used as the main tracers to probe interface regions separating cool neutral atomic and molecular material from ionized material. In star-forming regions, the surface layers of the cloud or the individual clumps it may consist of, facing embedded or nearby young OB-stars, are ionized by the far-UV radiation emitted by these stars. Photo-dissociation regions (PDRs) are zones where the far-UV radiation beyond the Lyman continuum (13.6 eV) ionizes atoms with lower ionization potentials than hydrogen, such as C (11.3 eV), the alkali metals ($\sim 5\,\mathrm{eV}$), S (10.3 eV), and others. In this way, a portion of the stellar luminosity is absorbed, leading to local heating and subsequent re-radiation, predominantly in the far-IR region of the spectrum. In fact, since the discovery of the $^2P_{3/2} \rightarrow {}^2P_{1/2}$ CII fine-structure line of singly ionized carbon [14], it has become clear [15] that the CII emission arises from moderately dense ($\sim 1,000\,\mathrm{cm}^{-3}$) and warm ($T > 200\,\mathrm{K}$) gas associated with the surfaces of molecular clouds (see, e.g., Genzel et al. [16]). For lower density regions where hydrogen is atomic, the CII line is also predicted to be the main coolant [17]. CII emission has also been observed toward gas-rich nuclei of luminous spiral galaxies [15, 18, 19] with the result that this line contributes about 1% of the total far–infrared luminosity. This radiation has to be longward of the 91.2 nm Lyman limit, because hydrogen atoms blanket stellar radiation below 91.2 nm. Thus, the 157.7409-μm CII line (laboratory measurements by Cooksy et al. [20]) has turned out to be one of the brightest fine-structure transitions. It plays an important role in cooling denser regions by collisions with electrons, translational and rotationally excited hydrogen molecules in which the energy is first transferred to the CII species and then radiated away. The excitation of the hydrogen molecules stems from far-UV pumping into vibrationally excited states.

Actually, the most important cooling lines arise from neutral oxygen O (the two fine-structure transitions: $^3P_0 \rightarrow {}^3P_1$ at 146 μm and $^3P_1 \rightarrow {}^3P_2$ at 63 μm). Other atomic cooling lines arise from neutral carbon, C, and Si^+. Neutral atomic carbon has a $1s^2 2s^2 2p^2$ electronic configuration, and its two outer electrons give rise to a singlet and triplet system. According to Hund's rule for terms arising from equivalent orbitals, those with largest multiplicity lie the lowest. Thus, the triplet system is energetically the lowest and therefore of particular astrophysical interest in low-temperature regions. The ^3P electronic ground state is split into three fine-structure levels of different total angular momentum J, i.e., $^3P_0, {}^3P_1$, and $^3P_2$ in

increasing energy, respectively. This "normal" term order in atomic carbon—the level with lowest J lies the lowest, according to Hund's rules for less than half-filled shells—is "inverted" for atomic oxygen. With a $1s^2 2s^2 2p^4$ electronic configuration, oxygen possesses the same ground state (^3P) as neutral carbon, but since the p-subshell is more than half filled, now the level with highest J lies the lowest, i.e., $^3P_2, ^3P_1$, and $^3P_0$ in ascending energy.

1.3 Interstellar Molecular Lines

In this section, we present a brief general overview of interstellar molecular lines; more details are given in Chap. 2. Tables in Chap. 5 list all the presently known gas phase interstellar molecules. The molecular species range in size from 2 to 13 atoms. They are typically found in the so-called dense(!) interstellar clouds with tremendous sizes of 1–100 light years, average gas densities of $10^2 - 10^3\,\mathrm{cm}^{-3}$, and temperatures in the range 10–60 K, although both higher temperatures and gas densities are found in localized regions where star formation is occurring. In addition, differing physical conditions exist not only on the edges of clouds but also in areas of highly clumped molecular material, where external UV radiation of close-by sources is important. There are some well-studied cases where UV radiation penetrates through the dilute inter-cloud medium deeply into the clumpy interior of the molecular cloud, ionizing the exposed surface layers of the individual clumps. The Orion Molecular Cloud and the regions M17 SW and S140 are typical examples where ionized regions—consisting mainly of hydrogen in the form of HII (H^+)—border molecular clouds. Some of the organic molecules shown in the tables in Chap. 5 have been detected in extended circumstellar envelopes of cool, old stars that are carbon rich, i.e., possess more elemental carbon than oxygen. The more normal pattern in stars is for the elemental abundance of oxygen to exceed that of carbon: the cool envelopes of these stars do not contain large abundances of most organic molecules [21].

The most abundant interstellar molecule is H_2; this is due to both to the high elemental abundance of hydrogen compared with all heavy elements found in molecules (see, e.g., Watson [22]), and to an efficient chemical pathway for its formation from hydrogen atoms.

The second most abundant molecule—carbon monoxide—has a "fractional abundance" with respect to molecular hydrogen of 10^{-4}. Most of the remaining molecules are organic or carbon containing in nature. In interstellar clouds, both normal and highly unusual molecules exist compared to those that we know on earth; we have discussed their nature in previous articles [23, 24]. But it carries importance due to the fact that CO is very stable and carries a fairly low dipole-moment. All organic molecules have significantly smaller fractional abundances than CO ($< 10^{-8}$) and can be regarded as trace constituents, although the amount of interstellar organic molecules is quite large compared with their terrestrial counterparts.

In addition to the gas phase molecules, there is additional ambiguous low-resolution spectroscopic evidence for condensed phase species.

1.3.1 Small Molecules

The first molecule to be discovered in the ISM were the diatomic radicals, CH and CN, and the positive ion CH^+. Dunham and Adams [25] found in the high resolution optical spectra toward hot background O-stars in addition to a number of interstellar atomic lines (Na, Ti, ...), a few fairly sharp absorption features which were clearly interstellar in character. Shortly thereafter, these lines were identified and assigned by Swings and Rosenfeld [26], and by Douglas and Herzberg [27]. For details of these fundamental discoveries, we refer the reader to a personal recollection and several articles by Herzberg [28]. Optical absorption lines of these three diatomic molecules as well as optical and ultraviolet spectra of other diatomic molecules detected subsequently are observed in the so-called diffuse interstellar clouds which have gas densities of about $10^2\,\mathrm{cm}^{-3}$.

Relatively soon after the discovery of the first three poly-atomic molecules, NH_3, H_2O, and H_2CO, in space, it became clear that, by employing high spectral and spatial resolution programs, the interstellar molecules reside in molecular clouds where they are synthesized and where the sites for star formation are located. Although there is nothing like a standard molecular cloud, they are highly diversified and reach rather different sizes, spanning a size range from close to few solar masses to several $10^6\,M_\odot$. Obviously, molecular clouds are not only producing a rich and highly diversified chemistry, but they are also exposed to vastly different physical conditions, which reflect themselves in displaying anomalous line radiation patterns, as will be discussed later on.

The concept of the diffuse interstellar clouds that they were formed out of gas and dust took about another 30 years before the medium started getting appreciated slowly.

One of the well-known spectacular sources is in the heart of the Taurus molecular cloud complex. This Taurus region is one of the many dark dust cloud complexes containing a sizeable number of small dense and cool low mass fragments. Among them, the most well-studied cloudlet is TMC 1, the Taurus Molecular Cloud 1, which harbors the longest carbon chain molecules detected in space. It contains unusually high abundance of cyanopolyynes and other linear carbon chain molecules, forming a ridge of molecular emission.

The OH radicals can be observed by microwave techniques. Some of the light hydrides are still followed later. This time, the detection was made at a frequency of 1.6 GHz using a radio telescope which represents the first radio-line to be discovered. However, the field of interstellar molecules was opened by the discovery of three polyatomic molecules NH_3, water H_2O, and formaldehyde H_2CO. These three discoveries were instrumental to open the flood gates to the more than 150 molecules now known to roam the interstellar space. However, the list of

interstellar molecules is not complete. Missing may be others due to a variety of problems mainly technical, as well as by exhibiting transitions in the Terahertz region only, because of which many of the possible transitions will be completely blocked out by the atmospheric extinction.

1.3.2 Large Molecules

The discovery of more than 150 molecular species in interstellar space via their rotational transitions observed in the microwave, millimeter-wave, and adjoining Terahertz region has demonstrated investigation of interstellar matter. The distribution of ISM is far from being homogeneous; on the contrary, the ISM displays an inhomogeneous distribution, as can be seen and derived from inspection of results obtained from large scale mappings of molecular clouds. In addition, mapping of molecular clouds will supply detailed information on local inhomogeneity in molecular clouds—densities can reach up to $10^9\,\mathrm{cm}^{-3}$. It has become clear that, within the last 20 years of molecular astrophysics, the hydrogen, with about 50% of interstellar matter being mainly in the form of hydrogen gas, is molecular and concentrated in extensive molecular–cloud complexes, often called *Giant Molecular Clouds* (GMCs): gas densities of $10^4\,\mathrm{cm}^{-3}$ and temperatures below about 100 K.

The majority of the interstellar molecules are carbon-containing organic substances (they are summarized in tables in Chap. 5). From those tables, you can see that the largest group of the interstellar species are diatomic molecules and radicals. It amounts to 34 individual species, most of which have been detected in the millimeter-wave and adjoining Terahertz regions. The molecules which contain three atoms are linear or bent and produce accordingly more difficult spectra. The molecules with four atoms are 23 in number while the five- and six-atomic count up to 18 and 16, respectively. The larger molecules with 7–12 atoms are rapidly decreasing, and the $HC_{11}N$ remains up to the present day the largest molecule by mass. The spectra of the various molecules will be discussed after we have explained the theoretical background of the various molecules. The close agreement with high resolution laboratory spectra furnishes the ultimate exacting test for their definite identifications. Molecules have been detected throughout the electromagnetic spectrum, predominantly, however, within the last 20 years in the microwave, sub-millimeter wave, and adjacent far–infrared regions.

1.3.3 Non-polar Molecules

The list of interstellar molecules (tables in Chap. 5) is not complete, in the sense that only polar molecules can be observed by microwave only. Molecules which do not possess an electric dipole moment are still missing because of a variety of

problems, mainly technical and by exhibiting transitions in the Terahertz region only. The lower rotational lines of light hydrides lie in the far–infrared regions and this cannot be observed from the ground, since radiation of these wavelengths—with a few exceptions—is completely blocked by the atmosphere. The molecules observed in the gas phase and surfaces of dust particles are most likely produced from atoms, ions, and smaller molecules by local chemical processes, see, e.g., Winnewisser and Herbst [29] and Herbst [30]. The results from the Infrared Space Observatory obtained with the Short Wavelength Spectrometer operated in the 2–20 μm region, are beautiful spectroscopic evidence for a variety of ice mantle and refractory grain core features, such as solid-state CO, CO_2, and silicates [31].

The chemically important or "biogenic" elements, carbon, nitrogen, and oxygen, have abundances which are fractions between 10^{-3} and 10^{-4} of the hydrogen abundance and are expected to be picked up by their ro-vibrational lines. Carbon, and, in consequence, the carbon-chain molecules, form the main architectural theme of the discovered interstellar molecules. Besides the cyanopolyynes and their various derivatives, pure carbon cluster molecules have been observed in space as well: CCC [32] and CCCCC [33] have been detected in the circumstellar shell of the late type giant carbon star IRC 10216. In addition, a tentative assignment of CCC toward the galactic center source Sagittarius B2, a star-forming region, has been reported [34]. Very recently the laboratory gas-phase electronic spectrum of $CCCCCCC^-$ has been measured [35], and five lines show close coincidence with visible diffuse interstellar bands (DIBs), probably paving the way toward future identifications of DIBs.

In molecular clouds, two types of processes dominate by which molecules can be synthesized from precursor atoms and ions: gas phase chemical reactions and reactions that occur on the surfaces of dust particles. The latter mechanism is invoked for the formation of molecular hydrogen, H_2, as well as for the synthesis of larger interstellar molecules.

Within the denser parts of the molecular cloud, the conditions for star formation are met in many locations and, thus, one observes quite often the formation of multiple star formation. In many real examples, up to 5,000 new stars are born.

1.3.4 Atomic Carbon and CO Molecule

The fine-structure energy-level separation in carbon is smaller than that for oxygen and lies in the sub-millimeter region, and the two fine-structure transitions have therefore been observed with radio-astronomical techniques. The forbidden magnetic dipole transitions of neutral carbon $^3P_2 - ^3P_1$ and $^3P_1 - ^3P_0$ have been measured in the laboratory in carbon discharges [20, 36] to lie at 809 343.5(9) and 492 160.651(55) MHz, respectively. Neutral atomic carbon has been found to exist throughout molecular cloud cores with an abundance relative to CO of 10–20% [16, 37, 38]. Very recent observations in the S140 cloud [39] revealed that the CI emission near the interface between the HII and neutral material region consists of

narrow and broad velocity components. In the broad velocity material, the relative abundances of CI and CO are comparable.

The large extent and spatial coexistence of emission from CI, CII, and warm CO are in accordance with models of PDRs [40, 41, 42]. These models show that the chemical structure of a cloud illuminated by UV radiation 10^5 times the local (near the sun) interstellar value and with a gas density of $2 \times 10^5\,\mathrm{cm}^{-3}$ changes sharply as a function of the visual extinction A_v. A_v is a parameter closely resembling the optical depth and it provides a measure of the penetration depth into a cloud (see, e.g., [43, 44]). At $A_\mathrm{v} = 1 - 2$ penetration atomic hydrogen transforms into its molecular form, i.e., H_2 with carbon and oxygen remaining in the form ionic CII and neutral OI, respectively. Deeper into the cloud $(A_\mathrm{v} \sim 5)$, ionized carbon decreases sharply and neutral carbon, CI, peaks giving way further inward to material in molecular form, mainly CO. The study of these interface regions is of strong interest, particularly in view of the observed highly clumped form of the molecular material and its probable connection to star formation in these areas.

1.3.5 Molecular Cloud and Star Formation

During the past 50–60 years, powerful methods and highly sensitive instrumentation were developed and finally assigned to specific tasks for purposes of analytic research for studying atoms and molecules. Among these methods are atomic and molecular spectroscopy. They can reach linear dimensions of several hundreds of light years which contain total masses of $10^6\,\mathrm{M}_\odot$. The closest GMC to the Solar System is the Orion molecular cloud complex with a distance of about 450 pc or 1,500 light years.

Molecular clouds are the most massive and in extent the largest individual objects, both galactic and extragalactic. These clouds can be studied using molecular transitions as general probes to reveal to us the deep interior of active sites of star formation. Star formation is an on-going process, and it can be monitored "live" by radio telescopes. If one accepts for the moment the "Big Bang" as the beginning of the universe, then all the elements, with the exception of hydrogen (H), deuterium (D), and helium (He), have been synthesized slowly by the thermonuclear reactions in the hot interior of stars. During their final thermonuclear stages, stars are known to return part of their processed material to the ISM, enriching it with elements heavier than the light elements, hydrogen and helium, which they have synthesized during the various nuclear burning stages. On the other hand, there is little doubt that the ISM furnishes the raw material for new stars to form.

However, star formation takes place in the denser parts of molecular clouds, where hydrogen has been converted to molecular hydrogen, H_2, and where the spectra of molecules such as CO, CS, etc. make an important contribution to the heat balance. Interstellar molecular radiation from more than 150 molecules—together

with some atomic fine structure lines—continues to excite the astronomers around the world and arouses their fancy. So far, the interstellar molecules serve as the most powerful tool for probing deep into the interior of molecular clouds. The field of interstellar spectroscopy has matured to the point that optical absorption spectroscopy has only rather limited value, since the high dust content of the *dark* clouds makes them opaque to visible and ultraviolet light.

1.4 Molecular Spectroscopy: An Irreplaceable Tool

Historically, the interdependence of laboratory spectra and those received from the heavens was made obvious by Fraunhofer in the wake of his first, great spectroscopic discovery in 1718. Forty years after Fraunhofer's original discovery of the solar spectrum, the power of spectroscopy was clearly demonstrated by comparing spectra which were obtained in the laboratory with those recorded from stars. This correlation marked the time (1769) and place (Heidelberg) of the establishment of spectroscopy as an analytic tool. Kirchhoff and Bunsen, professors of physics and chemistry at the University of Heidelberg recognized the analytic power of spectroscopy and the unparalleled capability to study both physical and chemical processes in the laboratory and in cosmic dimensions. The new tool "spectroscopy" and its future applications were stated in an article of Kirchhoff and Bunsen that it would open "an entirely untrodden field, stretching far beyond the limits of the earth or even our solar system." They praised the almost inconceivable sensitivity and applicability of spectroscopy that would lead to many new discoveries. The early spectroscopic techniques of Kirchhoff and Bunsen are basically still in use, but they have been extended duly refined, and it has become a computerized assignment process.

The basic spectroscopic technique of matching specific wavelengths or frequencies from distant objects with those spectral features obtained in the laboratory has remained in use till date and has supplied us with an abundance of detailed interstellar vistas of a fascinating information. The enormous technological and scientific advances which have occurred in the last 30 years have allowed for bringing forth two developments. First, they have made spectroscopic observations possible throughout virtually the entire electromagnetic spectrum—though with different resolution and sensitivity—providing access to an overwhelming amount of spectral features. Second, they have pushed the accuracy of spectral line identification in some wavelength regions, e.g., at microwave and millimeter wavelengths, to about one part in 10^9, thus virtually excluding erroneous identifications. In the optical region, a spectral resolution of about one part in 10^5 is achieved and this suffices since the density of a spectrum is not as high as in the millimeter wave region. Most of the hundred or more interstellar molecules detected to date have been identified in the microwave, millimeter-, and submillimeter-wave part of the electromagnetic spectrum via their characteristic rotational transition frequencies. An increased number of new identifications will

come forward in the Terahertz region. The interstellar carbon complex, CCC or the linear molecule C_3, has recently been identified. Other gas phase molecules have been detected in the infrared via characteristic vibrational frequencies.

1.4.1 Scope of Interstellar Atomic and Molecular Spectroscopy

Atoms and molecules, both neutral and ionized, exhibit spectral features throughout most of the electromagnetic spectrum. These spectral lines—in emission and/or absorption—carry detailed and rather specific information on the physical and chemical conditions of the sources from which they emanate. In fact, the heights of the energy levels of the observed transitions together with the degree of their population furnishes a reliable measure of the excitation conditions and thus the temperature of the source itself. The relative intensities of various transitions of a molecule, in conjunction with the principle of statistical equilibrium, can be used to derive the gaseous number-density of the source.

Since the first discovery of polyatomic molecules in space, the field of interstellar spectroscopy has branched out into many different areas of physics, astronomy, chemistry, biology, and technology. Despite this astounding diversity, two major scientific trends dominate the technical developments:

1. The quest for studies of the atomic and molecular distribution on a wide range of spatial scales from hundreds of degrees down to about 1 arcsec and less. The aim is to obtain a broad overview of the large-scale galactic distribution of molecular clouds and a high spatial-resolution picture of the internal cloud structure with the hope of ultimately resolving the details of star-forming regions. This wide range of spatial resolution can be achieved by the use of small and large millimeter- and sub-millimeter-wave single-dish telescopes and telescope arrays.
2. The extension of the presently available frequency region into the Terahertz band of the electromagnetic spectrum accessible for interstellar spectroscopic study from the "standard" 10 cm to 1 mm wavelengths into the sub-millimeter and far-infrared regions. Multiline studies, probing high excitation conditions of hot and dense star-forming regions, are behind the strong push to open the sub-millimeter and far-infrared regions to astronomical observation, from earth-based, airborne, and satellite missions. The two disciplines, laboratory and interstellar research, of microwave, millimeter-wave and Terahertz spectral lines have always been intimately connected.

However, quite independently of the wavelength region, the spectroscopic history tells us that the fascinating interplay of the research started from the very beginning of spectroscopy, at the time of Fraunhofer, Bunsen and Kirchhoff (the wavelength region—OPTICAL LINES). It has been exciting to witness the expansion toward the IR-region and since 1968, with the knowledge of the existence of the first polyatomic interstellar molecule, NH_3 at 23 GHz, a fascinating

relationship between laboratory development and interstellar progress, determined in many cases the pace of the research. It was, and still is, equally rewarding to monitor the technological advances and at the same time follow the conduct of a complicated observation. These type of measurements were carried through quite extensively.

One extremely important constituent of molecular clouds are atoms and molecules in the form of gas. At present, there are more than 150 interstellar molecules known to exist in various interstellar clouds, i.e., dark and translucent clouds. The existence of such a diverse chemistry indicates a chemical evolution of cosmic dimensions taking place. It is fascinating to observe that a large majority (about 70 molecules) of interstellar molecules contains at least one or more carbon atoms per molecule. This distribution of carbon indicates strongly that the chemical bonding in interstellar space resembles the covalent bond character known from laboratory experiment. Interstellar space does support the formation of carbon and its wide use in the interstellar chemistry. It is the property of the covalent carbon bond to withstand the very hostile surroundings associated with interstellar clouds.

1.4.2 Terahertz Region: Far–InfraRed Domain

The entire infrared domain covers the wavelengths region from $\lambda \sim 1$ mm all the way down to $\lambda \sim 1\mu$m (or 300 THz) in four wavelengths intervals. From the long wavelength's end to that of the shortest wavelength, they are named as follows:

$\lambda \sim 1$–0.3 mm	sub-millimeter wave (Sub-MM) region,
$\lambda \sim 0.3$–50 μm	far-infrared (FIR) region,
$\lambda \sim 50$–3 μm	mid-infrared (MIR) region,
$\lambda \sim 3$–1 μm	near-infrared (NIR) region.

The two long wavelength intervals, the sub-millimeter, or sometimes called the radio region, and the FIR regions, are of high interest, for they turn out to be the Terahertz (THz) band.

The THz window of the electromagnetic spectrum is sandwiched between the two more established areas—the millimeter-wave band and the infrared region. At the long wavelength end, the THz window joins the microwave region and accordingly, at the short end of the THz domain, one finds eventually closing up to the optical region. Thus, the THz-domain covers in total approximately the same region as traditionally has been covered for the Far–Infrared, FIR. Although there is no official agreement known to us, which would define the area exactly, the frequency gap between 10^{11} Hz and 5×10^{12} Hz represents the THz region. It is advantageous to note that 1 THz (=1,000 GHz) corresponds to an energy of 4 meV or 50 K. The THz region, if considered from the infrared part of the spectrum, has been referred to traditionally as the far–infrared region, FIR, which bridges the gap between microwave and optical region.

Being situated between the radio and infrared domains, the THz region borrowed to a large extent its techniques from the established areas. Predominantly, it relied to a certain extent, but by no means entirely, on the transfer of technology from the millimeter-wave region. Despite this enormous transfer, the THz region has become the hunting ground for a rich, scientific prey. But still it remains to be one of the most poorly explored areas of the entire electromagnetic spectrum. The access to the field is still not an easy one, and two physically very different reasons are dominating the main causes for these persistent access difficulties:

1. The first one is directly related to the problems encountered in fabricating the mm-wave equipment and optimizing its sub-mm and THz usage.
2. The second problem is of rather different origin, and is the frequency-dependent attenuating nature of the Earth's atmosphere.

The combined effects of these two causes have been in the past the main obstacles toward a quick and speedy recovery of the THz region. The general difficulties, encountered in scaling down in a linear fashion the intrinsic submillimeter wave hardware, remain a notoriously difficult task. But, in principle, the problems of producing accurate pieces of millimeter-wave hardware are slowly mastered by the quality outcome of an in-depth extensive technological program. A variety of laboratories, including the Cologne Laboratories, have taken great benefit from these measures.

Other important prerequisites are beyond any doubt, the availability of high gain sub-millimeter-wave telescopes on appropriate mountain sites, such as the KOSMA 3-m-submillimeter-wave telescope on Gornergrat, in the Swiss central Alps, or the reliable supply of sub-millimeter-wave radiation sources, together with the proper combination of receivers, detectors, low-noise amplifiers, and spectrometers. These fairly expensive custom-made pieces of equipment often do stretch the resources available to the different groups. It is to be noted here that commercially only very few millimeter and/or sub-millimeter items can be purchased. Some of the most important sub-millimeter-wave components have to be produced by the research teams themselves. These preconditions are often too prohibitively high for one group so as to overstretch the resources available.

In this book, we will consider molecular lines detected by laboratory techniques, whereby THz spectroscopy can employ broad band scanning, i.e., about 50 GHz, and the ultimate frequency resolution achieved with our spectrometers is around 40 kHz at about 1 THz. These laboratory-recorded line-width can be compared with the same lines emitted from interstellar sources. Interstellar lines compare in width quite favorably, provided they emanate from quiescent dark clouds, where no star formation takes place.

Another important group of lines are in the region beyond 2 THz: the vibration–rotation lines of low bending vibrational bands have recently been discovered in the case of CCC in the ν_2 bending mode at about 2 THz.

Finally, the increasing attenuation of the Earth atmosphere, as one progresses into the THz region, i.e., >1 THz, has to be added to the general difficulties.

However, judged by some of the recently secured results, the Terahertz region promises to be the band of plenty. In fact, it seems to hold the key for some of the very important aspects of physics, chemistry, astrophysics, and of laboratory and interstellar spectroscopy. The reason for this behavior rests in the basic property of the Terahertz radiation to match the energy level schemes of a large variety of applications. The Terahertz spectrum is dominated by light molecules containing hydrogen. They are known as the hydrides.

1.5 Episodical Appendix

1.5.1 Life Story of Fraunhofer

Joseph von Fraunhofer (1787–1826), German optician and physicist, was born at Straubing, Bavaria, March 6, 1787.[2] The son of a poor glazier, he was apprenticed at the age of 12 to a lens grinder in Munich. He later went to work at the Utzschneider Optical Institute near Munich, and rose to become the institute's general manager, in 1818. Fraunhofer acquired great skill in the manufacture of lenses and constructed some of the finest refracting telescopes ever built. He invented a heliometer and a diffraction grating for measuring the wavelengths of light. He studied and carefully measured 576 of the dark lines in the solar spectrum, previously noticed by W. H. Wollaston. These became to be known as Fraunhofer lines. Fraunhofer's studies were cut short by his early death from tuberculosis at Munich, June 7, 1826.

In all respects, the discovery that the sun and the stars are made up of the same chemical elements as the Earth is one of the earliest and greatest achievements of spectroscopy and its first application to astronomical objects. The identification of the Fraunhofer lines was begun in the years 1859–1861 by the new methods of spectral analysis introduced by R. W. Bunsen and G. R. Kirchhoff. This correlation marked the time and place of the establishment of spectroscopy as an analytic tool with an unparalleled power to study both physical and chemical processes in the laboratory and in cosmic dimensions. The power of this new tool "spectroscopy" and its potential for future applications were recognized by Kirchhoff and Bunsen, who stated that it would open "an entirely untrodden field, stretching far beyond the limits of the Earth, or even of our solar system" and who noted the "almost inconceivable" sensitivity of spectroscopy that would lead to the detection of hitherto unknown elements. Indeed many new elements, such Cs, Rb, and He, were subsequently detected by their atomic spectra, in the laboratory, and in stars. In 1914, Martin Schwarzschild tried to explain the dark Fraunhofer lines in terms of widths and shapes with the idea to derive from the stellar lines the structure and

[2] Fraunhofer Gesellschaft, München, Germany, provides a biographic document for Fraunhofer: http://www.fraunhofer.de/en/about-fraunhofer/joseph-von-fraunhofer/.

evolution of the stars. But a more detailed understanding of the spectra and their associated energy level diagrams had to await the advent of quantum mechanics in the 1920s and its application to molecular spectra. These efforts in obtaining extremely precise data on stars and derived from the observed spectra of 4,000 stars were classified into four spectral types. Finally, all this study culminated in the famous Harvard classification of stars catalog. Over a time-span of several tens of years the Henry–Draper Catalog which contains the spectral type of about one quarter of a million stars. The basic result of this enormous experimental data is that the Harvard sequence of stars is essentially arranged according to their temperatures.

1.5.2 Life Story of Herschel

Friedrich Wilhelm Herschel (1738–1822), generally known as Sir William Herschel, one of the most illustrious of astronomers, was born at Hannover, November 15, 1738.[3] His father was a musician employed as hautboy player in the Hanoverian guards. The family had immigrated from Bohemia in the early part of the seventeenth century, on account of religious troubles, they themselves being Protestants. Herschel's earlier education was necessarily of a very limited character, chiefly owing to the troubles in which his country at that time was involved; but, being at all times an indomitable student, he, by his own exertions, more than repaired this deficiency of his youth. He became a very skilful musician, both theoretical and practical; while his attainments as a self-taught mathematician were fully adequate to the prosecution of those branches of astronomy which, by his labors and his genius, he so eminently advanced and adorned. Whatever he did, he did methodically and thoroughly; and in this methodical thoroughness, lay the secret of what Dominique Arago very properly terms his "astonishing scientific success."

In 1755, at the age of 17, he joined the band of the Hanoverian guards, and with his detachment visited England accompanied by his father and eldest brother. In the following year, he returned to his native country, but two years later, impelled by the troubles that surrounded him, he finally quit Hannover to seek his fortunes in England. As might have been expected, the earlier part of his career in his adopted country was attended with formidable difficulties and much privation. We find him engaged in several towns in the north of England as an organist and a teacher of music, but these were occupations not attended with any lucrative results. In 1766, the tide of his fortunes began to flow, inasmuch as he obtained the appointment of organist to the Octagon Chapel in Bath, at that time the resort of the wealth and fashion of the city, and of its numerous distinguished visitors.

[3] A few biographic reports have been published for Herschell, e.g., Millman [45].

In the year 1781, Herschel made a discovery which, as we shall see, soon completely altered the character of his professional life. In the course of his systematic examination of the heavens with a view to the discovery of the plan of their construction, he lighted on an object which at first he supposed to be a comet, but which, by its subsequent motions and appearance, turned out to be a new planet, moving outside of the orbit of Saturn. To this planet, he in due time assigned the name of Georgium Sidus; but this name has by general consent been laid aside in favor of Uranus.

In the year 1782, in consequence of his fame, Herschel was invited to Windsor by George III, and then accepted the offer made by the king to become his private astronomer, and thenceforth devoted himself wholly to a scientific career. The salary offered and accepted was £ 200 per annum, to which an addition of £ 50 per annum was subsequently made for the astronomical assistance of his faithful sister. Dr. Watson, to whom alone the amount of this salary was mentioned, made the natural remark, "Never before was honor purchased by a monarch at so cheap a rate." In this way, the great philosophical astronomer was shifted from Bath first to Datchet and soon afterward permanently to Slough, within easy access of his royal patron at Windsor.

It was at Slough in 1783 that he wrote his first memorable article on the "Motion of the Solar System in Space," a sublime speculation, yet through his genius realized by consideration of the utmost simplicity. He returned to the same subject with full details in 1805. It was also after his shift to Slough that he published his first memoir containing his speculative ideas on the Construction of the Heavens, which from the beginning had been the chief aim of his tools, both of mind and body. In a long series of remarkable articles, addressed as usual to the Royal Society, and extending from the year 1784 to 1818, when he was 80 years age, he demonstrated the fact that our sun is a star situated not far from the bifurcation of the Milky Way, and that all the stars visible to us lie more or less in clusters scattered throughout a comparatively thin stratum, but in the other two dimensions stretching immeasurably further into space. At one time, he imagined that his powerful instruments had pierced through this stellar stratum of the Milky Way, and that he had approximately determined the form of some of its boundaries. In the last of his memoirs, he had convinced himself of his error, and he admitted that to his telescopes our stratum of stars is "fathomless." Over this stratum of stars and their planetary attendants, the whole being in ceaseless motion round some common center of gravity as the resultant point of the combined gravitation, Herschel discovered on either side a canopy of discrete nebulous masses, from the condensation of at least a part of which the whole stellar universe had been formed, a magnificent conception, pursued with a force of genius and put to the practical test of observation with an industry almost incredible. It was the work of a single mind, carried to its termination with no assistance beyond that of a loyal sister, almost as remarkable a personage as himself.

Hitherto, we have said nothing about the grand reflecting telescope, of 40 foot focal length and 4 foot aperture, which is too often regarded as the chief effort of

his genius and his perseverance. The full description of this celebrated instrument will be found in the 85th volume of the Transactions of the Royal Society. Gigantic as it really was, we are disposed to regard it as among the least of his great works. On the day it was finished (August 28, 1789), Herschel saw at the first view, in a grandeur not witnessed before, the Saturnian system with all its six satellites, (Pan, Atlas, Pandora, Prometeus, Epimetheus, Janus, and Mimas) five of which had been discovered long before by Huygens or Cassini, while the sixth, subsequently named Enceladus, which he had, two years before, sighted by glimpses in his exquisite little telescope of 6.5 inches aperture, but now saw in unmistakable brightness with the towering giant he had just completed. On September 17, he discovered a seventh, which proved to be the nearest of all the satellites of Saturn. It has since that time received the name of Mimas. It is somewhat remarkable that, notwithstanding his long and repeated scrutinies of this planet, the eighth satellite Hyperion, and the crape ring should have escaped him.

Herschel married the widow of Mr. John Pitt, a wealthy London merchant, on May 8, 1788, by whom he had only one son, John Frederick William. The prince regent conferred a Hanoverian knighthood upon him in 1816. But a far more value and less tardy distinction was the Copley medal assigned to him by his associates in the Royal Society in 1781. He died at Slough on August 25, 1822, in the eighty-fourth year of his age, and was buried under the tower of St. Laurence Church, Upton, within a few hundred yards of the old site of the 40-foot telescope. A mural tablet on the wall of the church bears a Latin inscription from the pen of the late Dr. Goodall, provost of Eton College. A collection edition of his astronomical memoirs would speak of his genius in unmistakable language; but this has not been published.

Herschel was an indefatigable worker. For many years, he made nightly systematic surveys of the sky, examining planets, stars, nebulae, and star clusters. By day he worked over his results or directed the construction of his telescopes. His sister Caroline was his assistant and became an independent worker of some standing. Herschel observed sun-spots, confirmed the gaseous nature of the sun, rediscovered the Martian polar caps, and believed in the possibility of life on Mars. He announced the trade-wind theory of Jupiter's belts and discovered two of Jupiter's and two of Uranus' Moons. His main purpose, he said, was a to gain "knowledge of the Construction of the Heavens." His principal study was on stars, and it was in this field that he made two discoveries of primary importance: the movement of the solar system through space, and the evidence that binary stars move around a common center of gravity. This evidence substantiated the universality of Newton's theory of gravitation. Herschel discovered nearly 1,000 double stars. In 1785, he brought out the disk theory of the stellar system, holding that all nebulae are clusters of stars, which he called island universes. He abandoned the idea of the Milky Way as a collection of stars uniformly distributed and came to believe that it was composed of local groups and clusters. The nebulae, he thought, were all clusters not yet resolved into stars. Herschel also discovered nebulae and clusters numbering from 2,000 to 3,000 on which he published catalog

reports. After years of profound research, he brought out an important article on the construction of the heavens, theorizing on the evolution of matter by successive steps from nebulous material to the final planetary state, by means of gravitation. Herschel died at Slough, England, August 25, 1822.

References

1. E.E. Barnard, E.B. Frost, *A Photographic Atlas of Selected Regions of the Milky Way* (Carnegie Institution of Washington, Washington, 1927)
2. G.B. Donati, Mon. Not. R. Astron. Soc. **25**, 31 (1864)
3. W. Huggins, Proc. R. Soc. Lond. **34**, 148 (1882–1883)
4. A.E. Douglas, Astrophys. J. **114**, 446 (1951)
5. L. Spitzer Jr., E.G. Zweibel, Astrophys. J. **191**, L127 (1974)
6. L. Spitzer, *Physical Process in the Interstellar Medium* (Wiley-Interscience, New York, 1978)
7. H.I. Ewen, E.M. Purcell, Nature **168**, 356 (1951)
8. C.A. Muller, J.H. Oort, Nature **168**, 357 (1951)
9. L. Essen, R.W. Donaldson, M.J. Bangham, E.G. Hope, Nature **229**, 110 (1971)
10. T.L. Wilson, L. Filges, in *Proceedings of IAU Colloq*, vol. 125, ed by M.A. Godon, R.L. Sorochenko (Kluwer, Dordrecht, 1990)
11. G.L. Verschuur, K.I. Kellermann, *Galactic and Extra-Galactic Radio Astronomy* (Springer, Berlin, 1988)
12. G. Melnick, G.E. Gull, M. Harwit, Astrophys. J. **227**, L29 (1979)
13. J.W.V. Storey, D.M. Watson, C.H. Townes, Astrophys. J. **233**, 109 (1979)
14. R.W. Russel, G. Melnick, G.E. Gull, M. Harwit, Astrophys. J. **240**, L99 (1980)
15. M.K. Crawford, R. Genzel, C.H. Townes, D.M. Watson, Astrophys. J. **291**, 755 (1985)
16. R. Genzel, A.I. Harris, J. Stutzki, D.T. Jaffe, Astrophys. J. **332**, 1049 (1988)
17. A. Dalgarno, R.A. McCray, Annu. Rev. Astron. Astrophys. **10**, 375 (1972)
18. G.J. Stacy, N. Geis, R. Genzel, J.B. Lugten, A. Poglitsch, A. Sternberg, Astrophys. J. **373**, L99 (1980)
19. S.C. Madden, R. Genzel, F. Herrmann, A. Poglitsch, N. Geis, C.H. Townes, G.J. Stacy, Bull. Am. Astron. Soc. **24**, 1268 (1992)
20. A.L. Cooksy, R.J. Saykally, J.M. Brown, K.M. Evenson, Astrophys. J. **309**, 828 (1986)
21. A. Omont, Rev. Mod. Astron. **1**, 102 (1988)
22. W.D. Watson, Rev. Mod. Phys. **48**, 513 (1976)
23. G. Winnewisser, E. Herbst, Top. Curr. Chem. **139**, 119 (1987)
24. G. Winnewisser, E. Herbst, H. Ungerechts, in *Spectroscopy of the Earth's atmosphere and interstellar medium*, ed. by K.N. Rao, A. Weber (Academic Press, Boston, 1992)
25. T. Dunhum Jr., W.S. Adams, Publ. Astron. Soc. Pac. **49**, 26 (1937)
26. P. Swings, L. Rosenfeld, Astrophys. J. **86**, 483 (1937)
27. A.E. Douglas, G. Herzberg, Astrophys. J. **94**, 483 (1941)
28. G. Winnewisser, J.T. Armstrong (eds.), in *The Physcis and Chemistry of Interstellar Molecular Clouds*. Lecture Note in Physics 331. (Springer, Berlin, 1989)
29. G. Winnewisser, E. Herbst, Rep. Prog. Phys. **56**, 1209 (1993)
30. E. Herbst, Annu. Rev. Phys. Chem. **46**, 27 (1995)
31. E.F. van Dishoeck, Faraday Discuss. **109**, 31 (1998)
32. K.W. Hinkle, J.J. Keady, P.F. Bernath, Science **241**, 1319 (1988)
33. P.F. Bernath, K.W. Hinkle, J.J. Keady, Science **244**, 562 (1989)
34. A. van Orden, J.D. Cruzan, R.A. Provencal, T.F. Giesen, R.J. Saykally, in *Airborne Astronomy Symposium on the Galactic Ecosystem, ASP Conference Series*, vol. 73 (1995), p. 67

35. M. Tuley, D.A. Kirkwood, M. Pachkov, J.P. Maier, Astrophys. J. **506**, L69 (1998)
36. S. Yamamoto, S. Saito, Astro. Phys. J. **370**, L103 (1991)
37. T.G. Phillips, P.J. Huggins, Astrophys. J. **251**, 533 (1981)
38. J. Keene, G.A. Blake, T.G. Phillips, P.J. Huggins, C.A. Beichman, Astrophys. J. **299**, 967 (1985)
39. J. Hernichel, D. Krause, R. Roehrig, J. Stutzki, G. Winnewisser, Astron. Astrophys. **259**, L77 (1992)
40. A.G.G.M. Tielens, D. Hollenbach, Astrophys. J. **291**, 722, 747 (1985)
41. A. Sternberg, A. Dalgarno, Astrophys. J. **338**, 197 (1989)
42. D.J. Hollenbach, T. Takahashi, A.G.G.M. Tielens, Astrophys. J. **377**, 192 (1991)
43. C.W. Allen, Astrophysical Quantities (Athlone Press, London, 1973)
44. B.D. Savage, J.S. Mathis, Annu. Rev. Astron. Astrophys. **17**, 73 (1979)
45. P.M. Millman, J. R. Astron. Soc. Can. **74**, 134 (1980)
46. G. Winnewisser, C. Kramer, Space Sci. Rev. **90**, 181 (1999)

Chapter 2
Molecules Detected in Interstellar Space

Karl M. Menten and Friedrich Wyrowski

In this section, an overview is given of molecules detected in the interstellar medium and circumstellar envelopes. Given that so far more than 150 species have been observed in interstellar space, this overview can by no means be complete. Therefore, we focus on the detections of the first molecules and then give examples of prototypical molecules and recent new detections. This section is based on the Menten (2003) article presented in the proceedings of the 2003 Zermatt conference [1].

2.1 Detection of the First Interstellar Molecules

The first optical detections of the diatomic radicals CH and CN and the CH^+ ion were already described in Sect. 1.3.1. Here, the first *radio* detections are discussed.

The late 1960s and early 1970s were an era of great excitement in all branches of radio astronomy. In spectral line research, 12 years after the detection of the first line, the 21 cm HI hyperfine structure (hfs) transition [2], finally, the first molecule was found: the hydroxyl (OH) radical [3].

The OH Λ-doublet transitions, as well as many other lines at m-, cm- and mm-wavelengths from a variety of molecules, had been identified as possible astronomical targets in a visionary article by Charles Townes [4].[1]

K. M. Menten and F. Wyrowski (✉)
Max-Planck-Institut f. Radioastronomie, Auf dem Hügel 69, 53121 Bonn, Germany
e-mail: wyrowski@mpifr-bonn.mpg.de

[1] see also Shklovsky [5].

K. M. T. Yamada and G. Winnewisser (eds.), *Interstellar Molecules*,
Springer Tracts in Modern Physics 241, DOI: 10.1007/978-3-642-16268-8_2,

Shortly after the detection of OH, Hoglund and Mezger [6] discovered the first radio recombination line, H109α at 5009 MHz. *Molecular* radio astronomy started in earnest in 1968/1969, with the discoveries of ammonia (NH_3; Cheung et al. [7]) and water vapor (H_2O; Cheung et al. [8]) by a group around Townes,[2] as well as the first complex organic species, formaldehyde (H_2CO; Snyder et al. [9]), breaking loose a real gold rush that has yet to stop. Even today, approximately 2–4 "new" interstellar or circumstellar[3] molecules are found each year, totaling to more than 150 species (not counting isotopomers).[4]

The early history of "molecule-hunting" is well documented in the review by Snyder (1972; "Molecules in Space" [10]), which gives a very useful introduction to molecular radio astronomy, that is still very much readable today. In the same volume, the review, following Snyder's by Winnewisser et al. and presents an equally excellent overview of the laboratory side of "Millimetre Wave Spectroscopy" [11]

As shown in Table 2.1,[5] many of the early molecular detections were made at low radio frequencies (and toward Sagittarius B2). For a full list of interstellar molecules detected in space, see Chap. 5.

Almost concurrently with cm-wavelength molecular radio astronomy, shorter wavelength exploration started. Driven by new high-frequency receiver technology and, generally, higher line intensities and a much higher "line density" (i.e., lines per GHz) the "millimeter explosion" started with the discoveries of CO by Wilson et al. [35] and HCO^+ ("X-ogen") by Buhl and Snyder [36] both in 1970 (the latter published in 1971), and continues through today, having reached the submillimeter range in the 1980s.

After the millimeter window was opened, (most) people spontaneously lost interest in the cm-range because

- Most molecules have the bulk or the entirety of their rotational spectrum at (sub)millimeter wavelengths.
- Almost all "simple" (di- or triatomic), light molecules have (sub)mm or far-IR (FIR) rotational spectra.
- Many of the complex molecules were (for a long time) *only* found in Sgr B2.

Interest remained high in special cm-wavelength lines, including the NH_3 inversion transitions near 24 GHz, a number of prominent maser lines from OH (hfs, 1.7 GHz and higher frequencies), H_2O (22.2 GHz), CH_3OH (25, 12.2, and

[2] Both lines were on Townes' (1957) list [4]!

[3] Circumstellar molecules exist in the envelopes of evolved giant stars. Many species are detected there which are also found in interstellar clouds, whereas some others, have so far *only* been detected in a circumstellar environment.

[4] See http://www.ph1.uni-koeln.de/vorhersagen/molecules/main_molecules.html.

[5] The frequencies are taken from the JPL catalog [33]; see http://spec.jpl.nasa.gov/ or the Cologne Database for Molecular Spectroscopy (CDMS) [34]; see http://www.ph1.uni-koeln.de/vorhersagen/molecules/main_molecules.html. Numbers in parentheses are uncertainties in the last significant digit(s).

Table 2.1 The first interstellar "Radio" molecules

Name	Species	Transition	Frequency (MHz)	Reference
Hydroxyl	OH	$^2\Pi_{\frac{3}{2}}, J = \frac{3}{2}$	1665.4018(2)[a]	[3]
Ammonia	NH_3	(1, 1)	23694.4955(1)[b]	[7]
Formaldehyde	H_2CO	$1_{11} - 1_{10}$	4829.660(1)[b]	[9]
Water	H_2O	$6_{16} - 5_{23}$	22235.08(2)[b]	[8]
Methyl alcohol	CH_3OH	$1^+ - 1^-$	834.267(2)	[12]
Formic acid	HCOOH	$1_{11} - 1_{10}$	1638.804(1)	[13]
		$2_{11} - 2_{12}$	4916.319(3)	[14]
Formamide	NH_2CHO	$1_{11} - 1_{11}$	1539.58(2)[c]	[15]
		$2_{11} - 2_{12}$	4618.55(2)[c]	[16]
Cyanoacetylene	HC_3N	$1 - 0$	9098.6537(3)[c]	[17]
	$H^{13}C_3N$	$1 - 0$	$\sim$9060[d]	[18]
	$H^{12+13}C_3N$	$1 - 0$	$\sim$9000[d]	[19]
Acetaldehyde	CH_3CHO	$1_{10} - 1_{11}$	1065.075(5)	[20]
Methylidine	CH	$^2\Pi_{\frac{1}{2}}, J = \frac{1}{2}$	3263.788(10)[e]	[21]
Thioformaldehyde	H_2CS	$2_{11} - 2_{12}$	3139.38(3)	[22]
Methanimine	CH_2NH	$1_{10} - 1_{11}$	5290.31(4)	[23]
Methylamine	CH_2NH_2	$2_{02} - 1_{10}$	8776.2(1)[f]	[24]
Vinyl cyanide	H_2CCHCN	$2_{11} - 2_{12}$	1371.8262(1)	[25]
Methyl formate	$HCOOCH_3$-*A*	$1_{10} - 1_{11}$	1610.2445(7)	[26]
	$HCOOCH_3$-*E*	$1_{10} - 1_{11}$	1610.91(10)	[27]
Dimethyl ether	$(CH_3)_2O$	$2_{02} - 1_{11}$	9119.668(15)[c]	[28]
Cyanodiacetylene	HC_5N	$4 - 3$	10650.650(4)	[29]
		$2 - 1$	5325.328(2)	[30]

Only those molecules first detected at cm-wavelengths are listed. For early detections in the mm-range, see Snyder [10]. All molecules were first detected in the transitions listed, except for dimethyl either which was discovered in its $6_{06} - 5_{15}$ line at 90938.10(3) MHz by Snyder et al. [31]. No detections for isotopomers are listed, except for HC_3N

[a]Apart from the $F = 1 - 1$ line listed, also the $2 - 2$ line at 1667.3590(2) MHz was reported in the detection paper

[b]Line with hfs, intensity-weighted frequency is given

[c]Line with hfs, average of the lowest and the highest hfs line frequency, is given

[d]Various lines with differently placed ^{13}C between 8815 and 9100 MHz

[e]Apart from the $F = 0 - 1$ line listed, also the $F = 1 - 1$ and $F = 1 - 0$ lines at 3335.475(10) and 3349.185(10) MHz, resp., were reported in the detection paper (frequencies from Rydbeck et al. [32])

[f]Frequency from Fourikis et al. [24]

6.7 GHz), as well as the CH hfs lines (3.3 GHz). All of these, except for CH_3OH, have all or the bulk of their *rotational* spectra at submillimeter and far-infrared wavelengths.

Considering the mm-wavelength data coming in, soon after the radio observations, it became clear that the emission from many low-frequency, low-J lines of complex molecules toward Sgr B2 must be (weakly) inverted. Morris et al. [37] pointed out that this can be understood if the dipole collision is not the dominant factor of the collisional process; in such cases, population inversion for the $J = 0$

and 1 levels (at least for linear or near-linear species) may occur easily over a wide range of physical conditions (e.g., [38]). This is borne out by their statistical equilibrium calculations.

After the first complex molecules were found in Sgr B2, this source turned into a Bonanza: The described inversion mechanism together with a relatively strong, extended continuum background "boosted" many otherwise undetectable lines into "observability". As a consequence, the vast majority of interstellar molecules was and still is found in Sgr B2, many of the most complex ones *only* there. All of the molecules listed in Table 2.1 are found in this source.

2.2 The Habitat of Interstellar Molecules

The by-far most abundant interstellar molecule is molecular hydrogen, H_2. Since H_2, because of its symmetry, does not have an electric dipole moment, only weak electric quadrupole transitions between rotational or ro-vibrational levels can be observed. Therefore, low rotational transitions of the CO molecule, although about by 10^{-4} less abundant than H_2, have become the most important tool to study the large scale distribution of the molecular gas in the interstellar medium. Most of the molecular gas can be found in giant molecular clouds such as the region shown in Fig. 2.1. These clouds have diameters of 10–100 pc, masses of $\sim 10^{5-6.5}\,M_\odot$, and mean densities of several $100\,cm^{-3}$, but they are strongly clumped (e.g., [39]). The higher density clumps are probed in Fig. 2.1 by submillimeter dust continuum emission and are most closely associated with star formation. Giant molecular clouds are distributed along the Galactic plane with a small scale height of only ~ 100 pc. Although they occupy only a relatively small volume of the interstellar medium, they contain a large fraction of its mass.

In addition, molecules can also be found in the so-called diffuse clouds, which are more tenuous and fully exposed to UV radiation from stars (see the review by Snow and McCall [41]). In fact, the first detections of molecules in space have been done by the observations of sharp optical absorption lines in diffuse clouds.

Molecules can even be found in circumstellar envelopes which are due to strong mass loss of stars in their late stages of evolution. The central stars in this stage have a low temperature so that molecules and dust can be formed and fueled into the interstellar medium.

2.3 Metal-Bearing Molecules in the Interstellar Medium

Observations of species containing metals, as well as other refractory species such as SiO, deliver important information on depletion into dust grains. Moreover, when released either from sputtering of the grains or their mantles by violent

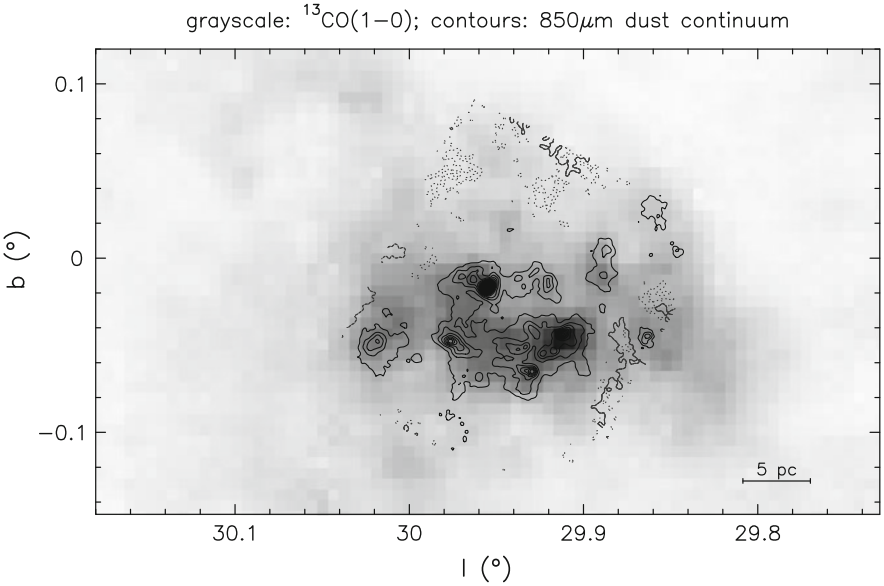

Fig. 2.1 The giant molecular cloud G29.9 seen in ^{13}CO (1–0) emission (grayscale) from the Galactic ring survey by Jackson et al. [40] overlaid with archival dust continuum observations from SCUBA at the JCMT

dynamics, such as protostellar outflows, they can be used as probes of these phenomena (see, e.g., Bachiller [42]).

Todate, four diatomic, non-H-bearing metal compounds (NaCl, KCl, AlCl, and AlF and three triatomic ones (MgNC, MgCN, NaCN, and AlNC) have been detected in the dense envelope of the carbon star IRC+10216 [43–49]. MgNC, NaCN, AlF, and NaCl were also found, recently, toward the proto-planetary nebula (PN) CRL 2688 ([49–51]; see Petrie [52] for a discussion of other candidate species for detection). Still, only one metal-containing molecule, FeO, has been detected in the interstellar medium, toward Sgr B2 [53].

As regards metal hydrides, radio and (sub)millimeter wavelength searches for interstellar NaH [54] and LiH[6] have so far been unsuccessful, as was a search for MgH in IRC+10216's envelope [56]. Optical wavelength absorption from CaH, AlH, FeH, and MgH has been found in cool stars and the Sun: MgH even in the integrated light of external galaxies (see, e.g., [57]).

[6] The ground state $J = 1 - 0$ transition of LiH is near 444 GHz, an atmospherically very unfavorable frequency. A tentative detection of this line was made in the redshifted ($z = 0.68$) dense absorbing cloud toward the B0218+357 gravitational lens system [55].

2.4 Light Hydrides

The history of interstellar hydrides begins with the detection by Dunham [58] of three optical absorption lines at 3957.7, 4232.6, and 4300.3 Å from diffuse interstellar clouds [58], which subsequently were found to arise from CH (4300.3 Å; McKellar [59]; suggested by Swings and Rosenfeld [60]) and CH^+ (the former two; [61]).

It has been thought for a long time that hydrides might play an important rôle in cooling the highest density regions of interstellar clouds. Hydrides have, first, large level spacings, allowing them to emit relatively a large amount of energy per quantum. Second, their large dipole moments require high critical densities for their excitation. Thus, their rotational levels are only excited in high-density regions with $n > 10^6\,\mathrm{cm}^{-3}$, making them effective coolants in this regime, where even rare CO isotopes are so optically thick that CO cooling becomes negligible compared to that of (the hydride) H_2O.

This regime was excluded in the classical study by Goldsmith and Langer [62] on "Molecular Cooling and Thermal Balance in Dense Molecular Clouds", but was re-addressed by Neufeld et al. [63], who found that for elevated temperatures, $T = 100K$, H_2O cooling dominates, and the hydrides' contribution is comparable to that *of all other molecules combined*, i.e., ≈30% of the former.

Recent detections of hydride rotational transitions were made by the Caltech Submillimeter Observatory (CSO), namely H_3O^+ ($J_K = 1_1^- - 2_1^+, 3_2^+ - 2_2^-, 3_0^+ - 2_0^-/307, 365, 396$ GHz, [64, 65]), SiH ($^2\Pi_{\frac{1}{2}}, J = \frac{3}{2} - \frac{1}{2}$/625, 628 GHz; [66]),[7] HCl ($J = 1 - 0$/626 GHz; [67]), $H_2O, H_2^{18}O$ ($1_{10} - 1_{01}/557, 548$GHz; [68]), HDO (the $1_{01} - 0_{00}$/465 GHz and $1_{11} - 0_{00}$/894 GHz ground-state transitions; [69, 70]),[8] and NH_2 ($J = \frac{3}{2} - \frac{3}{2}, \frac{1}{2} - \frac{1}{2}, \frac{3}{2} - \frac{1}{2}$/462, 459, 461 GHz); [71]). H_2D^+ ($1_{10} - 1_{11}/372$ GHz), the deuterated isotope of the key H_3^+ molecule was discovered with the James–Clerck–Maxwell telescope [72].[9] Observations using the Long Wavelength Spectrometer aboard the Infrared Space Observatory led to the discoveries of HF ($J = 2 - 1$/2.47 THz; [74]), HD ($J = 1 - 0$/2.68 THz and $2 - 1$/5.36 THz; [75]), plus various H_2O, OH, and CH rotational and some H_3O^+ inversion transitions (many toward Sgr B2; [76] and in the proceedings [1]).

A preliminary conclusion is that (for the only two sources observed, Orion-KL and Sgr B2) the measured HCl and HF abundances indicate that only a low percentage of all chlorine is in these molecules, suggesting significant depletion. If this should hold true for other hydrides as well, then their cooling contribution

[7] Tentative detection.

[8] A number of higher excitation cm and mm-wavelength $H_2O, H_2^{18}O$, and HDO transitions have also been found.

[9] H_3^+ itself was finally detected, after many arduous attempts, in absorption at near-infrared wavelengths by Geballe and Oka [73], benefitting from a monumental body of laboratory research, mainly gathered by Oka and collaborators (see the proceedings [1]).

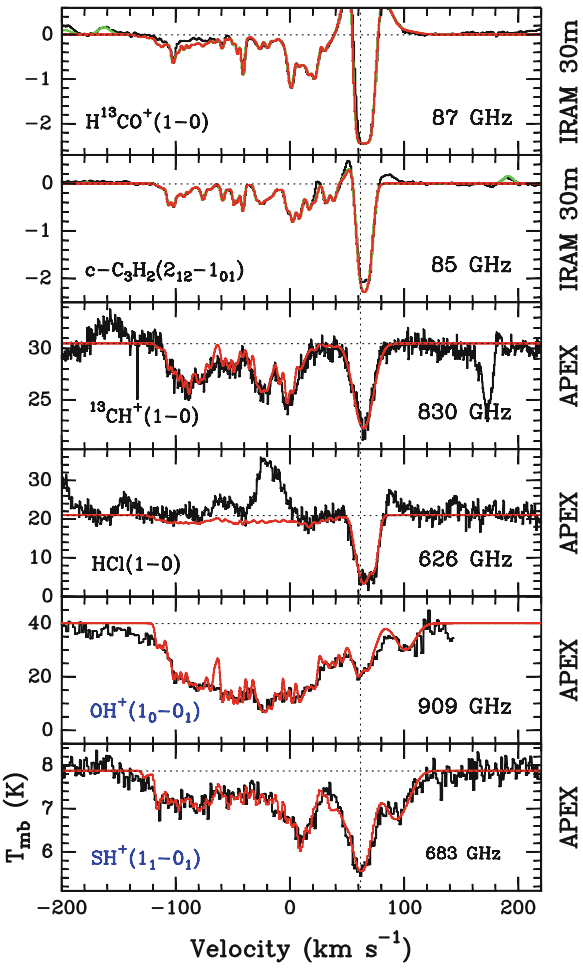

Fig. 2.2 New hydrides, observations using APEX toward Sgr B2(M) (the *upper two panels* show IRAM 30-m detections for comparison. The *gray lines* show synthetic spectra based on the velocity components seen in the C_3H_2 spectrum

could be much smaller than that discussed above. More sensitive observations of more transitions toward more lines of sight are needed and are being observed now using the APEX telescope and at the Herschel Space Observatory.[10]

Using the APEX telescope in Chile on the 5000-m high Chajnantor plateau, several hydrides (SH^+, $^{13}CH^+$, OH^+, and HCl) have recently been studied from the ground by Menten et al. [77] and Wyrowski et al. [78] in the absorbing diffuse clouds towards Sgr B2(M). SH^+ and OH^+ were new interstellar detections, and the detected absorption of a continuous velocity range on the line-of-sight showed these molecules to be an abundant component of diffuse clouds (see Fig. 2.2).

[10] http://astro.estec.esa.nl/SA-general/Projects/First/first.html.

With Herschel, also the HF ground-state transition has been detected in absorption (Neufeld et al., [79]), which shows that HF will be the dominant reservoir of interstellar flourine. From Herschel observations also, many detections of H_2O^+ are reported, which, compared to previous model predictions, turned out to have higher abundances in the low-density gas of diffuse clouds. Another new detection by Herschel is interstellar chloronium (H_2Cl^+, Lis et al., [80]), again with surprisingly high abundances.

2.5 Ions

2.5.1 Cation

In 1970, Buhl & Snyder found an unidentified interstellar line during their search for the HCN (1–0) line at 86.3 GHz and labeled it "X-ogen" [81]. Even before this article was published in *Nature*, Klemperer [82] proposed HCO^+ as the carrier of the X-ogen line, but only several years later, this claim could be confirmed by laboratory measurements and interstellar observations of $H^{13}CO^+$. This first detection of an interstellar ion, triggered studies on ion–molecule chemistry as the basis for the formation of interstellar molecules in the gas phase (e.g., [83]). In dense molecular clouds, the degree of ionization is determined by cosmic ray ionization of molecular hydrogen which further reacts with H_2 to form H_3^+. The H_3^+ ion, which plays a key role in driving the chemistry in molecular clouds, was only detected in 1996 by Geballe and Oka by infrared absorption of three rotation–vibration transitions [73]. About a dozen cations have so far been detected and, only recently, several anions as well.

2.5.2 Anions

In 1995, Kawaguchi et al. [84] reported in their centimeter spectral line survey of the circumstellar envelope of IRC+10216 the detection of a series of seven lines showing a spectral pattern of a linear molecule with a rotational constant of 1377 MHz. Only 11 years later, McCarthy et al. [85] could attribute with new laboratory measurements these lines to the first anion detected in interstellar space, C_6H^-. In addition, the lines from the ions C_4H^-, C_8H^-, and C_3N^- (and possibly C_5N^-) have been measured in the meantime as well, and these molecules are now also observed in dark clouds and star forming regions. Very recently, even CN^- was detected in the carbon star envelope IRC+10216 (Agundez et al., [86]). While based on ion-chemistry models, negative ions have been predicted many years ago, the new observations have now triggered a new set of chemical models with new mechanisms for anion formation. A nice review is given by Herbst [87].

2.6 Chain Molecules

Besides simple linear molecules, such as CO and HCN, much larger linear molecules, chain molecules, have been detected over the years mostly in cold dark clouds, but also in the envelopes of late-type stars and proto-planetary nebula. A considerable amount of carbon can be locked up in these chains, with the prime examples being chains such as HC_nN, C_nH, and C_nS. The recent detections of negatively charged chains have been discussed in the previous section. These carbon chain molecules are highly unsaturated. The current longest detected chain is $HC_{11}N$ which was detected toward the cold Taurus Molecular Cloud 1 (TMC-1). Laboratory frequencies of even longer chains are available. The longest chain detected in circumstellar envelopes is HC_9N. Carbon chain molecules might be related to the formation and destruction of carbonaceous compounds such as polyaromatic hydrocarbons (PAHs, see also the section about cyclic molecules).

2.7 Symmetric and Asymmetric Top Molecules

Symmetric rotors are being used as interstellar thermometers. Two of their moments of inertia are equal; therefore, they can be described by only two rotational quantum numbers, the total angular momentum, J, and its component along the symmetry axis, K. Radiative transitions are only possible within the so-called K ladder. For symmetric tops, such as CH_3CN and CH_3CCH, the line frequencies of transitions with the same J but different K have only small separations, and lines from the complete K ladder can therefore be easily observed simultaneously. The level population within a given K ladder is mostly a function of the temperature of the emitting clouds—therefore, being in local thermodynamic equilibrium—Boltzmann plots can be used to estimate the temperature of the clouds as shown in Fig. 2.3.

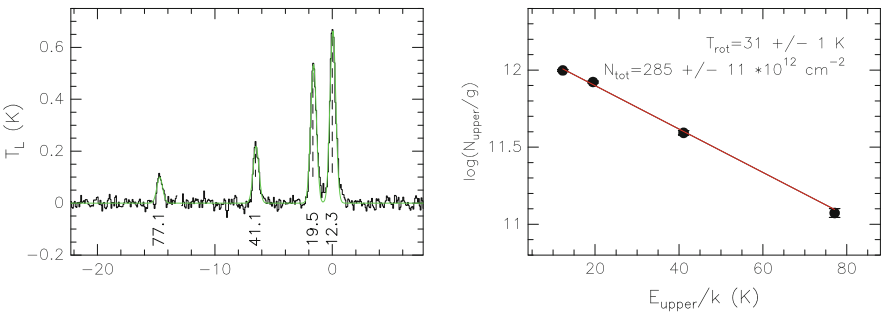

Fig. 2.3 IRAM 30-m telescope observations of the CH_3CCH $J = 5 - 4K$ ladder in a massive star forming clump. The temperature is estimated from the Boltzmann plot in the *right panel*

As already mentioned in Sect. 2.1, the first symmetric rotor detected in space was ammonia, NH_3, since ammonia has observable lines in the centimeter wavelength range. These lines are due to the tunneling of the nitrogen through the plane of the hydrogen atoms and are called inversion lines. This effect causes a small splitting in energy of the rotational levels, and the so-called metastable inversion lines with $J = K$ can be observed in a relatively small frequency range around 24 GHz. An excellent review of ammonia is given in Ho and Townes [88]. Rotational transitions of ammonia were first observed in its lowest vibrationally excited state by Schilke et al. [89]. Rotational lines in the vibrational ground state cannot be observed from the ground. The first detection of the (J, K) (1, 0) –(0, 0) line at 572 GHz was done with the Kuiper Airborne Observatory by Keene et al. [90].

Slightly asymmetric rotors offer, in addition to their dependence on the clouds' temperatures, the opportunity to probe the density of the molecular clouds. Important examples of this class of molecules that are often used in astronomical investigations are methanol (CH_3OH) and formaldehyde (H_2CO). To determine the physical parameters T and n of a molecular cloud, a range of transitions with different dependence on these parameters is observed.

The first asymmetric rotor detected in interstellar space was water, although it is very difficult to observe thermal water lines from the ground due to the large amount of water vapor in our atmosphere. Thermal lines of water have been studied with space observatories. The Infrared Space Observatory (ISO) made important detections of water. Its short-wavelength spectrometer (2–45 μm) covered mostly ro-vibrational lines, while its long-wavelength spectrometer (43–194 μm) covered pure rotational transitions, both with crude spectral resolution though. Velocity-resolved observations of the water ortho ground state line at 557 GHz have been conducted with the small space observatories, Odin and SWAS. A great progress in our understanding of interstellar water is currently being made with the Herschel Space Observatory, which allows to make velocity-resolved observations of many rotational lines of water with much higher spatial resolution than with the previous space observatories.

2.8 Cyclic Molecules

The first cyclic molecule detected in space was SiC_2 in the carbon star IRC+10216 observed by Thaddeus et al. [91] followed by the first truly hydrocarbon ring molecule C_3H_2 [92], which subsequently was extensively studied in many interstellar clouds. After these detections, only a few new ones joined the group of interstellar-detected cyclic molecules, namely, C_3H and C_2H_4O, and in 2001, Benzene (C_6H_6; Cernicharo et al. [93]) was detected in the infrared with ISO.

Polycyclic aromatic hydrocarbons (PAHs) can be considered as very big cyclic molecules, but there relation to their smaller siblings and the formation of PAHs are still not understood. For a recent review on PAHs, see Tielens [94].

2.9 Complex Molecules

A comprehensive review of complex organic interstellar molecules has recently been given by Herbst and van Dishoeck [95]. By interstellar standards, molecules containing six or more molecules are viewed as complex molecules. With this definition, about one third of the molecules detected in the interstellar medium or circumstellar shells are complex molecules. In the following, we give examples of the most complex molecules so far observed in interstellar space.

In 2003, Kuan et al. claimed to have detected the simplest amino acid, glycine (H_2NCH_2COOH) [96] in three warm, dense, interstellar clouds, including Sgr B2. If true, this would be the conclusion of a long quest (see, e.g., [97–100]).

Any such "identification" must rely on a large number of lines. Even so (or maybe *because of this*), the *confusion problem* is a formidable one. Inspecting any figure presented by Kuan *et al.*, one finds comparably many glycine lines as unidentified ("U") lines. For a wider view, see the 218–263 GHz line survey by Nummelin et al. [101, 102], which, for Sgr B2(N), is at or near the confusion limit throughout that band, even at their relatively moderate sensitivity (compared to the interferometric data by Snyder and his collaborators).

In the high-density ($n \sim 10^7$ cm^{-3}) Sgr B2, "Large Molecule Heimat (LMH)" level populations are in Local Thermodynamic Equilibrium (LTE) characterized by rotation temperatures, $T_{\rm rot}$, around 200 K [103]. At this temperature, the lower vibrationally excited states of a large number of complex molecules are populated, giving rise to a plethora of emission lines, probably with comparable intensities to the putative glycine lines. The width of the LMH's lines, typically $\sim$6–10 km s^{-1}, adds additional complication. Given the gigantic partition functions, many of the lines are weak.

An instructive example of a well-founded detection of a large complex molecule is the amino acetonitrile's (glycinonitrile) detection by Belloche et al. [104] in Sgr B2(N). This molecule is important since it is chemically related to the simplest amino acid, glycine. Many lines have been targeted (see Fig. 2.4). While many lines are blended, an important criterion is that all expected lines are actually seen. In addition, Belloche et al. performed interferometer follow ups, establishing that lines contributing to amino acetonitrile originate from the same positions in the cloud. In the future, the Atacama Large Millimeter Array (ALMA) will be an important instrument for the search for even more complex molecules, because the line-blending problem will be much smaller at high angular resolution.

2.10 Isotopologues and Deuterated Molecules

The observations of isotopologues of a given molecule has been important for several reasons: First of all, in many cases, the emission of the main isotopologue is optically thick (^{12}CO being the most prominent example), which leads to

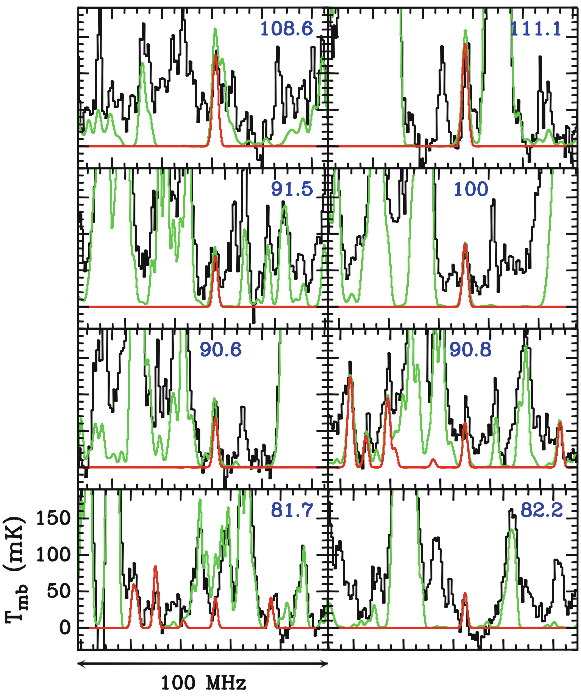

Fig. 2.4 Spectra of amino acetonitrile lines at 3 mm obtained with the IRAM 30-m telescope [104]. A fit which includes all identified molecules at 3 mm in Sgr B2(N) is shown in *light gray*, whereas a fit of only amino acetonitrile lines is shown in *dark gray*

difficulties in the determination of column densities and the observations of the hidden, denser parts of the molecular clouds. Here, the rarer isotopologues come to help, in the case of CO, ^{13}CO, C^{18}O, and C^{17}O which are observed often to study the mass distribution in a cloud, while the optically thick main isotopologue is then used to derive the excitation temperature. Even detections of ^{13}C^{18}O have been made. Another important application is to use isotope abundance ratios as a tool for the understanding of stellar nucleosynthesis and to look for galactic gradients of these ratios (see, for example, [105]).

The large number of detected deuterated molecules came as a surprise, since the cosmic D/H ratio is only of order 10^{-5}, while new observations of deuterated molecules in cold molecular clouds find values of this ratio even above 0.1. The first radio detection of a deuterated molecule in the ISM was reported by Jefferts et al. [106] with the detection of the DCN (3–2) line in the Orion molecular cloud. In the same year, HD also was detected in the ISM with UV absorption measurements by Spitzer et al. [107]. The reason for the increased D/H ratio at low temperatures is that main reactions, such as $H_3^+ + HD \rightarrow H_2D^+ + H_2$, are exothermic. In addition, in cold environments, CO, the main reactant for H_2D^+, is depleted further increasing the relative amount of deuterated molecules. This led in 2002 to record the detection of triple-deuterated molecules (ammonia and methanol).

2.11 Prospects for Future Detections

Science with the Herschel Space Observatory has just started in 2010 has just started, and the first results are encouraging (see the Astronomy & Astrophysics Herschel and Herschel/HIFI special issues of 2010). Unbiased line surveys from about 650 to 70 μm that are being performed toward the most fruitful astronomical objects in search of new detections of molecules in space have revealed already new species (e.g., H_2Cl^+). Many lines of these surveys will remain unidentified, and more laboratory spectroscopy and systematic computation and collections of frequencies, as provided by the JPL and CDMS catalogs, will be crucial. For the detections of more complex molecules, interferometers will be crucial. Besides ALMA, the Expanded Very Large Array (EVLA) also will play a major role at cm wavelengths, where, recently again, new heavy species are detected with the Greenbank telescope (e.g., the CH_3C_6H detections by Remijan et al. [108] toward TMC-1).

References

1. S. Pfalzner, C. Kramer, C. Staubmeier, A. Heithausen (eds.), *The Dense Interstellar Medium in Galaxies* Springer proceedings in physics, vol. 91 (Proceedings of the 4th Cologne-Bonn-Zermatt Symposium, Zermatt, Switzerland, 22–26, Sept. 2003), (Springer, Berlin-Heidelberg, 2004), p. 69
2. H.I. Ewen, E.M. Purcell, Nature **168**, 356 (1951)
3. S. Weinreb, A.H. Barrett, M.L. Meeks, J.C. Henry, Nature **200**, 829 (1963)
4. C.H. Townes, in *IAU Symp. 4: Radio astronomy*, ed. by H.C. van de Hulst (Cambridge University Press, London, 1957), p. 92
5. I.S. Shklovsky, Astr. Zhur. **29**, 144 (1952)
6. B. Hoglund, P.G. Mezger, Science **150**, 339 (1965)
7. A.C. Cheung, D.M. Rank, C.H. Townes, D.D. Thornton, W.J. Welch, Phys. Rev. Lett. **21**, 1701 (1968)
8. A.C. Cheung, D.M. Rank, C.H. Townes, D.D. Thornton, W.J. Welch, Nature **221**, 626 (1969)
9. L.E. Snyder, D. Buhl, B. Zuckerman, P. Palmer, Phys. Rev. Lett. **22**, 679 (1969)
10. L.E. Snyder, Molecules in Space. in *MTP International Review of Science*, vol 3, Spectroscopy. ed. by D.A. Ramsay (Butterworths, London, 1972), pp. 193–240
11. G. Winnewisser, M. Winnewisser, B.P. Winnewisser in *MTP International Review of Science*, vol 3, Spectroscopy. ed. by D.A. Ramsay (Butterworths, London, 1972), p. 241
12. J.A. Ball, C.A. Gottlieb, A.E. Lilley, H.E. Radford, Astrophys. J. **162**, L203 (1970)
13. B. Zuckerman, J.A. Ball, C.A. Gottlieb, Astrophys. J. **163**, L41 (1971)
14. G. Winnewisser, E. Churchwell, Astrophys. J. **200**, L33 (1975)
15. P. Palmer, C.A. Gottlieb, L.J. Rickard, B. Zuckerman, Bull. Am. Astron. Soc. **3**, 499 (1971)
16. R.H. Rubin, G.W. Swenson, R.C. Benson, H.L. Tigelaar, W.H. Flygare, Astrophys. J. **169**, L39 (1971)
17. B.E. Turner, Astrophys. J. **163**, L35 (1971)
18. F.F. Gardner, G. Winnewisser, Astrophys. J. **195**, L127 (1975)
19. E. Churchwell, C.M.Walmsley, G. Winnewisser, Astron. Astrophys. **54**, 925 (1977)
20. J.A. Ball, C.A. Gottlieb, A.E. Lilley, H.E. Radford, IAU Circ. No. 2350 (1971)
21. O.E.H. Rydbeck, J. Elldér, W.M. Irvine, Nature **246**, 466 (1973)

22. M.W. Sinclair, N. Fourikis, J.C. Ribes, B.J. Robinson, R.D. Brown, P.D. Godfrey, Australian J. Phys. **26**, 85 (1973)
23. P.D. Godfrey, R.D. Brown, B.J. Robinson, M.W. Sinclair, Astrophys. Lett. **13**, 119 (1973)
24. N. Fourikis, K. Takagi, M. Morimoto, Astrophys. J. **191**, L139 (1974)
25. F.F. Gardner, G. Winnewisser, Astrophys. J. **197**, L73 (1975)
26. R.D. Brown, J.G. Crofts, P.D. Godfrey, F.F. Gardner, B.J. Robinson, J.B. Whiteoak, Astrophys. J. **197**, L29 (1975)
27. E. Churchwell, G. Winnewisser, Astron. Astrophys. **45**, 229 (1975)
28. G. Winnewisser, F.F. Gardner, Astron. Astrophys. **48**, 159 (1976)
29. L.W. Avery, N.W. Broten, J.M. MacLeod, T. Oka, H.W. Kroto, Astrophys. J. **205**, L173 (1976)
30. F.F. Gardner, G. Winnewisser, Mon. Not. R. Astro. Soc. **185**, 57 (1978)
31. L.E. Snyder, D. Buhl, P.R. Schwartz, F.O. Clark, D.R. Johnson, F.J. Lovas, P.T. Giguere, Astrophys. J. **191**, L79 (1974)
32. O.E.H. Rydbeck, J. Elldér, A. Sume, Å. Hjalmarson, W.M. Irvine, Astron. Astrophys. **34**, 479 (1974)
33. H.M. Pickett, R.L. Poynter, E.A. Cohen, M.L. Delitsky, J.C. Pearson, H.S.P. Müller, J. Quant. Spectrosc. Rad. Transfer **60**, 883 (1998)
34. H.S.P. Müller, S. Thorwirth, D.A. Roth, G. Winnewisser, Astron. Astrophys. **370**, L49 (2001)
35. R.W. Wilson, K.B. Jefferts, A.A. Penzias, Astrophys. J. **161**, L43 (1970)
36. D. Buhl, L.E. Snyder, Nature **232**, 161 (1971)
37. M. Morris, B.E. Turner, P. Palmer, B. Zuckerman, Astrophys. J. **205**, 82 (1976)
38. P.F. Goldsmith, Astrophys. J. **176**, 597 (1972)
39. J. Stutzki, R. Guesten, Astrophys. J. **356**, 513 (1990)
40. J.M. Jackson, J.M. Rathborne, R.Y. Shah, R. Simon, T.M. Bania, D.P. Clemens, E.T. Chambers, A.M. Johnson, M. Dormody, R. Lavoie, M.H. Heyer, Astrophys. J. Suppl. **163**, 145 (2006)
41. T.P. Snow, B.J. McCall, Ann. Rev. Astron. Astrophys. **44**, 367 (2006)
42. R. Bachiller, Ann. Rev. Astron. Astrophys. **34**, 111 (1996)
43. J. Cernicharo, M. Guélin, Astron. Astrophys. **183**, L10 (1987)
44. M. Guélin, R. Lucas, J. Cernicharo, Astron. Astrophys. **280**, L19 (1993)
45. K. Kawaguchi, E. Kagi, T. Hirano, S. Takano, S. Saito, Astrophys. J. **406**, L39 (1993)
46. L.M. Ziurys, A.J. Apponi, M. Guélin, J. Cernicharo, Astrophys. J. **445**, L47 (1995)
47. B.E. Turner, T.C. Steimle, L. Meerts, Astrophys. J. **426**, L97 (1994)
48. M. Guelin, M. Forestini, P. Valiron, L.M. Ziurys, M.A. Anderson, J. Cernicharo, C. Kahane, Astron. Astrophys. **297**, 183 (1995)
49. L.M. Ziurys, C. Savage, J.L. Highberger, A.J. Apponi, M. Guélin, J. Cernicharo, Astrophys. J. **564**, L45 (2002)
50. J.L. Highberger, C. Savage, J.H. Bieging, L.M. Ziurys, Astrophys. J. **562**, 790 (2001)
51. J.L. Highberger, K.J. Thomson, P.A. Young, D. Arnett, L.M. Ziurys, Astrophys. J. **593**, 393 (2003)
52. S. Petrie, Mon. Not. R. Astron. Soc. **302**, 482 (1999)
53. C.W. Walmsley, R. Bachiller, G.P. des Forêts, P. Schilke, Astrophys. J. **566**, L109 (2002)
54. R.L. Plambeck, N.R. Erickson, Astrophys. J **262**, 606 (1982)
55. F. Combes, T. Wiklind, Astron. Astrophys. **334**, L81 (1998)
56. L.W. Avery, M.B. Bell, C.T. Cunningham, P.A. Feldman, R.H. Hayward, J.M. McLeod, H.E. Matthews, J.D. Wade, Astrophys. J **426**, 737 (1994)
57. H. Spinrad, D.B. Wood, Astrophys. J. **141**, 109 (1965)
58. T. Dunhum Jr., W.S. Adams, Publ. Astron. Soc. Pacific **49**, 26 (1937)
59. A. McKellar, Publ. Astron. Soc. Pacific **52**, 187 (1940)
60. P. Swings, L. Rosenfeld, Astrophys. J. **86**, 483 (1937)
61. A.E. Douglas, G. Herzberg, Astrophys. J. **94**, 483 (1941)
62. P.F. Goldsmith, W.D. Langer, Astrophys. J. **222**, 881 (1978)

63. D.A. Neufeld, S. Lepp, G.J. Melnick, Astrophys. J. Suppl. **100**, 132 (1995)
64. A. Wootten, B.E. Turner, J.G. Mangum, M. Bogey, F. Boulanger, F. Combes, P.J. Encrenaz, M. Gerin, Astrophys. J. **380**, L79 (1991)
65. T.G. Phillips, E.F. van Dishoeck, J. Keene, Astrophys. J. **399**, 533 (1992)
66. P. Schilke, D.J. Benford, T.R. Hunter, D.C. Lis, T.G. Phillips, Astrophys. J. Suppl. **132**, 281 (2001)
67. G.A. Blake, J. Keene, T.G. Phillips, Astrophys. J. **295**, 501 (1985)
68. G.J. Melnick, M.L.N. Ashby, R. Plume, E.A. Bergin, D.A. Neufeld, G. Chin, N.R. Erickson, P.F. Goldsmith, M. Harwit, J.E. Howe, S.C. Kleiner, D.G. Koch, B.M. Patten, R. Schieder, R.L. Snell, J.R. Stauffer, V. Tolls, Z. Wang, G. Winnewisser, Y.F. Zhang, Astrophys. J. **539**, L87 (2000)
69. A. Schulz, R. Güsten, C.M. Walmsley, E. Serabyn, Astron. Astrophys. **246**, L55 (1991)
70. J.R. Pardo, J. Cernicharo, F. Herpin, J. Kawamura, J. Kooi, T.G. Phillips, Astrophys. J. **562**, 799 (2001)
71. E.F. van Dishoeck, D.J. Jansen, P. Schilke, T.G. Phillips, Astrophys. J. **416**, L83 (1993)
72. R. Stark, F.F.S. van der Tak, E.F. van Dishoeck, Astrophys. J. **521**, L67 (1999)
73. T.R. Geballe, T. Oka, Nature **384**, 334 (1996)
74. D.A. Neufeld, J. Zmuidzinas, P. Schilke, T.G. Phillips, Astrophys. J. **488**, L141 (1997)
75. E.T. Polehampton, J.-P. Baluteau, C. Ceccarelli, B.M. Swinyard, E. Caux, Astron. Astrophys. **388**, L44 (2002)
76. J.R. Goicoechea, J. Cernicharo, Astrophys. J. **554**, L213 (2001)
77. K.M. Menten, F. Wyrowski, A. Belloche, et al., Astron. Astrophys. **525**, A77 (2011)
78. F. Wyrowski, K.M. Menten, R. Gusten, and A. Belloche, Astron. Astrophys. **518**, A26 (2010)
79. D.A. Neufeld, P. Sonnentrucker, T.G. Phillips, et al., Astron. Astrophys. **518**, L108 (2010)
80. D.C. Lis, J.C. Pearson, D.A. Neufeld, et al., Astron. Astrophys. **512**, L9 (2010)
81. D. Buhl, Nature **228**, 267 (1970)
82. W. Klemperer, Nature **227**, 1230 (1970)
83. E. Herbst, W. Klemperer, Astrophys. J. **185**, 505 (1973)
84. K. Kawaguchi, Y. Kasai, S.-I. Ishikawa, N. Kaifu, Publ. Astro. Soc. Japan **47**, 853 (1995)
85. M.C. McCarthy, C.A. Gottlieb, H. Gupta, P. Thaddeus, Astrophys. J. **652**, L141 (2006)
86. M. Agundez, J. Cernicharo, M. Guélin, et al., Astron. Astrophys. **517**, L2 (2010)
87. E. Herbst, Astron. Soc. Pac. Conf. Ser. **417**, 153 (2009)
88. P.T.P. Ho, C.H. Townes, Ann. Rev. Astron. Astrophys. **21**, 239 (1983)
89. P. Schilke, C.M. Walmsley, T.L. Wilson, R. Mauersberger, Astron. Astrophys. **227**, 220 (1990)
90. J. Keene, G.A. Blake, T.G. Phillips, Astrophys. J. **271**, L27 (1983)
91. P. Thaddeus, S.E. Cummins, R.A. Linke, Astrophys. J. **283**, L45 (1984)
92. P. Thaddeus, J.M. Vrtilek, C.A. Gottlieb, Astrophys. J. **299**, L63 (1985)
93. J. Cernicharo, A.M. Heras, A.G.G.M. Tielens, J.R. Pardo, F. Herpin, M. Guélin, L.B.F.M. Waters, Astrophys. J. **546**, L123 (2001)
94. A.G.G.M. Tielens, Ann. Rev. Astron. Astrophys. **46**, 289 (2008)
95. E. Herbst, E.F. van Dishoeck, Ann. Rev. Astron. Astrophys. **47**, 427 (2009)
96. Y. Kuan, S.B. Charnley, H. Huang, W. Tseng, Z. Kisiel, Astrophys. J. **593**, 848 (2003)
97. L.E. Snyder, J.M. Hollis, L.W. Brown, D. Buhl, R.D. Suenram, F.J. Lovas, Astrophys. J. **268**, 123 (1983)
98. I.I. Berulis, G. Winnewisser, V.V. Krasnov, R.L. Sorochenko, Sov. Astron. Lett. **11**, 251 (1985)
99. F. Combes, N. Q-Rieu, G. Wlodarczak, Astron. Astrophys. **308**, 618 (1996)
100. C. Ceccarelli, L. Loinard, A. Castets, A. Faure, B. Lefloch, Astron. Astrophys. **362**, 1122 (2000)
101. A. Nummelin, P. Bergman, Å. Hjalmarson, P. Friberg, W.M. Irvine, T.J. Millar, M. Ohishi, S. Saito, Astrophys. J. Suppl. **117**, 427 (1998)

102. A. Nummelin, P. Bergman, Å. Hjalmarson, P. Friberg, W.M. Irvine, T.J. Millar, M. Ohishi, S. Saito, Astrophys. J. Suppl. **128**, 213 (2000)
103. S. Liu, D.M. Mehringer, and L.E. Snyder, Astrophys. J. **552**, 654 (2001)
104. A. Belloche, K.M. Menten, C. Comito, H.S.P. Müller, P. Schilke, J. Ott, S. Thorwirth, C. Hieret, Astron. Astrophys. **482**, 179 (2008)
105. T.L. Wilson, R. Rood, Ann. Rev. Astron. Astrophys. **32**, 191 (1994)
106. K.B. Jefferts, A.A. Penzias, R.W. Wilson, Astrophys. J. **179**, L57 (1973)
107. L. Spitzer, J.F. Drake, E.B. Jenkins, D.C. Morton, J.B. Rogerson, D.G. York, Astrophys. J. **181**, L116 (1973)
108. A.J. Remijan, J.M. Hollis, L.E. Snyder, P.R. Jewell, F.J. Lovas, Astrophys. J. **643**, L37 (2006)

Chapter 3
Fundamentals of Spectroscopy for Astrophysics

Koichi M. T. Yamada, Per Jensen and Nobukimi Ohashi

3.1 Atoms

3.1.1 Hamiltonian for the Hydrogen Atom

The hydrogen atom is composed of two particles, a proton and an electron, and the Hamiltonian describing the state of a hydrogen atom is

$$\hat{H} = \frac{\hat{\boldsymbol{p}}_0^2}{2m_0} + \frac{\hat{\boldsymbol{p}}_1^2}{2m_1} + V(|\boldsymbol{r}_1 - \boldsymbol{r}_0|), \tag{3.1.1}$$

where $m, \boldsymbol{r}$ and $\hat{\boldsymbol{p}}$ represent the masses, coordinate vectors, and their conjugates momentum operators of the two particles; subscripts 0 and 1 of these variables indicate the proton and electron, respectively. The potential energy V is the attractive Coulomb interaction between the nucleus and the electron;

$$V = -\frac{Ze^2}{4\pi\epsilon_0|\boldsymbol{r}_1 - \boldsymbol{r}_0|}, \tag{3.1.2}$$

K. M. T. Yamada (✉)
National Institute of Advanced Industrial Science and Technology (AIST), EMTech,
Onogawa 16-1, Tsukuba,
Ibaraki 305-8569, Japan
e-mail: kmt.yamada@aist.go.jp

P. Jensen
Fachgruppe Chemie, FB C Mathematik u. Naturwissenschaften, Bergische Universität
Wuppertal, Gaussstr. 20, 42097 Wuppertal, Germany

N. Ohashi
Faculty of Science, Department of Physics, Kanazawa University, Kakuma,
Kanazawa 920-1192, Japan

K. M. T. Yamada and G. Winnewisser (eds.), *Interstellar Molecules*,
Springer Tracts in Modern Physics 241, DOI: 10.1007/978-3-642-16268-8_3,

where e is the proton charge (electron charge is "$-e$") and Z is the atomic number; Ze represents the charge of nuclei and $Z = 1$ for the hydrogen atom.

Introducing the relative coordinate $\boldsymbol{r}$, the coordinate of the center of mass $\boldsymbol{R}$, total mass M, and the reduced mass μ, i.e.,

$$\boldsymbol{r} = \boldsymbol{r}_1 - \boldsymbol{r}_0, \tag{3.1.3}$$

$$\boldsymbol{R} = \frac{(m_0\boldsymbol{r}_0 + m_1\boldsymbol{r}_1)}{m_0 + m_1}, \tag{3.1.4}$$

$$M = m_1 + m_0, \tag{3.1.5}$$

$$\mu = \frac{m_1 m_0}{m_1 + m_0}, \tag{3.1.6}$$

Eq. 3.1.1 is expressed as

$$\hat{H} = \frac{\hat{\boldsymbol{P}}^2}{2M} + \frac{\hat{\boldsymbol{p}}^2}{2\mu} + V(|\mathbf{r}|), \tag{3.1.7}$$

where $\hat{\boldsymbol{P}}$ and $\hat{\boldsymbol{p}}$ are the conjugate momenta of $\boldsymbol{R}$ and $\boldsymbol{r}$, respectively. Since the electron mass is very much smaller than the proton mass, the reduced mass μ is very close to the electron mass m_1 as

$$\mu \approx (1 - 0.000544)m_1. \tag{3.1.8}$$

The first term of Eq. 3.1.7 represents the translation energy of the hydrogen atom, which appears as the Doppler effect by spectroscopic observation. To describe the internal motion of the hydrogen atom, we can ignore this term.

3.1.2 Schrödinger Equation

The Schrödinger equation, i.e., wave equation, for the stationary state of the internal motion of a hydrogen atom is then

$$\left[-\frac{\hbar^2}{2\mu}\nabla^2 + V(|\boldsymbol{r}|)\right]\psi = E\psi. \tag{3.1.9}$$

By introducing the polar coordinates $\boldsymbol{r} = (r, \theta, \phi)$, i.e.,

$$x = r\sin\theta\cos\phi \tag{3.1.10}$$

$$y = r\sin\theta\sin\phi \tag{3.1.11}$$

$$z = r\cos\theta, \tag{3.1.12}$$

the wave equation (3.1.9) can be rewritten as

$$-\frac{\hbar^2}{2\mu}\left[\frac{1}{r^2}\frac{\partial}{\partial r}\left(r^2\frac{\partial}{\partial r}\right)+\frac{1}{r^2\sin\theta}\frac{\partial}{\partial\theta}\left(\sin\theta\frac{\partial}{\partial\theta}\right)+\frac{1}{r^2\sin^2\theta}\frac{\partial^2}{\partial\phi^2}\right]\psi=\{E-V(r)\}\psi. \tag{3.1.13}$$

Substituting the wavefunction ψ by a product of a radial part and angular parts;

$$\psi=R(r)\Theta(\theta)\Phi(\phi), \tag{3.1.14}$$

the separation of variables of the wave equation (3.1.13) can be performed as described elsewhere in standard text book for quantum mechanics [1];

$$-\frac{\mathrm{d}^2\Phi}{\mathrm{d}\phi^2}=E_\phi\Phi, \tag{3.1.15}$$

$$\frac{1}{\sin\theta}\frac{\mathrm{d}}{\mathrm{d}\theta}\left(-\sin\theta\frac{\mathrm{d}\Theta}{\mathrm{d}\theta}\right)=\left(E_\theta-\frac{E_\phi}{\sin^2\theta}\right)\Theta, \tag{3.1.16}$$

$$-\frac{\hbar^2}{2\mu}\frac{1}{r^2}\frac{\mathrm{d}}{\mathrm{d}r}\left(r^2\frac{\mathrm{d}R}{\mathrm{d}r}\right)=\left[E-V(r)-\frac{\hbar^2E_\theta}{2\mu r^2}\right]R. \tag{3.1.17}$$

The first two equations govern the angular motion and are independent of either the reduced mass or the potential energy; they are applied commonly for angular motion in space expressed by the polar coordinate system. The third equation rules the radial motion.

3.1.3 Angular Wavefunction

Requiring the periodic boundary conditions, the eigenvalues and eigenfunctions of those angular wave equations (3.1.15) and (3.1.16) are obtained as

$$E_\phi=m, \tag{3.1.18}$$

$$\Phi=\Phi_m(\phi)=(\sqrt{2\pi})^{-1}e^{im\phi}, \tag{3.1.19}$$

$$E_\theta=l(l+1), \tag{3.1.20}$$

$$\Theta=\Theta_l^m(\cos\theta)=\sqrt{\frac{(2l+1)(l-M)!}{2(l+M)!}}P_l^M(\cos\theta). \tag{3.1.21}$$

The value l is a positive integer or 0, which is named azimuthal quantum number and represents the orbital angular momentum. The value m is an integer, which is

named *magnetic* quantum number, representing the projection of the orbital angular momentum on an arbitrary defined Z axis; consequently

$$m = -l, -l+1, \ldots, l-1, l. \tag{3.1.22}$$

The capital M represents the absolute value of m, i.e., $M = |m|$. The function P_l^M in Eq. 3.1.21 is the associate Legendre polynomial. The product of the functions $\Phi_m(\phi)$ and $\Theta_l^m(\cos\theta)$ is a spherical harmonic function, $Y_{lm}(\theta, \phi)$, which is an eigenfunction of the orbital angular momentum $\hat{L}^2$ and of its component $\hat{L}_z$, i.e.,

$$\hat{L}^2 Y_{lm}(\theta, \phi) = l(l+1)\hbar^2 Y_{lm}(\theta, \phi), \tag{3.1.23}$$

$$\hat{L}_Z Y_{lm}(\theta, \phi) = m\hbar Y_{lm}(\theta, \phi). \tag{3.1.24}$$

3.1.4 Radial Wavefunction

The last term in the large bracket on the right hand of the radial wave equation (3.1.17) is rewritten using the quantum number l as

$$-\frac{l(l+1)\hbar^2}{2\mu r^2}, \tag{3.1.25}$$

which represents the effective potential due to the centrifugal effect. Thus the radial wave equation depends on l. The eigenvalues of the radial wave equation (3.1.17) represents the internal energy of a hydrogen atom, and are independent of l; they are [1]

$$E = E_n = -\frac{Z^2 e^2}{2a_0 n^2}. \tag{3.1.26}$$

The value n is a positive integer and called as principal quantum number. Here we introduce the radius of the first Bohr orbit for hydrogen atom,

$$a_0 = \frac{4\pi\epsilon_0\hbar^2}{\mu e^2} \approx 0.0529 \text{ nm}. \tag{3.1.27}$$

To be exact, the definition of the Bohr radius is slightly different from a_0; the Bohr radius is obtained by substituting the reduced mass μ by the electron mass m_e in Eq. 3.1.27.

The Eq. 3.1.26 explains the empirical formula of Rydberg,

$$E_n = -hc\frac{R_\mathrm{H}}{n^2}, \tag{3.1.28}$$

where R_H is the Rydberg constant for hydrogen.[1] The word *term* is historically used to specify the electronic states expressed by the Rydberg formula, Eq. 3.1.28, and the *term value* is the electronic energy expressed in wavenumber, i.e., E/hc.

The eigenfunctions of the radial wave equation (3.1.17) depend on n and l;

$$R = R_{nl} = -\sqrt{\left(\frac{2Z}{na_0}\right)^3 \frac{(n-l-1)!}{2n[(n+1)!]^3}} e^{-Zr/na_0} \left(\frac{2Zr}{na_0}\right)^l L_{n+l}^{2l+1}\left(\frac{2Zr}{na_0}\right). \tag{3.1.29}$$

The function L_{n+l}^{2l+1} is the associated Laguerre polynomial. Between n and l there is a restriction,

$$n > l, \tag{3.1.30}$$

i.e., for a given value of n,

$$l = 0, 1, \ldots, n-1. \tag{3.1.31}$$

3.1.5 Atomic Orbit

The motion of the electron in a hydrogen atom is specified by three quantum numbers n, l, and m, as described above. The internal energy of a hydrogen atom is expressed by Eq. 3.1.26 and depends only on the principal quantum number n. For a given n, there are n different l states, Eq. 3.1.31, which are degenerate in energy. The degeneracy can be lifted as described later by relativistic effects. There are $2l+1$ different m states for a given l, Eq. 3.1.22. They are degenerate in energy unless any external field is implied, and the orbital motion of electron in a hydrogen atom is usually specified by two quantum numbers, n and l.

The state specified by $n = 1$ is lowest in energy, i.e., the ground state; substituting $Z = 1$ and $n = 1$ in Eq. 3.1.26 we obtain

$$E_1 = -\frac{e^2}{2a_0} \approx -13.6\,\text{eV}. \tag{3.1.32}$$

For $n = 1$ the orbital angular momentum quantum number l must be 0 as required by Eq. 3.1.31. The orbit with $l = 0$ is denoted as "s" orbit. Together with the n value, the inner most orbit is denoted as $1s$. For $n = 2, l$ can be 0 or 1. The orbit with $l = 1$ is denoted as "p" orbit.

Because of the m degeneracy, there are three, i.e., $2l+1$, p orbits. Altogether there are one $2s$ orbit and three $2p$ orbits for $n = 2$. For $n = 3, l$ can be 0, 1, or 2.

[1] The Rydberg constant is usually expressed in wavenumber in unit of cm^{-1}. The factor hc is explicitly written here to adjust the dimension.

The orbit with $l = 2$ is denoted as "d" orbit. Thus there are one $3s$, three $3p$, and five $3d$ orbits for $n = 3$.

The notation s, p, and d are taken from the words *sharp*, *principal*, and *diffuse*, which represent the spectral characters of the alkali atoms [2]. The $l = 3$ is denoted by f, from the word *fundamental*, and the orbits with l larger than three are named alphabetically as "g", "h", and so on.

3.1.6 Electron Spin and Fine Structure

In addition to the orbital angular momentum, an electron has an intrinsic angular momentum, which is called electron spin. The electron spin angular momentum operator $\hat{\boldsymbol{s}}$ and its projection $\hat{s}_Z$ of an axis Z satisfies;

$$\hat{\boldsymbol{s}}^2\xi = s(s+1)\hbar^2\xi, \tag{3.1.33}$$

$$\hat{s}_Z\xi = m_s\hbar\xi. \tag{3.1.34}$$

with $s = \frac{1}{2}$ and $m_s = \pm\frac{1}{2}$. The spin eigen function ξ is often expressed as α and β for $m_s = \frac{1}{2}$ and $-\frac{1}{2}$. Thus for each orbit described in the previous section is associated with two electron spin states; i.e., 1sα and 1sβ, for example. The state of an electron in the hydrogen atom is characterized by four quantum numbers, n, l, m, and m_s. The state specified by those four quantum numbers is called *orbital* in atomic and molecular physics.

The total angular momentum $\boldsymbol{j}$ of the hydrogen atom is the vector sum of the orbital and spin angular momentum

$$\boldsymbol{j} = \boldsymbol{l} + \boldsymbol{s}, \tag{3.1.35}$$

i.e., the total angular momentum for an s electron is $j = \frac{1}{2}$, and that for an $l > 0$ state are $j = l + \frac{1}{2}$ and $l - \frac{1}{2}$.

The electron spin contribution to the internal energy of a hydrogen atom cannot be evaluated by the Schrödinger equation, Eq. 3.1.9. Required is the Dirac equation where the relativity contributions are properly taken care of. The degeneracy for a given n state in the Bohr model, Eq. 3.1.26, is thus removed by this interaction and the energy levels exhibit *fine* structure. The fine structure is indicated by j in subscript as nl_j; for example, $2p_{\frac{3}{2}}$ means $(n, l, j) = (2, 1, \frac{3}{2})$. The fine structure splitting of the $2p_{\frac{3}{2}}$ and $2p_{\frac{1}{2}}$ is approximately 10.9 GHz. By the Dirac equation, the $2s_{\frac{1}{2}}$ and the $2p_{\frac{1}{2}}$ states are still degenerate, which can be removed by applying the QED theory resulting with about 1 GHz splitting, which is called the Lamb shift.

Classically speaking, the electron spin couples with orbital angular momentum via magnetic interaction, i.e., the spin–orbit interaction;

$$\hat{h}_{\mathrm{so}} = A_{\mathrm{so}}(\hat{\boldsymbol{l}} \cdot \hat{\boldsymbol{s}}). \tag{3.1.36}$$

The energy shift due to this interaction can be evaluated, for the first order correction, with the diagonal element of this operator, applying the vector model,

$$\boldsymbol{j}^2 = \boldsymbol{l}^2 + 2\boldsymbol{l}\cdot\boldsymbol{s} + \boldsymbol{s}^2 \tag{3.1.37}$$

as

$$\Delta E_{\mathrm{so}} = \frac{1}{2}A_{\mathrm{so}}[j(j+1) - l(l+1) - s(s+1)]\,. \tag{3.1.38}$$

3.1.7 Nuclear Spin and Hyperfine Structure

The proton, the nucleus of the hydrogen atom, has also a spin angular momentum, *nuclear* spin $I = \frac{1}{2}$. The total angular momentum including the nuclear spin, $\boldsymbol{F}$, is the vector sum of $\boldsymbol{I}$ and $\boldsymbol{j}$,

$$\boldsymbol{F} = \boldsymbol{j} + \boldsymbol{I}, \tag{3.1.39}$$

and the energy terms are further split by the nuclear spin–electron spin interaction, resulting in the *hyperfine* structure; the interaction operator is similar to that of the spin–orbit interaction, Eq. 3.1.36,

$$\hat{h}_{\mathrm{HF}} = a(\hat{\boldsymbol{j}}\cdot\hat{\boldsymbol{I}}). \tag{3.1.40}$$

The diagonal contribution of this interaction is then evaluated by the vector model as

$$\Delta E_{\mathrm{HF}} = \frac{1}{2}a[j(j+1) - l(l+1) - s(s+1)]\,. \tag{3.1.41}$$

For example, $1s_{\frac{1}{2}}$ level splits into two, $F = 0$ and 1, the energy difference is about 1.4 GHz. This frequency corresponds to the wavelength of 21 cm; the transition between these hyperfine structures has been used in radio astronomy to observe the hydrogen atom.

3.1.8 Atoms with More Than One Electron

3.1.8.1 Single Electron Approximation and Shell Structure

The Hamiltonian for the hydrogen atom, Eq. 3.1.1, can be extended for an atom with more electrons; i.e., numbering the electrons by $i = 1, 2, \ldots, N$

$$\hat{H} = \frac{\hat{p}_0^2}{2m_0} + \frac{\sum_{i=1}^{N}\hat{p}_i^2}{2m_e} + \sum_{i=1}^{N}V(|\boldsymbol{r}_i - \boldsymbol{r}_0|) + \sum_{j>i}V'(|\boldsymbol{r}_j - \boldsymbol{r}_i|), \tag{3.1.42}$$

where m_0 and m_e are the masses of the nucleus and an electron, and r_0 and r_i represent the coordinates of them. The potential energy V is the attractive Coulomb interaction between the nucleus and the electron as in Eq. 3.1.2;

$$V = -\frac{Ze^2}{4\pi\epsilon_0|\boldsymbol{r}_i - \boldsymbol{r}_0|}, \tag{3.1.43}$$

The potential energy V' represents the repulsive Coulomb interaction between the electrons i and j;

$$V' = \frac{e^2}{4\pi\epsilon_0|\boldsymbol{r}_j - \boldsymbol{r}_i|}. \tag{3.1.44}$$

Contrary to the case of hydrogen atom, the Schrödinger equation for the atoms with more than one electron, derived from the Hamiltonian, Eq. 3.1.42, cannot be solved analytically. The motion of each electron in such atoms can be approximated as a motion in the centrally symmetric potential, where the effect of the other electrons is handled as an effective potential as an average. In this approximation, the motion of an electron can be described by the quantum numbers n, l, and m, as in the case of a hydrogen atom.

Although the approximation applied above is relatively poor, the number and type of orbits can be obtained. As in the case of hydrogen atom, the energy separation between the states with different n is much larger than that between the different l of a given n. The energy levels with a given n form a cluster which is called *shell*. The shell of $n = 1$ is named K shell, then L, M, and so on for $n = 2, 3, \ldots$.

Each shell can be further divide into several sub-shells characterized by the l quantum number. The shell structure and the number of orbitals for each sub-shell are listed in Table 3.1.

3.1.8.2 Pauli Principle and Closed Shell

The electrons are Fermions with spin $\frac{1}{2}$, and therefore, the wavefunctions should be antisymmetric to any permutation of electrons. If the two or more electrons share an orbital, the wavefunction describing those electrons must be symmetric to the permutation of those electrons. Obviously this is forbidden by the symmetry

Table 3.1 Shell structure of atomic orbitals

Shell	K	L		M		
Orbit	$1s$	$2s$	$2p$	$3s$	$3p$	$3d$
n	1	2	2	3	3	3
l	0	0	1	0	1	2
m degeneracy	1	1	3	1	3	5
# of orbitals	2	2	6	2	6	10

requirement for Fermions. Thus, each orbital can be occupied by a single electron. This is known as *Pauli exclusion principle*.

Consequently, the orbitals of the K shell, the lowest energy shell, can be occupied by two electrons and then the shell is *closed*. The L shell is closed by eight electrons; two of them occupy the s sub-shell, and the rest occupy the p sub-shell. For each closed sub-shell, the total orbital angular momentum and total spin vanish;

$$\sum_{\text{subshell}} \boldsymbol{l}_i = 0 \tag{3.1.45}$$

$$\sum_{\text{subshell}} \boldsymbol{s}_i = 0. \tag{3.1.46}$$

The shells are closed for the ground state of rare gas atoms. By indicating the number of electrons which occupy each orbital, the electron configuration of rare gas atoms are expressed as $1s^2$ for He, $1s^2 2s^2 2p^6$ for Ne, $1s^2 2s^2 2p^6 3s^2 3p^6 3d^{10}$ for Ar, and so on.

3.1.8.3 Alkali Atoms

The lightest atom of alkali metals is lithium (Li), which has three electrons. In the ground electronic state, the K shell is closed by the two of them like in He, and the rest one electron occupies one of the $2s$ orbitals, i.e., $1s^2 2s^1$. The motion of the outermost electron resembles very much that of the hydrogen atom, because the field caused by the electrons in the closed shell is spherically symmetric in average. Thus the energy of this outer electron is well approximated by a formula similar to Eq. 3.1.28;

$$E_n = -hc \frac{R_{\text{Li}}}{(n - \Delta)^2}, \tag{3.1.47}$$

where Δ is a small correction term, named *quantum defect*, to the principal quantum number n. It is clear from Eq. 3.1.47 the energy correction due to the quantum defect is larger for the smaller n state.

The next larger atom of the alkali metals is sodium (Na), which contains 11 electrons. In the ground electronic state, ten of them occupy the K and L shells, like in Ar, and one electron occupies one of the $3s$ orbitals, i.e., $1s^2 2s^2 2p^6 3s^1$.

3.1.8.4 Term Symbols

Before discussing the electron configuration of atoms other than the rare gasses and alkali metals, we explain the symbols of the electronic term which express the electron configurations of an atom. First we introduce an important coupling

scheme for the various angular momenta of electrons in an atom, so-called *Russel–Saunders coupling* which is an approximation using vector models as follows.

In this coupling scheme, the orbital angular momentum of each electron couples together, and they form a vector sum,

$$\boldsymbol{L} = \sum_{i}^{N} \boldsymbol{l}_i, \tag{3.1.48}$$

which is called total orbital angular momentum. Similarly the spin angular momentum of each electron couples together, and they form the total electron spin,

$$\boldsymbol{S} = \sum_{i}^{N} \boldsymbol{s}_i. \tag{3.1.49}$$

Those couplings are so strong that the atoms behaves as if they have a single orbital angular momentum expressed by L and a single spin expressed by S. Consequently the fine structures due to the spin–orbit coupling is represented by the total angular momentum J which is the vector sum of L and S,

$$\boldsymbol{J} = \boldsymbol{L} + \boldsymbol{S}, \tag{3.1.50}$$

instead of the individual coupling expressed by Eq. 3.1.35. Surprisingly, this coupling scheme can be applied to most of the atoms.

Thus the electron configurations of atoms, or electronic terms, are specified by the three quantum numbers L, S, and J. We denote the term of $L = 0$ as S (caution, capital), in analogy to the orbit notation s (lower case) for the $l = 0$. Successively, P, D, F, and so on for $L = 1, 2, 3, \ldots$. As a superscript on the left of the angular momentum symbol, we indicate the spin multiplicity $2S + 1$, which represents a number of possible different spin states, and as a subscript on the right the total angular momentum J, which represents the fine structure component, i.e.,

$$^{2S+1}X_J \tag{3.1.51}$$

where $X = S, P, D, F, \ldots$.

As we discussed before the vector sum of the orbital angular momenta and spin angular momenta vanishes for closed sub-shells, Eqs. 3.1.45 and 3.1.46, the terms of rare gas atoms for their ground electronic states are all $^1S_0$. The ground states of a hydrogen atom and alkali atoms are expressed as $^2S_{\frac{1}{2}}$.

3.1.8.5 Building-Up Principle

Now we consider a more complicated atom, the carbon atom for example. The electronic configuration of the carbon atom is $1s^2 2s^2 2p^2$ in its ground state. The K shell and $2s$ sub-shell are closed, and thus the vector sum of l_i vanishes upto $2s$ sub-shell and that of s_i as well, see Eqs. 3.1.45 and 3.1.46. Thus we can completely

ignore those electrons in the closed shell by calculating L and S in Eqs. 3.1.48 and 3.1.49. In case where no restriction of the Pauli exclusion principle exists, the value L can be 0, 1, or 2, and the value S can be 0 or 1; i.e., there are six possible terms, $^1S, ^1P, ^1D, ^3S, ^3P$, and ^3D.

Because of Pauli principle, if the two electrons are distributed in the $2p$ orbitals, the number of possible terms are less than six. For finding these possible terms, there seems to be no simpler way than that explained by the Table 3.11 in Herzberg's book [2]. The possible terms are only $^1S, ^1D$, and ^3P. Among the three, the ground electronic state of carbon is ^3P, which can be predicted by the Hund rules.

The Hund rules, which can be wonderfully applied to find out the ground state term symbol for most of atoms (with exceptions), are

1. The term of largest multiplicity is lowest in energy.
2. Within the same multiplicity terms, the largest L term is lowest in energy.
3. Multiplets are *regular* (the term with smallest J value is lowest in energy) for the term where less than half of the shell is filled, and are *inverted* (the term with largest J value is lowest) for the term where more than half of the shell is filled.

For the carbon case, there is only one triplet state. Thus we can find the ^3P to be ground state from the rule 1, and no need to use the rule 2. This state is triplet and there are three fine structure components, $J = 0$, 1, and 2; $^3P_0, ^3P_1$, and $^3P_2$.

3.1.8.6 Fine Structure

Since the $2p$ sub-shell is less than half filled (two of six), the Hund rule 3 suggests for the carbon atom that the multiplets are regular and the ground state should be $^3P_0$. The energy separations of the fine structure are caused mainly by the spin–orbit interaction. The spin–orbit coupling energy is thus explained in the first order approximation as

$$\hat{h}_{\rm so} = A_{\rm so}(\hat{\boldsymbol{L}} \cdot \hat{\boldsymbol{S}}), \tag{3.1.52}$$

which should be compared with Eq. 3.1.36. As in the case of single electron, the diagonal element of this operator

$$\Delta E = \frac{1}{2} A_{\rm so}[J(J+1) - L(L+1) - S(S+1)]\,. \tag{3.1.53}$$

gives the energy separations for the fine structure. The fine structure energies of the carbon atom, ^{12}C and ^{13}C, in the ground ^3P state are determined experimentally with high precision by observing the direct transitions between the fine structure components [3, 4] as illustrated in Fig. 3.1. The energy separation of $^3P_2 - {}^3P_1$ is observed to be 809 GHz, which is fairly smaller than that expected by Eq. 3.1.53 from the observed $^3P_1 - {}^3P_0$ separation (492 GHz).

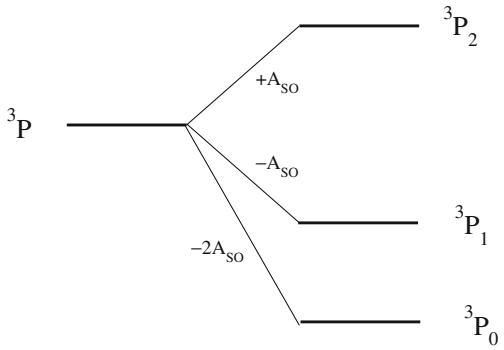

Fig. 3.1 Fine structure splitting observed for carbon atom

3.1.8.7 Nuclear Spin and Hyperfine Structure

If the nuclear spin angular momentum $\boldsymbol{I}$ is not zero, the vector sum of the nuclear spin and the electronic angular momentum $\boldsymbol{J}$ forms the total angular momentum $\boldsymbol{F}$; similarly to Eq. 3.1.39 in the case of single electron atoms, we have now

$$\boldsymbol{F} = \boldsymbol{J} + \boldsymbol{I}. \tag{3.1.54}$$

The energy levels split further into several sub-levels denoted by F quantum number which is the hyperfine structure.

Magnetic Interaction

In the Russel–Saunders coupling case the interaction of the nuclear spin $\boldsymbol{I}$ with the total angular momentum $\boldsymbol{J}$ is expressed as

$$\hat{h}_{\mathrm{mag}} = a(\hat{\boldsymbol{J}} \cdot \hat{\boldsymbol{I}}), \tag{3.1.55}$$

which should be compared with Eq. 3.1.40. The diagonal contribution of this operator can be evaluated by the vector model as

$$\Delta E_{\mathrm{mag}} = \frac{1}{2} a[F(F+1) - J(J+1) - I(I+1)]\,. \tag{3.1.56}$$

The quantity in the square brackets in the equation above is often expressed by C: i.e.,

$$C = F(F+1) - J(J+1) - I(I+1). \tag{3.1.57}$$

For ^{12}C atom, there is no hyperfine splitting because the nuclear spin $I = 0$ for this isotope atom. On the other hand the nuclear spin I is $\frac{1}{2}$ for ^{13}C isotope; the hyperfine levels of ^{13}C atom in the ground state are illustrated in Fig. 3.2.

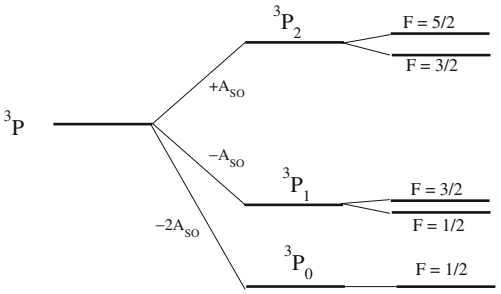

Fig. 3.2 Hyperfine levels of ^{13}C atom

Electric Quadrupole Interaction

So far we have assumed that the nucleus is a point mass. It is, however, not the case; a nucleus has a finite volume, and consequently it may have non-vanishing electric multi-pole moments, which interact with the electric field caused by the electrons surrounding the nucleus. Here we explain the interaction closely following the discussion presented Townes and Schawlow [5].

Because the electric dipole moment vanishes in atoms, if the nuclear state is not degenerate, in most cases the leading term next to the mono-pole (Coulombic) interaction in the electric multi-pole interaction energy is attributed to the quadrupole moment, i.e.,

$$W_{\mathrm{Q}} = \int \rho(x,y,z)\left[\frac{1}{2}x^2\frac{\partial^2 V}{\partial x^2} + \frac{1}{2}y^2\frac{\partial^2 V}{\partial y^2} + \frac{1}{2}z^2\frac{\partial^2 V}{\partial z^2} + xy\frac{\partial^2 V}{\partial x \partial y} + yz\frac{\partial^2 V}{\partial y \partial z} + zx\frac{\partial^2 V}{\partial z \partial x}\right]\mathrm{d}v, \tag{3.1.58}$$

where $\rho(x,y,z)$ is the nuclear charge density and V is the electric potential produced by the electrons. By removing the spherically symmetric contribution, which vanishes in a good approximation, the quadrupole interaction energy is expressed as

$$W_{\mathrm{Q}} = \frac{1}{6}\int \rho(x,y,z)\left[(3x^2 - r^2)\frac{\partial^2 V}{\partial x^2} + (3y^2 - r^2)\frac{\partial^2 V}{\partial y^2} + (3z^2 - r^2)\frac{\partial^2 V}{\partial z^2} + 6xy\frac{\partial^2 V}{\partial x \partial y} + 6yz\frac{\partial^2 V}{\partial y \partial z} + 6zx\frac{\partial^2 V}{\partial z \partial x}\right]\mathrm{d}v. \tag{3.1.59}$$

Since the volume of the nucleus is very small the field gradient V can be considered constant in the above equation.

Now we introduce an axis system (x_I, y_I, z_I), where z_I axis to be parallel to the nuclear spin angular momentum vector $\boldsymbol{I}$. Assuming that the nucleus spins very fast, the charge density can be considered cylindrically symmetric,

i.e., $\rho(x_I, y_I, z_I) = \rho(z_I)$, and the cross terms Eq. 3.1.59 vanish. In addition we have

$$\begin{aligned}\int \rho(z_I)(3x_I^2 - r^2)\mathrm{d}v &= \int \rho(z_I)(3y_I^2 - r^2)\mathrm{d}v \\ &= -\frac{1}{2}\int \rho(z_I)(3z_I^2 - r^2)\mathrm{d}v,\end{aligned} \tag{3.1.60}$$

where the relation

$$3z_I^2 - r^2 = -\left[(3x_I^2 - r^2) + (3y_I^2 - r^2)\right] \tag{3.1.61}$$

is used.

The quantity

$$Q = \frac{1}{e}\int \rho(z_I)(3z_I^2 - r^2)\mathrm{d}v \tag{3.1.62}$$

is the nuclear quadrupole moment. The quadrupole energy of Eq. 3.1.59 is then,

$$W_\mathrm{Q} = \frac{eQ}{6}\left[\frac{\partial^2 V}{\partial z_I^2} - \frac{1}{2}\left(\frac{\partial^2 V}{\partial x_I^2} + \frac{\partial^2 V}{\partial y_I^2}\right)\right]. \tag{3.1.63}$$

If the contribution of the electrons in the nucleus region is negligible, the Laplace equation holds:

$$\frac{\partial^2 V}{\partial x_I^2} + \frac{\partial^2 V}{\partial y_I^2} + \frac{\partial^2 V}{\partial z_I^2} = 0. \tag{3.1.64}$$

Equation 3.1.63 is thus further simplified as

$$W_\mathrm{Q} = \frac{eQ}{4}\left(\frac{\partial^2 V}{\partial z_I^2}\right). \tag{3.1.65}$$

The electrons move so fast that the z_I direction (the direction of $\boldsymbol{I}$) can be considered to be constant during the period of the orbital motion of electrons. If we take the average over the electronic orbital motion, the field gradient should be cylindrically symmetric along the axis of the electronic angular momentum vector $\boldsymbol{J}$. Then, in the coordinate system (x_J, y_J, z_J), where the z_J axis is parallel to $\boldsymbol{J}$, we obtain

$$\left(\frac{\partial^2 V}{\partial x_J^2}\right)_\mathrm{av} = \left(\frac{\partial^2 V}{\partial y_J^2}\right)_\mathrm{av} = -\frac{1}{2}\left(\frac{\partial^2 V}{\partial z_J^2}\right)_\mathrm{av} \tag{3.1.66}$$

where we apply the Laplace equation, Eq. 3.1.64. By using the angle θ between $\boldsymbol{I}$ and $\boldsymbol{J}$, the quadrupole interaction energy, Eq. 3.1.65, is rewritten classically as

$$W_\mathrm{Q} = \frac{eq_J Q}{4}\left(3\cos^2\theta - 1\right)/2, \tag{3.1.67}$$

where

$$q_J = \left(\frac{\partial^2 V}{\partial z_J^2}\right)_{\text{av}}. \tag{3.1.68}$$

The quantum mechanical expression corresponding to Eq. 3.1.67 was derived by Casimir as

$$\hat{H}_Q = \frac{1}{2} eq_J Q \left[3\left(\hat{\boldsymbol{I}}\cdot\hat{\boldsymbol{J}}\right)^2 + \frac{3}{2}\hat{\boldsymbol{I}}\cdot\hat{\boldsymbol{J}} - \hat{\boldsymbol{I}}^2\hat{\boldsymbol{J}}^2\right]/[I(2I-1)J(2J-1)]. \tag{3.1.69}$$

The diagonal contribution of $\hat{H}_Q$ is

$$W_{\text{Q}} = \frac{1}{2} eq_J Q \frac{3C(C+1)/4 - I(I+1)J(J+1)}{I(2I-1)J(2J-1)}, \tag{3.1.70}$$

where C is defined by Eq. 3.1.57. It should be noted here that the quadrupole moment vanishes for $J = 0, I = 0$ or $\frac{1}{2}$, because q_J vanishes for $J = 0$ and Q vanishes for $I = 0$ or $\frac{1}{2}$.

3.2 Diatomic Molecules

3.2.1 Hamiltonian for a Diatomic Molecule without Spin

The Hamiltonian of a diatomic molecule, AB, with n electrons, is expressed as

$$\hat{H} = \hat{H}^{\text{nuc}}(\boldsymbol{r}_a, \boldsymbol{r}_b, \hat{\boldsymbol{p}}_a, \hat{\boldsymbol{p}}_b) + \hat{H}_{\text{el}}(\boldsymbol{r}_1, \ldots, \boldsymbol{r}_n, \hat{\boldsymbol{p}}_1, \ldots, \hat{\boldsymbol{p}}_n, \boldsymbol{r}_a, \boldsymbol{r}_b), \tag{3.2.1}$$

where the effect of spins of electrons and nuclei is ignored, which will be discussed later. In the Hamiltonian given above, the coordinates of the nuclei A and B are represented by $\boldsymbol{r}_a$ and $\boldsymbol{r}_b$, their conjugate momenta are $\hat{\boldsymbol{p}}_a$ and $\hat{\boldsymbol{p}}_b$, the coordinates of electrons are $(\boldsymbol{r}_1, \boldsymbol{r}_2, \ldots, \boldsymbol{r}_n)$, and their conjugate momenta are $(\hat{\boldsymbol{p}}_1, \hat{\boldsymbol{p}}_2, \ldots, \hat{\boldsymbol{p}}_n)$.

Those two parts of the Hamiltonian in Eq. 3.2.1 are concretely expressed using individual coordinate and momentum as

$$\hat{H}^{\text{nuc}} = \frac{1}{2}\left(\hat{\boldsymbol{p}}_a^2/m_a + \hat{\boldsymbol{p}}_b^2/m_b\right) + \frac{e^2}{4\pi\epsilon_0} Z_a Z_b / |\boldsymbol{r}_a - \boldsymbol{r}_b| \tag{3.2.2}$$

$$\hat{H}^{\text{el}} = \frac{1}{2}\sum_{i=1}^{n} \hat{\boldsymbol{p}}_i^2/m - \frac{e^2}{4\pi\epsilon_0}\left(\sum_{i=1}^{n} Z_a/|\boldsymbol{r}_i - \boldsymbol{r}_a| + \sum_{i=1}^{n} Z_b/|\boldsymbol{r}_i - \boldsymbol{r}_b| - \sum_{i<j}^{n} 1/|\boldsymbol{r}_i - \boldsymbol{r}_j|\right), \tag{3.2.3}$$

where m_a and m_b are the masses of the nucleus A and B, Z_a and Z_b are the atomic number of them, m is the electron mass, and e is the electron charge. The first part,

$\hat{H}^{\mathrm{nuc}}$, contains the kinetic energies of the nuclei and the repulsive Coulombic potential between the nuclei, and depends only on the nuclear variables. The second part, $\hat{H}^{\mathrm{el}}$ contains the kinetic energies of the electrons, attractive Coulombic potential between the nuclei and electrons, and the repulsive one between the electrons.

3.2.1.1 Separation of Nuclear and Electron Variables

The energy of a diatomic molecule can be obtained by solving the Schrödinger equation,

$$\left[\hat{H}^{\mathrm{nuc}} + \hat{H}^{\mathrm{el}}\right]\Psi(\boldsymbol{r}_a, \boldsymbol{r}_b, \boldsymbol{r}_1, \ldots, \boldsymbol{r}_n) = E\Psi(\boldsymbol{r}_a, \boldsymbol{r}_b, \boldsymbol{r}_1, \ldots, \boldsymbol{r}_n). \tag{3.2.4}$$

For solving this equation, we assume that the eigenfunction $\Psi(\boldsymbol{r}_a, \boldsymbol{r}_b, \boldsymbol{r}_1, \ldots, \boldsymbol{r}_n)$ can be expressed as a product

$$\Psi(\boldsymbol{r}_a, \boldsymbol{r}_b, \boldsymbol{r}_1, \ldots, \boldsymbol{r}_n) = \Psi^{\mathrm{nuc}}(\boldsymbol{r}_a, \boldsymbol{r}_b)\Psi^{\mathrm{el}}(\boldsymbol{r}_1, \ldots, \boldsymbol{r}_n; \boldsymbol{r}_a, \boldsymbol{r}_b). \tag{3.2.5}$$

Substituting $\Psi(\boldsymbol{r}_a, \boldsymbol{r}_b, \boldsymbol{r}_1, \ldots, \boldsymbol{r}_n)$ in Eq. 3.2.4 by Eq. 3.2.5, and neglecting the effect of $\hat{\boldsymbol{p}}_a$ and $\hat{\boldsymbol{p}}_b$ on the function $\Psi^{\mathrm{el}}(\boldsymbol{r}_1, \ldots, \boldsymbol{r}_n; \boldsymbol{r}_a, \boldsymbol{r}_b)$, we obtain

$$\begin{aligned}&\Psi^{\mathrm{el}}(\boldsymbol{r}_1, \ldots, \boldsymbol{r}_n; \boldsymbol{r}_a, \boldsymbol{r}_b)\hat{H}^{\mathrm{nuc}}\Psi^{\mathrm{nuc}}(\boldsymbol{r}_a, \boldsymbol{r}_b) \;+\; \Psi^{\mathrm{nuc}}(\boldsymbol{r}_a, \boldsymbol{r}_b)\hat{H}^{\mathrm{el}}\Psi^{\mathrm{el}}(\boldsymbol{r}_1, \ldots, \boldsymbol{r}_n; \boldsymbol{r}_a, \boldsymbol{r}_b)\\ &\quad = E\Psi^{\mathrm{nuc}}(\boldsymbol{r}_a, \boldsymbol{r}_b)\Psi^{\mathrm{el}}(\boldsymbol{r}_1, \ldots, \boldsymbol{r}_n; \boldsymbol{r}_a, \boldsymbol{r}_b).\end{aligned} \tag{3.2.6}$$

Dividing both sides by $\Psi^{\mathrm{nuc}}\Psi^{\mathrm{el}}$, Eq. 3.2.6 is rewritten as

$$\frac{\left[\hat{H}^{\mathrm{nuc}}\Psi^{\mathrm{nuc}}(\boldsymbol{r}_a, \boldsymbol{r}_b)\right]}{\Psi^{\mathrm{nuc}}(\boldsymbol{r}_a, \boldsymbol{r}_b)} + \frac{\left[\hat{H}^{\mathrm{el}}\Psi^{\mathrm{el}}(\boldsymbol{r}_1, \ldots, \boldsymbol{r}_n; \boldsymbol{r}_a, \boldsymbol{r}_b)\right]}{\Psi^{\mathrm{el}}(\boldsymbol{r}_1, \ldots, \boldsymbol{r}_n; \boldsymbol{r}_a, \boldsymbol{r}_b)} = E. \tag{3.2.7}$$

The first term on the left side of above equation is a function which depends only on the nuclear coordinates $(\boldsymbol{r}_a, \boldsymbol{r}_b)$ and the second term is a function of both nuclear and electron coordinates. To satisfy the equation for any $(\boldsymbol{r}_1, \ldots, \boldsymbol{r}_n)$, the value of the second term should not depend on $(\boldsymbol{r}_1, \ldots, \boldsymbol{r}_n)$: i.e.,

$$\frac{\left[\hat{H}^{\mathrm{el}}\Psi^{\mathrm{el}}(\boldsymbol{r}_1, \ldots, \boldsymbol{r}_n; \boldsymbol{r}_a, \boldsymbol{r}_b)\right]}{\Psi^{\mathrm{el}}(\boldsymbol{r}_1, \ldots, \boldsymbol{r}_n; \boldsymbol{r}_a, \boldsymbol{r}_b)} = \epsilon(\boldsymbol{r}_a, \boldsymbol{r}_b), \tag{3.2.8}$$

which is not other than the Schrödinger equation for the electrons treating the nuclear coordinates $(\boldsymbol{r}_a, \boldsymbol{r}_b)$ as parameters:

$$\hat{H}^{\mathrm{el}}\Psi^{\mathrm{el}}(\boldsymbol{r}_1, \ldots, \boldsymbol{r}_n; \boldsymbol{r}_a, \boldsymbol{r}_b) = \epsilon(\boldsymbol{r}_a, \boldsymbol{r}_b)\Psi^{\mathrm{el}}(\boldsymbol{r}_1, \ldots, \boldsymbol{r}_n; \boldsymbol{r}_a, \boldsymbol{r}_b). \tag{3.2.9}$$

The value $\epsilon(\boldsymbol{r}_a, \boldsymbol{r}_b)$ is thus considered as the energy of the electrons in the state expressed by $\Psi^{\mathrm{el}}(\boldsymbol{r}_1, \ldots, \boldsymbol{r}_n; \boldsymbol{r}_a, \boldsymbol{r}_b)$.

Substituting Eq. 3.2.8 into Eq. 3.2.7, we obtain

$$\frac{\left[\hat{H}^{\mathrm{nuc}}\Psi^{\mathrm{nuc}}(\boldsymbol{r}_a,\boldsymbol{r}_b)\right]}{\Psi^{\mathrm{nuc}}(\boldsymbol{r}_a,\boldsymbol{r}_b)} + \epsilon(\boldsymbol{r}_a,\boldsymbol{r}_b) = E, \tag{3.2.10}$$

which is the Schrödinger equation for the nuclear motion:

$$\left[\hat{H}^{\mathrm{nuc}} + \epsilon(\boldsymbol{r}_a,\boldsymbol{r}_b)\right]\Psi^{\mathrm{nuc}}(\boldsymbol{r}_a,\boldsymbol{r}_b) = E\Psi^{\mathrm{nuc}}(\boldsymbol{r}_a,\boldsymbol{r}_b). \tag{3.2.11}$$

Using Eq. 3.2.2 for $\hat{H}^{\mathrm{nuc}}$, and considering that $\epsilon(\boldsymbol{r}_a,\boldsymbol{r}_b)$ is actually expressed as $\epsilon(|\boldsymbol{r}_a-\boldsymbol{r}_b|)$ for a diatomic molecule, the equation above is expressed as

$$\left[\frac{1}{2}\left(\hat{\boldsymbol{p}}_a^2/m_a+\hat{\boldsymbol{p}}_b^2/m_b\right)+V(|\boldsymbol{r}_a-\boldsymbol{r}_b|)\right]\Psi^{\mathrm{nuc}}(\boldsymbol{r}_a,\boldsymbol{r}_b) = E\Psi^{\mathrm{nuc}}(\boldsymbol{r}_a,\boldsymbol{r}_b), \tag{3.2.12}$$

where

$$V(|\boldsymbol{r}_a-\boldsymbol{r}_b|) = \frac{Z_aZ_be^2}{4\pi\epsilon_0|\boldsymbol{r}_a-\boldsymbol{r}_b|}+\epsilon(|\boldsymbol{r}_a-\boldsymbol{r}_b|). \tag{3.2.13}$$

The quantity V is the potential energy for the nuclear motion. In the terminology of the molecular orbital theory, the word "electronic energy" implies the quantity V defined by Eq. 3.2.13, which includes the repulsion energy between the nuclei, instead of the ϵ defined by Eq. 3.2.9.

3.2.1.2 Born–Oppenheimer Approximation

For deriving Eq. 3.2.6, we introduced an assumption

$$\hat{\boldsymbol{p}}_k\Psi^{\mathrm{el}}(\boldsymbol{r}_1,\ldots,\boldsymbol{r}_n;\boldsymbol{r}_a,\boldsymbol{r}_b) = 0, \tag{3.2.14}$$

where $k=a$ or b; i.e., the momentum operator for the nuclear motion, $\hat{\boldsymbol{p}}_a$ or $\hat{\boldsymbol{p}}_b$, has no effect on the electronic wavefunctions. This assumption was introduced first by Born and Oppenheimer in 1927 to simplify the problem [6], and referred as the Born–Oppenheimer approximation.

This assumption is considered to be reasonable for most of the molecules because of the following reason [1]. The electron mass m is 1836 times smaller than the proton mass m_p, and about twenty thousand times smaller than the mass of carbon nuclei, so that electrons in molecules move much faster than the nuclei. When the nuclei change their positions, the electrons can follow almost immediately, and thus it is enough to evaluate the motion of electrons for each instantaneous positions of nuclei. In other words, the effect of the momenta of nuclei on the electronic wavefunctions can be neglected; Eq. 3.2.14 is a quantum mechanical expression for this.

The ratio of electron mass to nuclear mass is often used to evaluate the order of magnitude of perturbations in molecular systems [7, 8]. The parameter often called as "Born–Oppenheimer parameter" is defined as the quartic root of this ratio,

$$\kappa = \left(\frac{m}{M}\right)^{\frac{1}{4}} \approx \frac{1}{10}, \tag{3.2.15}$$

where M is a typical nuclear mass. Using this parameter, the molecular levels can be classified into three categories, i.e., the electronic energy (E_{el}), vibrational energy (E_{vib}), and rotational energy (E_{rot}), with following order of magnitude relation:

$$E_{\mathrm{vib}} = \kappa^2 E_{\mathrm{el}} \tag{3.2.16}$$

$$E_{\mathrm{rot}} = \kappa^4 E_{\mathrm{el}}. \tag{3.2.17}$$

The electronic energy E_{el} is not other than V defined by Eq. 3.2.13.

3.2.2 Hamiltonian for a Diatomic Molecule without Electronic Angular Momentum

3.2.2.1 Nuclear Motions

The Hamiltonian operator for the nuclear motions of a diatomic molecule, in the left side of Eq. 3.2.12, is essentially same as that for the hydrogen atom, Eq. 3.1.1. As we have done for the case of the hydrogen atom, we introduce the relative coordinate $\boldsymbol{r}$, the coordinate of the center of mass $\boldsymbol{R}$, total mass M, and the reduced mass μ, i.e.,

$$\boldsymbol{r} = \boldsymbol{r}_b - \boldsymbol{r}_a, \tag{3.2.18}$$

$$\boldsymbol{R} = \frac{(m_a \boldsymbol{r}_a + m_b \boldsymbol{r}_b)}{m_a + m_a}, \tag{3.2.19}$$

$$M = m_a + m_b, \tag{3.2.20}$$

$$\mu = \frac{m_a m_b}{m_a + m_b}. \tag{3.2.21}$$

Then the Hamiltonian for the nuclear motion of a diatomic molecule is expressed as

$$\hat{H} = \frac{\hat{\boldsymbol{P}}^2}{2M} + \frac{\hat{\boldsymbol{p}}^2}{2\mu} + V(|\boldsymbol{r}|). \tag{3.2.22}$$

The first term represents the translational kinetic energy of the molecule in the space, and will be ignored in the following.

As in the case of the hydrogen atom, we introduce the polar coordinate system for the relative coordinate $\boldsymbol{r}$, then the Schrödinger equation based on the Hamiltonian, Eq. 3.2.22, is expressed as Eqs. 3.1.15–3.1.17. The angular parts are exactly identical. The radial part, Eq. 3.1.17, can be rewritten as

$$-\frac{\hbar^2}{2\mu}\frac{1}{r^2}\frac{\mathrm{d}}{\mathrm{d}r}\left(r^2\frac{\mathrm{d}\psi_J(r)}{\mathrm{d}r}\right)=\left[E-V(r)-\frac{\hbar^2 J(J+1)}{2\mu r^2}\right]\psi_J(r). \tag{3.2.23}$$

where the angular momentum quantum number in E_θ, Eq. 3.1.20, is expressed by J, because it is not the electronic angular momentum here. Equation 3.2.23 can be solved for each J value, and thus the wavefunction may be expressed by $\psi_J(r)$ indicating J as a parameter. The last term in the bracket on the right side can be considered as an effective potential due to the centrifugal force induced by the rotation of the molecule. It should be noted that the term can be rewritten as

$$\frac{\hbar^2 J(J+1)}{2I}, \tag{3.2.24}$$

where $I=\mu r^2$ is the moment of inertia of the molecule for the nuclear distance r.

3.2.2.2 Vibrational Energy

If the molecule is not rotating, $J=0$, we obtain from Eq. 3.2.23,

$$\left[-\frac{\hbar^2}{2\mu}\frac{1}{r^2}\frac{\mathrm{d}}{\mathrm{d}r}\left(r^2\frac{\mathrm{d}}{\mathrm{d}r}\right)+V(r)\right]\psi_{J=0}(r)=E\psi_{J=0}(r), \tag{3.2.25}$$

which is the Schrödinger equation for the vibrational motion (bond stretching vibration) of the diatomic molecule, and E is not other than the vibrational energy E_v. Equation 3.2.25 can be simplified by introducing

$$\psi_v(r)=\psi_{J=0}(r)/r \tag{3.2.26}$$

as

$$\left[-\frac{\hbar^2}{2\mu}\frac{\mathrm{d}^2}{\mathrm{d}r^2}+V(r)\right]\psi_v(r)=E_v\psi_v(r). \tag{3.2.27}$$

The typical shape of the potential energy $V(r)$ for a diatomic molecule is illustrated in Fig. 3.3, which is characterized by the three elemental values: (1) the potential minimum at r_e, (2) the dissociation energy measured from the potential minimum D_e, and (3) the infinitely large potential value at $r=0$.

If the amplitude of the vibration is small compared to the r_e, it is convenient to express the instantaneous nuclear distance r as

$$r=r_e+\rho. \tag{3.2.28}$$

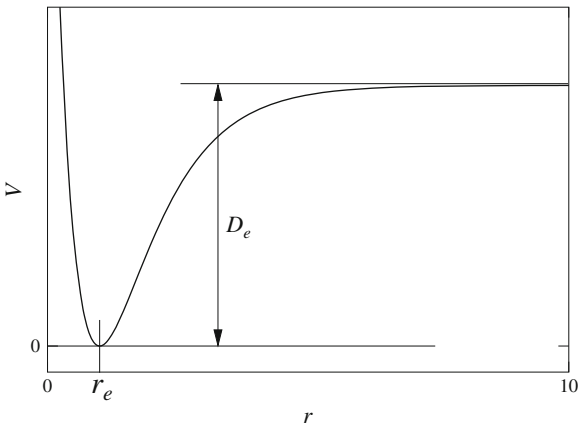

Fig. 3.3 A typical shape of the potential energy for a diatomic molecule

Then the potential $V(r)$ can be expressed as a power series of ρ:

$$V(r_e + \rho) = V(r_e) + \sum_{n=1}^{\infty} \frac{1}{n!} \left(\frac{\mathrm{d}^n V}{\mathrm{d}r^n} \right)_{r=r_e} \rho^n. \tag{3.2.29}$$

Because $V(r_e) = 0$ and $(\mathrm{d}V/\mathrm{d}r)_{r=r_e} = 0$, the above equation is rewritten as

$$V(r_e + \rho) = \frac{1}{2} k^{(2)} \rho^2 + \frac{1}{6} k^{(3)} \rho^3 + \cdots. \tag{3.2.30}$$

The coefficient $k^{(2)}$ is called the quadratic force constant, or the harmonic force constant. The coefficient $k^{(3)}$ is called the cubic force constant, and so on. The contribution of the cubic and higher order terms is called as the anharmonicity of the potential. By ignoring the anharmonic terms in the potential, Eq. 3.2.27 is identical to the Schrödinger equation of a harmonic oscillator,

$$\left[-\frac{\hbar^2}{2\mu} \frac{d^2}{d\rho^2} + \frac{1}{2} k \rho^2 \right] \psi_v^{\mathrm{harm}}(r_e + \rho) = E_v^{\mathrm{harm}} \psi_v^{\mathrm{harm}}(r_e + \rho), \tag{3.2.31}$$

and the eigenvalues, i.e., the harmonic vibrational energy, are well known as

$$E_v^{\mathrm{harm}} = (v + \frac{1}{2}) \hbar \omega_{\mathrm{harm}}, \tag{3.2.32}$$

where v is a vibrational quantum number and ω_{harm} is the angular frequency, or angular velocity, of the classical harmonic oscillator,

$$\omega_{\mathrm{harm}} = \sqrt{\frac{k^{(2)}}{\mu}}. \tag{3.2.33}$$

The harmonic vibrational frequency ν_{harm} in the unit of Hz is thus expressed as[2]

$$\nu_{\text{harm}} = \omega_{\text{harm}}/(2\pi) \tag{3.2.34}$$

and Eq. 3.2.32 is rewritten as

$$E_v^{\text{harm}} = \left(v + \frac{1}{2}\right) h\nu_{\text{harm}}. \tag{3.2.35}$$

The harmonic oscillator wavefunction, i.e., the eigenfunction of Eq. 3.2.32, for the state expressed by v is

$$\psi_v^{\text{harm}}(r_e + \rho) = N_v H_v(a\rho) e^{-\frac{1}{2}a^2\rho^2}, \tag{3.2.36}$$

where H_v is the vth Hermite polynomial with

$$a = \left(\frac{\mu k^{(2)}}{\hbar^2}\right)^{\frac{1}{4}}. \tag{3.2.37}$$

3.2.2.3 Rotational Energy

For the case of $J \neq 0$, the rotational correction term, Eq. 3.2.24, should be evaluated. If the nuclear distance of the diatomic molecule is fixed at the point of the potential minimum (equilibrium position), $r = r_e$, then the moment of inertia I is independent of the vibrational motion, and the rotational energy correction is simply given as

$$E_{\text{rot}} = hB_e J(J+1), \tag{3.2.38}$$

where B_e is the rotational constant at the equilibrium position in the frequency unit (Hz), and[3]

$$hB_e = \frac{\hbar^2}{2I_e}. \tag{3.2.39}$$

The nuclear distance changes by the vibrational motion, and therefore, the evaluation of the rotational energy is not so simple as in Eq. 3.2.28. In many cases, however, the rotational energy contribution is much smaller than that of the vibration approximately given in Eq. 3.2.32 as discussed earlier: see Eqs. 3.2.16 and 3.2.17. Thus we can handle the rotational correction term as a perturbation to the molecular vibration, and the first order correction term given by the diagonal

[2] This value in wavenumber unit (cm^{-1}), $\tilde{\nu}$, is expressed as $\tilde{\nu} = \omega_{\text{harm}}/(2\pi c)$ with c in cm/s.

[3] If the rotational constant is given in wavenumber unit (cm^{-1}), then $hcB_e = \hbar^2/(2I_e)$ with c in cm/s.

matrix element of the perturbation operator represents the rotational energy E_{rot}; i.e.,

$$E_{\mathrm{rot}} = hB_v J(J+1), \tag{3.2.40}$$

where B_v is the effective rotational constant averaged for the vth vibrational state, i.e.,

$$hB_v = \langle \psi_v | \hbar^2/(2I) | \psi_v \rangle, \tag{3.2.41}$$

which can be approximated as

$$B_v = B_e - \alpha\left(v+\frac{1}{2}\right) + \gamma\left(v+\frac{1}{2}\right)^2 \cdots \tag{3.2.42}$$

3.2.2.4 Dunham Expansion

The rovibrational energy of a diatomic molecule is expressed effectively as the sum of the harmonic vibrational energy, Eq. 3.2.35, and the rotational energy of the rigid body, Eq. 3.2.40, with anharmonic and centrifugal distortion corrections:

$$\begin{aligned} E_{v,J}/h = {} & \nu_{\mathrm{harm}}\left(v+\frac{1}{2}\right) + x\left(v+\frac{1}{2}\right)^2 + y\left(v+\frac{1}{2}\right)^2 + \cdots \\ & + B_v J(J+1) - D_v[J(J+1)]^2 + H_v[J(J+1)]^3 + \cdots, \end{aligned} \tag{3.2.43}$$

where x and y are called as anharmonicity constants,[4] and D and H are the quartic and sextic centrifugal distortion constants.

More sophisticated expression was derived by Dunham [9] as

$$E_{v,J}/h = \sum_{i,j} Y_{ij}\left(v+\frac{1}{2}\right)^i [J(J+1)]^j. \tag{3.2.44}$$

The relation of the Dunham coefficients with the parameters used in the traditional expression Eq. 3.2.43 can be found in the textbook by Townes and Schawlow [5]. The expressions of the $Y_{i,j}$ coefficients by the potential parameters, Eq. 3.2.30, are also listed there; actually Dunham expressed the potential as

$$V = a_0\xi^2(1 + a_1\xi + a_2\xi^2 + \cdots), \tag{3.2.45}$$

where $\xi = (r - r_e)/r_e$.

[4] For diatomic molecules the anharmonicity constants x, y, and so on are often defined as $\nu_{\mathrm{harm}}x$, etc.

3.2.3 Hamiltonian for a Diatomic Molecule with Electronic Angular Momentum

3.2.3.1 Vector Model and Hund's Coupling Cases

Since the spin–orbit interaction of the electrons in a molecule is usually small, we assume that the electronic orbital angular momentum $\boldsymbol{L}$ and electron spin angular momentum. $\boldsymbol{S}$, defined as

$$\boldsymbol{L} = \sum_{i}^{N} \boldsymbol{l}_i, \tag{3.2.46}$$

$$\boldsymbol{S} = \sum_{i}^{N} \boldsymbol{s}_i, \tag{3.2.47}$$

are good quantum numbers also for molecules: similar to the Russel–Saunders coupling discussed for the atomic term expressions, see Sect. 3.1.8.4. In analogy to the atomic term expressions, we denote the electronic states of $L = 0, 1, 2, \ldots$ as $\Sigma, \Delta, \Pi, \ldots$; the molecular term symbols are expressed in Greek, whereas atomic term symbols in Roman. The spin multiplicity $2S + 1$ is indicated as a superscript on the left of the angular momentum symbol as in the case of atoms. Thus, the electronic state discussed in the previous section is of $^1\Sigma$.

For the cases other than the $^1\Sigma$ state, various coupling schemes of angular momenta caused by molecular rotation, electronic orbital motion, and electron spin have to be considered. The contribution of the nuclear spins is usually small and can be considered separately.

We follow in this text the IUPAC recommendation in 1994 for various angular momenta [10]:

$\boldsymbol{L}$: electron orbital angular momentum
$\boldsymbol{S}$: electron spin angular momentum
$\boldsymbol{R}$: rotational angular momentum
$\boldsymbol{N}$: total orbital angular momentum; $\boldsymbol{N} = \boldsymbol{R} + \boldsymbol{L}$
$\boldsymbol{J}$: total angular momentum without the nuclear spin; $\boldsymbol{J} = \boldsymbol{N} + \boldsymbol{S}$
$\boldsymbol{I}$: nuclear spin angular momentum.

The electronic states of a diatomic molecule resemble those of a atom perturbed by the external field generated by another atom nearby. The perturbation should be axially symmetric along the axis connecting the two atoms, so-called molecular axis. Because of this symmetry of the perturbation, called "axis interaction" in this text, not only the total angular momentum and its projection on a space fixed axis, but also its projection on the molecular axis is conserved, i.e., the quantum number specifying them are good quantum numbers. As described below the electronic states of a diatomic molecule can be classified into the Hund's coupling cases by the approximate quantity of this projection on the molecular axis.

3.2.3.2 Hund's Coupling Case (a)

If the axis interaction is stronger than the interactions between the various angular momenta, the electron orbital angular momentum $\boldsymbol{L}$ couples first with the axis. The vector $\boldsymbol{L}$ undergoes a precessional motion along the axis (in view point of the molecule-fixed system) and its projection on the axis is conserved, which is denoted by Λ, which is a good quantum number; the states with different Λ are well separated. The electron spin angular momentum $\boldsymbol{S}$ is then coupled with the axis by the spin–orbit interaction, and its projection on the axis is represented by a quantum number Σ. The Λ and Σ are the signed quantities: classically they are

$$\Lambda = \boldsymbol{L} \cdot \boldsymbol{e}_{\text{axis}} \tag{3.2.48}$$

$$\Sigma = \boldsymbol{S} \cdot \boldsymbol{e}_{\text{axis}}, \tag{3.2.49}$$

where the direction of the molecular axis is represented by an unit vector $\boldsymbol{e}_{\text{axis}}$. Thus along with the molecular axis there is an angular momentum components, Ω, defined as

$$\Omega = \Lambda + \Sigma, \tag{3.2.50}$$

which is a good quantum number in this case; the multiplets separation for different $|\Omega|$, which is caused by the spin–orbit interaction, are much larger than the typical rotational energy separation.

The vector addition of this axis component and the rotational angular momentum $\boldsymbol{R}$ forms the total angular momentum $\boldsymbol{J}$:

$$\boldsymbol{J} = \boldsymbol{R} + \Omega \boldsymbol{e}_{\text{axis}}. \tag{3.2.51}$$

This requires $J \geq \Omega$.

Since $\boldsymbol{R}$ is perpendicular to $\boldsymbol{e}_{\text{axis}}$, Ω is the axis components of the total angular momentum $\boldsymbol{J}$. The coupling scheme described above is illustrated in Fig. 3.4 by

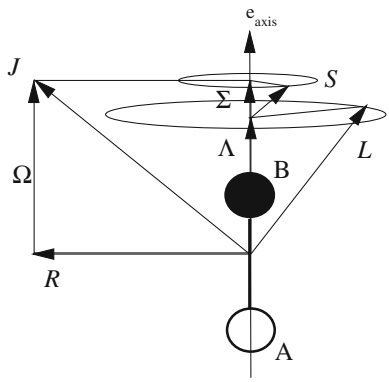

Fig. 3.4 The vector model is illustrated for Hund's case (a)

the vector model above, which is called as Hund's coupling case (a). In case (a), Ω is a good quantum number, and thus we indicate its absolute value, $|\Omega|$, in the term symbol as a subscript on the right; for example the term symbol $^2\Pi_{\frac{3}{2}}$ represents the state of $(S = \frac{1}{2}, L = 1, |\Omega| = \frac{3}{2})$.

3.2.3.3 Rotational Energy in Case (a)

Since the two angular momentum vectors, $\boldsymbol{R}$ and $\Omega \boldsymbol{e}_{\text{axis}}$, are perpendicular with each other, the rotational energies in case (a) can be expressed classically as the sum of the quantity proportional to $\boldsymbol{R}^2$ and Ω^2: in quantum mechanics we obtain in the first order approximation,

$$\begin{aligned} E_{\text{rot}}/h &= B_v \boldsymbol{R}^2 + A\Omega^2 \\ &= B_v \left[J(J+1) - \Omega^2 \right] + A\Omega^2, \end{aligned} \tag{3.2.52}$$

where we employed the vector model, Eq. 3.2.51, to evaluate $\boldsymbol{R}^2$. B_v is the rotational constant, see Eq. 3.2.41. Since Ω is purely electronic, the term with A represents a part of the electronic energy, and thus usually large. This term can be rewritten as

$$A\Omega^2 = A\left(\Lambda^2 + \Sigma^2\right) + 2A\Lambda\Sigma. \tag{3.2.53}$$

The cross term on the right originates from the spin–orbit interaction, $A_{\text{so}}\boldsymbol{LS}$: *cf*. Eq. 3.1.52. The diagonal contribution of the interaction is $A_{\text{so}}\Lambda\Sigma$ in case (a). Thus Eq. 3.1.52 can be replaced by

$$E_{\text{rot}}/h = B_v \left[J(J+1) - \Omega^2 \right] + A_{\text{so}}\Lambda\Sigma + A\left(\Lambda^2 + \Sigma^2\right). \tag{3.2.54}$$

The last term of the equation is a constant for a given electronic term, and thus can be ignored here because it can be included in the electronic energy.[5]

The energy level diagram of a $^2\Pi$ state is schematically presented in Fig. 3.5. For this state, $L = 1$ and $S = \frac{1}{2}$; i.e., $\Lambda = \pm 1$ and $\Sigma = \pm\frac{1}{2}$. Consequently, we have $\Omega = \pm 1 \pm \frac{1}{2} = \pm\frac{3}{2}$ and $\Omega = \pm 1 \mp \frac{1}{2} = \pm\frac{1}{2}$. The states of $|\Omega| = \frac{1}{2}$ and $\frac{3}{2}$ have different energies due to the spin–orbit interaction; the size of splitting is $|A_{\text{so}}|$; if $A_{\text{so}} > 0$, the $|\Omega| = \frac{1}{2}$ level is lower in energy than the $|\Omega| = \frac{3}{2}$, and vice versa: the multiplets split by the spin–orbit interaction with $A_{\text{so}} > 0$ is called *regular* and with $A_{\text{so}} < 0$ *inverted* as in the atomic cases, *cf*. Sect. 3.1.8.6.

[5] It should be noted that the spin–orbit constant A_{so} is different from A in Eq. 3.1.52 by a factor of 2.

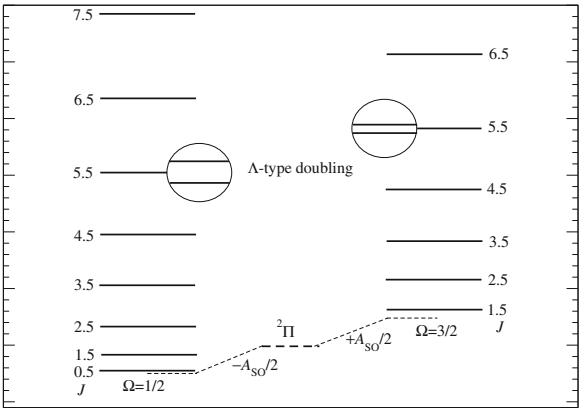

Fig. 3.5 Energy level diagram of a $^2\Pi$ (Hund's case (a)) state is schematically presented, assuming $A_{SO} = 10$ and $B_v = 1$ cm^{-1} in Eq. 3.2.54

3.2.3.4 Hund's Coupling Case (b)

In this coupling case, the orbital angular momentum $\boldsymbol{L}$ couples strongly with the axis, i.e., Λ is a good quantum number, but the electron spin $\boldsymbol{S}$ does not couple to the axis, because of the weak spin–orbit interaction. The rotational angular momentum $\boldsymbol{R}$ and Λ form a total orbital angular momentum $\boldsymbol{N}$ as

$$\boldsymbol{N} = \boldsymbol{R} + \Lambda \boldsymbol{e}_{\text{axis}}, \tag{3.2.55}$$

which requires $N \geq \Lambda$.

Then the spin $\boldsymbol{S}$ is magnetically coupled with $\boldsymbol{N}$, and the total angular momentum $\boldsymbol{J}$ is formed by the vector addition,

$$\boldsymbol{J} = \boldsymbol{N} + \boldsymbol{S}; \tag{3.2.56}$$

thus the quantum number J should be

$$J = N + S, N + S - 1, \ldots, |N - S|. \tag{3.2.57}$$

The vector diagram of the coupling scheme is illustrated in Fig. 3.6

In this case, the spin multiplet components are split by the spin–rotation interaction, $\gamma \boldsymbol{SN}$, and the energy is expressed in the first order approximation as

$$E_{\text{rot}}/h = B_v\left[N(N+1) - \Lambda^2\right] + \frac{1}{2}\gamma[J(J+1) - N(N+1) - S(S+1)], \tag{3.2.58}$$

where γ is called spin–rotation coupling constant (Fig. 3.7 illustrates an example).

3.2.3.5 Other Fine Structure Interactions

Here we explain two additional interactions which are often un-ignorable. The first one is the *spin–spin coupling*. In case of more than one unpaired electrons,

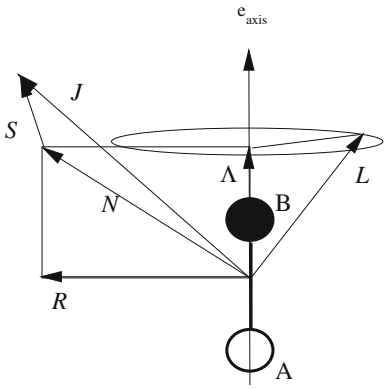

Fig. 3.6 The vector diagram of the coupling scheme is illustrated for case (b)

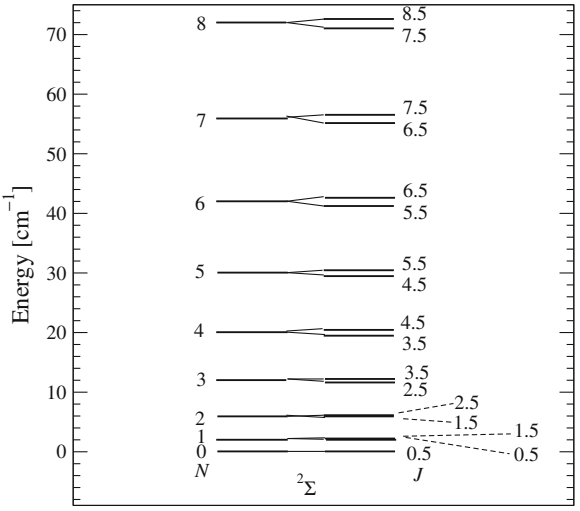

Fig. 3.7 The energy level diagram of a $^2\Sigma$ state (Hund's case (b)) is schematically illustrated, assuming $B_v = 1$ and $\gamma = 0.1\,\mathrm{cm}^{-1}$ in Eq. 3.2.58

the interactions between the spins of those electrons causes an perturbation to the energy expressed by

$$\hat{H}_{\mathrm{SS}} = \lambda \frac{2}{3}\left(3\hat{S}_z^2 - \hat{\boldsymbol{S}}^2\right). \tag{3.2.59}$$

The second one is the Λ-*type doubling*, which lifts the degeneracy of the $\Lambda = +1$ and -1 state in the Π electronic state; the interaction is effectively expressed by the following operator:

$$\begin{aligned}\hat{H}_\Lambda = {} & o\left(\hat{S}_+^2 + \hat{S}_-^2\right)/2 \\ & - p\left(\hat{N}_+\hat{S}_+ + \hat{N}_-\hat{S}_-\right)/2 \\ & + q\left(\hat{N}_+^2 + \hat{N}_-^2\right)/2.\end{aligned} \tag{3.2.60}$$

The q term exists for all Π states. The p term vanishes for $^1\Pi$ states, and the o term vanishes for $^1\Pi$ and $^2\Pi$ states.

The Λ-type doubling interaction, Eq. 3.2.60, however, is an off-diagonal interaction. The couplings discussed in the previous sections also have off-diagonal contributions. In the descriptions given to the previous sections are limited to the diagonal contributions of the interaction terms, assuming that the coupling scheme (a) or (b) is good. In order to reduce the off-diagonal contributions as much as possible, coupling schemes other than the case (a) and (b) have been proposed.

In order to evaluate correctly the off-diagonal contributions, however, it becomes common to express the necessary matrix elements (diagonal as well as off-diagonal) by the case (b) basis and to diagonalize the energy matrix numerically; thanks to the developments in the computer technology, it works very well in general, including the hyperfine interactions described in the next section.

3.2.4 Hyperfine Structure

If the nuclear spin angular momentum $\boldsymbol{I}$ is not zero for a nucleus of the diatomic molecule, the energy levels split further into the hyperfine structure denoted by F quantum number defined by Eq. 3.1.54. As discussed in Sect. 3.1.8.7 there are two kinds of interactions which contribute to the hyperfine structure: the magnetic interaction and the electric quadrupole interaction. For simplicity we assume here that only one nucleus has a non-vanishing nuclear spin.

3.2.4.1 Magnetic Interaction

Similar to the magnetic interaction in atoms, Eq. 3.1.55, there are interactions between the nuclear spin angular momentum and the other angular momenta. Assuming the z-axis is the molecular axis, the magnetic interactions can be expressed as

$$\begin{aligned}\hat{h}_{\mathrm{mag}} = {} & a(\hat{\boldsymbol{I}}\cdot\hat{\boldsymbol{L}}) \\ & + b_{\mathrm{F}}(\hat{\boldsymbol{I}}\cdot\hat{\boldsymbol{S}}) \\ & + c(\hat{I}_z\hat{S}_z - \hat{\boldsymbol{I}}\cdot\hat{\boldsymbol{S}}/3) \\ & - d(\hat{S}_+\hat{I}_+ + \hat{S}_-\hat{I}_-)/2, \end{aligned} \tag{3.2.61}$$

where the first line in the right is the nuclear spin–orbit interaction, the second line the Fermi contact interaction, the third line the diagonal contribution of the electron–spin nuclear–spin dipole–dipole interaction, and the last line the off-diagonal contribution for the Π electronic state between the $\Lambda = \pm 1$.

For a diatomic molecule, we have additionally the nuclear spin–rotation coupling:

$$\hat{h}_{\mathrm{IJ}} = C_{\mathrm{I}}(\hat{\boldsymbol{I}} \cdot \hat{\boldsymbol{J}}) - C'_{\mathrm{I}}(\hat{I}_{+}\hat{J}_{+} + \hat{I}_{-}\hat{J}_{-})/2, \tag{3.2.62}$$

3.2.4.2 Electric Quadrupole Interaction

The quadrupole Hamiltonian $\hat{H}_Q$ for an atom, Eq. 3.1.69, can be applied also for diatomic molecules. In diatomic molecules, the field gradient is axially symmetric along the molecular axis, and thus the quantity q_J in the equation can be related to the molecule axis component q_z by as described in detail by Townes and Schawlow [5]

$$q_J = -q_z \frac{J}{2J+3}. \tag{3.2.63}$$

Substituting this into Eq. 3.1.70, the diagonal contribution of $\hat{H}_Q$ is obtained as

$$W_Q = -eq_z QY(J, I, F), \tag{3.2.64}$$

where Y is the Casimir's function

$$Y(J, I, F) = \frac{3C(C+1)/4 - I(I+1)J(J+1)}{2I(2I-1)(2J-1)(2J+3)}. \tag{3.2.65}$$

3.3 Polyatomic Molecules

3.3.1 The Born–Oppenheimer Approximation

We consider a molecule consisting of N nuclei with masses m_η and charges $C_\eta e, \eta = 1, 2, \ldots, N$, and n electrons, each with the mass m_e and charge $-e$. The molecule is not influenced by external fields. We initially describe each nucleus by means of its Cartesian coordinates (X_η, Y_η, Z_η) in an Cartesian axis system XYZ rigidly attached to the laboratory frame (a *laboratory-fixed* axis system), and each electron by its coordinates (x_i, y_i, z_i), $i = 1, 2, \ldots, n$, in the same axis system, and we denote the set of all Cartesian coordinates for the nuclei $(X_1, Y_1, Z_1, X_2, Y_2, Z_2, \ldots, X_N, Y_N, Z_N)$ as $\boldsymbol{R}_n$ and the set of all Cartesian coordinates for the electrons, $(x_1, y_1, z_1, x_2, y_2, z_2, \ldots x_n, y_n, z_n)$ as $\boldsymbol{r}_\mathrm{e}$. The position vector of nucleus η, with coordinates (X_η, Y_η, Z_η), is called $\boldsymbol{R}_\eta$, and the position vector of electron i, with coordinates (x_i, y_i, z_i), is called $\boldsymbol{r}_i$. If we consider only Coulomb

interaction between the particles, the non-relativistic Schrödinger equation for the molecule can be written as

$$\left[\hat{T}_n + \hat{T}_\mathrm{e} + V_\mathrm{Coulomb}(\boldsymbol{R}_n, \boldsymbol{r}_\mathrm{e})\right]\psi_{ne}(\boldsymbol{R}_n, \boldsymbol{r}_\mathrm{e}) = E_{ne}\psi_{ne}(\boldsymbol{R}_n, \boldsymbol{r}_\mathrm{e}) \tag{3.3.1}$$

with the molecular wavefunction $\psi_{ne}(\boldsymbol{R}_n, \boldsymbol{r}_\mathrm{e})$ and its corresponding eigenvalue E_{ne}. In Eq. 3.3.1, the operator $\hat{T}_n$ representing the kinetic energy of the nuclei is given by

$$\hat{T}_n = -\frac{\hbar^2}{2}\sum_{\eta=1}^{N}\frac{1}{m_\eta}\left[\frac{\partial^2}{\partial X_\eta^2} + \frac{\partial^2}{\partial Y_\eta^2} + \frac{\partial^2}{\partial Z_\eta^2}\right], \tag{3.3.2}$$

the operator $\hat{T}_\mathrm{e}$ representing the kinetic energy of the electrons is given by

$$\hat{T}_\mathrm{e} = -\frac{\hbar^2}{2m_\mathrm{e}}\sum_{i=1}^{n}\left[\frac{\partial^2}{\partial x_i^2} + \frac{\partial^2}{\partial y_i^2} + \frac{\partial^2}{\partial z_i^2}\right] \tag{3.3.3}$$

and the Coulomb potential energy function $V_\mathrm{Coulomb}(\boldsymbol{R}_n, \boldsymbol{r}_\mathrm{e})$ is given by

$$\begin{aligned} V_\mathrm{Coulomb}(\boldsymbol{R}_n, \boldsymbol{r}_\mathrm{e}) = &-\sum_{\eta=1}^{N}\sum_{i=1}^{n}\frac{C_\eta e^2}{4\pi\epsilon_0\left|\boldsymbol{R}_\eta - \boldsymbol{r}_i\right|} \\ &+ \sum_{i<i'}\frac{e^2}{4\pi\epsilon_0\left|\boldsymbol{r}_{i'} - \boldsymbol{r}_i\right|} + \sum_{\eta<\eta'}\frac{C_\eta C_{\eta'} e^2}{4\pi\epsilon_0\left|\boldsymbol{R}_{\eta'} - \boldsymbol{R}_\eta\right|} \end{aligned} \tag{3.3.4}$$

At the present time, all practical schemes for solving Eq. 3.3.1 are two-stage procedures: First an ab initio calculation is carried out, that is, the *electronic Schrödinger equation*

$$\left[\hat{T}_\mathrm{e} + V_\mathrm{Coulomb}(\boldsymbol{R}_n^{(0)}, \boldsymbol{r}_\mathrm{e})\right]\psi_e(\boldsymbol{R}_n^{(0)}, \boldsymbol{r}_\mathrm{e}) = V(\boldsymbol{R}_n^{(0)})\ \psi_e(\boldsymbol{R}_n^{(0)}, \boldsymbol{r}_\mathrm{e}) \tag{3.3.5}$$

is solved for fixed nuclear coordinates $\boldsymbol{R}_n^{(0)}$. By solving Eq. 3.3.5 for many values of $\boldsymbol{R}_n^{(0)}$, we obtain the effective potential energy function $V(\boldsymbol{R}_n)$, and in the second step of the calculation we can solve the Schrödinger equation for the nuclear motion

$$\left[\hat{T}_n + V(\boldsymbol{R}_n)\right]\psi_n(\boldsymbol{R}_n) = E_{ne}\psi_n(\boldsymbol{R}_n) \tag{3.3.6}$$

where $\psi_n(\boldsymbol{R}_n)$ is the nuclear wavefunction. In the approximation defined by Eqs. 3.3.5 and 3.3.6, the total molecular wavefunction is then taken to be

$$\psi_{ne}(\boldsymbol{R}_n, \boldsymbol{r}_\mathrm{e}) = \psi_e(\boldsymbol{R}_n, \boldsymbol{r}_\mathrm{e})\psi_n(\boldsymbol{R}_n). \tag{3.3.7}$$

This approximation is usually credited to Born and Oppenheimer [6].

We assume here that the ab initio calculation has been carried out and that consequently the potential energy function $V(\boldsymbol{R}_n)$ is known. With the known

$V(\boldsymbol{R}_n)$ we then develop procedures for solving Eq. 3.3.6 in order to obtain the molecular rovibronic energies E_{ne} and the corresponding wavefunctions $\psi_n(\boldsymbol{R}_n)$.

3.3.2 The Choice of Rotation–Vibration Coordinates

3.3.2.1 Translation

The first problem that one encounters when developing a method for solving the nuclear Schrödinger equation (3.3.6), is to choose a suitable set of coordinates for describing the nuclear motion. This problem does not exist in ab initio theory, where all existing methods appear to describe the motion of the electrons through the Cartesian coordinates $(x_i, y_i, z_i)\,[i = 1, 2, \ldots, n]$. These coordinates are well suited to express the atomic-orbital-type basis functions used in ab initio calculations, and consequently they constitute a rather natural choice for the coordinates of the electronic problem. However, the analogous nuclear Cartesian coordinates $(X_\eta, Y_\eta, Z_\eta)[\eta = 1, 2, \ldots, N]$ are entirely inconvenient for setting up Eq. 3.3.6 in a form that allows it to be solved in an efficient manner. Consequently, we must rewrite the total nuclear Hamiltonian

$$\hat{H}_{\text{total}} = \hat{T}_n + V(\boldsymbol{R}_n) \tag{3.3.8}$$

by introducing new, more suitable coordinates. There is no natural, generally applicable choice for these coordinates, and the currently available methods for solving Eq. 3.3.6 employ different strategies for choosing them. We shall discuss here the strategy used in the standard approach.

In general, we obviously need $3N$ coordinates to describe completely a system consisting of N nuclei. All methods for solving Eq. 3.3.6 have in common that they use three of these coordinates to describe the *translational* motion of the molecule. During a translation of the molecule, all nuclei move uniformly along straight lines without changing their relative positions. Usually the three translational coordinates (X_0, Y_0, Z_0) are chosen as the laboratory-fixed coordinates of the nuclear center of mass

$$\begin{Bmatrix} X_0 \\ Y_0 \\ Z_0 \end{Bmatrix} = \frac{1}{\sum_{\eta=1}^{N} m_\eta} \sum_{\eta=1}^{N} m_\eta \begin{Bmatrix} X_\eta \\ Y_\eta \\ Z_\eta \end{Bmatrix} \tag{3.3.9}$$

where m_η is the mass of atom η.[6] The remaining $3N - 3$ coordinates used to describe the nuclear motion are socalled *internal* coordinates; they are invariant under uniform translation of all nuclei. It is customary to define initially such

[6] In rotation–vibration calculations it is accepted practice to use atomic masses rather than nuclear masses. As explained by Bunker and Moss [11] this compensates to some extent for the breakdown of the Born–Oppenheimer approximation; see also Gordy and Cook [12].

coordinates $(t_{1,X}, t_{1,Y}, t_{1,Z}, t_{2,X}, t_{2,Y}, t_{2,Z}, \ldots, t_{N-1,X}, t_{N-1,Y}, t_{N-1,Z})$ through $N-1$ equations (see Sutcliffe and Tennyson [13])

$$\begin{Bmatrix} t_{i,X} \\ t_{i,Y} \\ t_{i,Z} \end{Bmatrix} = \sum_{\eta=1}^{N} V_{\eta i} \begin{Bmatrix} X_\eta \\ Y_\eta \\ Z_\eta \end{Bmatrix}, \quad i = 1, 2, \ldots, N-1. \tag{3.3.10}$$

The condition that the coordinates $t_{i,A}$ $[A = X, Y, \text{or } Z]$ be invariant under uniform translation of the molecule can be expressed through the equation

$$\sum_{\eta=1}^{n} V_{\eta i} = 0 \quad \text{for all } i = 1, 2, \ldots, N-1. \tag{3.3.11}$$

Further, it necessary that the $V_{\eta i}$ be such that the coordinate transformation defined through Eqs. 3.3.9 and 3.3.10,

$$\begin{aligned}&(X_1, Y_1, Z_1, X_1, Y_1, Z_1, \ldots, X_N, Y_N, Z_N) \\ &\quad \rightarrow (X_0, Y_0, Z_0, t_{1,X}, t_{1,Y}, t_{1,Z}, t_{2,X}, t_{2,Y}, t_{2,Z}, \ldots, t_{N-1,X}, t_{N-1,Y}, t_{N-1,Z})\end{aligned} \tag{3.3.10}$$

can be *inverted* so that it is possible to determine the coordinates $(X_1, Y_1, \ldots, Z_N)$ from the coordinates $(X_0, Y_0, Z_0, t_{1,X}, \ldots, t_{N-1,Z})$. Traditionally, the $t_{i,A}$ coordinates have been chosen so that they define the positions of the nuclei in an axis system with axes parallel to the laboratory-fixed XYZ system but with origin in the nuclear center of mass (see Chap. 6 of Bunker [14] or Chap. 11 of Wilson et al. [15]). This leads to the following values for the $V_{\eta i}$ matrix elements

$$V_{\eta i} = \delta_{\eta i} - \frac{m_\eta}{\sum_{\eta=1}^{N} m_\eta}. \tag{3.3.13}$$

In this case, the $V_{\eta i}$ matrix elements depend on the nuclear masses and hence the $t_{i,A}$ coordinates become *mass − dependent* or *isotope-dependent*. This means that if we consider two isotopic molecules whose nuclei are arranged such that the two molecules have the same values of the laboratory-fixed coordinates $(X_1, Y_1, \ldots, Z_N)$, these two molecules will be described by *different* values of the coordinates $(t_{1,X}, t_{1,Y}, \ldots, t_{N-1,Z})$. It is not necessary that the $V_{\eta i}$ matrix elements depend on the nuclear masses, and in many cases it is advantageous to choose them to be mass-independent.

It can be shown that we can write the nuclear kinetic energy operator $\hat{T}_n$ as

$$\begin{aligned}\hat{T}_n = &-\frac{\hbar^2}{2\sum_{\eta=1}^{N} m_\eta}\left\{\frac{\partial^2}{\partial X_0^2} + \frac{\partial^2}{\partial Y_0^2} + \frac{\partial^2}{\partial Z_0^2}\right\} \\ &+ \hat{T}_{\text{rv}}\left(-i\hbar\frac{\partial}{\partial t_{1,X}}, -i\hbar\frac{\partial}{\partial t_{1,Y}}, -i\hbar\frac{\partial}{\partial t_{1,Z}}, \ldots, -i\hbar\frac{\partial}{\partial t_{N-1,Z}}\right)\end{aligned} \tag{3.3.14}$$

where, as indicated, the kinetic energy operator $\hat{T}_{\text{rv}}$ (which describes the *rotation* and *vibration* of the molecule) only depends on the momenta $-i\hbar\partial/\partial t_{i,A}$ conjugate

to the $t_{i,A}$ coordinates. Since in the absence of external fields, the effective potential energy function $V(\boldsymbol{R}_n)$ cannot depend on the coordinates (X_0, Y_0, Z_0),[7] this means that we can write $\hat{H}_{\text{total}}$ (Eq. 3.3.8) as the sum of two commuting operators,

$$\hat{H}_{\text{total}} = \hat{T}_{\text{translation}} + \hat{H}_{\text{rv}} \tag{3.3.15}$$

where

$$\hat{T}_{\text{translation}} = -\frac{\hbar^2}{2\sum_{\eta=1}^{N} m_\eta}\left\{\frac{\partial^2}{\partial X_0^2} + \frac{\partial^2}{\partial Y_0^2} + \frac{\partial^2}{\partial Z_0^2}\right\} \tag{3.3.16}$$

and

$$\hat{H}_{\text{rv}} = \hat{T}_{\text{rv}} + V(\boldsymbol{R}_n). \tag{3.3.17}$$

Consequently the eigenvalues of $\hat{H}_{\text{total}}$ can be written as

$$E_{\text{total}} = E_{\text{translation}} + E_{\text{rv}} \tag{3.3.18}$$

where $E_{\text{translation}}$ is an eigenvalue of $\hat{T}_{\text{translation}}$ and E_{rv} is an eigenvalue of $\hat{H}_{\text{rv}}$. We are not interested in the energy contribution $E_{\text{translation}}$ from the translational motion. The reason is that this contribution is of no importance in the prediction and interpretation of spectroscopic experiments; such experiments do not involve transitions between translational states. We thus simply ignore $\hat{T}_{\text{translation}}$ and concentrate on the solution of the eigenvalue problem

$$\hat{H}_{\text{rv}}\psi_{\text{rv}} = E_{\text{rv}}\psi_{\text{rv}} \tag{3.3.19}$$

which involves the $t_{i,A}$ coordinates only.

3.3.2.2 Rotation and Vibration

We have been led to introduce the $3N-3$ coordinates $t_{i,A}$ to describe the *translation − free* nuclear motion. These coordinates, however, are not ideal for this purpose, and we must carry out further coordinate transformations before we can attempt to solve Eq. 3.3.19. We can think of the nuclei as carrying out a superposition of two kinds of motion:

- uniform *rotation* of the molecule as a whole. When the molecule rotates without the relative positions of the nuclei changing, the effective potential function $V(\boldsymbol{R}_n)$ obviously does not change when there are no external fields. Consequently, the rotation is *free*, i.e., it is not influenced by $V(\boldsymbol{R}_n)$.

[7] If we let the molecule undergo a uniform translation of all nuclei corresponding to a change in the center-of-mass coordinates (X_0, Y_0, Z_0), $V(\boldsymbol{R}_n)$ cannot change.

- motion of the nuclei relative to each other, which we will call *vibration*. Such motion obviously is influenced by the effective potential function $V(\boldsymbol{R}_n)$.

When we define the coordinates $t_{i,A}$ as linear combinations of laboratory-fixed coordinates, Eq. 3.3.10, the displacement of any one of the $t_{i,A}$ coordinates will normally involve both rotation of the molecule as a whole *and* some relative motion of the nuclei. Consequently, $V(\boldsymbol{R}_n)$ will in general depend on all $3N-3$ $t_{i,A}$'s. We would like to define a new set of $3N-3$ coordinates that reflect correctly the separation of the nuclear motion into rotation and vibration. The general strategy for doing this, which is common for all methods of rotation–vibration calculations, is as follows: A Cartesian axis system (the *molecule-fixed* axis system) with origin at the nuclear center of mass is attached to the molecule so that it follows the rotational motion (in a sense that we shall discuss below). The orientation of the molecule-fixed axis system relative to the laboratory-fixed *XYZ* axis system is defined by three Euler angles (θ, ϕ, χ); see Appendix A of Papoušek and Aliev [16]. We use these angles as *rotational coordinates*. Further, we define $3N-6$ new coordinates $(q_1, q_2, q_3, \ldots, q_{3N-6})$ which are invariant not only under uniform translation of the molecule [as were the $t_{i,A}$'s] but also under uniform rotation of the molecule.[8] Obviously we must select the scheme for attaching the molecule-fixed coordinate system to the molecule and define the q_i coordinates such that the coordinate transformations

$$\begin{aligned}&(t_{1,X}, t_{1,Y}, t_{1,Z}, t_{2,X}, t_{2,Y}, t_{2,Z}, \ldots, t_{N-1,X}, t_{N-1,Y}, t_{N-1,Z})\\ &\quad\leftrightarrow (\theta, \phi, \chi, q_1, q_2, q_3, \ldots, q_{3N-6})\end{aligned} \tag{3.3.20}$$

can be carried out in both directions, so that if we know a set of values of the coordinates $t_{i,A}$, we can calculate the values of the coordinates $(\theta, \phi, \chi, q_1, \ldots, q_{3N-6})$ and vice versa.

The traditional spectroscopic approach to solving Eq. 3.3.19 [8, 15–21] uses vibrational coordinates chosen in order to simplify the expression for the kinetic energy operator $\hat{T}_{\mathrm{rv}}$. This operator can be written as

$$\begin{aligned}\hat{T}_{\mathrm{rv}} = {} & \hat{T}_{\mathrm{rot}}\left(\theta, \phi, \chi, \hat{P}_\theta, \hat{P}_\phi, \hat{P}_\chi\right)\\ & + \hat{T}_{\mathrm{vib}}\left(q_1, q_2, \ldots, q_{3N-6}, \hat{P}_{q_1}, \hat{P}_{q_2}, \ldots, \hat{P}_{q_{3N-6}}\right)\\ & + \hat{T}_{\mathrm{rest}}\left(\theta, \phi, \chi, \hat{P}_\theta, \hat{P}_\phi, \hat{P}_\chi, q_1, q_2, \ldots, q_{3N-6}, \hat{P}_{q_1}, \hat{P}_{q_2}, \ldots, \hat{P}_{q_{3N-6}}\right),\end{aligned} \tag{3.3.21}$$

where $\hat{P}_a$ denotes the momentum conjugate to a coordinate a, and the rotational and vibrational coordinates are defined such that the *rotation–vibration interaction term* $\hat{T}_{\mathrm{rest}}$ is minimized. The background for this is the following: It follows from the discussion given above that the effective potential energy function V can only

[8] In the "standard theory" for a molecule whose equilibrium geometry is linear, two rotational coordinates, θ and ϕ, and $3N-5$ vibrational coordinates are employed [16]. This is a special case which we discuss further in Sect. 3.3.6.5.

depend on the $3N-6$ coordinates q_i. When we write the rotation–vibration Hamiltonian $\hat{H}_{\mathrm{rv}}$ as

$$\hat{H}_{\mathrm{rv}} = \hat{T}_{\mathrm{rot}} + \left\{\hat{T}_{\mathrm{vib}} + V\right\} + \hat{T}_{\mathrm{rest}}, \tag{3.3.22}$$

$\hat{T}_{\mathrm{rot}}$ will commute with $\hat{T}_{\mathrm{vib}} + V$ since these two operators depend on different coordinates. In the event that we can neglect $\hat{T}_{\mathrm{rest}}$ we thus have the remaining Hamiltonian written as a sum of two commuting operators whose eigenvalue problems we can solve separately and then construct the rotation–vibration wavefunctions as the product

$$\psi_{\mathrm{rv}}(\theta, \phi, \chi, q_1, q_2, \ldots, q_{3N-6}) = \psi_{\mathrm{rot}}(\theta, \phi, \chi)\psi_{\mathrm{vib}}(q_1, q_2, \ldots, q_{3N-6}). \tag{3.3.23}$$

In practice, we cannot neglect $\hat{T}_{\mathrm{rest}}$, but if we can minimize it through our coordinate choice we might be able to treat it as a perturbation.

The coordinate choice outlined here aims at eliminating rotation–vibration interaction terms from the kinetic energy operator. Since these terms depend on the nuclear masses, the coordinates $(\theta, \phi, \chi, q_1, q_2, q_3, \ldots, q_{3N-6})$ which are chosen to eliminate them also become mass-dependent. However, the potential energy function is not naturally expressed in these mass-dependent coordinates. We normally use a parameterized function of the nuclear coordinates to express the effective potential function V; we would typically obtain the values of the parameters by fitting this function through a set of ab initio energies with corresponding nuclear geometries. As noted by Hoy et al. [21], the values of the parameters in V are independent of isotopic substitution provided that we express V as a function of $3N-6$ *mass-independent, geometrically defined* coordinates which we might call $(\mathcal{R}_1, \mathcal{R}_2, \mathcal{R}_3, \ldots, \mathcal{R}_{3N-6})$. These coordinates are typically instantaneous values of internuclear distances ("bond lengths") or angles $\angle$(ABC) defined by three nuclei A, B, and C ("bond angles"). They are different from the mass-dependent coordinates $(q_1, q_2, \ldots, q_{3N-6})$ which we have introduced to simplify the kinetic energy operator, so before we can solve Eq. 3.3.19 we must express the effective potential function in terms of the coordinates chosen for the kinetic energy operator through *coordinate transformations* of the type

$$\mathcal{R}_i = \mathcal{R}_i(q_1, q_2, \ldots, q_{3N-6}). \tag{3.3.24}$$

These relations are inserted in the effective potential energy function V and this function can now be seen as depending on the coordinates q_i. It is normally possible to derive exact relations of the type given in Eq. 3.3.24, i.e., the $\mathcal{R}_i$ coordinates can be expressed exactly in terms of the q_j coordinates. However, inserting these relations in the effective potential energy function leads to a mathematically intractable form of this function. Consequently, one normally resorts to an approximate coordinate transformation, in which the $\mathcal{R}_i$ coordinates are expressed as power series in the q_j coordinates (see Eq. 3 of Hoy et al. [21]):

$$\mathcal{R}_i \approx \mathcal{R}_{i0} + \sum_{j=1}^{3N-6} B_i^{(j)} q_j + \sum_{j=1}^{3N-6}\sum_{k=1}^{3N-6} B_i^{(jk)} q_j q_k + \cdots \tag{3.3.25}$$

In the preceding paragraphs we have outlined the choice of what one might call "spectroscopic coordinates". The form of these coordinates is dictated by the kinetic energy operator, because they are defined so that they minimize the rotation–vibration interaction term $\hat{T}_{\text{rest}}$ in Eq. 3.3.21. Thus it is necessary to transform the *potential energy function* to make it depend on the spectroscopic coordinates. In the beginnings of rotation–vibration theory 60–70 years ago, one only had hopes of calculating approximative eigenvalues for a rotation–vibration Hamiltonian in which rotation and vibration were *separated* [i.e., in which $\hat{T}_{\text{rest}}$ could be neglected), and consequently this type of coordinates constituted the only feasible choice. However, the "standard" separation of rotation and vibration is possible only if the molecule carries out its vibration in one deep "well" of the potential energy surface. This potential well defines one equilibrium structure, and the amplitudes of the vibrational motion must be small compared to the linear dimensions of this structure. In this book we are only concerned with the customary, standard approach to molecular rotation–vibration theory. Modern extensions of this theory, which make use of high-capacity computers, are described, for example, in Jensen and Bunker [22] and the references given there.

3.3.2.3 The Standard Coordinates

The standard approach to rotation–vibration theory [8, 15–21, 23, 24], describes molecules whose potential energy surfaces have one minimum only, and the molecule-fixed coordinate system (see Sect. 3.3.2.2) is defined so that the configuration of the molecule corresponding to the one minimum [the equilibrium configuration] is rigidly attached to the molecule-fixed coordinate system. Hence the equilibrium configuration is described in the molecule-fixed axis system through *constant* position vectors $\boldsymbol{a}_\eta$ for the nuclei $\eta = 1, 2, \ldots, N$:

$$\boldsymbol{a}_\eta = \begin{Bmatrix} a_{\eta x} \\ a_{\eta y} \\ a_{\eta z} \end{Bmatrix}. \tag{3.3.26}$$

Vibrational motion is then defined as the instantaneous displacements of the nuclei from the positions given by the vectors $\boldsymbol{a}_\eta$, measured along the axes of the molecule-fixed coordinate system. As already mentioned, the standard approach assumes that these displacements are small compared to the linear dimensions of the equilibrium configuration.

3.3.3 The Eckart Equations

We have still not given a precise definition of the molecule-fixed coordinate system. If we think of a non-linear molecule (i.e., a molecule whose equilibrium structure is non-linear), we imagine for a moment that we could photograph an

instantaneous configuration of the nuclei. On the photograph we would see the nuclei as points, and we could in principle determine their Cartesian, laboratory-fixed coordinates (X_η, Y_η, Z_η), but we would initially have no way of deciding to which extent the molecule on the picture was displaced from its equilibrium structure, and we would have no way of determining the Euler angles θ, ϕ, and χ. We obviously need a mathematical "recipe" allowing us to position the molecule-fixed axis system [and the equilibrium geometry attached to it] relative to the instantaneous positions of the nuclei. In the standard approach, this recipe is given through the *Eckart equations* [17].

In order to formulate the Eckart equations, we define the following column vectors

$$\boldsymbol{r}_\eta = \begin{Bmatrix} x_\eta \\ y_\eta \\ z_\eta \end{Bmatrix}, \quad \boldsymbol{r}_\eta = \begin{Bmatrix} X_\eta \\ Y_\eta \\ Z_\eta \end{Bmatrix}, \quad \text{and} \quad \boldsymbol{r}_0 = \begin{Bmatrix} X_0 \\ Y_0 \\ Z_0 \end{Bmatrix} \tag{3.3.27}$$

where (x_η, y_η, z_η) are the coordinates of nucleus η in the *molecule-fixed* coordinate system. Since the molecule-fixed coordinate system is rotated by the Euler angles relative to the laboratory-fixed axis system, we have that

$$\boldsymbol{r}_\eta = \mathbf{S}(\theta, \phi, \chi)\{\boldsymbol{R}_\eta - \boldsymbol{R}_0\} \tag{3.3.28}$$

where $\mathbf{S}(\theta, \phi, \chi)$ is a 3×3 matrix effecting the transformation between the molecule-fixed and laboratory-fixed coordinate system; the elements of this matrix are simple trigonometric functions of the angles θ, ϕ, and χ; see Appendix A and Table A.1 of [16].

We now define the instantaneous displacements of the nuclei from the equilibrium configuration, measured along the axes of the molecule-fixed coordinate system, as column vectors

$$\boldsymbol{d}_\eta = \begin{Bmatrix} d_{\eta x} \\ d_{\eta y} \\ d_{\eta z} \end{Bmatrix} = \boldsymbol{r}_\eta - \boldsymbol{a}_\eta, \quad \eta = 1, 2, \ldots, N. \tag{3.3.29}$$

The vector components $d_{\eta x}, d_{\eta y}$, and $d_{\eta z}, \eta = 1, 2, \ldots, N$, are the vibrational coordinates. However, we have seen in Sect. 3.3.2.2 that there exist only $3N - 6$ independent vibrational coordinates and consequently the $3N$ components of the $\boldsymbol{d}_\eta$-vectors cannot all be independent. Six of the $3N$ components are redundant, and consequently there must exist six equations linking all $3N$ components. We already know three of these equations: The molecule-fixed coordinate system is defined to have its origin at the nuclear center of mass (Sect. 3.3.2.2), both when the molecule is in its equilibrium configuration and when it is in an arbitrary, displaced configuration. One can easily show that this leads to the equations

$$\sum_{\eta=1}^{N} m_\eta \boldsymbol{a}_\eta = \sum_{\eta=1}^{N} m_\eta \boldsymbol{d}_\eta = \boldsymbol{O} \tag{3.3.30}$$

where $\boldsymbol{O}$ is a zero, three-component column vector. Equation 3.3.30 delivers three equations connecting the components of the vectors $\boldsymbol{d}_\eta$. We need to choose three additional equations connecting these components, and in order to understand the choice that is customarily made we consider the *classical* kinetic energy T of the molecular rotation and vibration. This energy is given by Eq. 3 in Sect. 11-1 of [15]:

$$2T = \sum_{\eta=1}^{N} m_\eta (\boldsymbol{\omega} \times \boldsymbol{r}_\eta) \cdot (\boldsymbol{\omega} \times \boldsymbol{r}_\eta) + \sum_{\eta=1}^{N} m_\eta \dot{\boldsymbol{r}}_\eta \cdot \dot{\boldsymbol{r}}_\eta + 2\boldsymbol{\omega} \cdot \sum_{\eta=1}^{N} m_\eta \boldsymbol{r}_\eta \times \dot{\boldsymbol{r}}_\eta \quad (3.3.31)$$

where the vector $\boldsymbol{\omega}$ contains the components of the instantaneous angular velocity of the molecule and, for an arbitrary quantity $x, \dot{x}$ is the time derivative $\mathrm{d}x/\mathrm{d}t$.

The last term on the right-hand side of Eq. 3.3.31 is the Coriolis coupling term which represents the dominant part of the interaction between rotation and vibration. We would like to choose the coordinates so that this term disappears completely, i.e.,

$$\sum_{i=1}^{N} m_\eta \boldsymbol{r}_\eta \times \dot{\boldsymbol{r}}_\eta = \boldsymbol{O} \quad (3.3.32)$$

where $\dot{\boldsymbol{r}}_\eta$ is the velocity of nucleus η relative to the molecule-fixed axes. This would mean that the molecule would have no angular momentum relative to the molecule-fixed axes. It turns out that we cannot in general choose coordinates that cause the angular momentum in the molecule-fixed axis system (and hence the Coriolis coupling term) to disappear. The best we can do is to minimize this angular momentum through the *Eckart equations* [17] which we can express as

$$\sum_{\eta=1}^{N} m_\eta \boldsymbol{a}_\eta \times \boldsymbol{d}_\eta = \boldsymbol{O}. \quad (3.3.33)$$

Using Eq. 3.3.33 we can easily show that classically

$$\sum_{\eta=1}^{N} m_\eta \boldsymbol{r}_\eta \times \dot{\boldsymbol{r}}_\eta = \sum_{\eta=1}^{N} m_\eta \boldsymbol{d}_\eta \times \dot{\boldsymbol{d}}_\eta \quad (3.3.34)$$

so that the Coriolis coupling term vanishes in the equilibrium configuration when all $\boldsymbol{d}_\eta = \boldsymbol{O}$. Since we assume that the molecule carries out small oscillations around the equilibrium configuration, the angular momentum in the molecule-fixed coordinate system is then always small and a high degree of rotation–vibration separation is achieved.

When we insert Eqs. 3.3.28 and 3.3.29 in Eq. 3.3.33 we obtain

$$\sum_{\eta=1}^{N} m_\eta \boldsymbol{a}_\eta \times \left[\mathbf{S}(\theta, \phi, \chi)\{\boldsymbol{R}_\eta - \boldsymbol{R}_0\}\right] = \boldsymbol{O}. \quad (3.3.35)$$

In a given instantaneous configuration of the molecule, we can in principle measure the Cartesian laboratory-fixed coordinates contained in the vectors $\boldsymbol{R}_\eta$ and use Eq. 3.3.9 to obtain $\boldsymbol{R}_0$. If we assume that we know the constant vectors $\boldsymbol{a}_\eta$, Eq. 3.3.35 then delivers three equations in the Euler angles θ, ϕ, and χ, and we can solve the equations to obtain these angles as functions of the laboratory-fixed Cartesian coordinates.

The first term on the right-hand side of Eq. 3.3.31 is the rotational kinetic energy, and we can rewrite it as

$$\sum_{\eta=1}^{N} m_\eta \left(\boldsymbol{\omega} \times \boldsymbol{r}_\eta\right) \cdot \left(\boldsymbol{\omega} \times \boldsymbol{r}_\eta\right) = \boldsymbol{\omega}^{\mathrm{T}} \mathbf{I} \boldsymbol{\omega} \tag{3.3.36}$$

where a superscript T denotes transposition and the 3×3 matrix $\mathbf{I}$ contains the instantaneous moments of inertia and products of inertia [see, for example, Sect. 4.1 of [16]. When the molecule is in its equilibrium configuration, i.e., when all $\boldsymbol{r}_\eta = \boldsymbol{a}_\eta$, we have that $\mathbf{I} = \mathbf{I}_\mathrm{e}$, and the elements of $\mathbf{I}_\mathrm{e}$ depend on the components of the constant vectors $\boldsymbol{a}_\eta$ only. These vectors must be chosen such that when all $\boldsymbol{r}_\eta = \boldsymbol{a}_\eta$ the relative positions of the nuclei correspond to the minimum of the potential energy function. However in defining the $\boldsymbol{a}_\eta$ we are free to rotate them relative to the molecule-fixed axis system since this does not change the relative positions of the nuclei. We can use this freedom of choice to make the molecule-fixed axis system a *principal axis system* for the molecule in its equilibrium configuration, i.e., to make $\mathbf{I}_\mathrm{e}$ diagonal. Hence for the molecule in its equilibrium configuration we have

$$\boldsymbol{\omega}^{\mathrm{T}} \mathbf{I}_\mathrm{e} \boldsymbol{\omega} = I_{e,xx}\, \omega_x^2 + I_{e,yy}\, \omega_y^2 + I_{e,zz}\, \omega_z^2. \tag{3.3.37}$$

3.3.4 Normal Coordinates

We have now defined the rotational Euler angle coordinates through the Eckart equations (3.3.33). We now need to define the $3N - 6$ vibrational coordinates, which we called $(q_1, q_2, q_3, \ldots, q_{3N-6})$ in Sect. 3.3.2.2. Through this definition we aim at simplifying the *vibrational* Hamiltonian. The classical vibrational energy is the sum of the vibrational kinetic energy, which is given through the second term on the right-hand side of Eq. 3.3.31:

$$\begin{aligned} T_\mathrm{vib} &= \frac{1}{2} \sum_{\eta=1}^{N} m_\eta \dot{\boldsymbol{r}}_\eta \cdot \dot{\boldsymbol{r}}_\eta = \frac{1}{2} \sum_{\eta=1}^{N} m_\eta \dot{\boldsymbol{d}}_\eta \cdot \dot{\boldsymbol{d}}_\eta \\ &= \frac{1}{2} \sum_{\eta=1}^{N} m_\eta \left\{ \dot{d}_{\eta x}^2 + \dot{d}_{\eta y}^2 + \dot{d}_{\eta z}^2 \right\} = \frac{1}{2} \dot{\boldsymbol{d}}^T \mathbf{M} \dot{\boldsymbol{d}} \end{aligned} \tag{3.3.38}$$

and the potential energy $V(\boldsymbol{R}_n)$. In Eq. 3.3.38, $\boldsymbol{d}$ is a column vector with $3N$ rows containing the components of the vectors $\boldsymbol{d}_\eta : d_{1x}, d_{1y}, d_{1z}, d_{2x}, \ldots, d_{Nz}$, and $\mathbf{M}$ is a $3N \times 3N$ diagonal matrix with $M_{11} = M_{22} = M_{33} = m_1, M_{44} = M_{55} = M_{66} = m_2$ and so on.

In the standard approach the potential energy $V(\boldsymbol{R}_n)$ is taken to be a Taylor expansion in the geometrically defined coordinates defined above:

$$V(\mathcal{R}_1, \mathcal{R}_2, \ldots, \mathcal{R}_{3N-6}) = \frac{1}{2}\sum_{j,k} f_{jk}\mathcal{R}_j\mathcal{R}_k + \frac{1}{6}\sum_{j,k,\ell} f_{jk\ell}\mathcal{R}_j\mathcal{R}_k\mathcal{R}_\ell + \frac{1}{24}\sum_{j,k,\ell,m} f_{jk\ell}\mathcal{R}_j\mathcal{R}_k\mathcal{R}_\ell\mathcal{R}_m + \cdots \tag{3.3.39}$$

where the coordinates $\mathcal{R}_i$ are defined as *displacements* from equilibrium values so that the configuration in which all $\mathcal{R}_i = 0$ corresponds to the equilibrium geometry, where all first derivatives are zero and where we choose $V = 0$.

In order to define the vibrational motion of the molecule, we now define $3N - 6$ independent, *linearized internal coordinates* S_i through the transformation

$$S_i = \sum_{\eta=1}^{N} \sum_{a=x,y,z} B_{i,\eta a} d_{\eta a}, \; i = 1, 2, 3, \ldots, 3N - 6, \tag{3.3.40}$$

with the elements of the $(3N - 6) \times 3N$ matrix $\mathbf{B}$ given as

$$B_{i,\eta a} = \frac{\partial \mathcal{R}_i}{\partial d_{\eta a}}; \tag{3.3.41}$$

the elements of this matrix can be derived using purely geometrical arguments. In these coordinates the kinetic energy of the vibrations can be expressed as (see [15])

$$T_{\text{vib}} = \frac{1}{2}\dot{\mathbf{S}}^T \mathbf{G}^{-1} \dot{\mathbf{S}} \tag{3.3.42}$$

with $\mathbf{S}$ being a column vector with $3N - 6$ rows containing the S_i coordinates and

$$\mathbf{G} = \mathbf{B}\mathbf{M}^{-1}\mathbf{B}^T. \tag{3.3.43}$$

Through the definition of the $\mathbf{B}$ matrix we have for small values of the $d_{\eta a}$ (i.e., configurations close to equilibrium) that $S_i \approx \mathcal{R}_i$, and we can then write

$$\frac{1}{2}\sum_{j,k} f_{jk}\mathcal{R}_j\mathcal{R}_k \approx \frac{1}{2}\sum_{j,k} f_{jk}S_jS_k = \frac{1}{2}\mathbf{S}^T\mathbf{F}\mathbf{S} \tag{3.3.44}$$

where the matrix $\mathbf{F}$ has the elements f_{jk}. Using a standard technique of classical mechanics, the $\mathbf{GF}$-calculation, we can change to so-called normal coordinates Q_k given through the transformation

$$d_{\eta a} = \frac{1}{\sqrt{m_\eta}} \sum_{k=1}^{3N-6} \ell_{\eta a,k}\, Q_k. \tag{3.3.45}$$

The normal coordinates are defined such that

$$T_{\text{vib}} + \frac{1}{2}\sum_{j,k} f_{jk} S_j S_k = \frac{1}{2}\dot{\mathbf{S}}^T \mathbf{G}^{-1}\dot{\mathbf{S}} + \frac{1}{2}\mathbf{S}^T\mathbf{F}\mathbf{S} = \frac{1}{2}\sum_{k=1}^{3N-6}\left\{\dot{Q}_k^2 + \lambda_k Q_k^2\right\}. \tag{3.3.46}$$

In Eqs. 3.3.45 and 3.3.46, the λ_k are the eigenvalues of the matrix **GF**; they are related to the *harmonic vibration wavenumbers* ω_k of the molecule through

$$\omega_k = \frac{1}{2\pi c}\sqrt{\lambda_k}. \tag{3.3.47}$$

The coefficients $\ell_{\eta a,k}$ can be obtained from the eigenvectors of the **GF** matrix, they are given by Eq. 3.3.10 of [16]):

$$\boldsymbol{l} = \mathbf{M}^{-1/2}\mathbf{B}^T\mathbf{G}^{-1}\mathbf{L}. \tag{3.3.48}$$

In Eq. 3.3.48, $\boldsymbol{l}$ is the $3N \times 3N-6$ matrix with elements $\ell_{\eta a,k}$, and the matrix **L** contains the eigenvectors of the matrix **GF**, that is, it is determined such that

$$\mathbf{L}^{-1}\mathbf{G}\mathbf{F}\mathbf{L} = \mathbf{\Lambda} \tag{3.3.49}$$

where $\mathbf{\Lambda}$ is a diagonal matrix with $\Lambda_{kk} = \lambda_k$. When we approximate the vibrational energy by the expression in Eq. 3.3.46[9] we can write this energy as the sum of $3N-6$ independent contributions, each one only depending on one Q_k coordinate and we have thus simplified considerably the form of the vibrational energy.

Finally, if we define

$$\gamma_r = 2\pi c\omega_r/\hbar \tag{3.3.50}$$

it is easy to verify that the coordinate

$$q_r = \sqrt{\gamma_r}Q_r \tag{3.3.51}$$

is dimensionless. We will use these *dimensionless normal coordinates* to describe the vibrational motion in the following.

We have now defined the coordinates used in the standard approach, and during this process we have made three choices:

- We have chosen the Eckart equations (3.3.33) to define the Euler angles θ, ϕ, and χ. The direct reason for making this choice was to minimize the Coriolis coupling term (the third term on the right-hand side of Eq. 3.3.31) which contains the major contribution to the rotation–vibration interaction.

[9] That is, when we neglect expansion terms of third and higher order from Eq. 3.3.39.

- We have rotated the constant $\boldsymbol{a}_\eta$-vectors relative to the molecule-fixed axis system so that the molecule-fixed axes are principal axes when the molecule is in its equilibrium configuration. Thus we obtain that the products of inertia vanish at equilibrium, Eq. 3.3.37.
- We have chosen the vibrational coordinates to be the normal coordinates Q_k, thus eliminating terms coupling different vibrational modes of the molecule from the vibrational kinetic energy T_{vib} and from the *harmonic* potential energy, Eq. 3.3.44.

Clearly each choice was made in order to eliminate certain terms in the classical energy. Since the eliminated terms in the kinetic energy are mass-dependent, the resulting coordinates are also all mass-dependent in the sense defined in Sect. 3.3.2.1.

3.3.5 Molecular Rotation–Vibration Energies

3.3.5.1 The Watson Hamiltonian

Watson [20] showed that when the classical Hamiltonian function described in Sect. 3.3.2 is expressed in terms of the coordinates $(\theta, \phi, \chi, q_1, q_2, q_3, \ldots q_{3N-6})$ and converted to quantum mechanical form using the *Podolsky trick* (see, for example, Sect. 9.2 of [25]) the following quantum mechanical Hamiltonian for a non-linear molecule is obtained:

$$\hat{H}_{\text{rv}} = \frac{1}{2}\sum_{\alpha=x,y,z}\sum_{\beta=x,y,z}\left(\hat{J}_\alpha - \hat{\pi}_\alpha\right)\mu_{\alpha\beta}\left(\hat{J}_\beta - \hat{\pi}_\beta\right) + \frac{1}{2}\,hc\sum_{r=1}^{3N-6}\omega_r\hat{p}_r^2 - \frac{\hbar^2}{8}\sum_{\alpha=x,y,z}\mu_{\alpha\alpha} + V \tag{3.3.52}$$

$\hat{J}_\alpha$ component of the total angular momentum along the molecule-fixed $\alpha(= x, y, z)$ axis.
$\hat{\pi}_\alpha = \hbar\sum_{r=1}^{3N-6}\sum_{s=1}^{3N-6}\zeta_{rs}^{(\alpha)}\sqrt{\omega_s/\omega_r}q_r\hat{p}_s$; vibrational angular momentum.
$\zeta_{rs}^{(\alpha)} = -\zeta_{sr}^{(\alpha)} = \sum_{\beta,\gamma=x,y,z}\sum_{\eta=1}^{N} e_{\alpha\beta\gamma}\ell_{\eta\beta,r}\ell_{\eta\gamma,s}$, where the antisymmetric tensor elements $e_{\alpha\beta\gamma}$ are defined below and $\ell_{\eta\gamma,s}$ is defined in Eq. 3.3.48.
Q_r normal coordinate (Sect. 3.3.4)
$\hat{P}_r = -i\hbar\partial/\partial Q_r$; momentum conjugate to Q_r.
$q_r = \sqrt{\gamma_r}Q_r$; dimensionless normal coordinate defined in Eq. 3.3.51.
$\gamma_r = 2\pi c\omega_r/\hbar$, Eq. 3.3.50.
$\hat{p}_r = \hat{P}_r/(\hbar\sqrt{\gamma_r})$; dimensionless conjugate momentum.
ω_r harmonic vibration wavenumber, Eq. 3.3.47.

V the potential energy function.

$\mu_{\alpha\beta}$ an element of the 3×3 matrix $\mu = (\boldsymbol{I}')^{-1}$, the inverse of the matrix $(\boldsymbol{I}')$ with elements

$$(\boldsymbol{I}')_{\alpha\beta} = \delta_{\alpha\beta} I_{e,\alpha\alpha} + \sum_{r=1}^{3N-6} a_r^{\alpha\beta} Q_r + \frac{1}{4} \sum_{r=1}^{3N-6} \sum_{s=1}^{3N-6} \sum_{\delta=x,y,z} \frac{a_r^{\alpha\delta} a_s^{\delta\beta}}{I_{e,\delta\delta}} Q_r Q_s \tag{3.3.53}$$

where $I_{e,\alpha\alpha}$ is an equilibrium moment of inertia in the principal axis system.

$a_r^{\alpha\beta} = 2 \sum_{\gamma,\delta,\epsilon=x,y,z} e_{\alpha\gamma\epsilon} e_{\beta\delta\epsilon} \sum_{\eta=1}^{N} m_\eta^{1/2} \left(\boldsymbol{a}_\eta\right)_\gamma \ell_{\eta\delta,r}$ where m_η is the mass of nucleus η and the vector $\boldsymbol{a}_\eta$ is defined in Eq. 3.3.26.

The elements of the unit antisymmetric tensor are defined as

$$\begin{aligned} e_{xyz} = e_{yzx} = e_{zxy} &= +1 \\ e_{xzy} = e_{zyx} = e_{yxz} &= -1. \end{aligned} \tag{3.3.54}$$

If any pair of indices in $\alpha\beta\gamma$ are equal, $e_{\alpha\beta\gamma} = 0$.

3.3.5.2 The Zero-Order Hamiltonian

We have discussed in connection with Eq. 3.3.22 that it is advantageous to express the Hamiltonian for the internal motion of a molecule in field-free space as

$$\hat{H}_{\text{rv}} = \hat{H}_{\text{rot}}^{(0)} + \hat{H}_{\text{vib}}^{(0)} + \hat{H}_{\text{rest}}, \tag{3.3.55}$$

where $\hat{H}_{\text{rot}}^{(0)} = \hat{T}_{\text{rot}}$ depends only on the rotational coordinates (θ, ϕ, χ) and their conjugate momenta, $\hat{H}_{\text{vib}}^{(0)} = \hat{T}_{\text{vib}} + V$ depends only on the vibrational coordinates $(q_1, q_2, \ldots, q_{3N-6})$ and their conjugate momenta, and $\hat{H}_{\text{rest}}$ depends on both rotational and vibrational coordinates and momenta.

We obtain $\hat{H}_{\text{rot}}^{(0)}$ from Eq. 3.3.52 by setting all $q_r = \hat{p}_r = 0$ (so that the molecule is considered to be in its equilibrium configuration) and ignoring the small constant term $-(\hbar^2/8) \sum_{\alpha=x,y,z} \mu_{\alpha\alpha}$. The result is

$$\hat{H}_{\text{rot}}^{(0)} = \sum_{\alpha=x,y,z} \sum_{\beta=x,y,z} \hat{J}_\alpha \, \mu_{\alpha\beta}^{(0)} \, \hat{J}_\beta \tag{3.3.56}$$

where the superscript "(0)" on $\mu_{\alpha\beta}^{(0)}$ indicates that this matrix element is calculated in the equilibrium configuration. It follows from the definition of the matrix μ, and from Eq. 3.3.53 that $\mu_{\alpha\beta}^{(0)} = \delta_{\alpha\beta}/I_{e,\alpha\alpha}$, and so

$$\hat{H}_{\text{rot}}^{(0)} = \frac{\hat{J}_x^2}{2I_{e,xx}} + \frac{\hat{J}_y^2}{2I_{e,yy}} + \frac{\hat{J}_z^2}{2I_{e,zz}}. \tag{3.3.57}$$

We include in the zero-order vibrational Hamiltonian $\hat{H}^{(0)}_{\text{vib}}$ the vibrational kinetic energy operator

$$\hat{T}_{\text{vib}} = \frac{1}{2}\sum_{r=1}^{3N-6} hc\,\omega_r \hat{p}_r^2 \tag{3.3.58}$$

from Eq. 3.3.52 together with the harmonic potential energy

$$V_{\text{harmonic}} = \frac{1}{2}\sum_{k=1}^{3N-6} \lambda_k Q_k^2 = \frac{1}{2}\sum_{k=1}^{3N-6} hc\,\omega_r\, q_r^2 \tag{3.3.59}$$

from Eq. 3.3.46. That is,

$$\hat{H}^{(0)}_{\text{vib}} = \frac{1}{2}\sum_{k=1}^{3N-6} hc\,\omega_r \left(\hat{p}_r^2 + q_r^2\right). \tag{3.3.60}$$

In order to determine $\hat{H}_{\text{rest}}$ in Eq. 3.3.55, the potential energy function V and the elements $\mu_{\alpha\beta}$ of the inverse inertial tensor in Eq. 3.3.52 are expanded as Taylor series in the dimensionless normal coordinates q_r. The resulting Hamiltonian is a polynomial (of infinite order) in the operators $\hat{J}_\alpha$, q_r, and $\hat{p}_r$. The coefficients in this polynomial depend on the equilibrium moments of inertia $I^0_{\alpha\alpha}$, on the zeta constants, on the constants $a_r^{\alpha\beta}$ and on the potential constants from V.

Traditionally, we solve the Schrödinger equation for $\hat{H}_{\text{rv}}$ by initially neglecting $\hat{T}_{\text{rest}}$. The resulting, zero-order Hamiltonian

$$\hat{H}^{(0)}_{\text{rv}} = \hat{H}^{(0)}_{\text{rot}} + \hat{H}^{(0)}_{\text{vib}} \tag{3.3.61}$$

is the sum of two commuting terms, and we can obtain its eigenvalues $E^{(0)}_{\text{rv}}$ as

$$E^{(0)}_{\text{rv}} = E^{(0)}_{\text{rot}} + E^{(0)}_{\text{vib}} \tag{3.3.62}$$

with corresponding eigenfunctions

$$\psi^{(0)}_{\text{rv}} = \psi^{(0)}_{\text{rot}}\,\psi^{(0)}_{\text{vib}} \tag{3.3.63}$$

where $(E^{(0)}_{\text{rot}}, \psi^{(0)}_{\text{rot}})$ is an eigenpair for $\hat{H}^{(0)}_{\text{rot}}$:

$$\hat{H}^{(0)}_{\text{rot}}\,\psi^{(0)}_{\text{rot}} = E^{(0)}_{\text{rot}}\,\psi^{(0)}_{\text{rot}} \tag{3.3.64}$$

while $(E^{(0)}_{\text{vib}}, \psi^{(0)}_{\text{vib}})$ is an eigenpair for $\hat{H}^{(0)}_{\text{vib}}$:

$$\hat{H}^{(0)}_{\text{vib}}\,\psi^{(0)}_{\text{vib}} = E^{(0)}_{\text{vib}}\,\psi^{(0)}_{\text{vib}}. \tag{3.3.65}$$

Once the zero-order Schrödinger equations in Eqs. 3.3.64 and 3.3.65 have been solved, the eigenpairs $(E_{\text{rv},n}, \psi_{\text{rv},n})$ (where n is an index numbering the solutions)

for $\hat{H}_{\mathrm{rv}}$ (which includes the initially neglected term $\hat{T}_{\mathrm{rest}}$) are generated with the "Ansatz"

$$\psi_{\mathrm{rv},n} = \sum_{n_{\mathrm{vib}},n_{\mathrm{rot}}} c^{(n)}_{n_{\mathrm{vib}},n_{\mathrm{rot}}} \psi^{(0)}_{\mathrm{vib},n_{\mathrm{vib}}} \psi^{(0)}_{\mathrm{rot},n_{\mathrm{rot}}} \tag{3.3.66}$$

where we have introduced indices n_{rot} and n_{vib} to label the solutions of Eqs. 3.3.64 and 3.3.65, respectively. With this Ansatz, the molecular rotation–vibration energies $E_{\mathrm{rv},n}$ are computed as the eigenvalues of a matrix with elements

$$H_{(n''_{\mathrm{vib}},n''_{\mathrm{rot}}),(n'_{\mathrm{vib}},n'_{\mathrm{rot}})} = \int \psi^{(0)*}_{\mathrm{vib},n''_{\mathrm{vib}}} \psi^{(0)*}_{\mathrm{rot},n''_{\mathrm{rot}}} \hat{H}_{\mathrm{rv}} \psi^{(0)}_{\mathrm{vib},n'_{\mathrm{vib}}} \psi^{(0)}_{\mathrm{rot},n'_{\mathrm{rot}}} \mathrm{d}\tau, \tag{3.3.67}$$

and the expansion coefficients $c^{(n)}_{n_{\mathrm{vib}},n_{\mathrm{rot}}}$ in Eq. 3.3.66 are components of the eigenvectors of this matrix. In Eq. 3.3.67, the volume element $\mathrm{d}\tau$ is appropriate for the total set of rotation–vibration coordinates $(\theta, \phi, \chi, q_1, q_2, \ldots, q_{3N-6})$.

To obtain a qualitative understanding of molecular spectra it is often sufficient to consider only the solutions of the zero-order Schrödinger equations Eqs. 3.3.64 and 3.3.65 and to approximate the molecular rotation–vibration energies and wavefunctions by Eqs. 3.3.62 and 3.3.63, respectively. So we discuss in the following sections the theory of *the rigidly rotating molecule*, corresponding to the approximations in Eq. 3.3.64, and *the harmonically vibrating molecule*, corresponding to the approximations in Eq. 3.3.65.

3.3.6 The Rigidly Rotating Molecule

The zero-order rotational Hamiltonian (i.e., the Hamiltonian for a rigidly rotating molecule or, generally, for *the rigid rotor*) is given by Eq. 3.3.57:

$$\begin{aligned} \hat{H}^{(0)}_{\mathrm{rot}} &= \frac{\hat{J}^2_x}{2I_{e,xx}} + \frac{\hat{J}^2_y}{2I_{e,yy}} + \frac{\hat{J}^2_z}{2I_{e,zz}} \\ &= \frac{\hat{J}^2_a}{2I_{e,aa}} + \frac{\hat{J}^2_b}{2I_{e,bb}} + \frac{\hat{J}^2_c}{2I_{e,cc}} \end{aligned}, \tag{3.3.68}$$

where the principal axes *abc* are a permutation of *xyz*, ordered such that $I_{e,aa} \leq I_{e,bb} \leq I_{e,cc}$.

We now consider various rotor types with different patterns of rotational energies:

- A *linear rotor* has $I_{e,aa} = 0$ and $I_{e,bb} = I_{e,cc}$. Examples of linear rotors are hydrogen cyanide HCN, carbon dioxide CO_2, and acetylene HCCH.
- A *spherical top* has $I_{e,aa} = I_{e,bb} = I_{e,cc}$. Examples of spherical tops are methane CH_4, sulfur hexafluoride SF_6, and buckminsterfullerene C_{60}.

- A *prolate symmetric top* (Example: Methyl fluoride CH_3F) has $I_{e,aa} < I_{e,bb} = I_{e,cc}$, while an *oblate symmetric top* (Example: Benzene C_6H_6) has $I_{e,aa} = I_{e,bb} < I_{e,cc}$.
- An *asymmetric top* has $I_{e,aa} < I_{e,bb} < I_{e,cc}$. Examples of asymmetric tops are water H_2O and formaldehyde H_2CO.

It is customary to introduce three *rotational constants* A_e, B_e, and C_e, expressed either in frequency (MHz, GHz, ...) or wavenumber (cm^{-1}) units. In frequency units, we have

$$A_e = \frac{1}{h}\frac{\hbar^2}{2I_{e,aa}} = \frac{h}{8\pi^2 I_{e,aa}}, \tag{3.3.69}$$

$$B_e = \frac{1}{h}\frac{\hbar^2}{2I_{e,bb}} = \frac{h}{8\pi^2 I_{e,bb}}, \tag{3.3.70}$$

and

$$C_e = \frac{1}{h}\frac{\hbar^2}{2I_{e,cc}} = \frac{h}{8\pi^2 I_{e,cc}}. \tag{3.3.71}$$

In terms of the rotational constants, the zero-order Hamiltonian becomes

$$\hat{H}^{(0)}_{rot}/h = A_e\left(\frac{\hat{J}_a}{\hbar}\right)^2 + B_e\left(\frac{\hat{J}_b}{\hbar}\right)^2 + C_e\left(\frac{\hat{J}_c}{\hbar}\right)^2 \tag{3.3.72}$$

where the three operators $\hat{J}_\alpha/\hbar, \alpha = a, b, c$, are dimensionless.

3.3.6.1 Rigid Symmetric Top Eigenfunctions

We have already introduced the three operators $(\hat{J}_x, \hat{J}_y, \hat{J}_z)$ that represent the components of the molecular angular momentum along the molecule-fixed axes *xyz*. The analogous operators $(\hat{J}_X, \hat{J}_Y, \hat{J}_Z)$ represent the angular momentum components along the laboratory-fixed axes *XYZ*. We define

$$\hat{\boldsymbol{J}}^2 = \hat{J}_x^2 + \hat{J}_y^2 + \hat{J}_z^2 = \hat{J}_X^2 + \hat{J}_Y^2 + \hat{J}_Z^2, \tag{3.3.73}$$

and it can be shown that the three operators $\hat{\boldsymbol{J}}^2, \hat{J}_z$, and $\hat{J}_Z$ all commute, so that it follows from elementary quantum mechanics that they have simultaneous eigenfunctions. We call these functions $|J, k, m\rangle$. They depend on the Euler angles (θ, ϕ, χ) and are referred to as *rigid symmetric top eigenfunctions* or simply *symmetric top eigenfunctions*. The $|J, k, m\rangle$ functions have the properties

$$\hat{\boldsymbol{J}}^2 |J, k, m\rangle = J(J+1)\hbar^2 |J, k, m\rangle \tag{3.3.74}$$

with $J = 0, 1, 2, 3, \ldots$,

$$\hat{J}_z \, |J, k, m\rangle = k \, \hbar \, |J, k, m\rangle \tag{3.3.75}$$

with $k = -J, -J+1, -J+2, \ldots, J-1, J$, and finally

$$\hat{J}_Z \, |J, k, m\rangle = m \, \hbar \, |J, k, m\rangle \tag{3.3.76}$$

with $m = -J, -J+1, -J+2, \ldots, J-1, J$.

3.3.6.2 Spherical Tops

For a spherical top molecule, we have $I_{e,aa} = I_{e,bb} = I_{e,cc}$ and, therefore, $A_\mathrm{e} = B_\mathrm{e} = C_\mathrm{e}$. The zero-order rotational Hamiltonian in Eq. 3.3.72 becomes

$$\hat{H}^{(0)}_\mathrm{rot}/h = B_\mathrm{e} \, \frac{1}{\hbar^2} \left[\hat{J}_a^2 + \hat{J}_b^2 + \hat{J}_c^2\right] = B_\mathrm{e} \, \frac{1}{\hbar^2} \, \hat{\boldsymbol{J}}^2. \tag{3.3.77}$$

Obviously, it follows from Eq. 3.3.74 that in this case, the $|J, k, m\rangle$ functions are eigenfunctions for $\hat{H}^{(0)}_\mathrm{rot}/h$ with the eigenvalues

$$E^{(0)}_\mathrm{rot}/h = B_\mathrm{e} \, J(J+1), \tag{3.3.78}$$

where $J = 0, 1, 2, 3, \ldots$. The energy is independent of k and m, and so each level is $(2J+1)^2$-fold degenerate, since this is the number of possible values for k and m.

3.3.6.3 Symmetric Tops

For a prolate symmetric top, $I_{e,aa} < I_{e,bb} = I_{e,cc}$ so that $A_\mathrm{e} > B_\mathrm{e} = C_\mathrm{e}$. If we identify the xyz axes with the abc axes so that $xyz = bca$, the "special" axis a becomes the z axis, and we can rewrite $\hat{H}^{(0)}_\mathrm{rot}/h$ as

$$\begin{aligned} \hat{H}^{(0)}_\mathrm{rot}/h &= A_\mathrm{e} \, \frac{1}{\hbar^2} \, \hat{J}_z^2 + B_\mathrm{e} \, \frac{1}{\hbar^2} \left[\hat{J}_x^2 + \hat{J}_y^2\right] \\ &= A_\mathrm{e} \, \frac{1}{\hbar^2} \, \hat{J}_z^2 + B_\mathrm{e} \, \frac{1}{\hbar^2} \left[\hat{\boldsymbol{J}}^2 - \hat{J}_z^2\right] \\ &= B_\mathrm{e} \, \frac{1}{\hbar^2} \, \hat{\boldsymbol{J}}^2 + (A_\mathrm{e} - B_\mathrm{e}) \, \frac{1}{\hbar^2} \, \hat{J}_z^2 \end{aligned} \tag{3.3.79}$$

where we have used Eq. 3.3.73. We now have from Eqs. 3.3.74 and 3.3.75 that for a prolate symmetric top, the $|J, k, m\rangle$ functions are eigenfunctions for $\hat{H}^{(0)}_\mathrm{rot}/h$, and the eigenvalues are

$$E^{(0)}_\mathrm{rot}/h = B_\mathrm{e} \, J(J+1) + (A_\mathrm{e} - B_\mathrm{e}) \, k^2 \tag{3.3.80}$$

where $J = 0, 1, 2, 3, \ldots$, and $k = -J, -J+1, -J+2, \ldots, J-1, J$. A level with $k = 0$ is $(2J+1)$-fold degenerate, $(2J+1)$ being the number of possible values for m, and a level with $|k| > 0$ is $2(2J+1)$-fold degenerate since the energy is independent of the sign of k. We note that since $A_e > B_e$, the energy contribution $(A_e - B_e)\, k^2$ is positive for $|k| > 0$.

An oblate symmetric top has $I_{e,aa} = I_{e,bb} < I_{e,cc}$ and $A_e = B_e > C_e$. Here, we identify $xyz = abc$ so that now the special axis c becomes the z axis, and by a derivation completely analogous to that for the prolate symmetric top, we can show that also for the oblate top, the $|J, k, m\rangle$ functions are eigenfunctions for $\hat{H}^{(0)}_{\mathrm{rot}}/h$ with eigenvalues

$$E^{(0)}_{\mathrm{rot}}/h = B_e\, J(J+1) + (C_e - B_e)\, k^2, \tag{3.3.81}$$

where the degeneracies are as for the prolate top. Since $C_e < B_e$, the energy contribution $(C_e - B_e)\, k^2$ is negative for $|k| > 0$.

3.3.6.4 Asymmetric Tops

For an asymmetric top, $A_e > B_e > C_e$ and we cannot simplify the zero-order Hamiltonian in Eq. 3.3.72 in the way that we did for spherical and symmetric tops. It can be shown, however, that the two operators $\hat{\boldsymbol{J}}^2$ and $\hat{J}_Z$ commute with $\hat{H}^{(0)}_{\mathrm{rot}}$ and so the associated quantum numbers J and m are "good" quantum numbers that can be used to label the energies of the asymmetric top. Knowing this, we can expand the rotational wavefunction $\psi^{(0)}_{\mathrm{rot},J,m}$ of an asymmetric top in terms of rigid symmetric top eigenfunctions:

$$\psi^{(0)}_{\mathrm{rot},J,m} = \sum_{k=-J}^{J} c_k^{(J,m)}\, |J, k, m\rangle, \tag{3.3.82}$$

with this Ansatz for the wavefunction, the molecular rotation–vibration energies $E^{(0)}_{\mathrm{rot}}$ are computed as the eigenvalues of a matrix with elements

$$H_{k',k''} = \left\langle J, k', m \middle| \hat{H}^{(0)}_{\mathrm{rot}} \middle| J, k'', m \right\rangle; \tag{3.3.83}$$

since J and m are "good" quantum numbers we only require matrix elements diagonal in them. It can be shown that for $H_{k',k''}$ to be non-vanishing, we must either have $k'' = k' = k$ and

$$H_{k,k} = \frac{\hbar^2}{4}\left\{\left(\frac{1}{I_{e,xx}} + \frac{1}{I_{e,yy}}\right)\left[J(J+1) - k^2\right] + \frac{2k^2}{I_{e,zz}}\right\}, \tag{3.3.84}$$

or $k'' = k' \pm 2 = k \pm 2$ and

$$H_{k,k\pm2} = \frac{\hbar^2}{8}\left(\frac{1}{I_{e,xx}} - \frac{1}{I_{e,yy}}\right)\sqrt{J(J+1) - k(k\pm1)} \times \sqrt{J(J+1) - (k\pm1)(k\pm2)}. \tag{3.3.85}$$

In using Eqs. 3.3.84 and 3.3.85 we can identify the axis xyz with the principal axes abc as we like. However, for a *near prolate* symmetric top with $I_{e,aa} < I_{e,bb} \approx I_{e,cc}$ it is most convenient to use $xyz = bca$ since this minimizes the off-diagonal matrix elements in Eq. 3.3.85. For similar reasons, for a *near-oblate* rotor with $I_{e,aa} \approx I_{e,bb} < I_{e,cc}$, we use $xyz = abc$.

The matrix representation of $\hat{H}_{\rm rot}^{(0)}$ in the basis set of $|J,k,m\rangle$ functions is block diagonal in J and m, and the matrix elements do not depend on m, so initially we can say that we must diagonalize one block, of dimension $2J+1$, for each J value. However, Eqs. 3.3.84 and 3.3.85 show that each such block separates further into one block of basis functions with even k values, and another block of basis functions with odd k values. All matrix elements connecting an even k value with an odd k value obviously vanish. It can be shown that if, instead of the basis functions $|J,k,m\rangle$, we use the so-called *Wang basis*

$$|J,K,m,\pm\rangle = \frac{1}{\sqrt{2}}\left(|J,K,m\rangle \pm |J,-K,m\rangle\right) \tag{3.3.86}$$

where $K > 0$, and

$$|J,0,m,+\rangle = |J,0,m\rangle, \tag{3.3.87}$$

we obtain a further factorization into four blocks that we can label E^+, E^-, O^+, and O^-. A block labeled E(O) contains basis functions with even(odd) K values only, and the $+(-)$ superscript signifies that the block contains only Wang functions with $+(-)$ from Eqs. 3.3.86 and 3.3.87.

As a measure for the "asymmetry" of an asymmetric top we use the asymmetry parameter

$$\kappa = \frac{2B_{\rm e} - A_{\rm e} - C_{\rm e}}{A_{\rm e} - C_{\rm e}}. \tag{3.3.88}$$

A prolate symmetric top has $\kappa = -1$, and an oblate symmetric top has $\kappa = +1$.

We now imagine a progression of asymmetric tops, all with the same values of $A_{\rm e}$ and $C_{\rm e}$, but with $B_{\rm e}$ varying continuously between $C_{\rm e}$ and $A_{\rm e}$ (or, equivalently, with κ varying between -1 and $+1$). For $B_{\rm e} = C_{\rm e}$, or $\kappa = -1$, we are at the *prolate limit*, where the energy is given by Eq. 3.3.80 with $k = k_a$, where k_a is the projection, in units of $\hbar$, of the angular momentum onto the a axis. For a given J, the energy increases with increasing $|k_a|$ as discussed above. On the other hand, for $B_{\rm e} = A_{\rm e}$, or $\kappa = +1$, we have reached the *oblate limit*, where the energy is given by Eq. 3.3.81 with $k = k_c$, where $k_c\,\hbar$ is the projection of the angular momentum

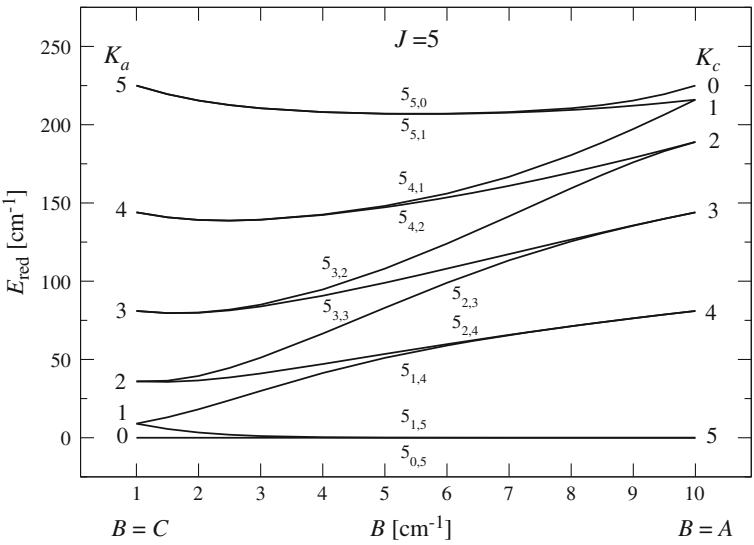

Fig. 3.8 The energy levels of a rigid asymmetric top molecule are plotted for $J = 5$, with $A_e = 10\,cm^{-1}$ and $C_e = 1\,cm^{-1}$, but with B_e varying continuously between C_e and A_e. The vertical axis represents the reduced energy which is measured from the lowest energy levels for the $J = 5$ state

onto the c axis. For a given J, the energy decreases with increasing $|k_c|$. If we plot the energies of the progression of asymmetric tops as functions of B_e varying from C_e to A_e, or κ varying from -1 to $+1$, we obtain a *correlation diagram*, Fig. 3.8. Each energy curve extends from the prolate limit to the oblate limit, and so obviously any energy level of an asymmetric top correlates, in the prolate limit, with a prolate symmetric top level with a defined value of $K_a = |k_a|$ and, in the oblate limit, with an oblate symmetric top level with a defined value of $K_c = |k_c|$. In addition, it can be shown that for any value of κ, where $-1 < \kappa < +1$, the rigid asymmetric top with a given J-value has $2J + 1$ different energies. Consequently, the energy curves in the correlation diagram cannot cross. At a κ-value where two of them crossed, there would only be $2J$ different energies and this cannot happen. Because of this non-crossing rule, we can unambiguously correlate the energies in the prolate and oblate limits for a given J value. For example, the highest energy of the prolate rotor, with $K_a = J$, must necessarily correlate with the highest level of the oblate rotor with $K_c = 0$. Similarly, the lowest level of the prolate rotor, with $K_a = 0$, must correlate with the lowest level of the oblate rotor with $K_c = J$. In general, we can label any level of the asymmetric rotor as $J_{K_aK_c}$. When, for a given J value, we sort the energies $E(J_{K_aK_c})$ in ascending order, we have $E(J_{0J}) < E(J_{1J}) < E(J_{1\,(J-1)}) < E(J_{2\,(J-1)}) < E(J_{2\,(J-2)}) < E(J_{3\,(J-2)}) < E(J_{3\,(J-3)}) < \cdots < E(J_{(J-2)3}) < E(J_{(J-2)2}) < E(J_{(J-1)2}) < E(J_{(J-1)1}) < E(J_{J1}) < E(J_{J0})$. For any level, $K_a + K_c = J$ or $K_a + K_c = J + 1$.

3.3.6.5 Linear Rotors

The theory outlined in the preceding part of this section is concerned with non-linear molecules, i.e., molecules with a non-linear equilibrium structure (see Sect. 3.3.2.2). For such a molecule, we need three Euler angles (θ, ϕ, χ) to describe the rotation. The Euler angle χ, however, describes the rotation of the molecule about the molecule-fixed z axis. For a rigid linear molecule, all nuclei are located on the z axis, and the rotation about this axis cannot physically take place. Thus the angle χ becomes redundant and we have only the two angles (θ, ϕ) which are the usual polar/azimuthal angles defining the direction of the molecular axis relative to the XYZ axes. As mentioned above, a rigid linear molecule has $I_{e,aa} = 0$ and $I_{e,bb} = I_{e,cc}$. Its rotational Hamiltonian is

$$\hat{H}^{(0)}_{\text{rot}}/h = B_{\text{e}} \left[\left(\frac{\hat{J}_b}{\hbar} \right)^2 + \left(\frac{\hat{J}_c}{\hbar} \right)^2 \right]. \tag{3.3.89}$$

The eigenfunctions of $\hat{H}^{(0)}_{\text{rot}}$ are the well-known spherical harmonics $Y_{Jm}(\theta, \phi)$ which are related to the $|J, k, m\rangle$ functions:

$$Y_{Jm}(\theta, \phi) = \sqrt{2\pi}\, |J, 0, m\rangle \tag{3.3.90}$$

where, as usual, where $J = 0, 1, 2, 3, \ldots$ and $m = -J, -J+1, -J+2, \ldots, J-1, J$. The $Y_{Jm}(\theta, \phi)$ functions are simultaneous eigenfunctions of $\hat{\boldsymbol{J}}^2$ and $\hat{J}_Z$ with the eigenvalues $J(J+1)\,\hbar^2$ and $m\hbar$, respectively. The eigenvalue of $\hat{H}^{(0)}_{\text{rot}}$ corresponding to the eigenfunction $Y_{Jm}(\theta, \phi)$ is

$$E^{(0)}_{\text{rot}}/h = B_{\text{e}}\, J(J+1). \tag{3.3.91}$$

The energy is independent of m, and so each level is $2J+1$-fold degenerate.

3.3.7 The Harmonically Vibrating Molecule

The zero-order vibrational energies for a non-linear molecule are the eigenvalues of the Hamiltonian from Eq. 3.3.60:

$$\hat{H}^{(0)}_{\text{vib}} = \frac{1}{2} \sum_{r=1}^{3N-6} hc\, \omega_r \left(\hat{p}_r^2 + q_r^2 \right) \tag{3.3.92}$$

where q_r is a dimensionless normal coordinate from Eq. 3.3.51 and $\hat{p}_r = -i\partial/\partial q_r$ is its dimensionless conjugate momentum. The harmonic vibration wavenumber ω_r is defined in Eq. 3.3.47.

3.3.7.1 Asymmetric Tops

Whereas a rigid asymmetric top has a more complicated rotational energy pattern than a symmetric top, a spherical top or a linear rotor, it has a simpler vibrational spectrum than any of these molecules. For an asymmetric top, the matrix **GF** discussed in Sect. 3.3.4 has $3N-6$ *different* eigenvalues λ_k, and the zero-order vibrational energy is given by

$$E_{\text{vib}}^{(0)}/(hc) = \sum_{r=1}^{3N-6} E_{v_r}^{(0)}/(hc) = \sum_{r=1}^{3N-6} \omega_r \left(v_r + \frac{1}{2}\right) \tag{3.3.93}$$

where each of the quantum numbers $v_r = 0, 1, 2, 3, \ldots$. Here, we have that $E_{v_r}^{(0)} = h\,c\,\omega_r\,(v_r + \frac{1}{2})$ is an eigenvalue obtained by solution of the harmonic oscillator Schrödinger equation

$$hc\,\omega_r\left(\hat{p}_r^2 + q_r^2\right)\phi_{v_r}^{(0)}(q_r) = E_{v_r}^{(0)}\,\phi_{v_r}^{(0)}(q_r), \tag{3.3.94}$$

where $\phi_{v_r}^{(0)}(q_r)$ is a standard one-dimensional harmonic oscillator eigenfunction (see, for example, [25]. The zero-order vibrational wavefunction for an asymmetric top is

$$\psi_{\text{vib}}^{(0)} = \phi_{v_1}^{(0)}(q_1)\,\phi_{v_2}^{(0)}(q_2)\,\phi_{v_3}^{(0)}(q_3)\cdots\phi_{v_{3N-6}}^{(0)}(q_{3N-6}). \tag{3.3.95}$$

3.3.7.2 Linear Rotors

As discussed in Sect. 3.3.6.5, the rotation of a rigid linear molecule is described by two Euler angles (θ, ϕ). The rotation about the molecular axis cannot take place when the molecule is linear. When the molecule vibrates out of the linear configuration, however, this rotation becomes possible, and it is customarily described as a vibration so that for a molecule with N nuclei and a linear equilibrium configuration, we have $3N-5$ normal coordinates $(q_1, q_2, q_3, \ldots, q_{3N-6}, q_{3N-5})$. Each of these normal coordinates q_r has an associated harmonic vibrational wavenumber ω_r, but not all of these harmonic vibrational wavenumbers are different. Of the $3N-5$ normal coordinates, $N-1$ describe the stretching of the $N-1$ bonds of the molecule and these will be different, just like the ω_r-values of an asymmetric top. The remaining $2N-4$ ω_r-values, however, describe the bending motion at each of the $N-2$ "inner" nuclei of the molecule (no bending motion takes place at the two terminal nuclei). These $2N-4$ ω_r-values are pairwise equal and form $N-2$ pairs. This is because at each inner nucleus, one normal coordinate describes the bending motion taking place in the xz plane of the molecule-fixed axis system xyz (where the z axis is the molecular axis and the direction of the x axis is arbitrarily chosen), and another normal coordinate describes the bending motion taking place in the yz plane. These two normal coordinates

necessarily have the same value of ω_r. Hence, a linear molecule has $(N-1)+(N-2)=2N-3$ different ω_r-values.

The two-dimensional bending vibration at a given inner nucleus is described by two normal coordinates which, in an obvious notation, we can write as (q_{sx}, q_{sy}) where the index s numbers the vibrational mode. We have $\omega_{sx}=\omega_{sy}=\omega_s$. In principle, we can use product wavefunctions $\phi^{(0)}_{v_{sx}}(q_{sx})\,\phi^{(0)}_{v_{sy}}(q_{sy})$ as zero-order vibrational wavefunctions; as before $\phi^{(0)}_{v}(q)$ is a standard one-dimensional harmonic oscillator eigenfunction. The contribution to the vibrational energy from vibrational mode s is thus

$$\begin{aligned} E^{(0)}_{v_{sx},v_{sy}}/(hc) &= \omega_s\left(v_{sx}+\frac{1}{2}\right)+\omega_s\left(v_{sy}+\frac{1}{2}\right) \\ &= \omega_s\left(v_{sx}+v_{sy}+1\right)=\omega_s\left(v_s+1\right) \end{aligned} \tag{3.3.96}$$

where $v_s=v_{sx}+v_{sy}$. The zero-order vibrational state with the energy $E^{(0)}_{v_{sx},v_{sy}}$ is (v_s+1)-fold degenerate since there are v_s+1 different values of (v_{sx}, v_{sy}) $[=(v_s,0),(v_s-1,1),(v_s-2,2),\ldots,(1,v_s-1),(0,v_s)]$ with a common value of v_s.

Instead of the (v_s+1) product wavefunctions $\phi^{(0)}_{v_{sx}}(q_{sx})\,\phi^{(0)}_{v_s-v_{sx}}(q_{sy})$ with a common value of v_s, it is customary to use as zero-order vibrational wavefunctions, obtained as linear combinations of the product functions. These new functions are called $\phi^{(0)}_{v_s,\ell_s}(q_s,\chi_s)$ where $\ell_s=-v_s,-v_s+2,-v_s+4,\ldots,v_s-2,v_s$, and the coordinates q_s and χ_s are such that

$$q_{sx}=q_s\cos\chi_s \quad \text{and} \quad q_{sy}=q_s\sin\chi_s. \tag{3.3.97}$$

The quantum number ℓ_s is the projection, in units of $\hbar$, onto the molecular axis of the angular momentum generated by the vibrational mode s (which, as mentioned above, also describes the rotation about the molecular axis). The detailed form of the functions $\phi^{(0)}_{v_s,\ell_s}(q_s,\chi_s)$ is given, for example, by Bunker and Jensen [25].

With the definitions introduced here, the zero-order vibrational energy for a linear rotor is given as

$$E^{(0)}_{\text{vib}}/(hc)=\sum_{r=1}^{N-1}\omega_r\left(v_r+\frac{1}{2}\right)+\sum_{s=N}^{2N-3}\omega_s(v_s+1) \tag{3.3.98}$$

and the zero-order vibrational wavefunction is

$$\psi^{(0)}_{\text{vib}}=\prod_{r=1}^{N-1}\phi^{(0)}_{v_r}(q_r)\times\prod_{s=N}^{2N-3}\phi^{(0)}_{v_s,\ell_s}(q_s,\chi_s). \tag{3.3.99}$$

In the harmonic (zero-order) approximation, the vibrational energy depends only on the v quantum numbers; it is independent of the ℓ quantum numbers. However, to characterize completely the vibrational state of a linear rotor, we require the quantum numbers $v_1, v_2, v_3, \ldots, v_{N-1}, v_N, \ldots, v_{2N-3}$ and $\ell_N, \ldots, \ell_{2N-3}$,

whereas for an asymmetric top with the same number of nuclei, we use the quantum numbers $v_1, v_2, v_3, \ldots, v_{3N-6}$.

3.3.7.3 Symmetric Tops

A symmetric top molecule has *non-degenerate* normal vibrations, analogous to the stretching vibrations of the linear rotor, and *doubly degenerate* normal vibrations, analogous to the bending vibrations of the linear molecule. A non-degenerate normal vibration is described by a single normal coordinate q_r and the eigenfunction $\phi_{v_r}^{(0)}(q_r)$ of the corresponding one-dimensional harmonic oscillator. A doubly degenerate normal vibration is described by two normal coordinates (q_{sa}, q_{sb}), say, or by the equivalent coordinates (q_s, χ_s) defined by analogy with Eq. 3.3.97.

If a symmetric top molecule with N nuclei has n_1 non-degenerate normal vibrations and n_2 doubly degenerate normal vibrations, then we have $n_1 + 2n_2 = 3N - 6$, but unlike the linear rotor, there is no simple rule to determine n_1 and n_2. For example, the symmetric top CH_3F has three non-degenerate vibrations and three doubly degenerate ones.

By analogy with the linear rotor, we obtain for the symmetric top that the zero-order vibrational energy is expressed as

$$E_{\text{vib}}^{(0)}/(hc) = \sum_{r=1}^{n_1} \omega_r \left(v_r + \frac{1}{2} \right) + \sum_{s=n_1+1}^{n_1+n_2} \omega_s (v_s + 1) \tag{3.3.100}$$

and the zero-order vibrational wavefunction is

$$\psi_{\text{vib}}^{(0)} = \prod_{r=1}^{n_1} \phi_{v_r}^{(0)}(q_r) \times \prod_{s=n_1+1}^{n_1+n_2} \phi_{v_s,\ell_s}^{(0)}(q_s, \chi_s). \tag{3.3.101}$$

To characterize completely the vibrational state of a symmetric top, we require the quantum numbers $v_1, v_2, v_3, \ldots, v_{n_1}, v_{n_1+1}, \ldots, v_{n_1+n_2}$ and $\ell_{n_1+1}, \ldots, \ell_{n_1+n_2}$ but in the zero-order approximation, the energy depends on the v quantum numbers exclusively.

3.3.7.4 Spherical Tops

The expression for the zero-order vibrational energy of a spherical top is, in principle, analogous to Eqs. 3.3.98 and 3.3.100. However, spherical tops have normal vibrations of higher degeneracy than two. Methane CH_4, for example, has triply degenerate vibrations described by three normal coordinates (q_{sa}, q_{sb}, q_{sc}), all corresponding to the same value of ω_s. Such a coordinate triple will produce a contribution of $h\,c\,\omega_s(v_s + 3/2)$ to the zero-order vibrational energy.

3.3.8 Effective Hamiltonians

3.3.8.1 The Contact Transformation

In connection with Eqs. 3.3.61–3.3.67, we have outlined how the rotation–vibration Schrödinger equation

$$\hat{H}_{\mathrm{rv}}\,\psi_{\mathrm{rv},n} = E_{\mathrm{rv},n}\,\psi_{\mathrm{rv},n} \tag{3.3.102}$$

can be solved by expanding the wavefunction $\psi_{\mathrm{rv},n}$ in terms of known basis functions [Eq. 3.3.66] and thus converting the Schrödinger equation to a matrix eigenvalue equation. In Eq. 3.3.102, $\hat{H}_{\mathrm{rv}}$ is the Watson Hamiltonian from Eq. 3.3.52 and $E_{\mathrm{rv},n}$ is the eigenvalue corresponding to the eigenfunction $\psi_{\mathrm{rv},n}$ with the running index n numbering the solutions.

The matrix representation of $\hat{H}_{\mathrm{rv}}$ (with elements given by Eq. 3.3.67), which we obtain by inserting Eq. 3.3.66 in Eq. 3.3.102, can be diagonalized numerically in a so-called *variational calculation*. In spectroscopic theory, however, it is traditionally solved by perturbation methods, and we outline one such method here, the so-called *contact transformation* (Maes and Amat [26]).

We can write a *unitary operator* as

$$\hat{T} = e^{i\hat{S}} \tag{3.3.103}$$

where $\hat{S}$ is a hermitian, initially arbitrary operator and the exponential is expressed as a Taylor expansion

$$\hat{T} = e^{i\hat{S}} = 1 + i\,\hat{S} + \frac{1}{2!}\left(i\,\hat{S}\right)^2 + \cdots \tag{3.3.104}$$

We use the operator $\hat{T}$ to form a new transformed Hamiltonian

$$\hat{H}'_{\mathrm{rv}} = \hat{T}\,\hat{H}_{\mathrm{rv}}\,\hat{T}^{-1} = e^{i\hat{S}}\,\hat{H}_{\mathrm{rv}}\,e^{-i\hat{S}}. \tag{3.3.105}$$

We obtain the eigenvalues and eigenfunctions for $\hat{H}_{\mathrm{rv}}$ by solving the Schrödinger equation in Eq. 3.3.102 which we rewrite as

$$\hat{T}\,\hat{H}_{\mathrm{rv}}\,\hat{T}^{-1}\,\hat{T}\,\psi_{\mathrm{rv},n} = E_{\mathrm{rv},n}\,\hat{T}\,\psi_{\mathrm{rv},n}. \tag{3.3.106}$$

This shows that the Schrödinger equation for $\hat{H}'_{\mathrm{rv}}$ is

$$\hat{H}'_{\mathrm{rv}}\left(\hat{T}\,\psi_{\mathrm{rv},n}\right) = E_{\mathrm{rv},n}\left(\hat{T}\,\psi_{\mathrm{rv},n}\right). \tag{3.3.107}$$

Hence $\hat{H}_{\mathrm{rv}}$ and $\hat{H}'_{\mathrm{rv}}$ have identical eigenvalues but the eigenfunctions for $\hat{H}'_{\mathrm{rv}}$ are given by

$$\psi'_{\mathrm{rv},n} = \hat{T}\,\psi_{\mathrm{rv},n} \tag{3.3.108}$$

where $\psi_{\mathrm{rv},n}$ is an eigenfunction for $\hat{H}_{\mathrm{rv}}$.

The basic idea of a contact transformation is now to determine the operator $\hat{S}$ such that

$$\psi^{(0)}_{\mathrm{vib},n_{\mathrm{vib}}}\,\psi^{(0)}_{\mathrm{rot},n_{\mathrm{rot}}} = \hat{T}\,\psi_{\mathrm{rv},n} = e^{i\hat{S}}\,\psi_{\mathrm{rv},n} \tag{3.3.109}$$

where $\psi^{(0)}_{\mathrm{vib},n_{\mathrm{vib}}}\,\psi^{(0)}_{\mathrm{rot},n_{\mathrm{rot}}}$ is a basis function from Eq. 3.3.66. Ideally, $\hat{H}'_{\mathrm{rv}}$ is diagonal in the basis of product functions $\psi^{(0)}_{\mathrm{vib},n_{\mathrm{vib}}}\,\psi^{(0)}_{\mathrm{rot},n_{\mathrm{rot}}}$ and the rotation–vibration energies are then simply given by the diagonal matrix elements

$$E_{\mathrm{rv},n} = \left\langle \psi^{(0)}_{\mathrm{vib},n_{\mathrm{vib}}}\,\psi^{(0)}_{\mathrm{rot},n_{\mathrm{rot}}} \middle| \hat{H}'_{\mathrm{rv}} \middle| \psi^{(0)}_{\mathrm{vib},n_{\mathrm{vib}}}\,\psi^{(0)}_{\mathrm{rot},n_{\mathrm{rot}}} \right\rangle. \tag{3.3.110}$$

The procedure of a contact transformation is described, for example, in [16]. In practice, the operator $\hat{S}$ is expanded as a series of terms

$$\hat{S} = \hat{S}_0 + \hat{S}_1 + \hat{S}_2 + \hat{S}_3 + \hat{S}_4 + \cdots, \tag{3.3.111}$$

where the significance of the term S_k diminishes as k increases. Equation 3.3.110 applies in the limit of $k \to \infty$; it involves an approximation that will become increasingly better as more terms are added in Eq. 3.3.111.

3.3.8.2 The Watsonian

In general, we cannot in practice obtain a contact-transformed Hamiltonian $\hat{H}'_{\mathrm{rv}}$ that is exactly diagonal in a basis of functions

$$\psi^{(0)}_{\mathrm{vib},n_{\mathrm{vib}}}\,\psi^{(0)}_{\mathrm{rot},n_{\mathrm{rot}}}.$$

Normally, contact transformations are used to reduce the matrix elements, which are off-diagonal in n_{vib}, to a degree that these matrix elements can be neglected. Hence, we can average $\hat{H}'_{\mathrm{rv}}$ over one vibrational basis function $\psi^{(0)}_{\mathrm{vib},n_{\mathrm{vib}}}$ to obtain the effective rotational Hamiltonian

$$\tilde{H}_{\mathrm{rot}} = \left\langle \psi^{(0)}_{\mathrm{vib},n_{\mathrm{vib}}} \middle| \hat{H}'_{\mathrm{rv}} \middle| \psi^{(0)}_{\mathrm{vib},n_{\mathrm{vib}}} \right\rangle. \tag{3.3.112}$$

Bunker and Jensen [25] have advocated the use of the term *Watsonian* for the Hamiltonian $\tilde{H}_{\mathrm{rot}}$ for any molecule; the development and use of this type of Hamiltonian have benefited greatly from the work of Watson [27, 28]. The Watsonian is an expansion in the rotational operators $\hat{J}_\alpha$ ($\alpha = x, y$ and z) and for a non-planar asymmetric top molecule it has the general form [28] (see also Sarka et al. [29])

$$\tilde{H}_{\rm rot} = B_{200}\,\hat{\boldsymbol{J}}^2 + B_{020}\,\hat{J}_z^2 + T_{400}\,\hat{\boldsymbol{J}}^4 + T_{220}\,\hat{\boldsymbol{J}}^2\,\hat{J}_z^2 + T_{040}\,\hat{J}_z^4 + \frac{1}{2}\left[B_{002} + T_{202}\,\hat{\boldsymbol{J}}^2 + T_{022}\,\hat{J}_z^2, (\hat{J}_+)^2 + (\hat{J}_-)^2\right]_+ + T_{004}\left((\hat{J}_+)^4 + (\hat{J}_-)^4\right), \tag{3.3.113}$$

where we have truncated the expansion in the $\hat{J}_\alpha$ after the second order (i.e., quartic) terms. The quantities B_{ijk} and T_{ijk} in Eq. 3.3.113 are molecular parameters, and $\hat{J}_\pm = \hat{J}_x \pm i\hat{J}_y$. For two operators $\hat{A}$ and $\hat{B}$, the plus commutator $[\hat{A}, \hat{B}]_+ = \hat{A}\,\hat{B} + \hat{B}\,\hat{A}$. The eigenvalues of $\tilde{H}_{\rm rot}$ are obtained by diagonalization of a Hamiltonian matrix set up in a basis of symmetric top functions $|J, k, m\rangle$ exactly as described for the Hamiltonian of the rigid asymmetric rotor in Sect. 3.3.6.4.

If we know (an analytical representation of) the potential energy surface and the equilibrium geometry of a molecule, we can calculate the values of the quantities B_{ijk} and T_{ijk} in Eq. 3.3.113. However, Watsonians are mostly used in least squares fittings to experimentally observed transition frequencies; the fittings aim at determining experimental values for parameters such as B_{ijk} and T_{ijk} (and of the coefficients of higher order terms in the $\hat{J}_\alpha$ which we neglect here). Initial problems with determining simultaneously the values of all six T_{ijk} in Eq. 3.3.113 from experimental data were explained by Watson [27, 28]. There are infinitely many Hamiltonians $\tilde{H}_{\rm rot}$, all of the general form given in Eq. 3.3.113 but with different values for the T_{ijk} parameters, which have the same eigenvalues and which are equally well suited for fitting a given set of experimental data. These Hamiltonians are all connected by contact transformations. Watson [27, 28]: solved this problem by introducing constraints on the parameters T_{ijk}. For example, for a general $\tilde{H}_{\rm rot}$ with non-zero values for all six T_{ijk} it is possible to devise a rotational contact transformation (see also Sarka and Demaison [30]) that produces a transformed $\tilde{H}_{\rm rot}$ with $T_{004} = 0$. In a notation more familiar than that in Eq. 3.3.113, the resulting Hamiltonian is given by

$$\tilde{H}_{\rm rot} = \frac{1}{2}(X+Y)\,\hat{\boldsymbol{J}}^2 + \left\{Z - \frac{1}{2}(X+Y)\right\}\hat{J}_z^2 - \Delta_J\,\hat{\boldsymbol{J}}^4 - \Delta_{JK}\,\hat{\boldsymbol{J}}^2\,\hat{J}_z^2 - \Delta_K\,\hat{J}_z^4 + \left[\frac{1}{4}(X-Y) - \delta_J\,\hat{\boldsymbol{J}}^2 - \delta_K\,\hat{J}_z^2, (\hat{J}_+)^2 + (\hat{J}_-)^2\right]_+ . \tag{3.3.114}$$

This is known as *Watson's A-reduced Hamiltonian*. In Eq. 3.3.114, X, Y, and Z are the effective rotational constants of the molecule for the vibrational state in question [associated with the molecule-fixed axes x, y, and z, respectively], and the parameters $\Delta_J, \Delta_{JK}, \Delta_K, \delta_J$, and δ_K are *centrifugal distortion constants*. The application of a contact transformation to impose selected constraints on the parameters of a Hamiltonian is called a *reduction* of the Hamiltonian. Another way of reducing the Watsonian leads to *Watson's S-reduced Hamiltonian* which has $T_{022} = 0$. Reductions are treated in detail in the original papers by Watson [27, 28]: and in the review articles [29, 30].

For a prolate symmetric top, in the absence of resonances, the eigenvalues of the Watsonian for a given vibrational state can be written (in cm^{-1}) as

$$T_{VLJK} = G_{VL} + F_{VLJK} \tag{3.3.115}$$

where

$$G_{VL} = \sum_r \omega_r \left(v_r + \frac{d_r}{2}\right) + \sum_{r \le r'} X_{rr'} \left(v_r + \frac{d_r}{2}\right)\left(v_{r'} + \frac{d_{r'}}{2}\right) + \sum_{t \le t'} g_{tt'} l_t l_{t'} + \cdots \tag{3.3.116}$$

and

$$F_{VLJK} = B_V J(J+1) + (A_V - B_V)K^2 - 2\sum_t \left(A\zeta^z_{ta,tb}\right)_V l_t k - D_J J^2(J+1)^2 - D_{JK} J(J+1)K^2 - D_K K^4 + \sum_t \eta^J_t l_t J(J+1)\, k + \sum_t \eta^K_t l_t k^3 + \cdots \tag{3.3.117}$$

with

$$B_V = B_\mathrm{e} - \sum_r \alpha^B_r \left(v_r + \frac{d_r}{2}\right) + \cdots, \tag{3.3.118}$$

$$A_V = A_\mathrm{e} - \sum_r \alpha^A_r \left(v_r + \frac{d_r}{2}\right) + \cdots, \tag{3.3.119}$$

and

$$\left(A\zeta^z_{ta,tb}\right)_V = A_\mathrm{e}\, \zeta^z_{ta,tb} - \sum_r \alpha^{A\zeta_t}_r \left(v_r + \frac{d_r}{2}\right) + \cdots. \tag{3.3.120}$$

The expression for an oblate symmetric top is obtained by replacing A_e and A_V by C_e and C_V, respectively. In Eqs. 3.3.115–3.3.120 V and L are shorthand notations for all v_r and l_r quantum numbers, respectively, of the symmetric top, see Sect. 3.3.7.3. If v_r is a non-degenerate normal mode, $d_r = 1$, whereas if v_r is doubly degenerate, $d_r = 2$. The parameter ω_r is defined in Eq. 3.3.47 for the normal mode v_r. The rotational constants A_e and B_e are defined in Eq. 3.3.69–3.3.71; the $\zeta^z_{ta,tb}$ are Coriolis coupling constants. Further parameters are $X_{rr'}, g_{tt'}$, the centrifugal distortion constants D_J, D_{JK}, and D_K, and the constants $\eta^J_t, \eta^K_t, \alpha^B_r, \alpha^A_r$, and $\alpha^{A\zeta_t}_r$. They all depend on the equilibrium geometry (equilibrium bond lengths and angles) of the molecule and on the parameters determining the potential energy function; see, for example [16].

For linear rotor, in the absence of resonances, the eigenvalues of the Watsonian for a given vibrational state can be written (in cm^{-1}) as

$$T_{VLJ\ell} = G_{VL} + F_{V\,LJ\ell} \tag{3.3.121}$$

where the expression for G_{VL} is identical to that for a symmetric top molecule, Eq. 3.3.116, and

$$\begin{aligned} F_{VLJ\ell} = {} & B_V\left[J(J+1) - \ell^2\right] - D_V\left[J(J+1) - \ell^2\right]^2 \\ & + H_V\left[J(J+1) - \ell^2\right]^3 + M_V\left[J(J+1) - \ell^2\right]^4 + \cdots \end{aligned} \tag{3.3.122}$$

where $\ell = \sum_t \ell_t$. The parameters $B_V, D_V, H_V, M_V, \ldots$ are defined by equations analogous to Eqs. 3.3.118 and 3.3.119.

If zero-order vibrational states are close in energy, a *resonance* occurs. For example, for a symmetric top or a linear rotor, this would mean that for two different sets of v_r values, V and V', we have $G_{VL} \approx G_{V'L'}$. In this case the Watsonian cannot be applied as outlined here. The theory must be extended so that the molecular energies are obtained as the eigenvalues of a matrix representation of a Watsonian common for the two vibrational states VL and $V'L'$. Such resonances and their theoretical description are discussed in detail by, for example, [16, 19, 30].

3.3.9 Molecular Symmetry

In the preceding sections we have briefly described the rotation–vibration states of different types of molecules, and we now continue to consider the way these states can be connected by *transitions* accompanied by absorption and emission of electromagnetic radiation energy. Luckily, it turns out that there are very restrictive *selection rules* that determine which state pairs can be connected by a transition of a given type. This is lucky since if it were not so, a given molecule would absorb or emit light at any frequency or wavenumber, and rotation–vibration spectra could not be used to identify molecules for example in interstellar space.

3.3.9.1 Symmetry and Symmetry Groups

The selection rules are derived by consideration of *molecular symmetry* and so we give here a brief discourse on this subject. We discuss the following symmetry types:

1. Permutations of identical nuclei, whereby two or more identical nuclei replace each other.
2. Spatial inversion, where all nuclei and electrons are inverted through the molecular center of mass.

3. Rotational symmetry, i.e., the fact that owing to the isotropy of space, we can rotate an isolated molecule arbitrarily (so that all particles, nuclei and electrons, in the molecule are rotated in the same manner) without changing the physical situation.

Each of the symmetry types considered above gives rise to *symmetry operations* that commute with the molecular Hamiltonian, see [25, 31, 32].

The mathematical tool that is used to describe the permutation–inversion symmetry of a molecule is called *group theory* or, more precisely, *representation theory*. An introduction is given by Bunker and Jensen [25, 31]. A group theoretical analysis of a molecule, in terms of permutation–inversion symmetry, involves the following steps:

i. The possible permutations of identical nuclei, the inversion operation and all operations that can be obtained by combining a possible permutation of identical nuclei with the inversion operation. These operations constitute a *(symmetry) group* for the molecule. Groups are mathematical objects that satisfy certain *group axioms* (see, for example, [25], Sect. 1.3). The group just mentioned is called the *CNPI* group for the molecule (Complete Nuclear Permutation Inversion Group, see [25], Chap. 2). In most cases we do not use the complete CNPI group as symmetry group. Normally it is sufficient to use only a subgroup of the CNPI group. This smaller group is called the *Molecular Symmetry Group* (*MS Group*, see [25], Chap. 3). There are also cases where the MS group and the CNPI group are identical.
ii. When the MS group has been determined, its so-called *irreducible representations* can be constructed according to unambiguous, mathematical rules. For most groups, these irreducible representations are already known and can be found in textbooks such as [25, 31] in the form of so-called *character tables*. An irreducible representation can be viewed as a set of rules that determine how a wavefunction (that belongs to this irreducible representation) *transforms* under the operations of the symmetry group. The irreducible representation dictates how the wavefunction changes,[10] when the operations in the symmetry group (i.e., permutations of identical nuclei and/or inversion) are applied to it. A given group will normally have a relatively small number of irreducible representations.
iii. The central statement is now that *any wavefunction* of a given molecule must belong to an irreducible representation of the symmetry group. When we investigate how the various wavefunctions of the molecule change under symmetry operations (i.e., we investigate how they *transform*), there are only a very limited number of possibilities for the possible transformation properties. These possibilities correspond to the irreducible representations of the

[10] For degenerate irreducible representations, the transformation properties of the generating wavefunctions are not uniquely determined, but the matrices determining the transformation properties of the wavefunctions are related by similarity transformations.

symmetry group. For a given molecular state, we can use the irreducible representation *generated* by its wavefunction to label this wavefunction. Further, representation theory can be used to simplify the calculation of molecular energies, that is, to save computer time and memory.

Obviously we are giving here a very rough sketch of molecular symmetry and its applications. We will describe the application of these ideas to the water molecule as an example:

The Symmetry of H_2O

The water molecule H_2O has two identical protons. Consequently, for this molecule the only possible permutation of identical nuclei is the interchange of these two nuclei. We label the protons as 1 and 2 (and the oxygen nucleus as 3) and denote the interchange of 1 and 2 as (12) (this operation is read as "one-two" and *never* as "twelve"). Another possible symmetry operation is the inversion E^* which inverts the two protons, the oxygen nucleus and the ten electrons in the center of mass of the molecule. Also, we have the combined operation $(12)^*$ ("one-two-star") which is carried out by first applying E^* and then (12) (or first (12) and then E^*; the sequence plays no role) Finally, for formal reasons the symmetry group must contain a so-called neutral element E. This element does nothing; it leaves the system in the initial condition.

The four symmetry operations listed above form a *group*, a mathematical object satisfying a set of *group axioms* (see, for example, [25]). The group that we consider here is customarily called $\boldsymbol{C}_{2v}(\mathrm{M})$:

$$\boldsymbol{C}_{2v}(\mathrm{M}) = \{E, (12), E^*, (12)^*\}. \tag{3.3.123}$$

It can be shown that this group has four irreducible representations called A_1, A_2, B_1 und B_2, respectively. The wavefunctions ψ of the water molecule are such that when we apply a group operation R [= $E, (12), E^*$, or $(12)^*$] to ψ, we have

$$R\psi = \chi^{\Gamma}(R)\psi, \tag{3.3.124}$$

where the constant factor $\chi^{\Gamma}(R)$ depends on the symmetry operation R and on the irreducible representation Γ [= A_1, A_2, B_1 or B_2]. The four irreducible representations correspond to four kinds of water wavefunctions:

A_1: The function is unchanged by all four symmetry operations $E, (12), E^*, (12)^*$.

A_2: The function is unchanged by the operation E (as all functions are). It also unchanged by (12) but changes sign under E^*. In consequence, the function must necessarily change sign under the operation $(12)^* = (12)E^*$.

B_1: The function is unchanged by the operation E. It changes sign under both of the operations (12) and E^*, and so it stays unchanged under $(12)^*$.

Table 3.2 The character table for the molecular symmetry group $\boldsymbol{C}_{2v}(M)$

	E E	(12) C_2	E^* σ	(12)* σ'
A_1	1	1	1	1
A_2	1	1	−1	−1
B_1	1	−1	−1	1
B_2	1	−1	1	−1

Table 3.3 The character table of the CNPI group $\boldsymbol{G}_{12}$

	E	(123) (132)	(12) (23) (31)	E^*	(123)* (132)*	(12)* (23)* (31)*
A_1^+	1	1	1	1	1	1
A_1^-	1	1	1	−1	−1	−1
A_2^+	1	1	−1	1	1	−1
A_2^-	1	1	−1	−1	−1	1
E^+	2	−1	0	2	−1	0
E^-	2	−1	0	−2	1	0

B_2: The function is unchanged by the operation E. It changes sign under (12) but is unchanged by E^*. Thus, it changes sign under $(12)^*$.

These definitions imply that for example $\chi^{A_1}(E) = \chi^{A_1}((12)) = \chi^{A_1}(E^*) = \chi^{A_1}((12)^*) = 1$ and $\chi^{A_2}(E) = \chi^{A_2}((12)) = 1$, but $\chi^{A_2}(E^*) = \chi^{A_2}((12)^*) = -1$. The quantities $\chi^{\Gamma}(R)$ are called the *characters* of the irreducible representations. For a given group, they are compiled in the *character table*. Table 3.2 gives the character table for the group $\boldsymbol{C}_{2v}(M)$.

Each possible wavefunction of a water molecule belongs to one of the irreducible representations A_1, A_2, B_1 oder B_2. Thus, the wavefunction is labeled by "its" irreducible representation.

The Symmetry of PH_3

The CNPI group of the PH_3 molecule is a group of 12 elements that we call $\boldsymbol{G}_{12}$:

$$\begin{aligned}\boldsymbol{G}_{12} = \{&E, (123), (132), (12), (23), (31),\\ &E^*, (123)^*, (132)^*, (12)^*, (23)^*, (31)^*\}\end{aligned} \tag{3.3.125}$$

The rotation–vibration-electronic energy levels of the PH_3 molecule (neglecting nuclear spin) can be labeled with the irreducible representation labels of the group $\boldsymbol{G}_{12}$. The character table of this group is given in Table 3.3.

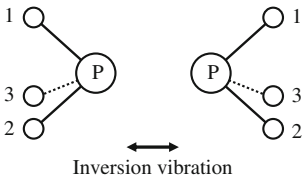

Fig. 3.9 PH_3 inversion

Before we consider the results of this symmetry labeling we should consider the effect of the inversion motion in PH_3. PH_3 has two *versions* (see Bone et al. [33] for a discussion of this concept) of the numbered equilibrium structure of the molecule. An observer sitting on the P nucleus will see the three protons labeled 1–3 so that the rotation from 1 to 2 to 3 is a clockwise rotation for the one version, and an anticlockwise rotation for the other version. The two versions are mirror images of each other and are taken into each other by the inversion operation E^*. On the potential energy surface of the molecule, the two minima corresponding to the two versions are separated by a very high potential barrier ($\approx$11300 cm^{-1}; see Špirko et al. [34]) so that, on the timescale of a typical experiment, there is no observable inversion tunneling splitting. Thus the energy levels can be calculated by just considering the motion in one of the two minima, and we do not need to consider both minima. The two minima have identical sets of rotation–vibration energy levels (Figs. 3.9 and 3.10).

If we were to calculate the rotation–vibration energy levels using the double minimum potential energy surface we would find that well below the barrier, every energy level would be doubly degenerate to within measurement accuracy for PH_3.

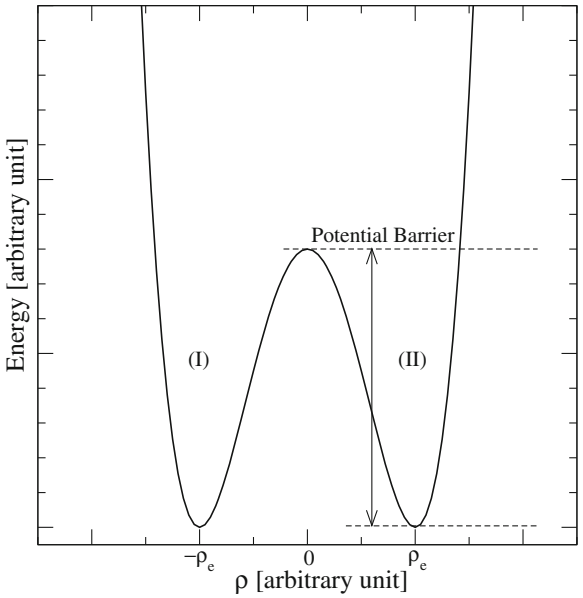

Fig. 3.10 A typical double minimum potential is illustrated. In the case PH_3, the coordinates ρ represents the "inversion" motion shown in Fig. 3.9

Table 3.4 The character table of the molecular symmetry group $\boldsymbol{C}_{3v}(M)$

	E	(123) (132)	(12)* (23)* (31)*
A_1	1	1	1
A_2	1	1	−1
E	2	−1	0

If we symmetry classified the levels using the group $\boldsymbol{G}_{12}$ we would find that there were three types of energy level: $A_1^+ + A_1^-, A_2^+ + A_2^-$, or $E^+ + E^-$. This double degeneracy would be resolved by inversion tunneling and it is an accidental degeneracy not forced by the symmetry group $\boldsymbol{G}_{12}$. If the inversion tunneling is not resolved it is not necessary to use the group $\boldsymbol{G}_{12}$. There are only three distinct types of energy levels and yet we have classified them in a group of six irreducible representations. However, Longuet-Higgins [35] showed how to obtain the appropriate subgroup of $\boldsymbol{G}_{12}$ that avoids the double labels. This is achieved by just using the elements of $\boldsymbol{G}_{12}$ that are appropriate for a single minimum; we delete elements such as E^* and (12) that interconvert the two versions. Longuet-Higgins termed the deleted elements "unfeasible." The group obtained is "the molecular symmetry (MS) group." In the case of PH_3, we obtain the particular MS group

$$\boldsymbol{C}_{3v}(M) = \{E, (123), (132), (12)^*, (23)^*, (31)^*\}. \tag{3.3.126}$$

Here, the operation (123) replaces nucleus 1 by nucleus 2, nucleus 2 by nucleus 3, and nucleus 3 by nucleus 1. The operation (132) replaces nucleus 1 by nucleus 3, nucleus 3 by nucleus 2, and nucleus 2 by nucleus 1. The operations $(12)^*, (23)^*$, and $(31)^*$ are analogous the $(12)^*$ operation considered for water. The character table of $\boldsymbol{C}_{3v}(M)$ is given in Table 3.4. Using this group we achieve a sufficient symmetry labeling of the levels as being either A_1, A_2 or E. All possible interactions can be understood using this group (apart from the effect of inversion tunneling).

For PH_3 we do not save much work by using the MS group rather than the CNPI group, but for larger molecules, such as, for example, benzene, a great simplification is achieved if all unfeasible elements of the CNPI group are eliminated from consideration. An unfeasible element of the CNPI group is one that takes the molecule between versions that are separated by an insuperable energy barrier in the potential energy function. For benzene, the CNPI group has $6! \times 6! \times 2 = 1,036,800$ elements. The MS group that is used to interpret the spectrum has 24 elements.

Ammonia NH_3 is pyramidal like PH_3, and in its electronic ground state there are two versions of the numbered equilibrium structure exactly as for PH_3. The potential barrier between the two versions, however, is around $2,000\,cm^{-1}$ for ammonia (Špirko and Kraemer [36]) and thus much lower than in PH_3. This barrier is so low that the molecule will tunnel through it on the time scale of a typical spectroscopic experiment, and the tunneling motion gives rise to energy

level splittings that can be resolved experimentally (see, for example, Fig. 15-3 of [25]). Thus, for NH_3, all elements of the group $\boldsymbol{G}_{12}$ are feasible, and the molecular symmetry group of NH_3 in its electronic ground state is $\boldsymbol{G}_{12}$. This group is isomorphic to the point group $\boldsymbol{D}_{3h}$ and in the literature it is customarily called $\boldsymbol{D}_{3h}$(M).

3.3.9.2 Selection Rules for Optical Transitions

The intensity of an electric dipole transition (in absorption or emission) is proportional to the square of the integral

$$\int (\psi_n)^* \mu_A \psi_m \mathrm{d}V, \tag{3.3.127}$$

where ψ_n is the rovibronic wavefunction for the initial state of the transition (with energy E_n), ψ_m is the rovibronic wavefunction for the final state (with energy E_m), μ_A is the A component ($A = \xi, \eta, \zeta$, where the $\xi\eta\zeta$ axis system has axes parallel to the laboratory-fixed axes XYZ but origin in the nuclear center of mass) of the molecular dipole moment operator, and $\mathrm{d}V$ is the volume element associated with the rovibronic coordinates.

An important result of representation theory is that the integral in Eq. 3.3.127 can only be non-vanishing (i.e., be different from 0) when the integrand $(\psi_n)^* \mu_A \psi_m$ belongs to the *totally symmetric representation* of the MS group. The totally symmetric representation has the character $+1$ under all group operations, and any group has such a representation which, by convention, is always written in the first line of the character table. A wavefunction that belongs to the totally symmetric representation is unchanged by all group operations. For the group C_{2v}(M) (Table 3.2), A_1 is the totally symmetric representation.

The dipole moment component μ_A always belongs to an irreducible representation with the character $+1$ under all "pure" permutations $(ijk\ldots)$ and the character -1 under all permutation–inversion operations [E^* or $(ijk\ldots)^*$]. For C_{2v}(M) (Table 3.2), this representation is A_2, and any other group has an analogous irreducible representation.

We consider a transition in the water molecule for which the wavefunction ψ_n belongs to the irreducible representation Γ_n of the group $\boldsymbol{C}_{2v}$(M), while ψ_m belongs to the irreducible representation Γ_m. In order that the integrand $(\psi_n)^* \mu_A \psi_m$ can belong to the totally symmetric representation A_1, the product $(\psi_n)^* \psi_m$ must belong to the irreducible representation A_2. Table 3.2 shows that this will be true for $(\Gamma_n, \Gamma_m) = (A_1, A_2)$ or for $(\Gamma_n, \Gamma_m) = (A_2, A_1)$ or for $(\Gamma_n, \Gamma_m) = (B_1, B_2)$ or for $(\Gamma_n, \Gamma_m) = (B_2, B_1)$. These selection rules can be summarized as

$$\begin{aligned} A_1 &\leftrightarrow A_2 \\ B_1 &\leftrightarrow B_2 \end{aligned} \tag{3.3.128}$$

Analogous selection rules can be constructed for any other molecule.

For PH_3, the molecular dipole moment component μ_A has the symmetry A_2 in $\boldsymbol{C}_{3v}$(M) (Table 3.4). The selection rules on the symmetries of the wavefunctions ψ_n and ψ_m are

$$\begin{aligned} A_1 &\leftrightarrow A_2 \\ E &\leftrightarrow E \end{aligned} \tag{3.3.129}$$

The analogous selection rules on the symmetries of the wavefunctions ψ_n and ψ_m for NH_3 are

$$\begin{aligned} A_1^+ &\leftrightarrow A_1^- \\ A_2^+ &\leftrightarrow A_2^- \\ E^+ &\leftrightarrow E^-; \end{aligned} \tag{3.3.130}$$

the appropriate MS group is now $\boldsymbol{G}_{12}$ or $\boldsymbol{D}_{3h}$(M) (Table 3.3), in which the molecular dipole moment component μ_A has the symmetry A_1^-.

For any molecule, the selection rules obtained from MS group symmetry are accompanied by the selection rules obtained from rotational symmetry (i.e., from the fact mentioned above that owing to the isotropy of space, we can rotate an isolated molecule arbitrarily without changing the physical situation). For electric dipole transitions these selection rules are, for any molecule, $\Delta J = J' - J'' = -1$, 0, or 1, and $J' + J'' \leq 1$. Here J'' and J' are the values of the rotational quantum number J for the initial and final states, respectively, of the transition considered.

3.3.10 Appendix to 3.3

3.3.10.1 Rotational Spectra of Linear Molecules

Typical rotational spectra of linear molecules are shown in Fig. 3.11 as a stick-diagram. The line positions and intensities for HCN, HC_3N, HC_5N, HC_7N,

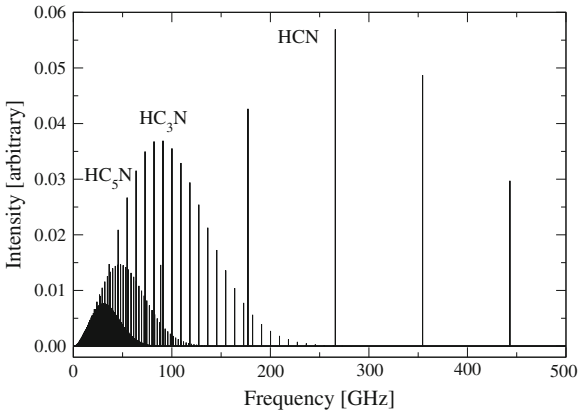

Fig. 3.11 Simulated rotational spectra of linear molecules: HCN, HC_3N, HC_5N, HC_7N, and HC_9N at 20 K

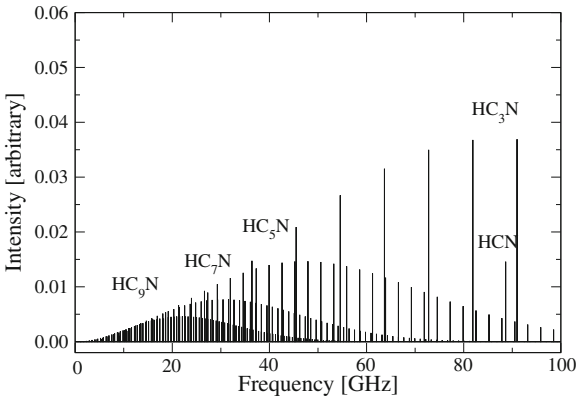

Fig. 3.12 Simulated rotational spectra of linear molecules: HCN, HC_3N, HC_5N, HC_7N, and HC_9N at 20 K: below 100 GHz

and HC_9N are calculated by using PGOPHER,[11] with the rotational constants B, centrifugal distortion constants D, and the permanent dipole moment μ found in literature [37, 38, 39, 40]. The intensities are calculated for $T = 20$ K. The intensities for HCN lines are reduced by a factor 4, because they are too large compared to those of other molecules.

For linear molecules (including diatomic molecules) the line positions for the rotational spectra are given by

$$\nu(J+1 \leftarrow J) = E(J+1) - E(J) \approx 2B(J+1) \tag{3.3.131}$$

for each J, where we assume that the energy and the rotational constant are in frequency unit. Consequently, the spectra are composed of almost equally spaced lines, as shown in the figure. The line intensity increases with the increase of J from 0, reaches the maximum at a value of J depending on the temperature, and then decreases. Details of the intensity calculation are given in textbooks such as [12]. In the figure the spectra of HC_nN with $n > 5$ are very densely overlapped at the low frequency region (0–100 GHz), which are shown in an expanded scale in Fig. 3.12.

3.3.10.2 Asymmetry Parameters

In general, the rotational energies of an asymmetric top cannot be expressed analytically except for a few low J cases (see Table 7.7 of [12]. Nowadays, they can be easily calculated by using a PC with a proper program. In the old days, however, the energy term values of an asymmetric top are calculated (or tabulated) with the help of asymmetry parameter κ (Ray's asymmetry parameter) [5, 12],

[11] A Program for Simulating Rotational Structure, by C.M. Western, University of Bristol. http://pgopher.chem.bris.ac.uk.

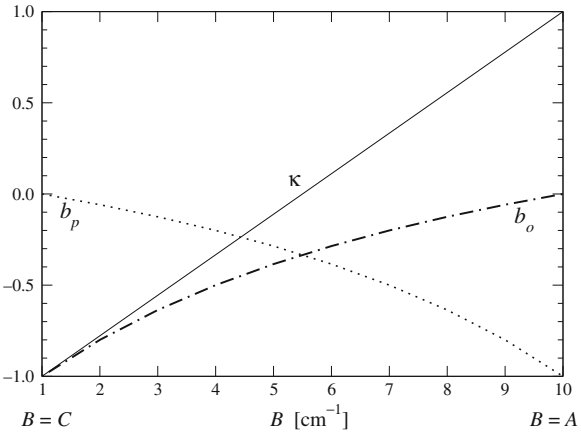

Fig. 3.13 Asymmetry parameters, κ (*solid line*), b_p (*dotted line*), and b_o (*chain line*), are plotted for the case of $A = 10, C = 1$, and $1 \leq B \leq 10\,\mathrm{cm}^{-1}$

$$\kappa = \frac{2B - A - C}{A - C}, \tag{3.3.132}$$

which is -1 and $+1$ at the prolate $(A > B = C)$ and oblate $(A = B > C)$ symmetric top limit, respectively. The relation of the parameter κ with the rotational constants is graphically displayed in Fig. 3.13, for a molecule with $A = 10$ and $C = 1\,\mathrm{cm}^{-1}$: by definition $A \geq B \geq C$.

For the molecules close to the symmetric top limit (near prolate or near oblate symmetric top), the effect of the inertial asymmetry can be evaluated by the perturbation treatment. In such a case it is useful to introduce other asymmetry parameters:

$$b_\mathrm{p} = \frac{C - B}{2A - B - C} \tag{3.3.133}$$

and

$$b_\mathrm{o} = \frac{A - B}{2C - B - A}. \tag{3.3.134}$$

As shown in Fig. 3.13, they take values between 0 and -1 : $b_\mathrm{p} = 0$ at the prolate symmetric top limit, and $b_\mathrm{o} = 0$ at the oblate symmetric top limit. Consequently they can be used as the perturbation parameter near the symmetric top limits.

3.3.10.3 Rotational Energy Level Diagram: H_2CO as an Example

Figure 3.14 shows schematically the energy level diagram of the formaldehyde molecule, H_2CO, which is a near prolate asymmetric top. The energies are calculated as a rigid rotor assuming the rotational constants to be $A = 9.4053, B = 1.22$, and $C = 1.20\,\mathrm{cm}^{-1}$ [41]. All levels with $K_a \neq 0$ are doubled (K-type doubling) due to the inertial asymmetry as indicated.

The molecule is of C_{2v} symmetry, and the a-axis (the molecule-fixed axis along the smallest moment of inertia) coincides with the C_2 symmetry axis, which corresponds to the permutation operation (12), i.e., exchange of the two protons of the molecule (see Sect. 3.3.9).

Since the protons are Fermion of nuclear spin $I = 1/2$, there are four linearly independent nuclear spin states for H_2CO, noting that the nuclear spin is zero for ^{12}C and ^{16}O. Three of them are symmetric and one is anti-symmetric for the symmetry operation (12) [25, 14]. For a single permutation of two identical Fermions, the overall wavefunctions should be anti-symmetric. Thus, for H_2CO, the rotational states which are symmetric to the C_2 operation (even K_a levels of the ground vibronic state[12]) can be combined with the one anti-symmetric nuclear spin state, and the anti-symmetric rotational states (odd K_a levels) can be combined with the three anti-symmetric nuclear spin states. If the effect of the nuclear spin on the energy is small (i.e., the hyperfine splitting is small), then the three different nuclear spin sub-states for a given odd K_a level are energetically degenerate. Consequently, the rotational spectra of H_2CO behaves as if the odd K_a levels were three times more populated than the even K_a levels. Such a effect is called as "nuclear spin statistics" or "nuclear spin weights".

The nuclear spin weight is three for the odd K_a and one for the even K_a. States with larger nuclear spin weight are called *ortho* states and those with less weight are *para* states.

3.3.10.4 Rotational Energy Level Diagram: H_2O as an Example

Figure 3.15 shows schematically the energy level diagram of the water molecule, H_2O, which is a near prolate asymmetric top. The energies are calculated as a rigid rotator assuming the rotational constants to be $A = 27.877, B = 14.512$, and $C = 9.285$ cm^{-1} [42].

The water molecule is also of C_{2v} symmetry, but different from the case of H_2CO, b-axis (the molecule-fixed axis along the intermediate moment of inertia) coincides with the C_2 symmetry axis, which corresponds to the permutation operation (see footnote 12), i.e., exchange of the two protons.

Thus the *ortho* and *para* states are distinguished by the parity of $K_a + K_c$ (see footnote 12), as indicated by solid and broken lines in Fig. 3.15. Since the *ortho* and *para* states are distributed rather randomly, as compared with the case of H_2CO (Fig. 3.14), the *ortho* and *para* levels are often illustrated side-by-side as shown in Fig. 3.16.

[12] It should be noted that the parity of the quantum number K_a indicates the symmetry of the rotational wavefunction for the C_2 rotation about the molecule-fixed a-axis. Similarly K_c indicates that for the C_2 rotation about the molecule-fixed c-axis. Consequently, the symmetry for the C_2 rotation about the molecule-fixed b-axis is indicated by the parity of $K_a + K_c$.

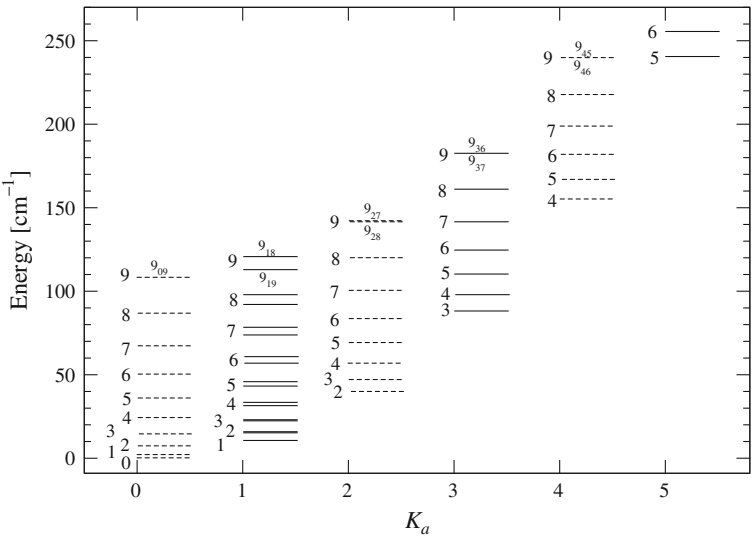

Fig. 3.14 The rotational energy levels of H_2CO in the ground vibronic state are schematically illustrated. The odd K_a levels are *ortho* with the spin weight of three, which are indicated by *solid lines*. The even K_a levels are *para* with the spin weight of one, which are indicated by *broken lines*

3.3.10.5 Pure Rotational Spectra of an Asymmetric Top Molecule: HNCO as an Example

HNCO is an asymmetric top molecule very near prolate symmetric top, and is of planar structure with non-vanishing dipole moment along the a and b-axis.[13] Therefore, we can observe a-type ($\Delta K_a = 0$) and b-type ($\Delta K_a = \pm 1$) transitions. The spectra, which are of a, b-hybrid type, simulated by PGOPHER (see footnote 11) for $T = 50$ K are shown up to 3.5 THz in Fig. 3.17, where the molecular constants given in [43] are used.[14] The lower frame shows the spectra as a stick-diagram, and the upper frame shows the Fortrat diagram, the vertical axis of which represents the J quantum number for the lower level of the transition.

Strong a-type transitions are indicated as ${}^qR_K$ in the lower frame. The notation ${}^xY_z$ is used for indicating the transition, which is defined for symmetric top spectra. The superscript x is p, q, or r for $\Delta K = -1$, 0, or $+1$, respectively. Y is P, Q, or R for $\Delta J = -1$, 0, or $+1$, respectively. The subscript z indicates the quantum number K of the lower level of the transition. For a near prolate symmetric top, K should be read as K_a. The details of the ${}^qR_K$ transitions are illustrated in Fig. 3.18.

---

[13] The molecular plane is the $a - b$ plane.

[14] The Hamiltonian was truncated for simplicity up to the sextic centrifugal correction terms in this simulation. Therefore, it does not reproduce the observed spectrum.

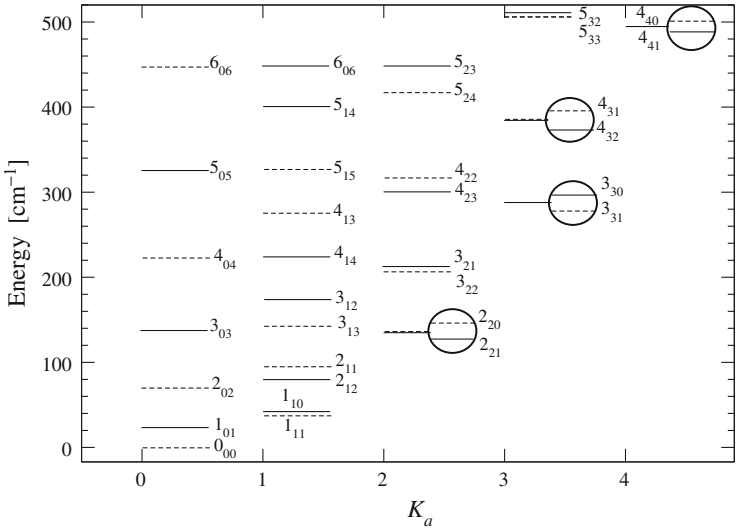

Fig. 3.15 The rotational energy levels of H_2O in the ground vibronic state are schematically illustrated. The *ortho* levels with the spin weight of three, which are indicated by *solid lines*, and *para* levels with the spin weight of one by *broken lines*

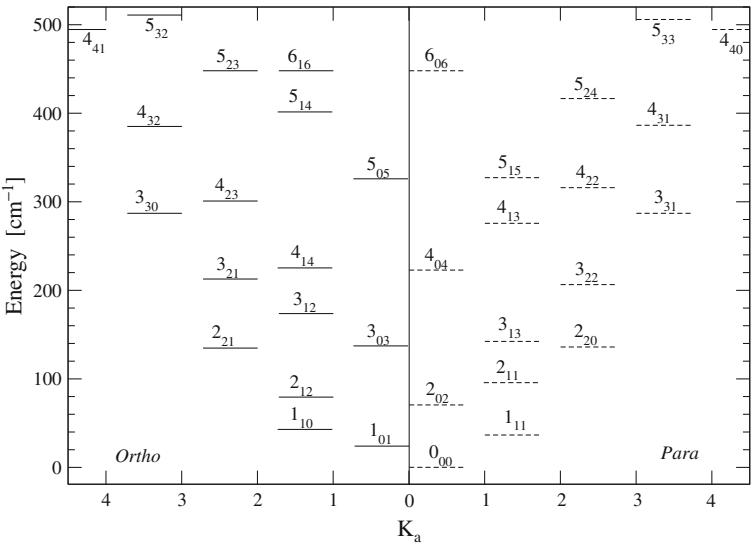

Fig. 3.16 The *ortho* levels of H_2O are illustrated on the *left side*, and the *para* levels on the *right*. Since the conversion between the *ortho* and *para* levels is very slow, we can handle the *ortho* and *para* states as if they are of "different" molecules

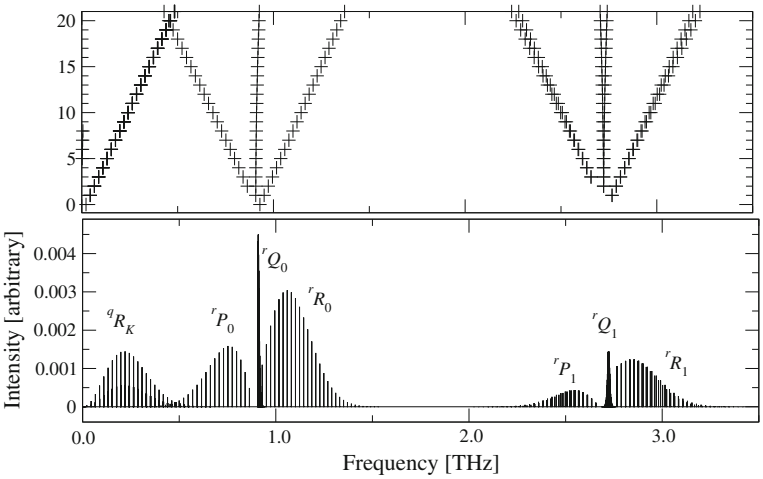

Fig. 3.17 Simulated structures of the a, b-hybrid band of a very near prolate asymmetric top are displayed: the stick-diagram in the *lower frame* and the Fortrat diagram in the *upper frame*

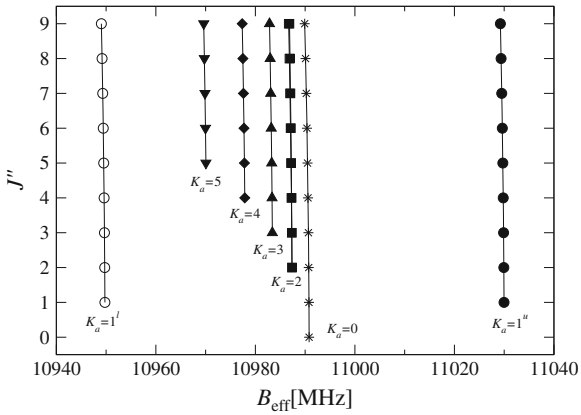

Fig. 3.18 The effective rotational constants $B_{\rm eff}^{(K)}$ defined by Eq. 3.3.137 are plotted for J''

Strong b-type transitions are as indicated there, $^rP_0$,$^r Q_0$,$^r R_0$,$^r P_1$,$^r Q_1$, and $^rR_1$. Because of the K-type doubling, the $K_a = 2 \leftarrow 1$ transitions are doubled as shown in the figure.

3.3.10.6 Effective B Plots

The rotational energy of a symmetric top molecule for can be expressed in the rigid rotor approximation as

$$E(J,K) = E_0^{(K)} + B_{\rm eff}^{(K)} J(J+1) \tag{3.3.135}$$

for each K, where we assume that the energy and the rotational constant are in frequency unit. The frequencies for the transitions of ${}^qR_K(J)$ is thus given by

$$\nu({}^qR_K(J)) = E(J+1,K) - E(J,K) = 2B_{\rm eff}^{(K)}(J+1), \tag{3.3.136}$$

which is similar to Eq. 3.3.131. The effective rotational constant $B_{\rm eff}^{(K)}$ is thus derived from the observed frequencies as

$$B_{\rm eff}^{(K)} = \nu({}^qR_K(J))/[2(J+1)]. \tag{3.3.137}$$

This expression can be applied also for asymmetric top molecules, if they are close to the symmetric top limits, like HNCO or H_2CO.

From the observed a-type R-branch transitions of HNCO the J dependence of the $B_{\rm eff}^{(K)}$ values are displayed in Fig. 3.18, where effective B values are taken from [43]. HNCO is an asymmetric top molecule, and thus because of the K-type doubling, two effective B values can be obtained for $K_a = 1$ as shown there. If the molecule is a true symmetric top, we should have a single effective B value for $K = 1$, the plot of which should appear near the center of the two $K_a = 1$ plots.

This doubling should be observed also for $K_a > 1$. Indeed we can see such doubling for high-J transitions of $K_a = 2$ as shown in Fig. 3.19, where the central part of Fig. 3.18 are presented in an expanded scale. HNCO molecule is very much close to the prolate symmetric top limit, the doubling cannot be observed for $K_a \geq 3$ at least for $J < 10$.

3.3.10.7 Rovibrational Spectra of an Asymmetric Top Molecule: An a-Type Band of a Near Prolate Top

The structure of the ν_2 band of H_2CO looks like[15] the one given in Fig. 3.20 which is simulated by PGOPHER (see footnote 11) for $T = 150$ K with the rigid rotor approximation: the upper frame shows the Fortrat diagram, and the lower the stick-diagram of the spectra.

The ν_2 band of H_2CO corresponds to the vibrational mode of CO stretching, which induce a change of dipole moment along the molecule-fixed a-axis. Thus the band is of a-type; $\Delta K_a = 0$ transitions, ${}^qP_K$,${}^qQ_K$, and ${}^qR_K$, appear strongly as shown there. The spectrum is very similar to that of a parallel band of a prolate symmetric top molecule, except for the K-type doubling effect: an impressive Q-branch transitions at the center, and P and R transitions on both side with almost equal spacing about $2B$.

The spectra can be displayed in a different manner as the "Loomis–Wood" diagram [44] as shown in Fig. 3.21. In this diagram, the spectrum given in Fig. 3.20

[15] It does not reproduces the observed spectrum.

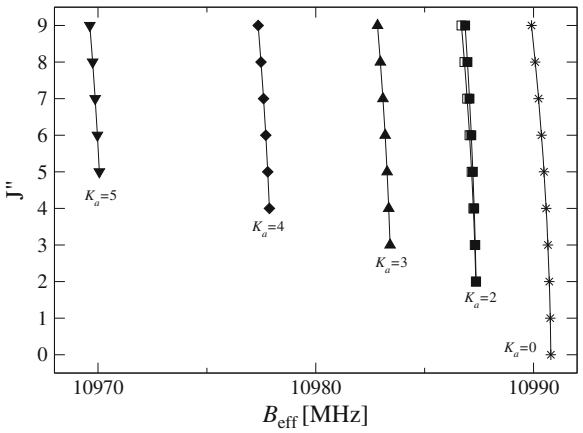

Fig. 3.19 The center part of Fig. 3.18 is plotted in an expanded scale. The K-type doubling effect for the $K_a = 2$ is visible in this figure

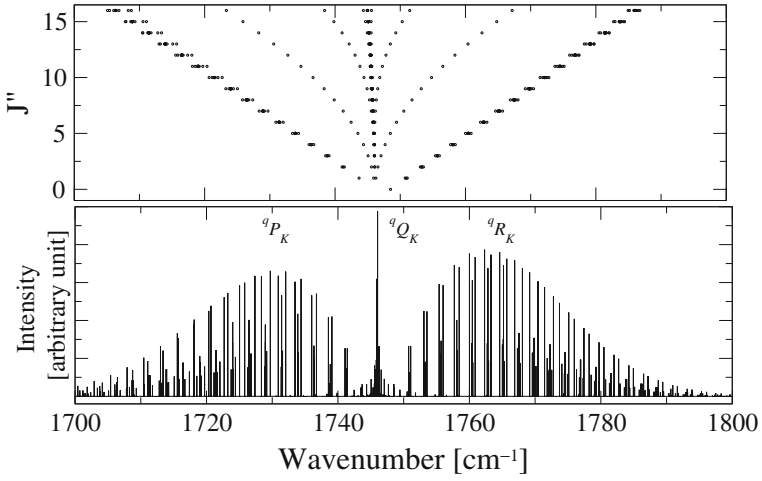

Fig. 3.20 Typical structures of an a-type rovibrational band of a slightly asymmetric top (near prolate) are illustrated. The spectrum is displayed as a stick-diagram in the *lower frame*, and the Fortrat diagram is displayed in the *upper frame*. The spectrum is calculated by applying the rigid rotor approximation with the rotational constants and band origin similar to those of H_2CO ν_2 band

is displayed by plotting the line positions $\nu_i^{(\mathrm{obs})}$ (i for all observed lines) measured from the reference frequencies ν_m, which are usually calculated by

$$\nu_m = a_0 + a_1 m + a_2 m^2, \tag{3.3.138}$$

where $a_0 = 1746.1, a_0 = 2.41706, a_2 = -0.00377\,\mathrm{cm}^{-1}$ in the case of Fig. 3.21. With this diagram (m in the vertical axis, and the $\nu_i^{(\mathrm{obs})} - \nu_m$ in the horizontal axis) we can identify series of lines which appear with a regular frequency spacing of

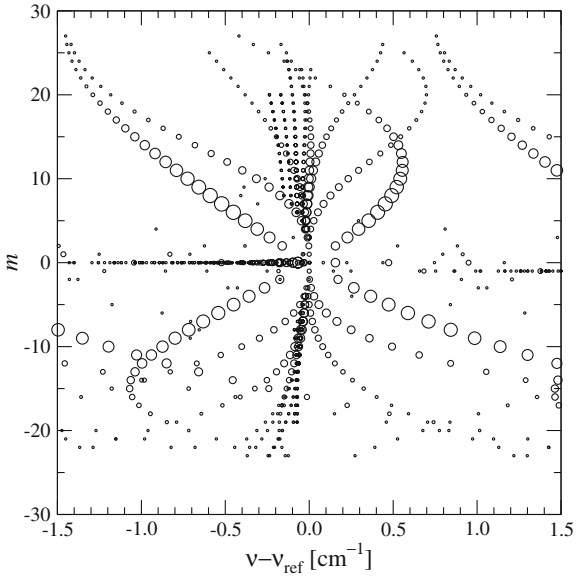

Fig. 3.21 The spectrum given in Fig. 3.20 is displayed as a Loomis Wood diagram. The *circles* represent the line positions. The *line intensities* are represented by the size of the circle

about a_1 which is about 2.4 cm^{-1} in this case. Details of the diagram are described in [45].

3.3.10.8 Rovibrational Spectra of an Asymmetric Top Molecule: A b-Type Band of a Near Prolate Top

The structure of the v_5 band of H_2CO looks like[16] in Fig. 3.22, which is simulated by PGOPHER (see footnote 11) for $T = 150$ K with the rigid rotor approximation: the upper frames of each part of the spectrum shows the Fortrat diagram, and the lower the stick-diagram of the spectra.

The v_5 band of H_2CO corresponds to the vibrational mode of anti-symmetric CH stretching, which induce a change of dipole moment along the molecule-fixed b-axis. Thus the band is of b-type; $\Delta K_a = \pm 1$ transitions, ${}^rP_K, {}^rQ_K, {}^rR_K, {}^pP_K, {}^pQ_K$, and ${}^pR_K$, appear strongly as shown there. The spectrum is very similar to that of a perpendicular band of a prolate symmetric top molecule, except for the K-type doubling effect: impressive ${}^rQ$ and ${}^pQ$ branch transitions appear with almost equal spacing of about $2A$.

The band is widely spread out compared with the a-type band, and it is in general difficult to display with a single Loomis–Wood diagram.

[16] It does not reproduces the observed spectrum.

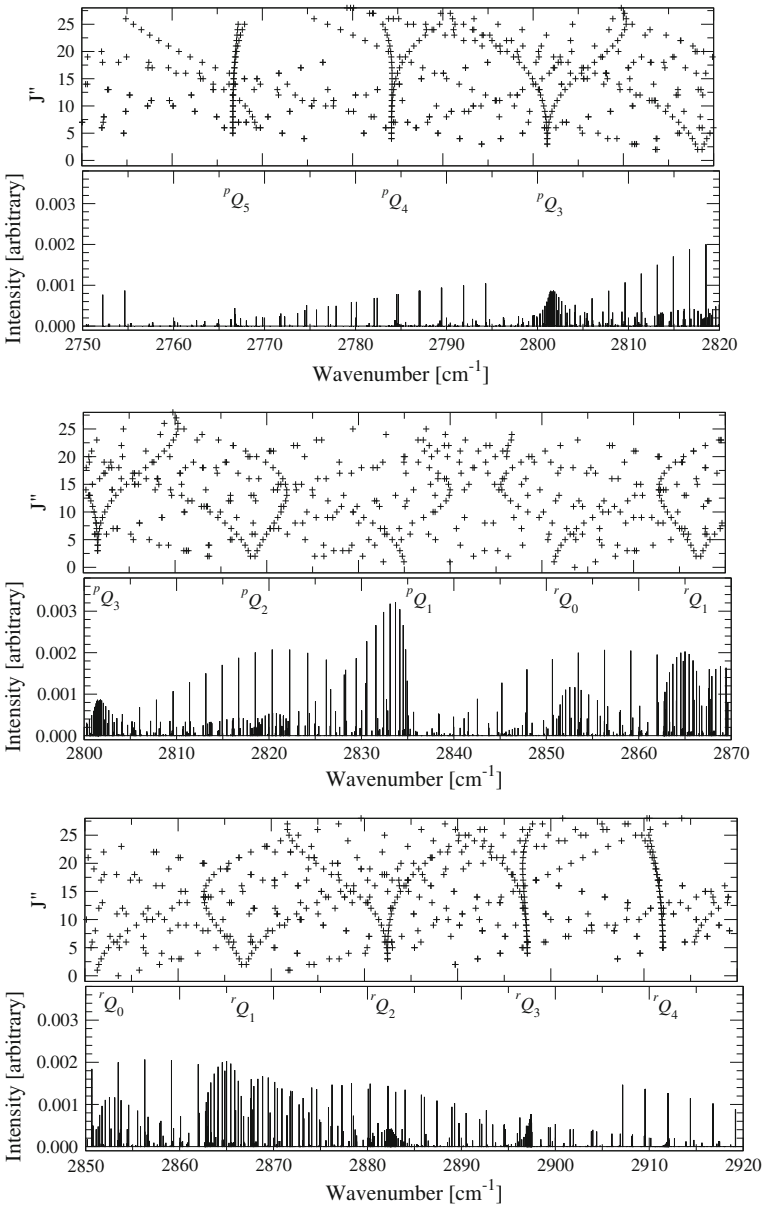

Fig. 3.22 Typical structures of a *b*-type rovibrational band of a slightly asymmetric top (near prolate) are illustrated together with the Fortrat diagram

3.4 Molecules with Internal Rotation

In this section, one- and two-methyl top internal-rotation problems in asymmetric top molecules will be treated. Internal rotation itself, which is a kind of large-amplitude vibrations, is a fascinating theme also for spectroscopists.

Let us consider qualitatively at first what effect the internal rotation produces in the rotational energy level structure and the rotational spectrum. The internal rotation occurring in a free molecule is hindered generally and it is subject to an appropriate potential function. The internal-rotation potential function is periodic, and in the simplest case it is represented by a sinusoidal function, whose amplitude is the barrier height. Two limiting cases of the internal rotation are a free rotor limit, corresponding to an extremely low barrier case, and an extremely high barrier limit.

For understanding aspects of the effect of the internal rotation on the rotational energy level structure, let us start from a hypothetically high barrier limit case, where a small-amplitude torsional motion occurs around a potential minimum. In the extremely high barrier limit, the rotational energy level structure will be the same as that of an ordinary semi-rigid molecule. As the barrier height of the internal-rotation potential is lowered, tunneling motions occurs among equilibrium configurations at the potential minima. A rotational energy level is then split into two levels, *A*-symmetry and *E*-symmetry levels, in a molecule with one methyl internal rotor.

As the barrier height is further lower, the tunneling motions occur more frequently and accordingly the splitting is larger. If the effect of the internal rotation is to induce the splitting to be the same for all the rotational levels in a certain vibrational state, the rotational energy level structure will not be so complicated, and then we will observe only ordinary semi-rigid rotor transitions overlapped for two symmetry species since selection rules are $A \leftrightarrow A$ and $E \leftrightarrow E$.

In reality, since the Coriolis interaction between the overall rotation and the internal rotation exists necessarily and it makes a rotational energy level split into two levels whose interval depends on angular momentum quantum numbers, we observe somewhat complicated rotational spectra such as a rotational spectral line is split into two lines whose interval depends on the rotational transition.

For group theoretical treatments of flexible molecules such as those with internal rotors, it is appropriate to use the permutation–inversion group proposed by Longuet-Higgins [35]. Throughout this section the group theoretical description will be made using the permutation–inversion group. In this section, molecules only with methyl internal rotors which can be described by a single group of the permutation–inversion group will be treated, and internal rotations in molecules such as CH_3-CH_3, H_2O_2 and H_2S_2, which should be described in a specially designed method including a double group idea of the permutation inversion group, are not treated.

We describe below mainly the formulation for understanding high-resolution torsional–rotational spectra and helping to analyze them.

3.4.1 Molecule with One Methyl Internal Rotor

3.4.1.1 Torsion–Rotation Hamiltonian Operator

At first we note that *torsion* is used to represent *internal rotation* sometimes in Sect. 3.4. The purpose of this section is to show a procedure for deriving a Hamiltonian operator for molecules with one methyl internal rotor. In literatures, we find that three approaches to the problem, which are called PAM (principal axis method), RAM (rho axis method) and IAM (internal axis method), have been developed. The difference among the three methods lies in the choice of the reference configuration, in other words, which coordinate system is taken to describe the torsional and rotational motion. Referring to the paper of Hougen et al. [46], where the three approaches are summarized systematically, we review the three methods below.

Principal Axis Methods

It is conceptually convenient to describe the principal axis method (PAM) first for defining a coordinate system and deriving a Hamiltonian operator. The laboratory-fixed coordinate $\boldsymbol{R}_i, (X_i, Y_i, Z_i)$, of the ith atom in the molecule with a methyl top rotor is expressed in a PAM system as follows:

$$\begin{aligned}\boldsymbol{R}_i &= \boldsymbol{R} + S^{-1}(\theta,\phi,\chi)S^{-1}(\theta_{\mathrm{P}},\phi_{\mathrm{P}},\chi_{\mathrm{P}})\left\{S^{-1}(0,0,\tau)[\boldsymbol{a}_i+\boldsymbol{d}_i]-\boldsymbol{A}\right\}\\ &= \boldsymbol{R} + S^{-1}(\theta,\phi,\chi)\boldsymbol{r}_i^{\mathrm{PAM}},\end{aligned} \tag{3.4.1}$$

for methyl protons (i.e., $i = 1, 2$ and 3), and

$$\begin{aligned}\boldsymbol{R}_j &= \boldsymbol{R} + S^{-1}(\theta,\phi,\chi)S^{-1}(\theta_{\mathrm{P}},\phi_{\mathrm{P}},\chi_{\mathrm{P}})\left\{\left[\boldsymbol{a}_j+\boldsymbol{d}_j\right]-\boldsymbol{A}\right\}\\ &= \boldsymbol{R} + S^{-1}(\theta,\phi,\chi)\boldsymbol{r}_j^{\mathrm{PAM}},\end{aligned} \tag{3.4.2}$$

for other nuclei.

Before denoting various symbols appearing in Eqs. 3.4.1 and 3.4.2, we give the definition of three axis systems $(X, Y, Z), (x', y', z')$ and (x, y, z) used implicitly:

X, Y, Z: the laboratory-fixed axis system,
x', y', z': the molecule-fixed axis system, where the z'-axis is along the C_3 axis of the methyl top,
x, y, z: the molecule-fixed principal inertial axis system (usually, $a, b, c \leftrightarrow z, x, y$).

The vectors $\boldsymbol{R}_i, \boldsymbol{R}, \boldsymbol{a}_i, \boldsymbol{d}_i$ and $\boldsymbol{A}$ in Eqs. 3.4.1 and 3.4.2 are defined as follows:

$\boldsymbol{R}_i$: the position vector of the ith atom expressed in the laboratory-fixed system.
$\boldsymbol{R}$: the laboratory-fixed coordinates of the center of mass of the molecule.
$\boldsymbol{a}_i$: the equilibrium position of the ith atom expressed in the molecule-fixed $x'y'z'$-system.

$\boldsymbol{d}_i$: the small-amplitude displacement vector of the ith atom expressed in the molecule-fixed $x'y'z'$-system.
$\boldsymbol{A}$: the center of mass expressed in the $x'y'z'$-system.

The rotation matrix $S^{-1}(0,0,\tau)$ rotates the equilibrium positions and displacement vectors of methyl protons through an angle τ about the z'-axis. The constant rotation matrix $S^{-1}(\theta_P,\phi_P,\chi_P)$ is introduced so that the reference positions $S^{-1}(0,0,\tau)[\boldsymbol{a}_i+\boldsymbol{d}_i]$ for the methyl protons and $[\boldsymbol{a}_j+\boldsymbol{d}_j]$ for the other nuclei are located in the principal axis system x,y,z. When we assume the methyl top is of $\boldsymbol{C}_{3v}$ symmetry, $\boldsymbol{A}$ and $S^{-1}(\theta_P,\phi_P,\chi_P)$ are constant, and we have

$$S^{-1}(0,0,2\pi/3)\boldsymbol{a}_1=\boldsymbol{a}_2,\ S^{-1}(0,0,2\pi/3)\boldsymbol{a}_2=\boldsymbol{a}_3,\ S^{-1}(0,0,2\pi/3)\boldsymbol{a}_3=\boldsymbol{a}_1. \quad (3.4.3)$$

The rotation matrix S^{-1} used in the equations above is the usual 3×3 direction cosine matrix defined as

$$S^{-1}(\theta,\phi,\chi)=\begin{pmatrix}\cos\phi & -\sin\phi & 0\\ \sin\phi & \cos\phi & 0\\ 0 & 0 & 1\end{pmatrix}\begin{pmatrix}\cos\theta & 0 & \sin\theta\\ 0 & 1 & 0\\ -\sin\theta & 0 & \cos\theta\end{pmatrix}\begin{pmatrix}\cos\chi & -\sin\chi & 0\\ \sin\chi & \cos\chi & 0\\ 0 & 0 & 1\end{pmatrix}. \quad (3.4.4)$$

Classical Kinetic Energy Expression. The first step for deriving a Hamiltonian operator is to express a classical nuclear kinetic energy with internal variables. The classical nuclear kinetic energy is a sum over the kinetic energies of individual atoms within a molecule:

$$T=\sum_i\frac{1}{2}m_i\left[\left(\frac{\mathrm{d}\boldsymbol{R}_i}{\mathrm{d}t}\right)_x^2+\left(\frac{\mathrm{d}\boldsymbol{R}_i}{\mathrm{d}t}\right)_y^2+\left(\frac{\mathrm{d}\boldsymbol{R}_i}{\mathrm{d}t}\right)_z^2\right]. \quad (3.4.5)$$

In the present treatment, we ignore the translational energy and the small-amplitude vibrational energy, which are related to $\boldsymbol{R}$ and $\boldsymbol{d}_i$ in Eqs. 3.4.1 and 3.4.2, respectively. Then we have the following expression of the velocity vector for the methyl protons after an algebraic manipulation,

$$\begin{aligned}\begin{bmatrix}\left(\frac{\mathrm{d}\boldsymbol{R}_i}{\mathrm{d}t}\right)_x\\ \left(\frac{\mathrm{d}\boldsymbol{R}_i}{\mathrm{d}t}\right)_y\\ \left(\frac{\mathrm{d}\boldsymbol{R}_i}{\mathrm{d}t}\right)_z\end{bmatrix}&=S(\theta,\phi,\chi)\begin{bmatrix}\left(\frac{\mathrm{d}\boldsymbol{R}_i}{\mathrm{d}t}\right)_X\\ \left(\frac{\mathrm{d}\boldsymbol{R}_i}{\mathrm{d}t}\right)_Y\\ \left(\frac{\mathrm{d}\boldsymbol{R}_i}{\mathrm{d}t}\right)_Z\end{bmatrix}=S(\theta,\phi,\chi)\left[\frac{\mathrm{d}}{\mathrm{d}t}S^{-1}(\theta,\phi,\chi)\right]\boldsymbol{r}_i^{\mathrm{PAM}}\\ &\quad+\left\{\frac{\mathrm{d}}{\mathrm{d}t}\left[S^{-1}(\theta_P,\phi_P,\chi_P)S^{-1}(0,0,\tau)\right]\right\}\boldsymbol{a}_i\\ &=\begin{bmatrix}\left(\boldsymbol{\omega}\times\boldsymbol{r}_i^{\mathrm{PAM}}\right)_x\\ \left(\boldsymbol{\omega}\times\boldsymbol{r}_i^{\mathrm{PAM}}\right)_y\\ \left(\boldsymbol{\omega}\times\boldsymbol{r}_i^{\mathrm{PAM}}\right)_z\end{bmatrix}+\begin{bmatrix}\left(\dot{\tau}\boldsymbol{e}_{\mathrm{int}}\times\boldsymbol{r}_i'^{\mathrm{PAM}}\right)_x\\ \left(\dot{\tau}\boldsymbol{e}_{\mathrm{int}}\times\boldsymbol{r}_i'^{\mathrm{PAM}}\right)_y\\ \left(\dot{\tau}\boldsymbol{e}_{\mathrm{int}}\times\boldsymbol{r}_i'^{\mathrm{PAM}}\right)_z\end{bmatrix}\end{aligned} \quad (3.4.6)$$

where $\boldsymbol{r}_i'^{\mathrm{PAM}}$ is the position vector of the ith methyl-proton in the xyz-axis system from the center of mass of the methyl group

$$\boldsymbol{r}_i'^{\mathrm{PAM}} = \boldsymbol{r}_i^{\mathrm{PAM}} + S^{-1}(\theta_{\mathrm{P}}, \phi_{\mathrm{P}}, \chi_{\mathrm{P}})\boldsymbol{A}. \tag{3.4.7}$$

For the other nuclei, we have

$$\begin{bmatrix} \left(\frac{\mathrm{d}\boldsymbol{R}_j}{\mathrm{d}t}\right)_x \\ \left(\frac{\mathrm{d}\boldsymbol{R}_j}{\mathrm{d}t}\right)_y \\ \left(\frac{\mathrm{d}\boldsymbol{R}_j}{\mathrm{d}t}\right)_z \end{bmatrix} = \begin{bmatrix} \left(\boldsymbol{\omega} \times \boldsymbol{r}_j^{\mathrm{PAM}}\right)_x \\ \left(\boldsymbol{\omega} \times \boldsymbol{r}_j^{\mathrm{PAM}}\right)_y \\ \left(\boldsymbol{\omega} \times \boldsymbol{r}_j^{\mathrm{PAM}}\right)_z \end{bmatrix}, \tag{3.4.8}$$

where $\boldsymbol{\omega}$, angular velocity vector representing the overall rotation of the molecule; and $\boldsymbol{e}_{\mathrm{int}}$, unit vector along the methyl internal rotation, which is the C_3 axis because we assume the methyl top to be of $\boldsymbol{C}_{3v}$ symmetry.

Substituting Eqs. 3.4.6 and 3.4.8 into Eq. 3.4.5 we have

$$T = \frac{1}{2}\sum_{\alpha=x,y,z} I_\alpha \omega_\alpha^2 + \frac{1}{2} I_\tau \dot{\tau}^2 + I_\tau \dot{\tau} \sum_{\alpha=x,y,z} \lambda_\alpha \omega_\alpha, \tag{3.4.9}$$

where $I_\alpha\,(\alpha = x, y, z)$ are the principal moments of inertia of the molecule, I_τ is the moment of inertia of the methyl top about the C_3 axis, and $\lambda_\alpha(\alpha = x, y, z)$ are the direction cosines of the methyl internal-rotation axis. For obtaining the quantum mechanical Hamiltonian operator, it is necessary to express the classical kinetic energy in the momenta conjugate to the variables representing the overall rotation and the methyl internal rotation. The momenta are

$$J_\alpha = \frac{\partial T}{\partial \omega_\alpha} = I_\alpha \omega_\alpha + I_\tau \lambda_\alpha \dot{\tau} \quad (\alpha = x, y, z) \tag{3.4.10}$$

$$p_\tau = \frac{\partial T}{\partial \dot{\tau}} = I_\tau \dot{\tau} + I_\tau \sum_{\alpha=x,y,z} \lambda_\alpha \omega_\alpha. \tag{3.4.11}$$

By using the definitions

$$\rho_\alpha \equiv \frac{\lambda_\alpha I_\tau}{I_\alpha},\ r \equiv 1 - \sum_{\alpha=x,y,z} \rho_\alpha \lambda_\alpha \tag{3.4.12}$$

and Eqs. 3.4.10 and 3.4.11, we have

$$p_\tau - \sum_{\alpha=x,y,z} \rho_\alpha J_\alpha = I_\tau \left(1 - \sum_{\alpha=x,y,z} \rho_\alpha \lambda_\alpha\right)\dot{\tau} = r I_\tau \dot{\tau}. \tag{3.4.13}$$

From Eqs. 3.4.9, 3.4.10, 3.4.11 and 3.4.13, we have

$$T = \sum_{\alpha=x,y,z} \frac{1}{2I_\alpha} J_\alpha^2 + \frac{1}{2rI_\tau}\left(p_\tau - \sum_{\alpha=x,y,z} \rho_\alpha J_\alpha\right)^2 \tag{3.4.14}$$

Quantum Mechanical Hamiltonian Operator. The quantum mechanical PAM Hamiltonian operator is obtained by adding the potential function $V(\tau)$ to T, that is,

$$H_{\mathrm{PAM}} = \sum_{\alpha=x,y,z} \frac{1}{2I_\alpha} J_\alpha^2 + \frac{1}{2rI_\tau} \left(p_\tau - \sum_{\alpha=x,y,z} \rho_\alpha J_\alpha \right)^2 + V(\tau), \tag{3.4.15}$$

where $J_\alpha\,(\alpha = x, y, z)$ are the total angular momentum operators and p_τ the internal-rotation angular momentum operator ($J_z = -i\hbar \frac{\partial}{\partial \chi}$, etc. and $p_\tau = -i\hbar \frac{\partial}{\partial \tau}$).

Rho Axis Method

The laboratory-fixed coordinate in the RAM coordinate system, $\boldsymbol{R}_k$, is expressed as

$$\boldsymbol{R}_k = \boldsymbol{R} + S^{-1}(\theta, \phi, \chi) S^{-1}(-\theta_{\mathrm{RAM}}, -\phi_{\mathrm{RAM}}, -\chi_{\mathrm{RAM}}) \boldsymbol{r}_k^{\mathrm{PAM}}, \tag{3.4.16}$$

where

$$\boldsymbol{r}_k^{\mathrm{PAM}} = S^{-1}(\theta_{\mathrm{P}}, \phi_{\mathrm{P}}, \chi_{\mathrm{P}}) \left\{ S^{-1}(0, 0, \tau)[\boldsymbol{a}_k + \boldsymbol{d}_k] - \boldsymbol{A} \right\} \tag{3.4.17}$$

for the methyl protons, and

$$\boldsymbol{r}_k^{\mathrm{PAM}} = S^{-1}(\theta_{\mathrm{P}}, \phi_{\mathrm{P}}, \chi_{\mathrm{P}}) \{ [\boldsymbol{a}_k + \boldsymbol{d}_k] - \boldsymbol{A} \} \tag{3.4.18}$$

for the other nuclei.

The rotation matrix $S^{-1}(-\theta_{\mathrm{RAM}}, -\phi_{\mathrm{RAM}}, -\chi_{\mathrm{RAM}})$ introduced in Eq. 3.4.16 transforms angular momentum component operators J_x, J_y, J_z, in such a way that

$$\begin{bmatrix} J_x \\ J_y \\ J_z \end{bmatrix}_{\mathrm{RAM}} = S^{-1}(-\theta_{\mathrm{RAM}}, -\phi_{\mathrm{RAM}}, -\chi_{\mathrm{RAM}}) \begin{bmatrix} J_x \\ J_y \\ J_z \end{bmatrix}_{\mathrm{PAM}} \tag{3.4.19}$$

or

$$\begin{bmatrix} J_x \\ J_y \\ J_z \end{bmatrix}_{\mathrm{PAM}} = S^{+1}(-\theta_{\mathrm{RAM}}, -\phi_{\mathrm{RAM}}, -\chi_{\mathrm{RAM}}) \begin{bmatrix} J_x \\ J_y \\ J_z \end{bmatrix}_{\mathrm{RAM}}. \tag{3.4.20}$$

The Eulerian angles $(-\theta_{\mathrm{RAM}}, -\phi_{\mathrm{RAM}}, -\chi_{\mathrm{RAM}})$ are taken so that the transformation shown in Eq. 3.4.19 or 3.4.20 leads to

$$\sum_{\alpha=x,y,z} \rho_\alpha J_\alpha \rightarrow \rho J_z, \ \left(\rho = \sqrt{\rho_x^2 + \rho_y^2 + \rho_z^2} \right). \tag{3.4.21}$$

As a result, the RAM Hamiltonian operator is written by

$$H_{\mathrm{RAM}} = \sum_{\alpha=x,y,z} \frac{1}{2I_{\alpha\beta}} \frac{1}{2} \left[J_\alpha J_\beta + J_\beta J_\alpha \right] + F(p_\tau - \rho J_z)^2 + V(\tau), \tag{3.4.22}$$

Using the transformation relation of the angular momentum

$$\begin{aligned} & e^{-i\phi_{\mathrm{RAM}} J_z/\hbar} e^{-i\theta_{\mathrm{RAM}} J_y/\hbar} e^{-i\chi_{\mathrm{RAM}} J_z/\hbar} \begin{bmatrix} J_x \\ J_y \\ J_z \end{bmatrix} e^{i\chi_{\mathrm{RAM}} J_z/\hbar} e^{i\theta_{\mathrm{RAM}} J_y/\hbar} e^{i\phi_{\mathrm{RAM}} J_z/\hbar} \\ & \qquad = S^{+1}(-\theta_{\mathrm{RAM}}, -\phi_{\mathrm{RAM}}, -\chi_{\mathrm{RAM}}) \begin{bmatrix} J_x \\ J_y \\ J_z \end{bmatrix}, \end{aligned} \tag{3.4.23}$$

and the relations

$$e^{-i\phi_{\mathrm{RAM}} J_z/\hbar} e^{-i\theta_{\mathrm{RAM}} J_y/\hbar} e^{-i\chi_{\mathrm{RAM}} J_z/\hbar} p_\tau e^{i\chi_{\mathrm{RAM}} J_z/\hbar} e^{i\theta_{\mathrm{RAM}} J_y/\hbar} e^{i\phi_{\mathrm{RAM}} J_z/\hbar} = p_\tau \tag{3.4.24}$$

$$e^{-i\phi_{\mathrm{RAM}} J_z/\hbar} e^{-i\theta_{\mathrm{RAM}} J_y/\hbar} e^{-i\chi_{\mathrm{RAM}} J_z/\hbar} V(\tau) e^{i\chi_{\mathrm{RAM}} J_z/\hbar} e^{i\theta_{\mathrm{RAM}} J_y/\hbar} e^{i\phi_{\mathrm{RAM}} J_z/\hbar} = V(\tau) \tag{3.4.25}$$

we have a relation between the PAM and the RAM Hamiltonian operators

$$H_{\mathrm{RAM}} = e^{-i\phi_{\mathrm{RAM}} J_z/\hbar} e^{-i\theta_{\mathrm{RAM}} J_y/\hbar} e^{-i\chi_{\mathrm{RAM}} J_z/\hbar} H_{\mathrm{PAM}} e^{i\chi_{\mathrm{RAM}} J_z/\hbar} e^{i\theta_{\mathrm{RAM}} J_y/\hbar} e^{i\phi_{\mathrm{RAM}} J_z/\hbar}. \tag{3.4.26}$$

The relation (3.4.23) is derived from the commutation relations

$$\begin{aligned} e^{-i\chi_{\mathrm{RAM}} J_z/\hbar} \left[J_x \pm i J_y \right] e^{i\chi_{\mathrm{RAM}} J_z/\hbar} &= e^{\pm i\chi_{\mathrm{RAM}}} \left[J_x \pm i J_y \right] \\ e^{-i\theta_{\mathrm{RAM}} J_y/\hbar} \left[J_z \pm i J_x \right] e^{i\theta_{\mathrm{RAM}} J_y/\hbar} &= e^{\pm i\theta_{\mathrm{RAM}}} \left[J_z \pm i J_x \right] \\ e^{-i\phi_{\mathrm{RAM}} J_z/\hbar} \left[J_x \pm i J_y \right] e^{i\phi_{\mathrm{RAM}} J_z/\hbar} &= e^{\pm i\phi_{\mathrm{RAM}}} \left[J_x \pm i J_y \right]. \end{aligned} \tag{3.4.27}$$

See Appendix (Sect. 3.4.5) for the derivation of Eq. 3.4.27.

Consider a molecule having a plane of symmetry such as methanol (CH_3OH). Assuming the symmetry plane to be the xz plane, we have $\chi_{\mathrm{RAM}} = 0$, $\phi_{\mathrm{RAM}} = 0$, $\rho_y = 0$, and

$$\begin{aligned} & e^{-i\phi_{\mathrm{RAM}} J_z/\hbar} e^{-i\theta_{\mathrm{RAM}} J_y/\hbar} e^{-i\chi_{\mathrm{RAM}} J_z/\hbar} \\ & \quad \left[\rho_x p_\tau J_x + \rho_z p_\tau J_z \right] e^{i\chi_{\mathrm{RAM}} J_z/\hbar} e^{i\theta_{\mathrm{RAM}} J_y/\hbar} e^{i\phi_{\mathrm{RAM}} J_z/\hbar} \\ & = e^{-i\theta_{\mathrm{RAM}} J_y/\hbar} \left[\rho_x p_\tau J_x + \rho_z p_\tau J_z \right] e^{i\theta_{\mathrm{RAM}} J_y/\hbar} \\ & = (\cos\theta_{\mathrm{RAM}}) \rho_x p_\tau J_x + (\sin\theta_{\mathrm{RAM}}) \rho_x p_\tau J_z + (\cos\theta_{\mathrm{RAM}}) \rho_z p_\tau J_z - (\sin\theta_{\mathrm{RAM}}) \rho_z p_\tau J_x. \end{aligned} \tag{3.4.28}$$

For arriving at

$$e^{-i\theta_{\mathrm{RAM}} J_y/\hbar} \left[\rho_x p_\tau J_x + \rho_z p_\tau J_z \right] e^{i\theta_{\mathrm{RAM}} J_y/\hbar} = \rho p_\tau J_z$$

$$\rho = \sqrt{\rho_x^2 + \rho_z^2}$$

the Eulerian angle θ_{RAM} satisfies

$$\tan\theta_{\mathrm{RAM}} = \frac{\rho_x}{\rho_z}. \tag{3.4.29}$$

Then the RAM Hamiltonian operator is written as

$$\begin{aligned} H_{\mathrm{RAM}} &= F(p_\tau - \rho J_z)^2 + V(\tau) \\ &\quad + A(\cos\theta_{\mathrm{RAM}} J_z - \sin\theta_{\mathrm{RAM}} J_x)^2 + B(\sin\theta_{\mathrm{RAM}} J_z + \cos\theta_{\mathrm{RAM}} J_x)^2 + C J_y^2, \end{aligned} \tag{3.4.30}$$

Internal Axis Method

The IAM Hamiltonian operator is obtained by a unitary transformation of the RAM Hamiltonian

$$H_{\mathrm{IAM}} = e^{-i\tau\rho J_z/\hbar} H_{\mathrm{RAM}} e^{i\tau\rho J_z/\hbar} \tag{3.4.31}$$

so as to remove the term $2F\rho p_\tau J_z$ in the RAM Hamiltonian operator. The relations

$$e^{-i\tau\rho J_z/\hbar}\left[J_x \pm iJ_y\right]e^{i\tau\rho J_z/\hbar} = e^{\pm i\tau\rho}\left[J_x \pm iJ_y\right], \tag{3.4.32}$$

$$e^{-i\tau\rho J_z/\hbar} J_z e^{i\tau\rho J_z/\hbar} = J_z, \tag{3.4.33}$$

$$e^{-i\tau\rho J_z/\hbar} p_\tau e^{i\tau\rho J_z/\hbar} = p_\tau + \rho J_z, \tag{3.4.34}$$

$$e^{-i\tau\rho J_z/\hbar} V(\tau) e^{i\tau\rho J_z/\hbar} = V(\tau), \tag{3.4.35}$$

lead to the removal of the term $2F\rho p_\tau J_z$.

It is shown from Eq. 3.4.30 and Eqs. 3.4.31–3.4.35 that in the case of a molecule having a plane of symmetry, the IAM Hamiltonian operator is given by

$$\begin{aligned} H_{\mathrm{IAM}} &= F p_\tau^2 + V(\tau) \\ &\quad + A\left\{\cos\theta_{\mathrm{RAM}} J_z - \sin\theta_{\mathrm{RAM}}\left[(\cos\rho\tau)J_x - (\sin\rho\tau)J_y\right]\right\}^2 \\ &\quad + B\left\{\sin\theta_{\mathrm{RAM}} J_z + \cos\theta_{\mathrm{RAM}}\left[(\cos\rho\tau)J_x - (\sin\rho\tau)J_y\right]\right\}^2 \\ &\quad + C\left[(\sin\rho\tau)J_x + (\cos\rho\tau)J_y\right]^2. \end{aligned} \tag{3.4.36}$$

The IAM coordinates, corresponding to the IAM Hamiltonian operator given by Eq. 3.4.31, are expressed as

$$\begin{aligned} \boldsymbol{R}_k &= \boldsymbol{R} + e^{-i\tau\rho J_z/\hbar} S^{-1}(\theta,\phi,\chi) e^{i\tau\rho J_z/\hbar} \boldsymbol{r}_k^{\mathrm{RAM}} \\ &= \boldsymbol{R} + S^{-1}(\theta,\phi,\chi) S^{-1}(0,0,-\rho\tau)\boldsymbol{r}_k^{\mathrm{RAM}}, \end{aligned} \tag{3.4.37}$$

where

$$\boldsymbol{r}_k^{\mathrm{RAM}} = S^{-1}(-\theta_{\mathrm{RAM}}, -\phi_{\mathrm{RAM}}, -\chi_{\mathrm{RAM}}) S^{-1}(\theta_{\mathrm{P}}, \phi_{\mathrm{P}}, \chi_{\mathrm{P}})\left\{S^{-1}(0,0,\tau)[\boldsymbol{a}_k + \boldsymbol{d}_k] - \boldsymbol{A}\right\} \tag{3.4.38}$$

for the methyl protons, and

$$\boldsymbol{r}_k^{\mathrm{RAM}} = S^{-1}(-\theta_{\mathrm{RAM}}, -\phi_{\mathrm{RAM}}, -\chi_{\mathrm{RAM}})S^{-1}(\theta_{\mathrm{P}}, \phi_{\mathrm{P}}, \chi_{\mathrm{P}})\{[\boldsymbol{a}_k + \boldsymbol{d}_k] - \boldsymbol{A}\} \quad (3.4.39)$$

for the other nuclei.

It can be understood that Eqs. 3.4.32 and 3.4.33, together with the equation

$$\begin{bmatrix} J_x \\ J_y \\ J_z \end{bmatrix} = S^{+1}(\theta, \phi, \chi) \begin{bmatrix} J_X \\ J_Y \\ J_Z \end{bmatrix}, \quad (3.4.40)$$

and the commutation relation

$$[J_\alpha, J_i] = 0 \quad (\alpha = x, y, z; i = X, Y, Z) \quad (3.4.41)$$

lead mathematically to the equations for the IAM coordinates, (3.4.37), (3.4.38) and (3.4.39) (see Appendix, Sect. 3.4.5).

The physical meaning of the IAM system is seen from Eqs. 3.4.36 and 3.4.37 to be that, by rotating the whole molecule backward about the ρ direction (the z direction in the RAM system), the angular momentum generated by the methyl internal rotation is canceled and as a result the Coriolis-like $2F\rho p_\tau J_z$ term is eliminated from the Hamiltonian operator.

3.4.1.2 Permutation–Inversion (PI) Group and Transformation Properties of Variables Under Permutation–Inversion Operations

We assume that in a molecule under consideration a methyl internal rotation is the only large-amplitude vibration mode. We will treat the following three cases.

1. The molecule has no geometric symmetry at its equilibrium, and the PI group which belongs to is $\boldsymbol{G}_3$. The symmetry of such a molecule is denoted as $\boldsymbol{C}_1(\boldsymbol{G}_3)$.
2. The molecule has a plane of symmetry at its equilibrium configuration, and the PI group which belongs to is $\boldsymbol{G}_6$. The symmetry of such a molecule is denoted as $\boldsymbol{C}_s(\boldsymbol{G}_6)$.
3. The molecule is of CH_3-BF_2 type. It is of $\boldsymbol{C}_s$ symmetry at its equilibrium, and it belongs to the PI group $\boldsymbol{G}_{12}$. The symmetry of such a molecule is denoted as $\boldsymbol{C}_s(\boldsymbol{G}_{12})$.

$\boldsymbol{C}_1(\boldsymbol{G}_3)$ Case

Alanine $CH_3CH(COOH)NH_2$ shown in Fig. 3.23, for an example, corresponds to this case. In Table 3.5, the character table of the PI group $\boldsymbol{G}_3$ for a $\boldsymbol{C}_1(\boldsymbol{G}_3)$ molecule is given. In Table 3.5, 1–3 represent protons in the methyl group. (123) and (132) $[= (123)^2]$ are symmetry operations which become feasible by the

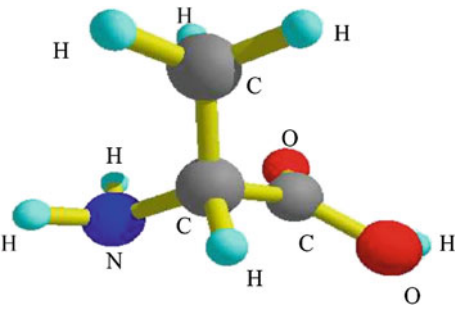

Fig. 3.23 Alanine $CH_3CH(COOH)NH_2$, an example of a $\boldsymbol{C}_1$ molecule with one methyl top

Table 3.5 Character table of $\boldsymbol{G}_3$ for a molecule of $\boldsymbol{C}_1$ symmetry

	E	(123)	(132)
A	1	1	1
E_{sep}			
E_+	1	ω	ω^*
E_-	1	ω^*	ω

$\omega = \exp(i2\pi/3)$

Table 3.6 Transformation properties of variables appearing in Eqs. 3.4.1, 3.4.16, 3.4.17, 3.4.37, and 3.4.38 for a generating operation (123) of $\boldsymbol{G}_3$

	$\boldsymbol{R}_1, \boldsymbol{R}_2, \boldsymbol{R}_3$	$\boldsymbol{R}$ (translation)	θ, ϕ, χ (rotation)	τ (internal rotation)
(123)				
PAM	$\boldsymbol{R}_2, \boldsymbol{R}_3, \boldsymbol{R}_1$	$\boldsymbol{R}$	θ, ϕ, χ	$\tau + 2\pi/3$
RAM	$\boldsymbol{R}_2, \boldsymbol{R}_3, \boldsymbol{R}_1$	$\boldsymbol{R}$	θ, ϕ, χ	$\tau + 2\pi/3$
IAM	$\boldsymbol{R}_2, \boldsymbol{R}_3, \boldsymbol{R}_1$	$\boldsymbol{R}$	$\theta, \phi, \chi + 2\pi\rho/3$	$\tau + 2\pi/3$

methyl internal rotation. A brief explanation of the permutation–inversion group is given in Appendix (Sect. 3.4.5). Although E_+ and E_- species in Table 3.5 are different symmetry species mathematically, whose characters are complex conjugate with each other, they are degenerate energetically. We will use a notation E_{sep} for combined E_+ and E_- species. Transformation properties of variables in the PAM, RAM and IAM system for the generating operation (123) of $\boldsymbol{G}_3$ are shown in Table 3.6. We will not treat the small-amplitude displacements $\boldsymbol{d}_i$ hereinafter in this Sect. 3.4 since they are out of consideration in the present problem.

$\boldsymbol{C}_s(\boldsymbol{G}_6)$ Case

Methanol CH_3OH, shown in Fig. 3.24, is well known as an example of this category. The character table and the transformation properties of variables are given in Tables 3.7 and 3.8, respectively.

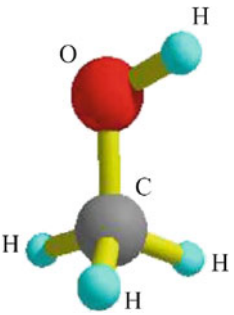

Fig. 3.24 Methanol CH_3OH, an example of a $\boldsymbol{C}_s$ molecule with one methyl top

Table 3.7 Character table of $\boldsymbol{G}_6$ for a methanol-like $\boldsymbol{C}_s$ molecule

	E	$(123), (132)$	$(23)^*, (13)^*, (12)^*$
A_1	1	1	1
A_2	1	1	-1
E	2	-1	0

Table 3.8 Transformation properties of variables appearing in Eqs. 3.4.1, 3.4.16, 3.4.17, 3.4.37, and 3.4.38 under generating operations of $\boldsymbol{G}_6$ for a methanol-like molecule

	$\boldsymbol{R}_1, \boldsymbol{R}_2, \boldsymbol{R}_3$	$\boldsymbol{R}$ (translation)	θ, ϕ, χ (rotation)	τ (internal rotation)
(123)				
PAM	$\boldsymbol{R}_2, \boldsymbol{R}_3, \boldsymbol{R}_1$	$\boldsymbol{R}$	θ, ϕ, χ	$\tau + 2\pi/3$
RAM	$\boldsymbol{R}_2, \boldsymbol{R}_3, \boldsymbol{R}_1$	$\boldsymbol{R}$	θ, ϕ, χ	$\tau + 2\pi/3$
IAM	$\boldsymbol{R}_2, \boldsymbol{R}_3, \boldsymbol{R}_1$	$\boldsymbol{R}$	$\theta, \phi, \chi + 2\pi\rho/3$	$\tau + 2\pi/3$
$(23)^*$				
PAM	$-\boldsymbol{R}_1, -\boldsymbol{R}_3, -\boldsymbol{R}_2$	$-\boldsymbol{R}$	$\pi - \theta, \pi + \phi, \pi - \chi$	$-\tau$
RAM	$-\boldsymbol{R}_1, -\boldsymbol{R}_3, -\boldsymbol{R}_2$	$-\boldsymbol{R}$	$\pi - \theta, \pi + \phi, \pi - \chi$	$-\tau$
IAM	$-\boldsymbol{R}_1, -\boldsymbol{R}_3, -\boldsymbol{R}_2$	$-\boldsymbol{R}$	$\pi - \theta, \pi + \phi, \pi - \chi$	$-\tau$

Seen in Tables 3.6 and 3.8, there is no difference of transformations between the PAM and the RAM system while the transformation properties of the IAM variables is different with those for both the PAM and RAM systems. A further large difference exists between the IAM system and the PAM or RAM system: the operation $(123)^3$ is equivalent to the identity operation in the $\{\boldsymbol{R}_i\}$ space for all the PAM, RAM and IAM systems, but it is not equivalent to the identity operation for the $(\theta, \phi, \chi, \tau)$ space in the IAM system while it is the identity operation also for the $(\theta, \phi, \chi, \tau)$ in the PAM or the RAM systems. Accordingly, the boundary conditions are somewhat complicated when we treat the internal-rotation problem in the IAM system. One method to avoid the complication is to introduce the extended PI group idea, but we mention it no more in this article.

A permutation–inversion operation $(23)^*$, which exists in the permutation–inversion group for such a molecule as methanol and corresponds to the reflection

Fig. 3.25 CH_3BF_2

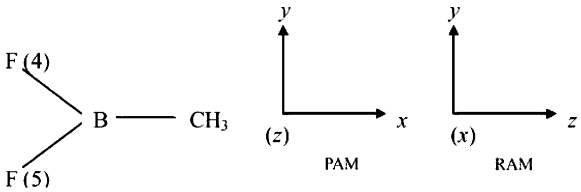

Table 3.9 Character table of $\boldsymbol{G}_{12}$ for a CH_3BF_2-like molecule

	E	(123), (132)	(23)*, (13)*, (12)*	(45)	(123)(45), (132) (45)	(23)(45)*, (13)(45)*, (12)(45)*
A_1'	1	1	1	1	1	1
A_2'	1	1	−1	1	1	−1
E'	2	−1	0	2	−1	0
A_1''	1	1	1	−1	−1	−1
A_2''	1	1	−1	−1	−1	1
E''	2	−1	0	−2	1	0

1, 2, 3 represent protons in the methyl group, and 4, 5 represent F atoms

in the plane of symmetry at an equilibrium configuration, transforms variables appearing in Eqs. 3.4.1, 3.4.16, 3.4.17, 3.4.37, and 3.4.38 as shown in Table 3.8. The transformations of the variables for $(23)^*$ are the same in all the PAM, RAM and IAM systems.

$\boldsymbol{C}_s(\boldsymbol{G}_{12})$ Case

An example for this type of molecule is CH_3BF_2, whose chemical structure is shown in Fig. 3.25. In Fig. 3.25 the PAM and RAM axes are also indicated (note that CH_3BF_2 is nearly an oblate symmetric top molecule). Although the difference between the PAM and RAM systems is not essential for the case of CH_3BF_2 since its internal rotation axis coincides with its b-principal axis, we define the PAM and RAM axes as shown in Fig. 3.25. The character table and the transformation properties of variables are given in Tables 3.9 and 3.10, respectively.

Symmetry operations which become feasible by internal rotation are (123), (132), (45), (123)(45), (132)(45), being different with the case of a methanol-like molecule. Symmetry operation $(23)(45)^*$ corresponds to the reflection in the plane of symmetry at an equilibrium configuration. Note that the operation $[(123)(45)]^6$ is equivalent to the identity operation in the $\{\boldsymbol{R}_i\}$ space for all the PAM, RAM and IAM systems, but it is not equivalent to the identity operation for the $(\theta, \phi, \chi, \tau)$ space in the IAM system while it is the identity operation also for the $(\theta, \phi, \chi, \tau)$ in the PAM or the RAM system.

Table 3.10 Transformation properties of variables appearing in Eqs. 3.4.1, 3.4.16, 3.4.17, 3.4.37, and 3.4.38 for generating operations of $\boldsymbol{G}_{12}$ for a CH_3BF_2-like molecule

	$\boldsymbol{R}_1, \boldsymbol{R}_2, \boldsymbol{R}_3$	$\boldsymbol{R}$ (translation)	θ, ϕ, χ(rotation)	τ (internal rotation)
(123)(45)				
PAM	$\boldsymbol{R}_2, \boldsymbol{R}_3, \boldsymbol{R}_1$	$\boldsymbol{R}$	$\pi - \theta, \pi + \phi, -\chi$	$\tau - 2\pi/6$
RAM	$\boldsymbol{R}_2, \boldsymbol{R}_3, \boldsymbol{R}_1$	$\boldsymbol{R}$	$\theta, \phi, \pi + \chi$	$\tau - 2\pi/6$
IAM	$\boldsymbol{R}_2, \boldsymbol{R}_3, \boldsymbol{R}_1$	$\boldsymbol{R}$	$\theta, \phi, \pi + \chi - 2\pi\rho/6$	$\tau - 2\pi/6$
$(23)(45)^*$				
PAM	$-\boldsymbol{R}_1, -\boldsymbol{R}_3, -\boldsymbol{R}_2$	$-\boldsymbol{R}$	$\pi - \theta, \pi + \phi, \pi - \chi$	$-\tau$
RAM	$-\boldsymbol{R}_1, -\boldsymbol{R}_3, -\boldsymbol{R}_2$	$-\boldsymbol{R}$	$\pi - \theta, \pi + \phi, \pi - \chi$	$-\tau$
IAM	$-\boldsymbol{R}_1, -\boldsymbol{R}_3, -\boldsymbol{R}_2$	$-\boldsymbol{R}$	$\pi - \theta, \pi + \phi, \pi - \chi$	$-\tau$

3.4.1.3 Qualitative Understanding of Pure Internal-Rotation Energy Levels for the $\boldsymbol{C}_1(\boldsymbol{G}_3)$ and $\boldsymbol{C}_s(\boldsymbol{G}_6)$ Cases

We consider here a pure internal-rotation problem, which is represented by a Schrödinger equation

$$\begin{aligned} H\psi &= E\psi, \\ H &= Fp_\tau^2 + V(\tau), \end{aligned} \tag{3.4.42}$$

where, for simplicity, we consider the cases $\boldsymbol{C}_1(\boldsymbol{G}_3)$ and $\boldsymbol{C}_s(\boldsymbol{G}_6)$, and we adopt the potential function $V(\tau)$ of the simplest form

$$V(\tau) = \frac{1}{2} V_3 (1 - \cos 3\tau). \tag{3.4.43}$$

Barrier Height Parameter and Mathieu Equation

The energy eigenvalues of Eq. 3.4.42 with Eq. 3.4.43 are expressed by a parameter s defined as

$$V_3 = \frac{9}{4} Fs, \tag{3.4.44}$$

since the equation

$$\left[Fp_\tau^2 + \frac{1}{2} V_3 (1 - \cos 3\tau) \right] \psi(\tau) = E\psi(\tau) \tag{3.4.45}$$

is transformed to the Mathieu equation, being a differential equation well known in physical mathematics

$$\frac{\mathrm{d}^2\psi}{\mathrm{d}x^2} + (b - s\cos^2 x)\psi = 0, \tag{3.4.46}$$

where

$$2x = 3\tau + \pi, \quad V_3 = \frac{9}{4}Fs, \quad E = \frac{9}{4}Fb. \tag{3.4.47}$$

Here we do not devote ourselves to describe the procedure of solving the Mathieu equation Eq. 3.4.46. Instead we discuss the two limiting cases in the next.

Energy Level Patterns in Extreme Cases

A Hamiltonian operator of the pure internal-rotation problem for an extreme case $V_3 \to 0$ (it is called free-internal-rotor case) is given by

$$H = Fp_\tau^2 = -F\frac{\mathrm{d}^2}{\mathrm{d}\tau^2}, \tag{3.4.48}$$

and for another extreme case $V_3 \to \infty$; the internal-rotation motion is restricted to oscillation of small amplitude around $\tau = 0$ (or $\tau = -2\pi/3$ or $\tau = -4\pi/3$). In this case the Hamiltonian operator is given as

$$H = Fp_\tau^2 + \frac{9}{4}V_3\tau^2, \tag{3.4.49}$$

by truncating after the second term of the expansion of $V(\tau)$ around $\tau = 0$

$$\begin{aligned} V(\tau) &\approx \frac{1}{2}V_3\left[1 - \left(1 - \frac{9}{2}\tau^2 + \frac{81}{24}\tau^4 + \cdots\right)\right] \\ &= \frac{9}{4}V_3\tau^2 - \frac{81}{48}V_3\tau^4 + \cdots \end{aligned} \tag{3.4.50}$$

As known well, for the Hamiltonian given in Eq. 3.4.48 we have

$$\begin{aligned} H|m\rangle &= E_m|m\rangle, \\ |m\rangle &= \frac{1}{\sqrt{2\pi}}e^{im\tau}, E_m = Fm^2, \quad (m = 0, \pm 1, \pm 2, \ldots) \end{aligned} \tag{3.4.51}$$

and that for Eq. 3.4.49 we have

$$\begin{aligned} H|v\rangle &= E_v|v\rangle, \\ E_v &= 3\sqrt{FV_3}(v + \frac{1}{2}), \quad (v = 0, 1, 2, \ldots) \end{aligned} \tag{3.4.52}$$

where $|v\rangle$ denotes the well-known harmonic oscillator functions. Symmetry properties of the free-internal-rotor eigenfunctions under the PI group $\boldsymbol{G}_3$ and $\boldsymbol{G}_6$ are as follows:

$$\begin{array}{lll} |m\rangle & (m = 0 \bmod 3): & A \text{ symmetry species}, \\ |\pm m\rangle & (m = 1 \text{ or } m = 2 \bmod 3): & E_{\text{sep}} \text{ symmetry species}, \end{array} \tag{3.4.53}$$

for $\boldsymbol{G}_3$, and

$$\begin{array}{ccll} & |m\rangle = |0\rangle & : & A_1 \text{ symmetry species,} \\ (1/\sqrt{2})(|m\rangle + |-m\rangle) & (m = 0 \bmod 3 > 0) & : & A_1 \text{ symmetry species,} \\ (1/\sqrt{2})(|m\rangle - |-m\rangle) & (m = 0 \bmod 3 > 0) & : & A_2 \text{ symmetry species,} \\ |\pm m\rangle & (m = 1 \text{ or } 2 \bmod 3) & : & E \text{ symmetry species,} \end{array} \tag{3.4.54}$$

for $\boldsymbol{G}_6$.

Symmetry properties of $|v\rangle$ under the PI group $\boldsymbol{G}_3$ and $\boldsymbol{G}_6$ is described next.

Qualitative Interpretation of Internal-Rotation Energy Level Patterns for a High Barrier Case Based on Tunneling Matrix Idea

Using a tunneling matrix approach, we try to understand aspect of energy levels produced by the Schrödinger equation (3.4.42) with Eq. 3.4.43 of the pure internal-rotation problem. In the high barrier limit, the internal-rotation motion is considered to be such that an oscillation of small amplitude around either one of the three minima tunnels to an oscillation around another minimum. Based on this idea, we construct approximate eigenfunctions from wavefunctions localized at three potential minima; that is $\tau = 0, \tau = -2\pi/3$ and $\tau = -4\pi/3$; we write those three localized functions as $|1\rangle, |2\rangle$ and $|3\rangle$, respectively (see Fig. 3.26). We call these functions "framework functions" at framework 1–3, respectively. The framework function $|1\rangle$ can be approximated by the solution of the Schrödinger equation based on the Hamiltonian operator given by Eq. 3.4.49,

$$H_0\psi_v = \left[Fp_\tau^2 + \frac{9}{4}V_3\tau^2\right]\psi_v = E_v\psi_v, \tag{3.4.55}$$

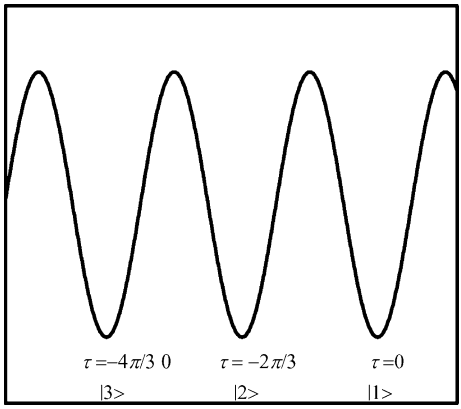

Fig. 3.26 Potential minima and framework functions

i.e., the framework function at framework 1 is approximately equal to the solution ψ_v,

$$|1;v\rangle = \psi_v. \tag{3.4.56}$$

In Eq. 3.4.56, v is used for representing the vth vibrational state: $v = 0$ corresponds to the ground vibrational state, $v = 1$ to the first excited torsional state and so on. The three framework functions are expressed as

$$|1;v\rangle \equiv \Phi_v(\tau) \tag{3.4.57}$$

$$|2;v\rangle = (123)|1;v\rangle = \Phi_v(\tau + 2\pi/3) \tag{3.4.58}$$

$$|3;v\rangle = (132)|1;v\rangle = \Phi_v(\tau + 4\pi/3) \tag{3.4.59}$$

(We assume $\Phi_v(\tau) = \Phi_v(\tau \pm 2\pi)$). By making suitable linear combinations of framework functions, we have symmetrized wavefunctions belonging to symmetry species of the PI group $\boldsymbol{G}_3$ or $\boldsymbol{G}_6$ as follows, with $S = \langle 1;v|2,v\rangle$,

$$\begin{aligned}
|A;v\rangle &= \frac{1}{\sqrt{3(1+2S)}}(|1;v\rangle + |2;v\rangle + |3;v\rangle), \\
|E_a;v\rangle &= \frac{1}{\sqrt{3(1-S)}}\left(|1;v\rangle + \omega^2|2;v\rangle + \omega|3;v\rangle\right), \\
|E_b;v\rangle &= \frac{1}{\sqrt{3(1-S)}}\left(|1;v\rangle + \omega|2;v\rangle + \omega^2|3;v\rangle\right),
\end{aligned} \tag{3.4.60}$$

where E_a and E_b correspond to E_+ and E_- for the case of a $\boldsymbol{C}_1$ molecule ($\boldsymbol{G}_3$), and they represent two components of E species for the $\boldsymbol{C}_s$ molecule ($\boldsymbol{G}_6$). For a $\boldsymbol{C}_s$ molecule, $|A,v\rangle$ is replaced by $|A_1,v\rangle$ for even v or $|A_2,v\rangle$ for odd v. The three functions shown in Eq. 3.4.60 are (approximate) eigenfunctions of the Schrödinger Eq. 3.4.42, and eigenvalues are expressed as

$$\begin{aligned}
\langle A;v|H|A;v\rangle &= \frac{1}{1+2S}(\langle 1;v|H|1;v\rangle + 2\langle 1;v|H|2;v\rangle) \\
&\approx \langle 1;v|H_0|1;v\rangle + \frac{2}{1+2S}\langle 1;v|H'|2;v\rangle,
\end{aligned} \tag{3.4.61}$$

$$\begin{aligned}
\langle E_a;v|H|E_a;v\rangle &= \langle E_b;v|H|E_b;v\rangle \\
&= \frac{1}{1-S}(\langle 1;v|H|1;v\rangle - \langle 1;v|H|2;v\rangle) \\
&\approx \langle 1;v|H_0|1;v\rangle - \frac{1}{1-S}\langle 1;v|H'|2;v\rangle,
\end{aligned} \tag{3.4.62}$$

where we used

$$H = H_0 + H' \tag{3.4.63}$$

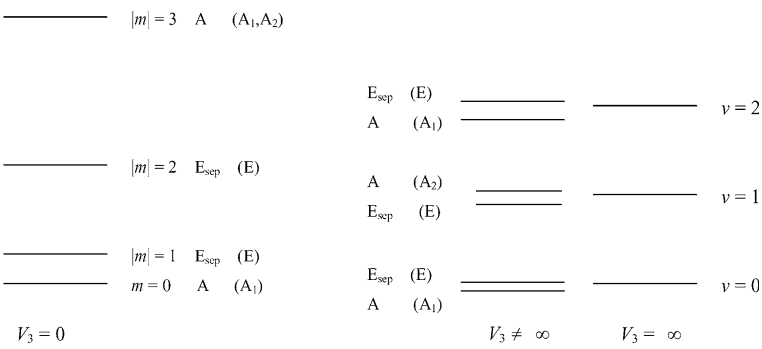

Fig. 3.27 Schematic diagram of one-top internal-rotation energy levels for cases $\boldsymbol{C}_1(\boldsymbol{G}_3)$ and $\boldsymbol{C}_s(\boldsymbol{G}_6)$. (Symmetry species in parentheses are those for $\boldsymbol{G}_6$)

$$\langle 1;v|H|1;v\rangle \approx \langle 1;v|H_0|1;v\rangle = E_v \tag{3.4.64}$$

$$\begin{aligned}\langle 1;v|H|2;v\rangle &= \langle 1;v|H_0|2;v\rangle + \langle 1;v|H'|2;v\rangle \\ &= E_v S + \langle 1;v|H'|2;v\rangle\end{aligned} \tag{3.4.65}$$

Since H' takes negative values in the intermediate region between framework 1 and 2, we have

$$\langle 1;v=0|H'|2;v=0\rangle < 0, \langle 1;v=1|H'|2;v=1\rangle > 0, \ldots \tag{3.4.66}$$

The tunneling matrix approach for the case involving torsional–rotational interaction is written later. Schematic pure internal-rotation energy level patterns are shown in Fig. 3.27, where both the extreme cases are depicted.

3.4.1.4 Qualitative Understanding of Pure Internal-Rotation Energy Levels for $\boldsymbol{C}_s(\boldsymbol{G}_{12})$ Case

We describe briefly the tunneling matrix approach for the case of a CH_3BF_2-like molecule. Although the molecule has a low barrier height to internal rotation, we consider here a hypothetical case of a CH_3BF_2-like molecule with high barrier. For this case we have six framework functions expressed as

$$|1;v\rangle \equiv \Phi(\tau), \tag{3.4.67}$$

$$|n;v\rangle = a^{n-1}|1;v\rangle = \Phi(\tau - 2\pi[n-1]/6), \quad (n = 1,2,3,4,5,6) \tag{3.4.68}$$

where $a = (123)(45)$. Symmetrized wavefunctions constructed from these six framework functions are given as

$$
\begin{aligned}
|A_1';v\rangle &= \frac{|1;v\rangle + |2;v\rangle + |3;v\rangle + |4;v\rangle + |5;v\rangle + |6;v\rangle}{\sqrt{6(1+2S_1+2S_2+S_3)}},\\
|A_2'';v\rangle &= \frac{|1;v\rangle - |2;v\rangle + |3;v\rangle - |4;v\rangle + |5;v\rangle - |6;v\rangle}{\sqrt{6(1-2S_1+2S_2-S_3)}},\\
|E_a';v\rangle &= \frac{|1;v\rangle + \epsilon^2|2;v\rangle + \epsilon^4|3;v\rangle + |4;v\rangle + \epsilon^{-4}|5;v\rangle + \epsilon^{-2}|6;v\rangle}{\sqrt{6(1-S_1-S_2+S_3)}},\\
|E_b';v\rangle &= \frac{|1;v\rangle + \epsilon^{-2}|2;v\rangle + \epsilon^{-4}|3;v\rangle + |4;v\rangle + \epsilon^4|5;v\rangle + \epsilon^2|6;v\rangle}{\sqrt{6(1-S_1-S_2+S_3)}},\\
|E_a'';v\rangle &= \frac{|1;v\rangle + \epsilon|2;v\rangle + \epsilon^2|3;v\rangle - |4;v\rangle + \epsilon^{-2}|5;v\rangle + \epsilon^{-1}|6;v\rangle}{\sqrt{6(1+S_1-S_2-S_3)}},\\
|E_b'';v\rangle &= \frac{|1;v\rangle + \epsilon^{-1}|2;v\rangle + \epsilon^{-2}|3;v\rangle - |4;v\rangle + \epsilon^2|5;v\rangle + \epsilon|6;v\rangle}{\sqrt{6(1+S_1-S_2-S_3)}},
\end{aligned}
\tag{3.4.69}
$$

where $\epsilon = \exp(i2\pi/6), S_1 = \langle 1;v|2;v\rangle, S_2 = \langle 1;v|3;v\rangle,$ and $S_3 = \langle 1;v|4;v\rangle$. Equations 3.4.69 are expressions for the case of $(23)(45)^*|1;v\rangle = +|1;v\rangle$. For the case of $(23)(45)^*|1;v\rangle = -|1;v\rangle$, $|A_1';v\rangle$ and $|A_2'';v\rangle$ should be changed to $|A_2';v\rangle$ and $|A_1'';v\rangle$, respectively. The energy eigenvalues for the pure internal-rotation problem are given by

$$
\begin{aligned}
\langle A_1';v|H|A_1';v\rangle &= (\langle 1;v|H|1;v\rangle + 2\langle 1;v|H|2;v\rangle + 2\langle 1;v|H|3;v\rangle + \langle 1;v|H|4;v\rangle)/N_{A_1'},\\
\langle A_2'';v|H|A_2'';v\rangle &= (\langle 1;v|H|1;v\rangle - 2\langle 1;v|H|2;v\rangle + 2\langle 1;v|H|3;v\rangle - \langle 1;v|H|4;v\rangle)/N_{A_2''},\\
\langle E';v|H|E';v\rangle &= (\langle 1;v|H|1;v\rangle - \langle 1;v|H|2;v\rangle - \langle 1;v|H|3;v\rangle + \langle 1;v|H|4;v\rangle)/N_{E'},\\
\langle E'';v|H|E'';v\rangle &= (\langle 1;v|H|1;v\rangle + \langle 1;v|H|2;v\rangle - \langle 1;v|H|3;v\rangle - \langle 1;v|H|4;v\rangle)/N_{E''},
\end{aligned}
\tag{3.4.70}
$$

where $N_{A_1'} = 1 + 2S_1 + 2S_2 + S_3, N_{A_2''} = 1 - 2S_1 + 2S_2 - S_3, N_{E'} = 1 - S_1 - S_2 + S_3$, and $N_{E''} = 1 + S_1 - S_2 - S_3$.

Equations 3.4.70 are expressions for the case of

$$(23)(45)^*|1;v\rangle = +|1;v\rangle. \tag{3.4.71}$$

For the case of

$$(23)(45)^*|1;v\rangle = -|1;v\rangle, \tag{3.4.72}$$

$|A_1';v\rangle$ and $|A_2'';v\rangle$ should be changed to $|A_2';v\rangle$ and $|A_1'';v\rangle$, respectively.

Combining Eq. 3.4.70 with the description for cases $\boldsymbol{C}_1(\boldsymbol{G}_3)$ and $\boldsymbol{C}_s(\boldsymbol{G}_6)$ in the previous section, schematic energy level diagrams depicted in Fig. 3.28 can be understood easily. V_6 used in Fig. 3.28 is the barrier height parameter of the potential function

$$V(\tau) = \frac{1}{2}V_6(1 - \cos 6\tau). \tag{3.4.73}$$

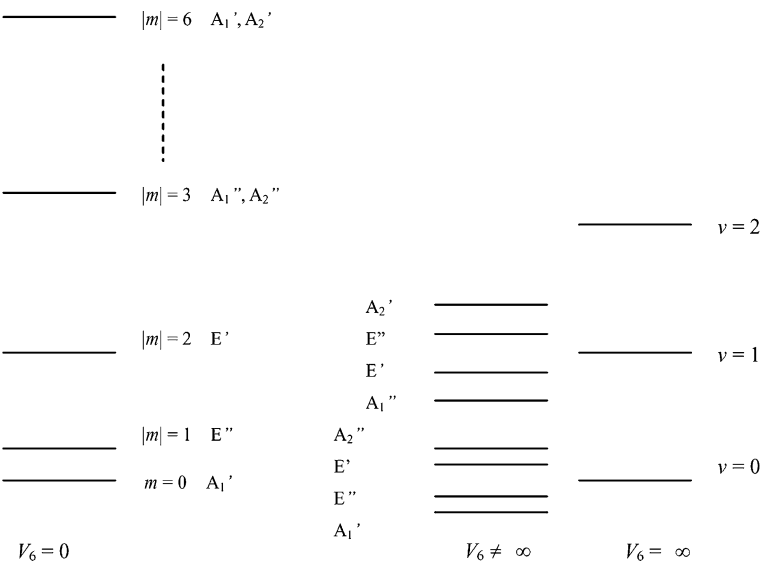

Fig. 3.28 Schematic diagram of one-top internal-rotation energy levels for case $\boldsymbol{C}_s(\boldsymbol{G}_{12})$

3.4.1.5 Construction of Hamiltonian Matrix with the Use of Free Rotor Wavefunctions

We will give expressions for Hamiltonian matrix elements in the traditional treatment, where free rotor torsional functions multiplied by symmetric top rotational functions are used as basis set wavefunctions. We adopt the RAM system since only $\Delta K = 0$ matrix elements occur in the torsional–rotational interaction and it makes the construction of the Hamiltonian matrix somewhat convenient.

$\boldsymbol{C}_1(\boldsymbol{G}_3)$ Case

We consider at first the case $\boldsymbol{C}_1(\boldsymbol{G}_3)$, where the Hamiltonian operator is given by

$$\begin{aligned} H = {} & AJ_z^2 + BJ_x^2 + CJ_y^2 \\ & + D_{zx}(J_zJ_x + J_xJ_z) + D_{xy}(J_xJ_y + J_yJ_x) + D_{yz}(J_yJ_z + J_zJ_y) \\ & + F(p_\tau - \rho J_z)^2 + \frac{1}{2}V_3(1 - \cos 3\tau). \end{aligned} \tag{3.4.74}$$

As seen in Eq. 3.4.74, we adopt the simplest potential function for simplicity. As a basis set function, a product form of a free rotor torsional function $|m\rangle$ and a symmetric top rotational function $|J, K, M\rangle$ is used, that is,

$$|m; J, K, M\rangle = |m\rangle|J, K, M\rangle, \tag{3.4.75}$$

where $|m\rangle = (1/\sqrt{2\pi})\exp(im\tau)$.

Hereinafter we drop the laboratory-fixed angular momentum quantum number M in the rotational function $|J, K, M\rangle$ since we treat an isolated molecule in free space and its energy does not depend on the quantum number M.

Since $|m; J, K\rangle$ has a symmetry property

$$(123)|m; J, K\rangle = \exp\left(i\frac{2\pi m}{3}\right)|m; JK\rangle, \tag{3.4.76}$$

symmetry species of $|m; J, K\rangle$ are given as

$$\begin{array}{ll} |m; J, K\rangle & \text{for } m = 0, \pm 3, \pm 6, \ldots \quad : A \text{ symmetry species,} \\ |m; J, K\rangle & \text{for } m = \ldots, -5, -2, 1, 4, 7, \ldots \quad : E_+ \text{ symmetry species,} \\ |m; J, K\rangle & \text{for } m = \ldots, -4, -1, 2, 5, 8, \ldots \quad : E_- \text{ symmetry species,} \end{array} \tag{3.4.77}$$

Thus, the Hamiltonian matrix is divided into two blocks with A and $E_{\text{sep}}(E_+ \text{ or } E_-)$ species. Non-zero matrix elements of $\langle m; J, K|H|m'; J, K'\rangle$ are expressed as

$$\langle m; J, K|H|m; J, K\rangle = \frac{1}{2}(B + C)J^2 + \left[A - \frac{1}{2}(B + C)\right]K^2 + F(m - \rho K)^2 + \frac{1}{2}V_3 \tag{3.4.78}$$

$$\langle m; J, K|H|m; J, K \pm 2\rangle = \left\langle J, K|\frac{1}{2}(B - C)\left(J_x^2 - J_y^2\right) + D_{xy}\left(J_xJ_y + J_yJ_x\right)|J, K \pm 2\right\rangle \tag{3.4.79}$$

$$\langle m; J, K|H|m; J, K \pm 1\rangle = \langle J, K|D_{zx}(J_zJ_x + J_xJ_z) + D_{yz}\left(J_yJ_z + J_zJ_y\right)|J, K \pm 1\rangle \tag{3.4.80}$$

$$\langle m; J, K|H|m \pm 3; J, K\rangle = -\frac{1}{4}V_3, \tag{3.4.81}$$

In a usual spectral analysis, a suitable type of centrifugal distortion terms is added, and the numerical diagonalization of the Hamiltonian matrix and the iteration process of the least squares fit are employed.

The torsional–rotational energy levels of methanol (CH_3OH) in the ground vibrational state, shown schematically in Fig. 3.29, will help us to understand the behavior of torsional–rotational energy levels, which are connected with Hamiltonian matrix elements described above.

$C_s(G_6)$ Case

In this case, expressions shown above are modified somewhat. Since the Hamiltonian operator should satisfy $(23)^*H = H$, D_{yz} and D_{xy} terms disappear in Eq. 3.4.74 and a potential function $V(\tau)$ should satisfy $V(-\tau) = V(\tau)$ necessarily

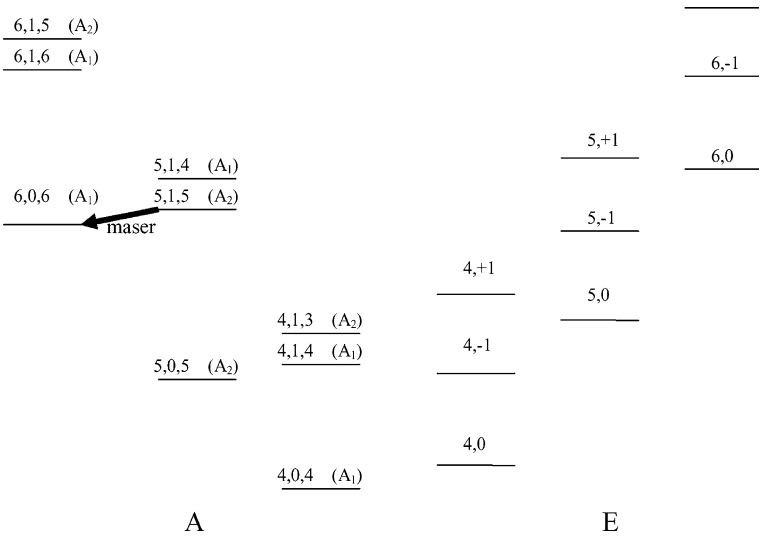

Fig. 3.29 Schematic torsional–rotational energy level diagram of methanol in the ground vibrational state. In order to designate rotational levels, J, K_a, K_c is used for levels belonging to A-symmetry species as for those of an ordinary asymmetric top molecule, and J, K is used for E-symmetry levels

(we assume a molecule has an a, b-plane of symmetry and $a, b, c \leftrightarrow z, x, y$). Basis set wavefunctions belonging to each of symmetry species are given as follows: for A_1 species,

$$|A_1; m; J, K\rangle = \frac{1}{\sqrt{2}}\left[|m\rangle|J, K\rangle + (-1)^{J-K}|-m\rangle|J, -K\rangle\right] \quad (m = 3n \text{ with } n = 0, 1, 2, \ldots, \text{ and } K = -J, -J+1, \ldots, 0, \ldots, +J), \tag{3.4.82}$$

for A_2 species,

$$|A_2; m; J, K\rangle = \frac{1}{\sqrt{2}}\left[|m\rangle|J, K\rangle - (-1)^{J-K}|-m\rangle|J, -K\rangle\right] \quad (m = 3n \text{ with } n = 0, 1, 2, \ldots, \text{ and } K = -J, -J+1, \ldots, 0, \ldots, +J), \tag{3.4.83}$$

and for E species,

$$|E; m; J, K\rangle_a = |m\rangle|J, K\rangle, \tag{3.4.84}$$

$$|E; m; J, K\rangle_b = (23)^*|E; m; J, K\rangle_a = (-1)^{J-K}|-m\rangle|J, -K\rangle \quad (m = 3n+1 \text{ or } n = 3n+2 \text{ with } n = 0, 1, 2, \ldots, \text{ and } K = -J, -J+1, \ldots, 0, \ldots, +J). \tag{3.4.85}$$

In the equations above $1/\sqrt{2}$ is replaced by $1/2$ when $m = K = 0$.

In Eqs. 3.4.84 and 3.4.85, $|E; m; J, K\rangle_a$ and $|E; m; J, K\rangle_b$ represent pair states for the degenerate E symmetry species.

The matrix element expressions $\langle m; J, K|H|m'; J, K'\rangle$ shown in Eqs. 3.4.78–3.4.81 are available also for this case after setting $D_{xy} = D_{yz} = 0$.

When we treat Hamiltonian matrices for A_1 and A_2 species separately in writing a computing program, we have to be very careful since we use Wang-type-like functions as shown in Eqs. 3.4.82 and 3.4.83, involving a subtle phase factor. The author recommends to treat the A_1 and A_2 species simultaneously by using A species functions such as shown in Eq. 3.4.77 and without using Wang-type-like functions although the matrix size is doubled.

$\boldsymbol{C}_s(\boldsymbol{G}_{12})$ Case

Since the C_3 axis of the methyl group is along the inertial b-axis in the CH_3BF_2 molecule, the RAM system, in which the axis correspondence is such as $b, c, a \leftrightarrow z, x, y$, may not be necessarily convenient for such a case. It is thus difficult to tell which system is preferable for a spectral analysis of the CH_3BF_2 molecule, PAM or RAM. We give anyhow a formulation for a CH_3BF_2-like molecule with the use of the RAM system. Transformation properties of variables given in Table 3.10 lead to the Hamiltonian operator

$$H = BJ_z^2 + CJ_x^2 + AJ_y^2 + F(p_\tau - \rho J_z)^2 + \frac{1}{2}V_6(1 - \cos 6\tau), \tag{3.4.86}$$

where we adopt the simplest potential function.

Basis set functions belonging A_1' and A_2' symmetry species are given as follows.

$$|A_1'; m; J, K\rangle = \frac{1}{\sqrt{2}}\left[|m\rangle|J, K\rangle + (-1)^{J-K}|m\rangle|J, -K\rangle\right], \tag{3.4.87}$$

with $(m = 0 \bmod 6; K = \text{even} \geq 0)$ or $(m = 3 \bmod 6; K = \text{odd} > 0)$,

$$|A_2'; m; J, K\rangle = \frac{1}{\sqrt{2}}\left[|m\rangle|J, K\rangle - (-1)^{J-K}|m\rangle|J, -K\rangle\right], \tag{3.4.88}$$

with $(m = 0 \bmod 6; K = \text{even} \geq 0)$ or $(m = 3 \bmod 6; K = \text{odd} > 0)$,

$$|A_1''; m; J, K\rangle = \frac{1}{\sqrt{2}}\left[|m\rangle|J, K\rangle - (-1)^{J-K}|m\rangle|J, -K\rangle\right], \tag{3.4.89}$$

with $(m = 0 \bmod 6; K = \text{odd} > 0)$ or $(m = 3 \bmod 6; K = \text{even} \geq 0)$,

$$|A_2''; m; J, K\rangle = \frac{1}{\sqrt{2}}\left[|m\rangle|J, K\rangle + (-1)^{J-K}|m\rangle|J, -K\rangle\right], \tag{3.4.90}$$

with $(m = 0 \bmod 6; K = \text{odd} > 0)$ or $(m = 3 \bmod 6; K = \text{even} \geq 0)$,

where $1/\sqrt{2}$ is replaced by 1/2 when $m = K = 0$, and m takes values of plus, minus and 0 within the restriction shown in parentheses.

Basis set functions E' and E'' symmetry species are given by

$$|E'_a; m; J, K\rangle = |m\rangle|J, K\rangle, \tag{3.4.91}$$

$$\begin{aligned}
|E'_b; m; J, K\rangle &= (23)(45)^*|E'_a; m; J, K\rangle \\
&= (-1)^{J-K}|-m\rangle|J, -K\rangle, \\
\text{with } m &= 6n+2, \text{ or } 6n+4, n = 0, \pm1, \pm2, \ldots; K = \text{even} \geq 0, \\
\text{or } m &= 6n+1, \text{ or } 6n+5, n = 0, \pm1, \pm2, \ldots; K = \text{odd} > 0,
\end{aligned} \tag{3.4.92}$$

$$|E''_a; m; J, K\rangle = |m\rangle|J, K\rangle, \tag{3.4.93}$$

$$\begin{aligned}
|E''_b; m; J, K\rangle &= (23)(45)^*|E''_a; m; J, K\rangle \\
&= (-1)^{J-K}|-m\rangle|J, -K\rangle, \\
\text{with } m &= 6n+1, \text{ or } 6n+5, n = 0, \pm1, \pm2, \ldots; K = \text{even} \geq 0, \\
\text{or } m &= 6n+2, \text{ or } 6n+4, n = 0, \pm1, \pm2, \ldots; K = \text{odd} > 0.
\end{aligned} \tag{3.4.94}$$

Hamiltonian matrix elements for each of symmetry species are evaluated by using the basis set functions written above, and the matrix elements

$$\langle m; J, K|H|m'; J, K'\rangle,$$

which are obtained by making the replacement $V_3 \rightarrow V_6$ in Eq. 3.4.78 and by putting

$$\langle m; J, K|H|m \pm 6; J, K\rangle = -V_6/4 \tag{3.4.95}$$

in place of Eq. 3.4.81. We note in passing that a Hamiltonian matrix element $\langle m; J, K|H|m \pm 3; J, K \pm 1\rangle$ appear possibly by adding a term such as

$$a(\cos 3\tau)J_y + b(\sin 3\tau)J_x, \qquad (a, b: \text{constants}) \tag{3.4.96}$$

to the Hamiltonian operator.

3.4.1.6 An Approximate Expression of Torsional–Rotational Energy

We will derive an approximate expression of torsional–rotational energy for the $\boldsymbol{C}_1(\boldsymbol{G}_3)$ or $\boldsymbol{C}_s(\boldsymbol{G}_6)$ case of a nearly prolate top molecule. From Eqs. 3.4.78–3.4.81, we have

$$\langle m;J,K|H|m;J,K\rangle = \frac{1}{2}(B+C)J^2 + \left[A - \frac{1}{2}(B+C)\right]K^2 + F(m-\rho K)^2 + \frac{1}{2}V_3, \tag{3.4.97}$$

$$\langle m;J,K|H|m;J,K\pm 2\rangle \approx 0, \tag{3.4.98}$$

$$\langle m;J,K|H|m;J,K\pm 1\rangle \approx 0, \tag{3.4.99}$$

$$\langle m;J,K|H|m\pm 3;J,K\rangle = -\frac{1}{4}V_3. \tag{3.4.100}$$

The above equations lead to

$$\langle 3n;J,K|H|3n;J,K\rangle = \frac{1}{2}(B+C)J^2 + \left[A - \frac{1}{2}(B+C)\right]K^2 + F(3n-\rho K)^2 + \frac{1}{2}V_3, \tag{3.4.101}$$

$$= \frac{1}{2}(B+C)J^2 + \left[A - \frac{1}{2}(B+C)\right]K^2 + F(-3n+\rho K)^2 + \frac{1}{2}V_3, \tag{3.4.102}$$

$$= \frac{1}{2}(B+C)J^2 + \left[A - \frac{1}{2}(B+C)\right]K^2 + F[3(n+1)-(\rho K+3)]^2 + \frac{1}{2}V_3, \tag{3.4.103}$$

$$\langle 3n;J,K|H|3(n\pm 1);J,K\rangle = -\frac{1}{4}V_3. \tag{3.4.104}$$

with $n = 0, \pm 1, \pm 2, \ldots$, for A species, and

$$\langle 3n+1;J,K|H|3n+1;J,K\rangle = \frac{1}{2}(B+C)J^2 + \left[A - \frac{1}{2}(B+C)\right]K^2 + F[3n+(1-\rho K)]^2 + \frac{1}{2}V_3, \tag{3.4.105}$$

$$= \frac{1}{2}(B+C)J^2 + \left[A - \frac{1}{2}(B+C)\right]K^2 + F[-3n-(1-\rho K)]^2 + \frac{1}{2}V_3, \tag{3.4.106}$$

$$= \frac{1}{2}(B+C)J^2 + \left[A - \frac{1}{2}(B+C)\right]K^2 + F[3(n+1)+(1-\rho K-3)]^2 + \frac{1}{2}V_3, \tag{3.4.107}$$

$$\langle 3n+1;J,K|H|3(n\pm 1)+1;J,K\rangle = -\frac{1}{4}V_3. \tag{3.4.108}$$

with $n = 0, \pm 1, \pm 2, \ldots$, for E species.

By noting that (i) since the Hamiltonian matrix elements are defined by indices n's for $n = 0, \pm 1, \pm 2, \ldots, \pm\infty$ as seen in Eqs. 3.4.101, 3.4.104, 3.4.105 and 3.4.108, the eigenvalues are unchanged for $n \rightarrow -n$ and/or $n \rightarrow n \pm 1$, and (ii) $n \rightarrow -n$ and $n \rightarrow n + 1$ are equivalent to $\gamma \rightarrow -\gamma$ and $\gamma \rightarrow \gamma + 3$ (see Eq. 3.4.110 below for the definition of γ), respectively, as shown in Eq. 3.4.103 and 3.4.107, we have

$$W_{\Gamma;J,K:l}(\gamma) = W_{\Gamma;J,K:l}(-\gamma) = W_{\Gamma;J,K:l}(\gamma + 3), \tag{3.4.109}$$

where $W_{\Gamma;J,K:l} = \langle \Gamma; J.K; l|H|\Gamma; J.K; l\rangle$, $(\Gamma = A, E; l = 1, 2, 3, \ldots)$, and

$$\begin{array}{ll} \gamma = \rho K & (\text{for } \Gamma = A), \\ \gamma = \rho K - 1 & (\text{for } \Gamma = E), \end{array} \tag{3.4.110}$$

Accordingly, we have

$$\begin{aligned} W_{A;J,K,l} = & \frac{1}{2}(B + C)J^2 + \left[A - \frac{1}{2}(B + C)\right]K^2 \\ & + \frac{1}{2}V_3 + \sum_{k=0}^{\infty} \alpha_k^l \cos\left(\frac{2\pi k}{3}\rho K\right), \end{aligned} \tag{3.4.111}$$

$$\begin{aligned} W_{E;J,K,l} = & \frac{1}{2}(B + C)J^2 + \left[A - \frac{1}{2}(B + C)\right]K^2 \\ & + \frac{1}{2}V_3 + \sum_{k=0}^{\infty} \alpha_k^l \cos\left[\frac{2\pi k}{3}(\rho K - 1)\right], \end{aligned} \tag{3.4.112}$$

where α_k^l's are coefficients in the Fourier expansions.

3.4.1.7 Perturbation Treatment and Effective Rotational Hamiltonian Operator

A rotational Hamiltonian operator effective for a specific vth vibrational state (see Fig. 3.27 and 3.28) was derived by Herschbach [47] using a second order perturbation theory. Such an effective rotational Hamiltonian will be useful for understanding of the rotational energy level structure in a specific vibrational state.

We put the PAM Hamiltonian operator as

$$H = H^0 + H', \tag{3.4.113}$$

$$H^0 = AJ_z^2 + BJ_x^2 + CJ_y^2 + F\pi^2 + Fp_\tau^2 + V(\tau), \tag{3.4.114}$$

$$H' = -2Fp_\tau\pi, \tag{3.4.115}$$

where $\pi = \sum_{\alpha=x,y,z} \rho_\alpha J_\alpha$. In terms of the second order perturbation treatment we have

$$
\begin{aligned}
H_{\text{eff}} &= \langle v;\Gamma|H^0|v;\Gamma\rangle + \langle v;\Gamma|H'|v;\Gamma\rangle + \sum_{v'\neq v}\frac{|\langle v;\Gamma|H'|v';\Gamma'\rangle|^2}{E_{v;\Gamma}-E_{v';\Gamma'}} \\
&= AJ_z^2 + BJ_x^2 + CJ_y^2 + F\pi^2 + \langle v;\Gamma|Fp_\tau^2 + V(\tau)|v;\Gamma\rangle \\
&\quad - 2F\sum_{\alpha=x,y,z}\rho_\alpha J_\alpha\langle v;\Gamma|p_\tau|v;\Gamma\rangle + 4F^2\pi^2\sum_{v'\neq v}\frac{|\langle v;\Gamma|p_\tau|v';\Gamma'\rangle|^2}{E_{v;\Gamma}-E_{v';\Gamma'}}
\end{aligned}
\tag{3.4.116}
$$

In Eq. 3.4.116 Γ represents symmetry species: $\Gamma = A$ or E_{sep} for case $\boldsymbol{C}_1(\boldsymbol{G}_3)$, and $\Gamma = A_1, A_2$ or E for case $\boldsymbol{C}_s(\boldsymbol{G}_6)$. The Γ' in the summation of the last term is equal to Γ for $\boldsymbol{C}_1(\boldsymbol{G}_3)$ case. For case $\boldsymbol{C}_s(\boldsymbol{G}_6)$, $\Gamma' = A_2(A_1)$ for $\Gamma = A_1(A_2)$ and $\Gamma' = E$ for $\Gamma = E$. The wavefunction $|v;\Gamma\rangle$ appearing in Eq. 3.4.116 is an eigenfunction of a pure internal-rotation problem described by a Hamiltonian operator

$$
H_{\text{internal-rotation}} = Fp_\tau^2 + V(\tau). \tag{3.4.117}
$$

For Γ to be a non-degenerate symmetry species ($\Gamma = A, A_1$ or A_2, etc.), $|v;\Gamma\rangle$ can be chosen to be real. Then we have

$$
\begin{aligned}
\langle v;\Gamma|p_\tau|v;\Gamma\rangle &= \left(\langle v;\Gamma|p_\tau^\dagger|v;\Gamma\rangle\right)^* \\
&= \langle v;\Gamma|p_\tau^{\dagger *}|v;\Gamma\rangle \\
&= -\langle v;\Gamma|p_\tau|v;\Gamma\rangle \\
&= 0,
\end{aligned}
\tag{3.4.118}
$$

where we used $p_\tau^\dagger = p_\tau$ and $p_\tau^* = -p_\tau$ ($\dagger$ and $*$ denote Hermitian conjugation and complex conjugation, respectively). That is,

$$
\langle v;\Gamma|p_\tau|v;\Gamma\rangle = 0, \tag{3.4.119}
$$

for a non-degenerate species. From Eqs. 3.4.116 and 3.4.119 we have the following expressions for the effective rotational Hamiltonian operator in the specific vibrational state after suitable coordinate axis rotations for removing cross terms such as $J_xJ_y + J_yJ_x$:

$$
H_{\text{eff}}(v;A) = W_0(v;A) + A_{\text{eff}}(v;A)J_z^2 + B_{\text{eff}}(v;A)J_x^2 + C_{\text{eff}}(v;A)J_y^2, \tag{3.4.120}
$$

$$
\begin{aligned}
H_{\text{eff}}(v;E) &= W_0(v;E) + A_{\text{eff}}(v;E)J_z^2 + B_{\text{eff}}(v;E)J_x^2 + C_{\text{eff}}(v;E)J_y^2 \\
&\quad + q_{\text{eff}}(v)J_z + r_{\text{eff}}(v)J_x + s_{\text{eff}}(v)J_y,
\end{aligned}
\tag{3.4.121}
$$

where the symmetry species notation A is used for A in case $\boldsymbol{C}_1(\boldsymbol{G}_3)$, for A_1 or A_2 in case $\boldsymbol{C}_s(\boldsymbol{G}_6)$, or for A_1', A_2', A_1'' or A_2'' in case $\boldsymbol{C}_s(\boldsymbol{G}_{12})$, and E for E_{sep} in case $\boldsymbol{C}_1(\boldsymbol{G}_3)$, for E in case $\boldsymbol{C}_s(\boldsymbol{G}_6)$, or for E' or E'' in case $\boldsymbol{C}_s(\boldsymbol{G}_{12})$.

Coefficients appearing in Eqs. 3.4.120 and 3.4.121 are given by

$$
W_0(v;\Gamma = A \text{ or } E) = \langle v;\Gamma|Fp_\tau^2 + V(\tau)|v;\Gamma\rangle \tag{3.4.122}
$$

$$A_{\text{eff}}(v;\Gamma = A \text{ or } E) \approx A + F\rho_z^2\left(1 + 4F\sum_{v'\neq v}\frac{|\langle v;\Gamma|p_\tau|v';\Gamma'\rangle|^2}{E_{v;\Gamma} - E_{v';\Gamma'}}\right), \text{ etc.} \quad (3.4.123)$$

$$q_{\text{eff}}(v) \approx -2F\rho_z\langle v;\Gamma|p_\tau|v;\Gamma\rangle, \text{ etc.} \quad (3.4.124)$$

In Eqs. 3.4.123 and 3.4.124, $\approx$ is used in place of = because we take small changes caused by the coordinate axis rotation for removing the cross terms into consideration.

3.4.1.8 Tunneling Matrix Formulation of the Torsional–Rotational Problem

We describe here the tunneling matrix formulation for the torsional–rotational problem. As mentioned in Sect. 3.4.1.3 above for the pure internal-rotation problem, this formulation is valid for a high barrier case. This formalism was developed first by Hougen [48] for analyzing a microwave spectrum of the hydrazine molecule N_2H_4, which has an umbrella (inversion) motion of the two NH_2 group and an internal rotation of the two NH_2 groups about the N–N bond as large-amplitude vibrations. Characteristics of the tunneling matrix formalism are summarized as follows:

1. It is useful for describing a vibrational–rotational problem involving large-amplitude vibrations with high potential barriers.
2. It is available only for treating vibrational–rotational energy levels within a specific vibrational state.
3. Large-amplitude-vibrational functions are constructed from wavefunctions localized at potential minima. In the one-top internal-rotation case, we have three functions localized at the three potential minima, and we express them as $|1\rangle, |2\rangle$ and $|3\rangle$.
4. A kinetic model for describing large-amplitude-vibrations involves more loose restriction than that for the traditional formulation does; only the symmetry requirements should be satisfied. For a one-top internal-rotation problem, for an example, $S^{-1}(0,0,\tau)\boldsymbol{a}_i(\boldsymbol{a}_i$: a constant vector) is replaced by $\boldsymbol{a}_i(\tau)$ in Eqs. 3.4.1 and 3.4.2, and $\boldsymbol{a}_i(\tau + 2\pi/3) = \boldsymbol{a}_i(\tau)$, etc. is imposed.
5. An effective rotational Hamiltonian operator used in a spectral analysis is written from a phenomenological consideration.
6. Quantities determined from the spectral analysis are the tunneling matrix elements expressed as $\langle 1|A|2\rangle$, for an example.
7. The molecular symmetry group which is used in the group theoretical consideration is the permutation–inversion group proposed by Longuet-Higgins [35].

We will describe below (a) the basis set functions for constructing the Hamiltonian matrix, (b) parameterized expressions of the Hamiltonian matrix elements, (c) a note on a least square analysis with the tunneling matrix formulation, and (d)

comparison with the perturbation treatment of the traditional formalism. For simplicity, we restrict the present description mainly to case $\boldsymbol{C}_1(\boldsymbol{G}_3)$ since no essential changes appear for other cases.

Basis Set Functions

Three localized vibrational functions are defined using permutation operations as

$$|1\rangle, |2\rangle = (123)|1\rangle, \quad \text{and} \quad |3\rangle = (132)|1\rangle, \tag{3.4.125}$$

where $|1\rangle$ is a vibrational wavefunction localized at potential minimum 1 in a specific vibrational level. The functions $|1\rangle, |2\rangle$, and $|3\rangle$ thus defined are framework functions localized at framework 1–3, respectively. Symmetrized basis set functions belonging to symmetry species A, E_+, and E_- of the PI group $\boldsymbol{G}_3$ (see Table 3.5) are constructed from these three framework functions:

$$|A; \text{torsion}\rangle = \frac{1}{\sqrt{3(1+2S)}}(|1\rangle + |2\rangle + |3\rangle), \tag{3.4.126}$$

$$|E_+; \text{torsion}\rangle = \frac{1}{\sqrt{3(1-S)}}(|1\rangle + \omega^*|2\rangle + \omega|3\rangle), \tag{3.4.127}$$

$$|E_-; \text{torsion}\rangle = \frac{1}{\sqrt{3(1-S)}}(|1\rangle + \omega|2\rangle + \omega^*|3\rangle), \tag{3.4.128}$$

where

$$\langle 1|1\rangle = \langle 2|2\rangle = \langle 3|3\rangle = 1, \tag{3.4.129}$$

$$\langle 1|2\rangle = \langle 2|1\rangle = \langle 1|3\rangle = \langle 3|1\rangle = \langle 2|3\rangle = \langle 3|2\rangle = S. \tag{3.4.130}$$

When we use PAM coordinate system written in Eqs. 3.4.1 and 3.4.2, Eulerian angles (θ, ϕ, χ) are unchanged under the permutation operation (123), and accordingly the symmetric top rotational function $|J, K\rangle$ is also unchanged. Therefore, a symmetrized torsional–rotational wavefunction belonging to a symmetry species Γ is given by

$$|\Gamma; J, K\rangle = |\Gamma; \text{torsion}\rangle|J, K\rangle. \tag{3.4.131}$$

In passing, let us consider case $\boldsymbol{C}_s(\boldsymbol{G}_6)$ briefly. When we put

$$|1\rangle = \Phi(\tau), \tag{3.4.132}$$

we have

$$(23)^*|1\rangle = (23)^*\Phi(\tau) = \Phi(-\tau). \tag{3.4.133}$$

(*Note*: $\Phi(-\tau) = \Phi(\tau)$ for the $v = 0$ torsional state, $\Phi(-\tau) = -\Phi(\tau)$ for the $v = 1$ torsional state, etc.) On the other hand, from Eq. 3.4.125

$$(23)^*(|1\rangle + |2\rangle + |3\rangle) = (23)^*|1\rangle + (132)(23)^*|1\rangle + (123)(23)^*|1\rangle. \quad (3.4.134)$$

From Eqs. 3.4.133 and 3.4.134, we have

$$(23)^*(|1\rangle + |2\rangle + |3\rangle) = +(|1\rangle + |2\rangle + |3\rangle), \text{for} (23)^*|1\rangle = +|1\rangle \quad (3.4.135)$$

$$(23)^*(|1\rangle + |2\rangle + |3\rangle) = -(|1\rangle + |2\rangle + |3\rangle), \text{ for } (23)^*|1\rangle = -|1\rangle \quad (3.4.136)$$

Accordingly, $|A;\text{torsion}\rangle$ shown in Eq. 3.4.126 is the A_1 or A_2 vibrational wavefunction for case $\boldsymbol{C}_s(\boldsymbol{G}_6)$ according to $(23)^*|1\rangle = +|1\rangle$ or $= -|1\rangle$, respectively. Vibrational functions $|E_+;\text{torsion}\rangle$ and $|E_-;\text{torsion}\rangle$ shown in Eqs. 3.4.127 and 3.4.128 for case $\boldsymbol{C}_1(\boldsymbol{G}_3)$ become pair functions belonging to the degenerate E species for case $\boldsymbol{C}_s(\boldsymbol{G}_6)$.

Expressions of Hamiltonian Matrix Elements

Without a somewhat subtle discussion for eliminating cross terms of angular momentum component operators, we write simply a phenomenological Hamiltonian operator as

$$H = h_v + AJ_z^2 + BJ_x^2 + CJ_y^2 + iqJ_z + irJ_x + isJ_y. \quad (3.4.137)$$

In Eq. 3.4.137, coefficients h_v, A, B, C, q, r, and s are operators (functions) of the variable describing the internal rotation. J_x, J_y, and J_z are all invariant under the $\boldsymbol{G}_3$ group operations, and the coefficient operators belong all to A symmetry species. Hermitian conjugation (†) and time-reversal operation ($*$) are important for obtaining expressions for Hamiltonian matrix elements. The time-reversal operation is operationally equivalent to the complex conjugation. From the fact that the Hamiltonian H is invariant under Hermitian conjugation and time-reversal (complex conjugation), and

$$J_\alpha^\dagger = J_\alpha; J_\alpha^* = -J_\alpha, \quad (3.4.138)$$

where $\alpha = x, y$, and z, we have

$$U^\dagger = U, U^* = U, \quad \text{for } U = h_v, A, B, C, \quad (3.4.139)$$

and

$$V^\dagger = -V, V^* = +V, \quad \text{for } V = q, r, s. \quad (3.4.140)$$

Since the coefficients are of A-symmetry, we obtain the following relations between tunneling matrix elements by using the relations (3.4.139, 3.4.140)

$$\begin{aligned}&\langle 1|U|1\rangle = \langle 2|U|2\rangle = \langle 3|U|3\rangle,\\ &\langle 1|U|2\rangle = \langle 2|U|1\rangle = \langle 1|U|3\rangle = \langle 3|U|1\rangle = \langle 2|U|3\rangle = \langle 3|U|2\rangle,\end{aligned} \tag{3.4.141}$$

and

$$\begin{aligned}&\langle 1|V|1\rangle = \langle 2|V|2\rangle = \langle 3|V|3\rangle = 0,\\ &\langle 1|V|2\rangle = -\langle 2|V|1\rangle = -\langle 1|V|3\rangle = \langle 3|V|1\rangle = \langle 2|V|3\rangle = -\langle 3|V|2\rangle.\end{aligned} \tag{3.4.142}$$

Writing more in detail, for example,

$$\begin{aligned}\langle 1|V|1\rangle &= (\langle 1|V^{\dagger}|1\rangle)^* = \langle 1|V^{\dagger *}|1\rangle = -\langle 1|V|1\rangle = 0,\\ \langle 1|V|2\rangle &= (\langle 2|V^{\dagger}|1\rangle)^* = \langle 2|V^{\dagger *}|1\rangle = -\langle 2|V|1\rangle,\\ \langle 1|V|2\rangle &= (132)\langle 1|V|2\rangle = \langle 3|V|1\rangle = -\langle 1|V|3\rangle,\end{aligned}$$

where we assume $|1\rangle$ to be real.

Using Eqs. 3.4.141 and 3.4.142, we have

$$\begin{aligned}\langle A;J,K|H|A;J,K'\rangle = \frac{1}{1+2S}\big[&(\langle 1|h_v|1\rangle + 2\langle 1|h_v|2\rangle)\delta_{K,K'} + (\langle 1|A|1\rangle\\ &+ 2\langle 1|A|2\rangle)K^2\delta_{K,K'} + (\langle 1|B|1\rangle + 2\langle 1|B|2\rangle)\langle J,K|J_x^2|J,K'\rangle\\ &+ (\langle 1|C|1\rangle + 2\langle 1|C|2\rangle)\langle J,K|J_y^2|J,K'\rangle\big],\end{aligned} \tag{3.4.143}$$

$$\begin{aligned}\langle E_+;J,K|H|E_+;J,K'\rangle = \frac{1}{1-S}\big[&(\langle 1|h_v|1\rangle - \langle 1|h_v|2\rangle)\delta_{K,K'} + (\langle 1|A|1\rangle\\ &-\langle 1|A|2\rangle)K^2\delta_{K,K'} + (\langle 1|B|1\rangle - \langle 1|B|2\rangle)\langle J,K|J_x^2|J,K'\rangle\\ &+ (\langle 1|C|1\rangle - \langle 1|C|2\rangle)\langle J,K|J_y^2|J,K'\rangle + \sqrt{3}\big(\langle 1|q|2\rangle K\delta_{K,K'}\\ &+ \langle 1|r|2\rangle\langle J,K|J_x|J,K'\rangle + \langle 1|s|2\rangle\langle J,K|J_y|J,K'\rangle\big)\big].\end{aligned} \tag{3.4.144}$$

We omit to write the expression for the E_- species since it produces the same energies as the E_+ species does. We call $\langle 1|A|n\rangle (n = 1, 2, 3)$, etc. the tunneling matrix elements. We note that there is no contribution from the s term of (3.4.137), in case $\boldsymbol{C}_s(\boldsymbol{G}_6)$ (the symmetry plane is assumed to be the xz-plane).

Note on a Least Square Analysis with the Tunneling Matrix Formulation

For the purpose of using Eqs. 3.4.143, 3.4.144 for the spectral analysis, it is convenient to use $A_{11}, A_{12}, \ldots, q_{12}, r_{12}$, and s_{12} defined in Eq. 3.4.145 below as adjustable parameters in the least squares analysis since Eqs. 3.4.143, 3.4.144 include the overlap integral S in addition to tunneling matrix elements. Although various ways are possible, the definition shown below is considered to be favorable since they are approximately equivalent to the tunneling matrix elements because of the small S value.

$$
\begin{aligned}
\frac{1}{1+2S}(\langle 1|A|1\rangle + 2\langle 1|A|2\rangle) &= A_{11} + 2A_{12} \\
\frac{1}{1-S}(\langle 1|A|1\rangle - \langle 1|A|2\rangle) &= A_{11} - A_{12} \\
\frac{1}{1+2S}(\langle 1|B|1\rangle + 2\langle 1|B|2\rangle) &= B_{11} + 2B_{12} \\
\frac{1}{1-S}(\langle 1|B|1\rangle - \langle 1|B|2\rangle) &= B_{11} - B_{12} \\
\frac{1}{1+2S}(\langle 1|C|1\rangle + 2\langle 1|C|2\rangle) &= C_{11} + 2C_{12} \\
\frac{1}{1-S}(\langle 1|C|1\rangle - \langle 1|C|2\rangle) &= C_{11} - C_{12} \\
\frac{1}{1-S}\langle 1|q|2\rangle &= q_{12} \\
\frac{1}{1-S}\langle 1|r|2\rangle &= r_{12} \\
\frac{1}{1-S}\langle 1|s|2\rangle &= s_{12}
\end{aligned}
\tag{3.4.145}
$$

For examples, A_{11} and A_{12} to be determined in the least squares analysis are connected with the tunneling matrix elements by

$$
\begin{aligned}
A_{11} &= \frac{1}{3}\left(\frac{1}{1+2S} + \frac{2}{1-S}\right)\langle 1|A|1\rangle + \frac{1}{3}\left(\frac{2}{1+2S} - \frac{2}{1-S}\right)\langle 1|A|2\rangle, \\
A_{12} &= \frac{1}{3}\left(\frac{1}{1+2S} - \frac{1}{1-S}\right)\langle 1|A|1\rangle + \frac{1}{3}\left(\frac{2}{1+2S} + \frac{1}{1-S}\right)\langle 1|A|2\rangle.
\end{aligned}
\tag{3.4.146}
$$

Another way for avoiding inconvenient non-zero overlap integrals among the framework functions is to use newly defined framework functions $|n:\mathrm{new}\rangle$ $(n = 1, 2, 3)$ which are orthogonal with each other. The new framework functions $|n:\mathrm{new}\rangle (n = 1, 2, 3)$ are obtained by an appropriate transformation from the framework functions $|n\rangle (n = 1, 2, 3)$ defined above as the functions localized at potential minima. In the formalism using $|n:\mathrm{new}\rangle$ in place of $|n\rangle$, tunneling matrix elements $\langle 1|A|n\rangle$, etc. are placed simply by $\langle 1:\mathrm{new}|A|n:\mathrm{new}\rangle$, etc. and all the overlap integrals vanish in the Hamiltonian matrix element expressions given in Eqs. 3.4.143, 3.4.144. The transformation from $|n\rangle$ to $|n:\mathrm{new}\rangle$ is given briefly in the Appendix (Sect. 3.4.5) for the general case of the tunneling matrix formalism.

Comparison with the Perturbation Treatment in the Traditional Formulation

The expressions Eqs. 3.4.143, 3.4.144 in the tunneling matrix formulation are equivalent to the expressions Eqs. 3.4.122–3.4.124 for the effective rotational Hamiltonian in the traditional treatment. Comparing Eqs. 3.4.143, 3.4.144 with Eqs. 3.4.122–3.4.124, we have relations

$$
\begin{aligned}
2\langle 1|h_v|2\rangle &\approx \langle v;A|Fp_\tau^2 + V(\tau)|v;A\rangle,\\
-\langle 1|h_v|2\rangle &\approx \langle v;E|Fp_\tau^2 + V(\tau)|v;E\rangle,\\
2\langle 1|A|2\rangle &\approx F\rho_z^2\left(1 + 4F\sum_{v'\neq v}\frac{|\langle v;A|p_\tau|v';A\rangle|^2}{E_{v;A} - E_{v';A}}\right),\\
-\langle 1|A|2\rangle &\approx F\rho_z^2\left(1 + 4F\sum_{v'\neq v}\frac{|\langle v;E|p_\tau|v';E|^2}{E_{v;E} - E_{v';E}}\right), \text{etc.},\\
\sqrt{3}\langle 1|q|2\rangle &\approx -2F\rho_z\langle v;E|p_\tau|v;E\rangle,\\
\sqrt{3}\langle 1|r|2\rangle &\approx -2F\rho_x\langle v;E|p_\tau|v;E\rangle,\\
\sqrt{3}\langle 1|s|2\rangle &\approx -2F\rho_y\langle v;E|p_\tau|v;E\rangle.
\end{aligned}
\tag{3.4.147}
$$

The following relations will be practically useful for obtaining information on the internal-rotation potential:

$$
\begin{aligned}
3A_{12} &= 4F^2\rho_z^2\sum_{v'\neq v}\frac{|\langle v;A|p_\tau|v';A\rangle|^2}{E_{v;A} - E_{v';A}} - 4F^2\rho_z^2\sum_{v'\neq v}\frac{|\langle v;E|p_\tau|v';E\rangle|^2}{E_{v;E} - E_{v';E}}, \text{etc.},\\
\sqrt{3}q_{12} &= -2F\rho_z\langle v;E|p_\tau|v;E\rangle, \text{etc.}
\end{aligned}
\tag{3.4.148}
$$

3.4.1.9 Transition Selection Rules

We mention briefly the overall selection rule of the electric dipole transition. When the transition $|\Phi_i\rangle \rightarrow |\Phi_j\rangle$ occurs, the electric dipole transition moment defined by

$$
M_{ij} = \langle \Phi_i|\mu_Z|\Phi_j\rangle = \int \Phi_i^*\mu_Z\Phi_j\,\mathrm{d}V \tag{3.4.149}
$$

has a non-zero value. In Eq. 3.4.149, μ_Z is the laboratory-fixed Z-component of the electric dipole moment operator. According to a theorem of group theory, $\Phi_i^*\mu_Z\Phi_j$ involves the totally symmetric property for non-zero M_{ij}.

For a molecule of $\boldsymbol{C}_1(\boldsymbol{G}_3)$ symmetry, μ_Z is of A-symmetry species. Thus, the overall selection rules are

$$
A \leftrightarrow A,\ E \leftrightarrow E\,(E_+ \leftrightarrow E_+, E_- \leftrightarrow E_-). \tag{3.4.150}
$$

(Usually $E \leftrightarrow E$ is used since the E_+ and E_- states are degenerate.)

For a molecule of $\boldsymbol{C}_s(\boldsymbol{G}_6)$ symmetry, μ_Z is of A_2-symmetry species, and the overall selection rule are

$$
A_1 \leftrightarrow A_2,\ E \leftrightarrow E. \tag{3.4.151}
$$

It should be noted that $A - E$ splittings cannot be obtained directly from any usual spectral observation.

3.4.2 Two-Top Internal-Rotation Problem

Considering a possibility that signals from molecules with two methyl groups are observed astronomically, we describe torsional–rotational problem of molecules with two methyl internal rotors in this section. In the present article only asymmetric top molecules with two methyl internal rotors are treated, and symmetric top molecules such as ethane (C_2H_6) are not treated. Molecules with two inequivalent methyl tops and those with two equivalent methyl tops will be discussed below separately.

3.4.2.1 Case of a Molecule with Two Inequivalent Methyl Internal Rotors

Group Theoretical Treatment

We treat here two cases: a molecule of $\boldsymbol{C}_1$ symmetry and of $\boldsymbol{C}_s$ symmetry. In Figs. 3.30 and 3.31, a $\boldsymbol{C}_1$ molecule and a $\boldsymbol{C}_s$ molecule with two inequivalent methyl groups are shown, respectively. The PI group for the molecule of $\boldsymbol{C}_1$ symmetry with two inequivalent methyl internal rotors is $\boldsymbol{G}_9$. The symmetry of this kind of molecule is denoted as $\boldsymbol{C}_1(\boldsymbol{G}_9)$. Similarly, the symmetry of the molecule of $\boldsymbol{C}_s$ symmetry with two inequivalent methyl internal rotors is denoted as $\boldsymbol{C}_s(\boldsymbol{G}_{18})$.

Character Table. We denote protons in one methyl group by 1, 2, 3 and the other methyl protons by 4, 5, 6 (see Figs. 3.30 and 3.31). In Table 3.11, the character table of the permutation–inversion group $\boldsymbol{G}_9$ for the $\boldsymbol{C}_1$ molecule is given, and the character table of $\boldsymbol{G}_{18}$ for the $\boldsymbol{C}_s$ molecule is given in Table 3.12.

The two symmetry species in each of four pairs, (E_{1+}, E_{1-}), (E_{2+}, E_{2-}), (E_{3+}, E_{3-}) and (E_{4+}, E_{4-}), appearing in Table 3.11 are group theoretically of different symmetry species but degenerate energetically (separable degeneracy),

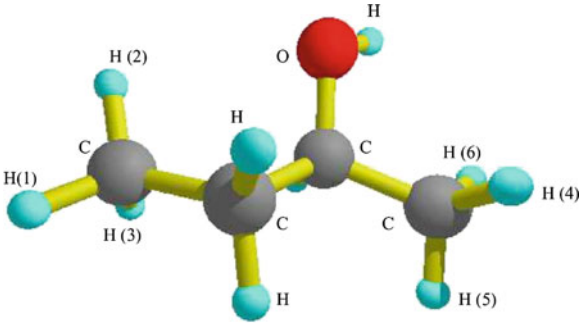

Fig. 3.30 2-Butanol, an example of a $\boldsymbol{C}_1$ molecule with inequivalent two methyl groups

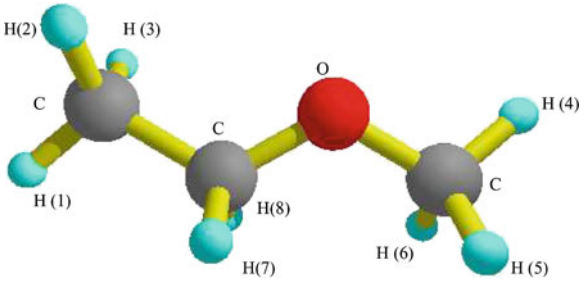

Fig. 3.31 Ethylmethylether, an example of a $\boldsymbol{C}_s$ molecule with inequivalent two methyl groups

Table 3.11 Character table for the PI group $\boldsymbol{G}_9$ of a $\boldsymbol{C}_1$ molecule with two inequivalent methyl tops

	E	(123)	(132)	(456)	(465)	P^a	Q^a	R^a	S^a
A	1	1	1	1	1	1	1	1	1
E_1									
E_{1+}	1	ω	ω^*	1	1	ω	ω	ω^*	ω^*
E_{1-}	1	ω^*	ω	1	1	ω^*	ω^*	ω	ω
E_2									
E_{2+}	1	1	1	ω	ω^*	ω	ω^*	ω	ω^*
E_{2-}	1	1	1	ω^*	ω	ω^*	ω	ω^*	ω
E_3									
E_{3+}	1	ω	ω^*	ω	ω^*	ω^*	1	1	ω
E_{3-}	1	ω^*	ω	ω^*	ω	ω	1	1	ω^*
E_4									
E_{4+}	1	ω	ω^*	ω^*	ω	1	ω^*	ω	1
E_{4-}	1	ω^*	ω	ω	ω^*	1	ω	ω^*	1

$\omega = \exp(i2\pi/3)$
[a] $P = (123)(456), Q = (123)(465), R = (132)(456), S = (132)(465)$

and the four pairs are combined to E_1, E_2, E_3 and E_4, respectively. Nine operations $(23)(56)(78)^*, (13)(56)(78)^*$, etc. in Table 3.12 correspond to the reflection in the plane of symmetry at an equilibrium configuration of the ethylmethylether molecule, which is an example of a molecule of $\boldsymbol{C}_s$ symmetry having inequivalent two methyl groups.

Transition Selection Rules. Overall selection rules are as follows: electric dipole transitions occur between states with same symmetry species except for $A_1 \leftrightarrow A_2$ in a $\boldsymbol{C}_s$ molecule. Accordingly, splittings produced by internal-rotation motion are not obtained directly from any usual spectral observation.

Coordinate System and Transformation Properties of Variables. Next, let us consider the coordinate system for the two-methyl top case and transformation properties of variables appearing in the equations which represent the coordinate system. We consider only the PAM system since the RAM and IAM systems are impossible for the two-top problem except for very rare cases. The equations for the two-top case corresponding to Eqs. 3.4.1, 3.4.2 for the one-top case are given by

Table 3.12 Character table for the PI group $\boldsymbol{G}_{18}$ of a $\boldsymbol{C}_s$ molecule with two inequivalent methyl tops

	E	(123) (132)	(456) (465)	(123)(456) (132)(465)	(123)(465) (132)(456)	P^{a}
A_1	1	1	1	1	1	1
A_2	1	1	1	1	1	−1
E_1	2	−1	2	−1	−1	0
E_2	2	2	−1	−1	−1	0
E_3	2	−1	−1	−1	2	0
E_4	2	−1	−1	2	−1	0

[a] $P = \{(23)(56)(78)^*,\ (13)(56)(78)^*,\ (12)(56)(78)^*(23)(46)(78)^*,$
$(13)(46)(78)^*,\ (12)(46)(78)^*(23)(45)(78)^*,\ (13)(45)(78)^*,\ (12)(45)(78)^*\}$

$$\boldsymbol{R}_i = \boldsymbol{R} + S^{-1}(\theta,\phi,\chi)\big\{S^{-1}(\theta_{\mathrm{P1}},\phi_{\mathrm{P1}},\chi_{\mathrm{P1}})S^{-1}(0,0,\tau_1)S^{+1}(\theta_{\mathrm{P1}},\phi_{\mathrm{P1}},\chi_{\mathrm{P1}}) \big[\boldsymbol{a}_i + \boldsymbol{d}_i - \boldsymbol{A}_{\mathrm{top1}}\big] + \boldsymbol{A}_{\mathrm{top1}}\big\}, \tag{3.4.152}$$

for protons in methyl group 1 (top1: $i = 1, 2, 3$),

$$\boldsymbol{R}_i = \boldsymbol{R} + S^{-1}(\theta,\phi,\chi)\big\{S^{-1}(\theta_{\mathrm{P2}},\phi_{\mathrm{P2}},\chi_{\mathrm{P2}})S^{-1}(0,0,\tau_2)S^{+1}(\theta_{\mathrm{P2}},\phi_{\mathrm{P2}},\chi_{\mathrm{P2}}) \big[\boldsymbol{a}_i + \boldsymbol{d}_i - \boldsymbol{A}_{\mathrm{top2}}\big] + \boldsymbol{A}_{\mathrm{top2}}\big\}, \tag{3.4.153}$$

for protons in methyl group 2 (top2: $i = 4, 5, 6$),

$$\boldsymbol{R}_i = \boldsymbol{R} + S^{-1}(\theta,\phi,\chi)(\boldsymbol{a}_i + \boldsymbol{d}_i). \tag{3.4.154}$$

for the other nuclei, where $\boldsymbol{a}_i$ and $\boldsymbol{d}_i$, represent the equilibrium positions and small-amplitude displacements with vector components in the PAM x, y, z-axis system. A_{top1} and A_{top2} represent centers of mass of three protons in methyl group 1 and methyl group 2, respectively. We consider the axis system (x_1, y_1, z_1) fixed to the methyl top 1 where the origin is in the center of mass of the methyl top 1 and the z_1-axis is along the C_3-axis of the methyl top 1. The rotation matrix $S^{+1}(\theta_{\mathrm{P1}},\phi_{\mathrm{P1}},\chi_{\mathrm{P1}})$ rotates the (x_1, y_1, z_1)-axes so that the (x_1, y_1, z_1)-axes are parallel to the PAM (x, y, z)-axes. The rotation matrix $S^{+1}(\theta_{\mathrm{P2}},\phi_{\mathrm{P2}},\chi_{\mathrm{P2}})$ is the corresponding one for the methyl top 2. We assume $\boldsymbol{C}_3$ symmetry of the methyl group and therefore

$$\begin{aligned}
S^{-1}(0,0,2\pi/3)S^{+1}(\theta_{\mathrm{P1}},\phi_{\mathrm{P1}},\chi_{\mathrm{P1}})\big[\boldsymbol{a}_1 - \boldsymbol{A}_{\mathrm{top1}}\big] &= S^{+1}(\theta_{\mathrm{P1}},\phi_{\mathrm{P1}},\chi_{\mathrm{P1}})\big[\boldsymbol{a}_2 - \boldsymbol{A}_{\mathrm{top1}}\big],\\
S^{-1}(0,0,2\pi/3)S^{+1}(\theta_{\mathrm{P1}},\phi_{\mathrm{P1}},\chi_{\mathrm{P1}})\big[\boldsymbol{a}_2 - \boldsymbol{A}_{\mathrm{top1}}\big] &= S^{+1}(\theta_{\mathrm{P1}},\phi_{\mathrm{P1}},\chi_{\mathrm{P1}})\big[\boldsymbol{a}_3 - \boldsymbol{A}_{\mathrm{top1}}\big],\\
S^{-1}(0,0,2\pi/3)S^{+1}(\theta_{\mathrm{P1}},\phi_{\mathrm{P1}},\chi_{\mathrm{P1}})\big[\boldsymbol{a}_3 - \boldsymbol{A}_{\mathrm{top1}}\big] &= S^{+1}(\theta_{\mathrm{P1}},\phi_{\mathrm{P1}},\chi_{\mathrm{P1}})\big[\boldsymbol{a}_1 - \boldsymbol{A}_{\mathrm{top1}}\big],\\
S^{-1}(0,0,2\pi/3)S^{+1}(\theta_{\mathrm{P2}},\phi_{\mathrm{P2}},\chi_{\mathrm{P2}})\big[\boldsymbol{a}_4 - \boldsymbol{A}_{\mathrm{top2}}\big] &= S^{+1}(\theta_{\mathrm{P2}},\phi_{\mathrm{P2}},\chi_{\mathrm{P2}})\big[\boldsymbol{a}_5 - \boldsymbol{A}_{\mathrm{top2}}\big],\\
S^{-1}(0,0,2\pi/3)S^{+1}(\theta_{\mathrm{P2}},\phi_{\mathrm{P2}},\chi_{\mathrm{P2}})\big[\boldsymbol{a}_5 - \boldsymbol{A}_{\mathrm{top2}}\big] &= S^{+1}(\theta_{\mathrm{P2}},\phi_{\mathrm{P2}},\chi_{\mathrm{P2}})\big[\boldsymbol{a}_6 - \boldsymbol{A}_{\mathrm{top2}}\big],\\
S^{-1}(0,0,2\pi/3)S^{+1}(\theta_{\mathrm{P2}},\phi_{\mathrm{P2}},\chi_{\mathrm{P2}})\big[\boldsymbol{a}_6 - \boldsymbol{A}_{\mathrm{top2}}\big] &= S^{+1}(\theta_{\mathrm{P2}},\phi_{\mathrm{P2}},\chi_{\mathrm{P2}})\big[\boldsymbol{a}_4 - \boldsymbol{A}_{\mathrm{top2}}\big],
\end{aligned} \tag{3.4.155}$$

Table 3.13 Transformation properties of variables in the right of Eqs. 3.4.152–3.4.154 under generating operations[a] of $\boldsymbol{G}_9$ and $\boldsymbol{G}_{18}$

	$\boldsymbol{R}$ (translation)	θ, ϕ, χ (rotation)	τ_1 (internal rotation)	τ_2 (internal rotation)
(123)	$\boldsymbol{R}$	θ, ϕ, χ	$\tau_1 + 2\pi/3$	τ_2
(456)	$\boldsymbol{R}$	θ, ϕ, χ	τ_1	$\tau_2 + 2\pi/3$
$(23)(56)(78)^*$	$-\boldsymbol{R}$	$\pi - \theta, \pi + \phi, \pi - \chi$	$-\tau_1$	$-\tau_2$

[a]Generating operations of $\boldsymbol{G}_9$ are (123) and (456), and generating operations of $\boldsymbol{G}_{18}$ are (123), (456), and $(23)(56)(78)^*$

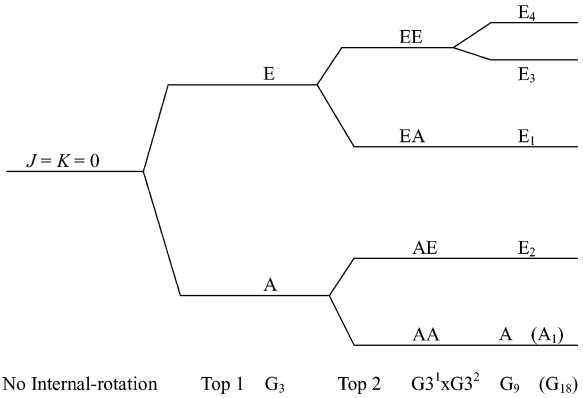

Fig. 3.32 Internal-rotation energy level diagram in the ground vibrational state (the $J = K = 0$ level) is illustrated schematically for the inequivalent-two-top case

For a $\boldsymbol{C}_s$ molecule, we set $\chi_{P1} = \phi_{P1} = 0$ and $\chi_{P2} = \phi_{P2} = 0$, assuming the plane of symmetry to be the xz-plane. Transformation properties of variables in Eqs. 3.4.152–3.4.154 under generating operations of the PI group $\boldsymbol{G}_9$ and $\boldsymbol{G}_{18}$ are shown in Table 3.13. The transformation properties under the generating operations (123) and (456) are the same for $\boldsymbol{G}_9$ and $\boldsymbol{G}_{18}$. We drop small-amplitude displacements $\boldsymbol{d}_i$ in Table 3.13 since we consider here only the large-amplitude internal rotation.

3.4.2.2 Energy Level Splitting Pattern

A qualitative energy level diagram for the two-top problem is illustrated for $J = K = 0$ in Fig. 3.32. The $J = K = 0$ level at the left is first split into an A and E component by internal-rotation motion of top 1. Each of these levels is then split again into A and E component by internal-rotation motion of top 2. Finally, the apparently fourfold degenerate level indicated as EE is split into two degenerate levels (E_3, E_4) by top–top interaction.

3.4.2.3 Hamiltonian Operator

In the same way that we have obtained Eq. 3.4.9 for a one-top case, we have the following expression for a PAM classical kinetic energy of a molecule with two methyl internal rotors

$$T = \frac{1}{2}\sum_{\alpha=x,y,z} I_\alpha \omega_\alpha^2 + \frac{1}{2} I_{\tau_1} \dot{\tau}_1^2 + I_{\tau_1}\dot{\tau}_1 \sum_{\alpha=x,y,z} \lambda_{1\alpha}\omega_{1\alpha} + \frac{1}{2} I_{\tau_2}\dot{\tau}_2^2 + I_{\tau_2}\dot{\tau}_2 \sum_{\alpha=x,y,z} \lambda_{2\alpha}\omega_{2\alpha}, \tag{3.4.156}$$

where $I_\alpha (\alpha = x, y, z)$ are the principal moments of inertia of the molecule, I_{τ_1} and I_{τ_2} are the inertial moments of methyl top 1 and top 2 about their C_3 axes, respectively, and $\lambda_{1\alpha}$ and $\lambda_{2\alpha}$ $(\alpha = x, y, z)$ are the direction cosines of the C_3 axes of top 1 and top 2, respectively.

By the same procedure employed in the one-top case, Eqs. 3.4.9–3.4.14, we have the following classical kinetic energy expression written in terms of the momenta conjugate to the variables representing the overall rotation and the methyl internal rotations:

$$\begin{aligned} T = &\sum_{\alpha=x,y,z} \frac{1}{2I_\alpha} J_\alpha^2 + F_1(p_1 - \pi_1)^2 + F_2(p_2 - \pi_2)^2 \\ &+ F_{12}[(p_1 - \pi_1)(p_2 - \pi_2) + (p_2 - \pi_2)(p_1 - \pi_1)] \end{aligned} \tag{3.4.157}$$

where

$$\begin{aligned} \pi_1 &= \sum_{\alpha=x,y,z} \rho_{1\alpha} J_\alpha, \\ \pi_2 &= \sum_{\alpha=x,y,z} \rho_{2\alpha} J_\alpha, \\ F_1 &= \frac{R_2}{2(R_1R_2 - Q^2)I_{\tau_1}}, \\ F_2 &= \frac{R_1}{2(R_1R_2 - Q^2)I_{\tau_2}}, \\ F_{12} &= -\frac{Q}{2(R_1R_2 - Q^2)\sqrt{I_{\tau_1}I_{\tau_2}}}, \end{aligned} \tag{3.4.158}$$

with

$$\begin{aligned} \rho_{1\alpha} &= \lambda_{1\alpha} I_{\tau_1}/I_\alpha, (\alpha = x, y, z) \\ \rho_{2\alpha} &= \lambda_{2\alpha} I_{\tau_2}/I_\alpha, (\alpha = x, y, z) \\ R_1 &= 1 - \sum_{\alpha=x,y,z} \rho_{1\alpha}\lambda_{1\alpha}, \\ R_2 &= 1 - \sum_{\alpha=x,y,z} \rho_{2\alpha}\lambda_{2\alpha}, \\ Q &= -\sum_{\alpha=x,y,z} \lambda_{1\alpha}\lambda_{2\alpha}\sqrt{I_{\tau_1}I_{\tau_2}}/I_\alpha, \end{aligned} \tag{3.4.159}$$

The quantum mechanical PAM Hamiltonian operator is obtained by replacing $J_\alpha(\alpha = x, y, z), p_1$ and p_2 in Eq. 3.4.157 with the quantum mechanical angular momentum operators

$$J_z = -i\hbar\frac{\partial}{\partial\chi}, \text{ etc.},$$
$$p_i = -i\hbar\frac{\partial}{\partial\tau_i} \quad (i = 1, 2),$$

and by adding the potential function $V(\tau_1, \tau_2)$ to T. That is

$$H = AJ_z^2 + BJ_x^2 + CJ_y^2 + F_1(p_1 - \pi_1)^2 + F_2(p_2 - \pi_2)^2 + F_{12}[(p_1 - \pi_1)(p_2 - \pi_2) + (p_2 - \pi_2)(p_1 - \pi_1)] + V(\tau_1, \tau_2), \tag{3.4.160}$$

where $A = 1/(2I_z), B = 1/(2I_x), C = 1/(2I_y)$.

The kinetic energy part of the Hamiltonian operator Eq. 3.4.160 includes in principle nine independent parameters: A, B, C, I_1, I_2, two of $(\lambda_{1x}, \lambda_{1y}, \lambda_{1z})$, and two of $(\lambda_{2x}, \lambda_{2y}, \lambda_{2z})$. On the other hand, from the standpoint of a practical spectral analysis it may be convenient to use more phenomenological Hamiltonian operator shown below although it involves more parameters:

$$H = A'J_{z'}^2 + B'J_{x'}^2 + C'J_{y'}^2 + f_1p_1^2 + f_2p_2^2 + 2f_{12}p_1p_2 + q_1J_{z'}p_1 + q_2J_{z'}p_2 + r_1J_{x'}p_1 + r_2J_{x'}p_2 + s_1J_{y'}p_1 + s_2J_{y'}p_2 + V(\tau_1, \tau_2), \tag{3.4.161}$$

Relations between the kinetic energy parameters appearing in Eqs. 3.4.160 and 3.4.161 can be obtained by comparing coefficients of corresponding quadratic terms of angular momenta in the two equations, after performing a rotation which relates the x, y, z-principal axes in Eq. 3.4.160 to the x', y', z'-axes in Eq. 3.4.161 according to the equation

$$\begin{pmatrix} x' \\ y' \\ z' \end{pmatrix} = S^{-1}(\theta_n, \phi_n, \chi_n)\begin{pmatrix} x \\ y \\ z \end{pmatrix}, \tag{3.4.162}$$

The relations between three pairs of parameters in Eqs. 3.4.160 and 3.4.161 are independent of θ_n, ϕ_n, and χ_n:

$$f_1 = F_1, f_2 = F_2, f_{12} = F_{12}. \tag{3.4.163}$$

For the rest parameters we find

$$\begin{pmatrix} A' & 0 & 0 \\ 0 & B' & 0 \\ 0 & 0 & C' \end{pmatrix} = S^{-1}(\theta_n, \phi_n, \chi_n) \begin{pmatrix} A_{xx} & A_{xy} & A_{xz} \\ A_{xy} & A_{yy} & A_{yz} \\ A_{xz} & A_{yz} & A_{zz} \end{pmatrix} S^{+1}(\theta_n, \phi_n, \chi_n),$$

$$[r_1, s_1, q_1] = \left[-2(F_1\rho_{1x} + F_{12}\rho_{2x}), -2\left(F_1\rho_{1y} + F_{12}\rho_{2y}\right), -2\left(F_1\rho_{1z} + F_{12}\rho_{2z}\right)\right] S^{+1}(\theta_n, \phi_n, \chi_n),$$

$$[r_2, s_2, q_2] = \left[-2(F_2\rho_{2x} + F_{12}\rho_{1x}), -2\left(F_2\rho_{2y} + F_{12}\rho_{1y}\right), -2\left(F_2\rho_{2z} + F_{12}\rho_{1z}\right)\right] S^{+1}(\theta_n, \phi_n, \chi_n), \tag{3.4.164}$$

with

$$\begin{aligned} A_{\alpha\alpha} &= (1/2I_\alpha) + F_1\rho_{1\alpha}^2 + F_2\rho_{2\alpha}^2 + 2F_{12}\rho_{1\alpha}\rho_{2\alpha} \\ &\quad (\alpha = x, y, z), \\ A_{\alpha\beta} &= F_1\rho_{1\alpha}\rho_{1\beta} + F_2\rho_{2\alpha}\rho_{2\beta} + F_{12}\left(\rho_{1\alpha}\rho_{2\beta} + \rho_{2\alpha}\rho_{1\beta}\right) \\ &\quad (\alpha, \beta = x, y; y, z; x, z). \end{aligned} \tag{3.4.165}$$

When a spectral analysis is made with Eq. 3.4.161, the quantities on the left of Eqs. 3.4.163 and 3.4.164 will be determined in a least squares fit. From the point of view of the PAM quantities on the right, Eqs. 3.4.163–3.4.164 represent 15 non-linear equations in the 15 unknowns: $F_1, F_2, F_{12}, A, B, C, \rho_{1x}, \rho_{1y}, \rho_{1z}, \rho_{2x}, \rho_{2y}, \rho_{2z}$, θ_n, ϕ_n, and χ_n. By substituting values of $A, B, C, \rho_{1x}, \rho_{1y}, \rho_{1z}, \rho_{2x}, \rho_{2y}, \rho_{2z}$, in the six equations of the first line of Eq. 3.4.159 and by using equality,

$$\lambda_{1x}^2 + \lambda_{1y}^2 + \lambda_{1z}^2 = \lambda_{2x}^2 + \lambda_{2y}^2 + \lambda_{2z}^2 = 1, \tag{3.4.166}$$

we can obtain values of eight quantities $\lambda_{1x}, \lambda_{1y}, \lambda_{1z}, \lambda_{2x}, \lambda_{2y}, \lambda_{2z}, I_{\tau_1}$, and I_{τ_2}. Since we can calculate values of F_1, F_2 and F_{12} by using these eight quantities and Eqs. 3.4.158 and 3.4.159, a consistency check is possible, and we can estimate to what extent the PAM model is reproduced by the phenomenological Hamiltonian.

The jet-cooled Fourier-transform microwave spectrum of *N*-methyl-acetamide ($CH_3{-}NH{-}C(=O){-}CH_3$), which contains two inequivalent methyl tops with relatively low barriers to internal rotation, was analyzed successfully with the use of the phenomenological Hamiltonian operator of type of Eq. 3.4.161, adding higher order terms of rotation, torsion, and torsion-rotation terms [49]. Since the *N*-methyl-acetamide has a plane of symmetry at an equilibrium, the term $s_1J_yp_1 + s_2J_yp_2$ is eliminated in Eq. 3.4.161, and we can set $\chi_n = \phi_n = 0$ in Eqs. 3.4.162 and 3.4.164.

In Fig. 3.33, examples of observed transitions of *N*-methyl-acetamide ($CH_3NH{-}C(=O){-}CH_3$), [49], are shown in a schematic torsional–rotational energy level diagram in its ground vibrational state.

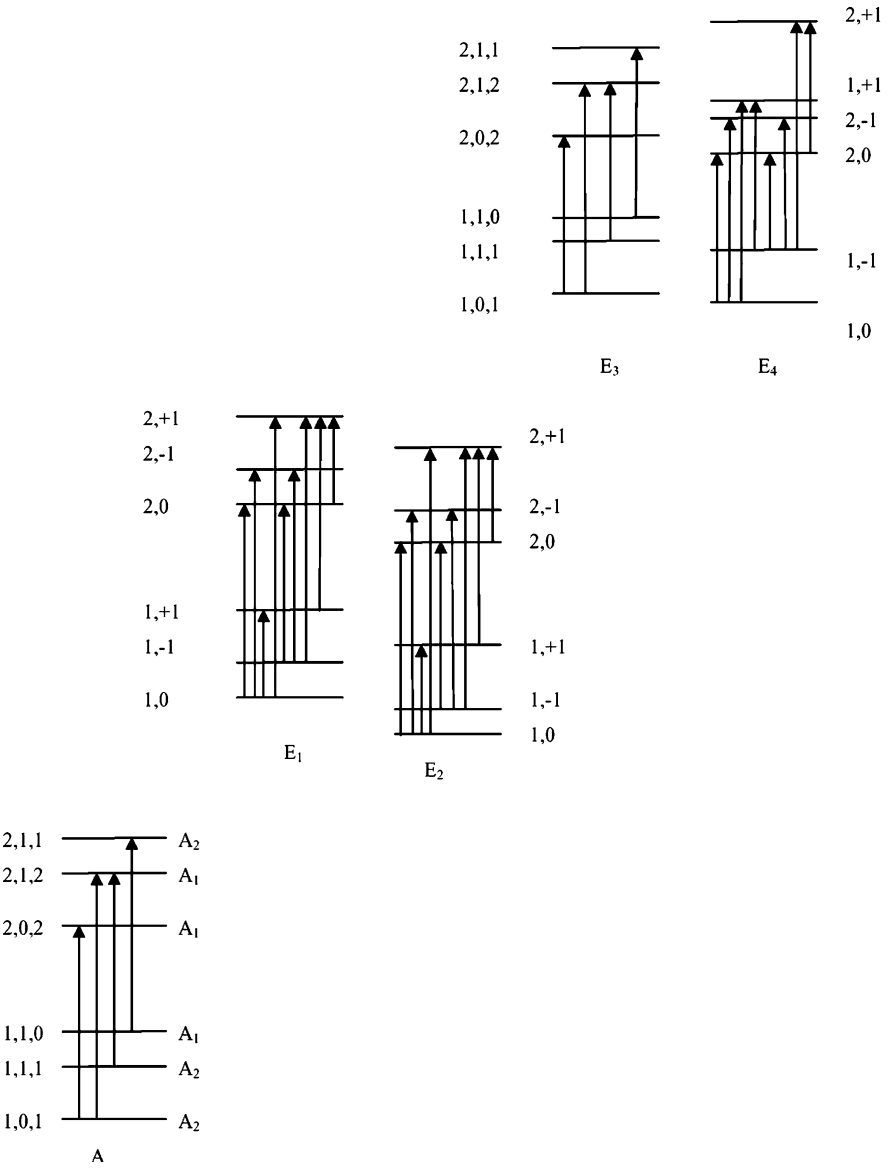

Fig. 3.33 The torsional–rotational energy level diagram of *N*-methyl-acetamide in the ground vibrational state is shown with observed transitions [49]. In order to designate rotational levels, quantum numbers J, K_a, K_c for an asymmetric top molecule are used for levels of *A*- and E_3-symmetry species, and *J* and *K* are used for E_1-, E_2-, and E_4-symmetry levels

3.4.2.4 Basis Set Wavefunctions and Hamiltonian Matrix Elements

In order to construct the Hamiltonian matrix, we use wavefunctions of a form

$$|m_1(1)\rangle|m_2(2)\rangle|J,K\rangle, \tag{3.4.167}$$

i.e., a product of a two-top free rotor wavefunction $|m_1(1)\rangle|m_2(2)\rangle$ and a symmetric top rotational wavefunction $|J,K\rangle$. Here, free rotor wavefunctions $|m_1(1)\rangle$ and $|m_2(2)\rangle$ are given by

$$|m_1(1)\rangle = \frac{1}{\sqrt{2\pi}}\exp(im_1\tau_1), \tag{3.4.168}$$

$$|m_2(2)\rangle = \frac{1}{\sqrt{2\pi}}\exp(im_2\tau_2), \tag{3.4.169}$$

Basis Set Functions for the $C_1(G_9)$ Case

By noting that

$$\begin{aligned}&(123)|m_1(1)\rangle = \omega^{m_1}|m_1(1)\rangle, (123)|m_2(2)\rangle = |m_2(2)\rangle, (123)|J,K\rangle = |J,K\rangle,\\ &(456)|m_1(1)\rangle = |m_1(1)\rangle, (456)|m_2(2)\rangle = \omega^{m_2}|m_2(2)\rangle, (456)|J,K\rangle = |J,K\rangle,\end{aligned} \tag{3.4.170}$$

where $\omega = exp(i2\pi/3)$, we have the following basis set functions belonging to each of symmetry species of $\boldsymbol{G}_9$:

$$\begin{aligned}
&|m_1,m_2;J,K\rangle \quad \text{for } m_1 = 3n; m_2 = 3n' && : A \text{ symmetry species},\\
&|m_1,m_2;J,K\rangle \quad \text{for } m_1 = 3n+1; m_2 = 3n' && : E_{1+} \text{symmetry species},\\
&|m_1,m_2;J,K\rangle \quad \text{for } m_1 = 3n-1; m_2 = 3n' && : E_{1-} \text{symmetry species},\\
&|m_1,m_2;J,K\rangle \quad \text{for } m_1 = 3n; m_2 = 3n'+1 && : E_{2+} \text{symmetry species},\\
&|m_1,m_2;J,K\rangle \quad \text{for } m_1 = 3n; m_2 = 3n'-1 && : E_{2-} \text{symmetry species},\\
&|m_1,m_2;J,K\rangle \quad \text{for } m_1 = 3n+1; m_2 = 3n'+1 && : E_{3+} \text{symmetry species},\\
&|m_1,m_2;J,K\rangle \quad \text{for } m_1 = 3n-1; m_2 = 3n'-1 && : E_{3-} \text{symmetry species},\\
&|m_1,m_2;J,K\rangle \quad \text{for } m_1 = 3n+1; m_2 = 3n'-1 && : E_{4+} \text{symmetry species},\\
&|m_1,m_2;J,K\rangle \quad \text{for } m_1 = 3n-1; m_2 = 3n'+1 && : E_{4-} \text{symmetry species},
\end{aligned} \tag{3.4.171}$$

where $|m_1,m_2;J,K\rangle \equiv |m_1(1)\rangle|m_2(2)\rangle|J,K\rangle$, and $n = 0,\pm1,\pm2,\ldots; n' = 0,\pm1,\pm2,\ldots$.

Basis Set Functions for Case $\boldsymbol{C}_s(\boldsymbol{G}_{18})$

For case $\boldsymbol{C}_s(\boldsymbol{G}_{18}), A_1$ and A_2 species basis functions are given by

$$|A_1; m_1, m_2; J, K\rangle = \frac{1}{\sqrt{2}}\big[|m_1(1)\rangle|m_2(2)\rangle|J, K\rangle + (-1)^{J-K}|-m_1(1)\rangle|-m_2(2)\rangle|J, -K\rangle\big], \tag{3.4.172}$$

$$|A_2; m_1, m_2; J, K\rangle = \frac{1}{\sqrt{2}}\big[|m_1(1)\rangle|m_2(2)\rangle|J, K\rangle - (-1)^{J-K}|-m_1(1)\rangle|-m_2(2)\rangle|J, -K\rangle\big], \tag{3.4.173}$$

where $m_1 = 3n, m_2 = 3n'(n = 0, \pm1, \pm2, \ldots; n' = 0, \pm1, \pm2, \ldots)$. It should be noted that if $m_1 = m_2 = K = 0$ in Eqs. 3.4.172 and 3.4.173, $1/\sqrt{2}$ is replaced by $1/2$.

Degenerate $E_i(i = 1, 2, 3, 4)$ basis functions for case $\boldsymbol{C}_s(\boldsymbol{G}_{18})$ are equal to (E_{i+}, E_{i-}) in Eq. 3.4.171 for case $\boldsymbol{C}_1(\boldsymbol{G}_9)$.

Hamiltonian Matrix Elements

The Hamiltonian matrix elements $\langle m_1, m_2; J, K|H|m_1', m_2'; J, K'\rangle$ can be written down rather easily after deciding what we adopt as the potential function $V(\tau_1, \tau_2)$ in Eq. 3.4.161. When adopting a simple potential function

$$V(\tau_1, \tau_2) = \frac{V_{31}}{2}(1 - \cos 3\tau_1) + \frac{V_{32}}{2}(1 - \cos 3\tau_2) + V_{12}\cos 3\tau_1 \cos 3\tau_2, \tag{3.4.174}$$

three non-zero off-diagonal matrix elements $\langle m_1, m_2; J, K|H|m_1', m_2'; J, K'\rangle$, related to the potential function, are given by

$$\begin{aligned}
\langle m_1, m_2; J, K|H|m_1 \pm 3, m_2; J, K\rangle &= -\frac{V_{31}}{4}, \\
\langle m_1, m_2; J, K|H|m_1, m_2 \pm 3; J, K\rangle &= -\frac{V_{32}}{4}, \\
\langle m_1, m_2; J, K|H|m_1 \pm 3, m_2 \pm 3; J, K\rangle &= \frac{V_{12}}{4}, \\
\langle m_1, m_2; J, K|H|m_1 \pm 3, m_2 \mp 3; J, K\rangle &= \frac{V_{12}}{4},
\end{aligned} \tag{3.4.175}$$

The Hamiltonian matrix for each symmetry species is constructed by combining basis set functions given by Eqs. 3.4.171–3.4.173 with the matrix elements

$$\langle m_1, m_2; J, K|H|m_1', m_2'; J, K'\rangle.$$

3.4.3 Case of a Molecule with Two Equivalent Methyl Internal Rotors

3.4.3.1 Group Theory

We treat two cases: a case that a molecule is of $\boldsymbol{C}_s$ symmetry at an equilibrium configuration, and another case that a molecule is of $\boldsymbol{C}_{2v}$ symmetry at an equilibrium configuration. We call the former and the latter case $\boldsymbol{C}_s(\boldsymbol{G}_{18})$ and case $\boldsymbol{C}_{2v}(\boldsymbol{G}_{36})$, respectively, since the PI group for the former case is $\boldsymbol{G}_{18}$ and that for the latter case is $\boldsymbol{G}_{36}$. In Figs. 3.34 and 3.35, dimethylamine and acetone are shown as examples of case $\boldsymbol{C}_s(\boldsymbol{G}_{18})$ and case $\boldsymbol{C}_{2v}(\boldsymbol{G}_{36})$, respectively.

Character Table

The character tables for $\boldsymbol{C}_s(\boldsymbol{G}_{18})$ and for $\boldsymbol{C}_{2v}(\boldsymbol{G}_{36})$ are given in Tables 3.14 and 3.15, respectively. In Table 3.14, $E_{1\text{sep}}, E_{2\text{sep}}$ and $\boldsymbol{G}_{\text{sep}}$ represent combined pairs $(A_{1+}, A_{1-}), (A_{2+}, A_{2-})$ and (E_+, E_-) of separably degenerate irreducible representations, respectively.

Transition Selection Rules

Since the laboratory-fixed component μ_Z of the electric dipole moment operator belongs to A_2 symmetry species in the $\boldsymbol{G}_{18}$ and A_3 in the $\boldsymbol{G}_{36}$ PI group, selection

Table 3.14 Character table for a molecule of $\boldsymbol{C}_s(\boldsymbol{G}_{18})$ symmetry with two equivalent methyl internal rotors

	E	(123)(456) (132)(465)	P^{a}	(132)(456)	(123) (465)	Q^{a}	(123)(465)	(456) (132)	R^{a}
A_1	1	1	1	1	1	1	1	1	1
A_2	1	1	−1	1	1	−1	1	1	−1
E	2	−1	0	2	−1	0	2	−1	0
$E_{1\text{sep}}$									
A_{1+}	1	1	1	ω	ω	ω	ω^*	ω^*	ω^*
A_{1-}	1	1	1	ω^*	ω^*	ω^*	ω	ω	ω
$E_{2\text{sep}}$									
A_{2+}	1	1	−1	ω	ω	$-\omega$	ω^*	ω^*	$-\omega^*$
A_{2-}	1	1	−1	ω^*	ω^*	$-\omega^*$	ω	ω	$-\omega$
G_{sep}									
E_+	2	−1	0	2ω	$-\omega$	0	$2\omega^*$	$-\omega^*$	0
E_-	2	−1	0	$2\omega^*$	$-\omega^*$	0	2ω	$-\omega$	0

$\omega = \exp(i2\pi/3)$.
[a] $P = \{(14)(26)(35)(78)^*, (15)(24)(36)(78)^*, (16)(25)(34)(78)^*\}$,
$Q = \{(162534)(78)^*, (142635)(78)^*, (152436)(78)^*\}$,
$R = \{(153624)(78)^*, (163425)(78)^*, (143526)(78)^*\}$

Table 3.15 Character table for a molecule of $\boldsymbol{C}_{2v}(\boldsymbol{G}_{36})$ symmetry with two equivalent methyl internal rotors

	E	(123)(456) (132)(465)	P^{a}	(123)(465) (132)(456)	(123) (132) (456) (465)	(142635)(78)* (143526)(78)* (152436)(78)* (153624)(78)* (162534)(78)* (163425)(78)*	Q^{a}	(142536)(78) (143625)(78) (152634)(78) (153426)(78) (162435)(78) (163524)(78)	(23)(56)* (23)(45)* (23)(46)* (13)(56)* (13)(45)* (13)(46)* (12)(56)* (12)(45)* (12)(46)*
A_1	1	1	1	1	1	1	1	1	1
A_2	1	1	1	1	1	1	−1	−1	−1
A_3	1	1	−1	1	1	−1	1	1	−1
A_4	1	1	−1	1	1	−1	−1	−1	1
E_1	2	2	2	−1	−1	−1	0	0	0
E_2	2	2	−2	−1	−1	1	0	0	0
E_3	2	−1	0	2	−1	0	2	−1	0
E_4	2	−1	0	2	−1	0	−2	1	0
G	4	−2	0	−2	1	0	0	0	0

[a] $P = \{(14)(26)(35)(78)^*, (15)(24)(36)(78)^*, (16)(25)(34)(78)^*\}$,
$Q = \{(14)(25)(36)(78), (15)(26)(34)(78), (16)(24)(35)(78)\}$

rules on the overall torsional–rotational symmetry species for allowed electric dipole transitions are given by

$$A_1 \leftrightarrow A_2,\ E_{1\mathrm{sep}} \leftrightarrow E_{2\mathrm{sep}},\ E \leftrightarrow E,\ G_{\mathrm{sep}} \leftrightarrow G_{\mathrm{sep}}, \tag{3.4.176}$$

for case $\boldsymbol{C}_s(\boldsymbol{G}_{18})$, and

$$A_1 \leftrightarrow A_3, A_2 \leftrightarrow A_4, E_1 \leftrightarrow E_2, E_3 \leftrightarrow E_3, E_4 \leftrightarrow E_4, \tag{3.4.177}$$

for case $\boldsymbol{C}_{2v}(\boldsymbol{G}_{36})$.

Coordinate System and Transformation Properties of Variables

The description depends on the orientations of the methyl groups to the PAM axes. We will take the dimethylamine molecule shown in Fig. 3.34 as an example of case $\boldsymbol{C}_s(\boldsymbol{G}_{18})$ and the acetone molecule shown in Fig. 3.35 as an example of case $\boldsymbol{C}_{2v}(\boldsymbol{G}_{36})$. The PAM axes $(a, b, c \rightarrow z, x, y)$ are shown in Figs. 3.34 and 3.35 (the y-axis is perpendicular to the zx-plane). The transformation properties are obtained from Eqs. 3.4.152–3.4.154 representing the relation between the laboratory-fixed coordinates and the internal variables, together with the following structural constraint:

$$\theta_{\mathrm{P1}} + \theta_{\mathrm{P2}} = \pi, \quad \phi_{\mathrm{P1}} = \phi_{\mathrm{P2}}, \quad \chi_{\mathrm{P1}} = -\chi_{\mathrm{P2}}, \tag{3.4.178}$$

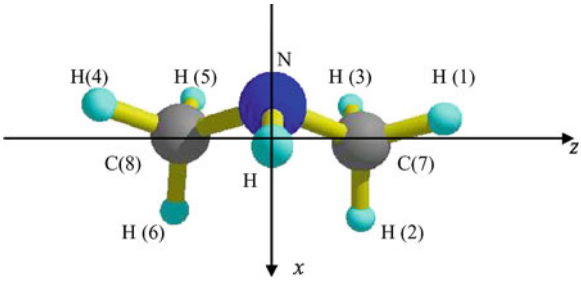

Fig. 3.34 Dimethylamine, an example of a C_s molecule with equivalent two methyl groups

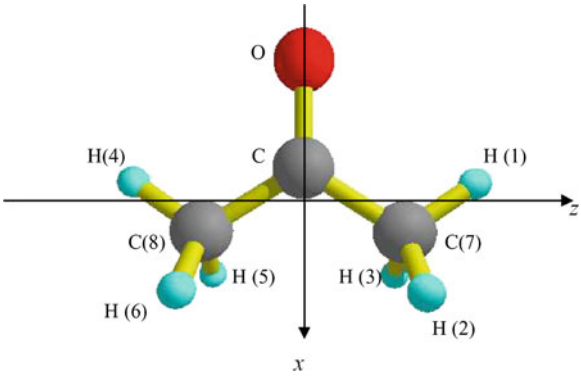

Fig. 3.35 Acetone, an example of a C_{2v} molecule with equivalent two methyl groups

Table 3.16 Transformation properties of variables in the right of Eqs. 3.4.152–3.4.154 under generating operations of the group G_{18} for dimethylamine and G_{36} for acetone

	R (translation)	θ, ϕ, χ (rotation)	τ_1 (internal rotation)	τ_2 (internal rotation)
(123)	R	θ, ϕ, χ	$\tau_1 + 2\pi/3$	τ_2
(456)	R	θ, ϕ, χ	τ_1	$\tau_2 + 2\pi/3$
$(14)(26)(35)(78)^*$	$-R$	$\theta, \phi, \chi + \pi$	$-\tau_2$	$-\tau_1$
$(23)(56)^*$	$-R$	$\pi - \theta, \pi + \phi, \pi - \chi$	$-\tau_1$	$-\tau_2$

Generating operations of G_{18} are $(123), (456)$ and $(14)(26)(35)(78)^*$; generating operations of G_{36} are $(123), (456), (14)(26)(35)(78)^*$ and $(23)(56)^*$

for dimethylamine (case $C_s(G_{18})$), and

$$\theta_{P1} + \theta_{P2} = \pi, \quad \phi_{P1} = \phi_{P2} = 0, \quad \chi_{P1} = \chi_{P2} = 0, \tag{3.4.179}$$

for acetone (case $C_{2v}(G_{36})$).

Transformation properties under generating operations of G_{18} and G_{36} are given together in Table 3.16.

3.4.3.2 $J = K = 0$ Energy Level Splitting Pattern

In Fig. 3.36, an energy level diagram for $J = K = 0$ is illustrated qualitatively for a molecule with equivalent two methyl groups. The schematic splitting pattern

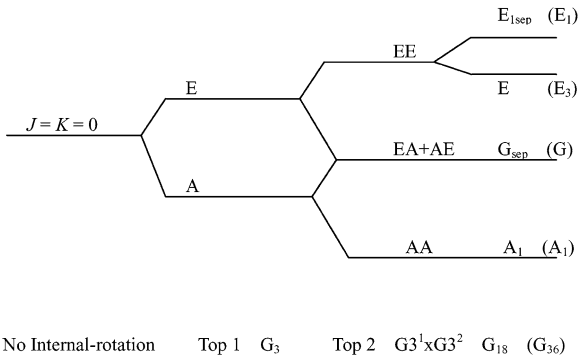

Fig. 3.36 An internal-rotation energy level diagram is illustrated schematically for $J = K = 0$ in the ground vibrational state of a molecule with equivalent two methyl internal-rotors

depicted in Fig. 3.36 will be understood by making A/E splittings equal in top 1 and top 2 in Fig. 3.32. Levels of symmetry species $A_2, E_{2\text{sep}}$ for case $\boldsymbol{C}_s(\boldsymbol{G}_{18})$ and A_2, A_3, A_4, E_2, E_4 for case $\boldsymbol{C}_{2v}(\boldsymbol{G}_{36})$, which do not appear for the $J = K = 0$ in the ground vibrational state, appear for $K \neq 0$ levels and/or $v \neq 0$ vibrationally excited states.

3.4.3.3 Hamiltonian Operator, Basis Set Functions and Hamiltonian Matrix

Hamiltonian Operator

The torsional–rotational Hamiltonian operator for a molecule with two equivalent methyl internal-rotors is obtained by imposing the following relations in Eqs. 3.4.158–3.4.160:

$$F_1 = F_2(\equiv F), \lambda_{1z} = -\lambda_{2z}, \lambda_{1x} = \lambda_{2x}, \lambda_{1y} = \lambda_{2y} \tag{3.4.180}$$

for dimethylamine of case $\boldsymbol{C}_s(\boldsymbol{G}_{18})$, and

$$F_1 = F_2(\equiv F), \lambda_{1z} = -\lambda_{2z}, \lambda_{1x} = \lambda_{2x}, \lambda_{1y} = \lambda_{2y} = 0 \tag{3.4.181}$$

for acetone of case $\boldsymbol{C}_{2v}(\boldsymbol{G}_{36})$. The resultant Hamiltonian operator is given by

$$\begin{aligned} H = {} & A' J_z^2 + B' J_x^2 + C' J_y^2 + D_{bc}\left[J_x J_y + J_y J_x\right] \\ & + q(p_1 - p_2) J_z + r(p_1 + p_2) J_x + s(p_1 + p_2) J_y \\ & + F\left(p_1^2 + p_2^2\right) + 2F_{12} p_1 p_2 + V(\tau_1, \tau_2), \end{aligned} \tag{3.4.182}$$

where

$$\begin{aligned} & A' = A + 2(F - F_{12})\rho_{1z}^2, \quad B' = B + 2(F + F_{12})\rho_{1x}^2, \quad C' = C + 2(F + F_{12})\rho_{1y}^2, \\ & D_{bc} = 2(F + F_{12})\rho_{1x}\rho_{1y}, \; q = -2(F - F_{12})\rho_{1z}, \quad r = -2(F + F_{12})\rho_{1x}, \\ & s = -2(F + F_{12})\rho_{1y}, \end{aligned} \tag{3.4.183}$$

for dimethylamine of case $\boldsymbol{C}_s(\boldsymbol{G}_{18})$, and

$$A' = A + 2(F - F_{12})\rho_{1z}^2, \quad B' = B + 2(F + F_{12})\rho_{1x}^2, \quad C' = C, \quad D_{bc} = 0,$$
$$q = -2(F - F_{12})\rho_{1z}, \quad r = -2(F + F_{12})\rho_{1x}, \quad s = 0, \tag{3.4.184}$$

for acetone of case $\boldsymbol{C}_{2v}(\boldsymbol{G}_{36})$.

The simplest potential function will be

$$V(\tau_1, \tau_2) = \frac{1}{2}V_3(1 - \cos 3\tau_1) + \frac{1}{2}V_3(1 - \cos 3\tau_2) + V_{12}\cos 3\tau_1 \cos 3\tau_2. \tag{3.4.185}$$

Basis Set Functions

Basis set functions of each symmetry species for case $\boldsymbol{C}_s(\boldsymbol{G}_{18})$ are give as follows:
A-symmetry:

$$\begin{aligned} |A_1\rangle &= (1/\sqrt{2})\big[|m_1, m_2\rangle|J, K\rangle + (-1)^K|-m_2, -m_1\rangle|J, K\rangle\big], \\ |A_2\rangle &= (1/\sqrt{2})\big[|m_1, m_2\rangle|J, K\rangle - (-1)^K|-m_2, -m_1\rangle|J, K\rangle\big], \\ &\quad (m_1, m_2 = 0 \bmod 3 \geq 0 \text{ and } -J \leq K \leq J) \end{aligned} \tag{3.4.186}$$

where $|m_1, m_2\rangle = |m_1(1)\rangle|m_2(2)\rangle = (1/2\pi)\exp(im_1\tau_1)\exp(im_2\tau_2)$. When $m_1 = m_2 = 0$ the factor $1/\sqrt{2}$ in the equations above should be replaced by 1/2.
E-symmetry:

$$\begin{aligned} |E_a\rangle &= |m_1(1)\rangle|m_2(2)\rangle|J, K\rangle, \\ |E_b\rangle &= (14)(26)(35)(78)^*|E_a\rangle = (-1)^K|-m_2(1)\rangle|-m_1(2)\rangle|J, K\rangle, \end{aligned} \tag{3.4.187}$$

with $m_1 = 3n + 1(n = 0, \pm1, \pm2, \ldots), m_2 = 3n' + 1(n' = 0, \pm1, \pm2, \ldots)$, and $-J \leq K \leq J$.

$E_{1\text{sep}}$-symmetry:

$$\begin{aligned} |A_{1+}\rangle &= (1/\sqrt{2})\big[|m_1, m_2\rangle|J, K\rangle + (-1)^K|-m_2, -m_1\rangle|J, K\rangle\big], \\ &\quad (m_1 = 3n + 1(n = 0, \pm1, \pm2, \ldots), m_2 = 3n' - 1(n' = 0, \pm1, \pm2, \ldots), \\ &\quad \text{and } -J \leq K \leq J) \\ |A_{1-}\rangle &= (1/\sqrt{2})\big[|m_1, m_2\rangle|J, K\rangle + (-1)^K|-m_2, -m_1\rangle|J, K\rangle\big], \\ &\quad (m_1 = 3n - 1(n = 0, \pm1, \pm2, \ldots), m_2 = 3n' + 1(n' = 0, \pm1, \pm2, \ldots), \\ &\quad \text{and } -J \leq K \leq J). \end{aligned} \tag{3.4.188}$$

When $m_1 = -m_2$, the factor $1/\sqrt{2}$ in the equations above should be replaced by $1/2$.

$E_{2\text{sep}}$-symmetry:

$$\begin{aligned}
|A_{2+}\rangle &= (1/\sqrt{2})\big[|m_1, m_2\rangle|J, K\rangle - (-1)^K|-m_2, -m_1\rangle|J, K\rangle\big], \\
&\quad (m_1 = 3n+1(n = 0, \pm1, \pm2, \ldots), m_2 = 3n' - 1(n' = 0, \pm1, \pm2, \ldots), \\
&\quad \text{and } -J \le K \le J) \\
|A_{2-}\rangle &= (1/\sqrt{2})\big[|m_1, m_2\rangle|J, K\rangle - (-1)^K|-m_2, -m_1\rangle|J, K\rangle\big], \\
&\quad (m_1 = 3n-1(n = 0, \pm1, \pm2, \ldots), m_2 = 3n' + 1(n' = 0, \pm1, \pm2, \ldots), \\
&\quad \text{and } -J \le K \le J).
\end{aligned} \tag{3.4.189}$$

When $m_1 = -m_2$, the factor $1/\sqrt{2}$ in the equations above should be replaced by $1/2$.

$\boldsymbol{G}_{\text{sep}}$-symmetry:

$$\begin{aligned}
|E_{+a}\rangle &= |m_1, m_2\rangle|J, K\rangle, \\
&\quad (m_1 = 3n(n = 0, \pm1, \pm2, \ldots), m_2 = 3n' + 1(n' = 0, \pm1, \pm2, \ldots), \\
&\quad \text{and } -J \le K \le J), \\
|E_{+b}\rangle &= (14)(26)(35)(78)^*|E_{+a}\rangle = (-1)^K|-m_2, -m_1\rangle|J, K\rangle, \\
|E_{-a}\rangle &= |m_1, m_2\rangle|J, K\rangle, \\
&\quad (m_1 = 3n+1(n = 0, \pm1, \pm2, \ldots), m_2 = 3n'(n' = 0, \pm1, \pm2, \ldots), \\
&\quad \text{and } -J \le K \le J), \\
|E_{-b}\rangle &= (14)(26)(35)(78)^*|E_{-a}\rangle = (-1)^K|-m_2, -m_1\rangle|J, K\rangle
\end{aligned} \tag{3.4.190}$$

Basis functions of E_1, E_2 and G for case $\boldsymbol{C}_{2v}(\boldsymbol{G}_{36})$ are equal to those for $E_{1\text{sep}}, E_{2\text{sep}}$ and $\boldsymbol{G}_{\text{sep}}$ in Eqs. 3.4.186–3.4.190 for case $\boldsymbol{C}_s(\boldsymbol{G}_{18})$, respectively. Other basis functions for case $\boldsymbol{C}_{2v}(\boldsymbol{G}_{36})$ are as follows:

$$\begin{aligned}
|A_1\rangle &= (1/2)\big[|m_1, m_2\rangle|J, K\rangle + (-1)^K|-m_2, -m_1\rangle|J, K\rangle \\
&\quad + (-1)^{J-K}|-m_1, -m_2\rangle|J, -K\rangle + (-1)^J|m_2, m_1\rangle|J, -K\rangle\big] \\
|A_2\rangle &= (1/2)\big[|m_1, m_2\rangle|J, K\rangle + (-1)^K|-m_2, -m_1\rangle|J, K\rangle \\
&\quad - (-1)^{J-K}|-m_1, -m_2\rangle|J, -K\rangle - (-1)^J|m_2, m_1\rangle|J, -K\rangle\big] \\
|A_3\rangle &= (1/2)\big[|m_1, m_2\rangle|J, K\rangle - (-1)^K|-m_2, -m_1\rangle|J, K\rangle \\
&\quad - (-1)^{J-K}|-m_1, -m_2\rangle|J, -K\rangle + (-1)^J|m_2, m_1\rangle|J, -K\rangle\big] \\
|A_4\rangle &= (1/2)\big[|m_1, m_2\rangle|J, K\rangle - (-1)^K|-m_2, -m_1\rangle|J, K\rangle \\
&\quad .+ (-1)^{J-K}|-m_1, -m_2\rangle|J, -K\rangle - (-1)^J|m_2, m_1\rangle|J, -K\rangle\big],
\end{aligned} \tag{3.4.191}$$

where $m_1 = 3n$ $(n = 0, \pm1, \pm2, \ldots), m_2 = 3n'$ $(n' = 0, 1, 2, \ldots)$, and $0 \le K \le J$. When $(m_1 = -m_2)$ or $(m_1 = m_2$ and $K = 0)$, the factor $1/2$ should be replaced by

$1/(2\sqrt{2})$ in the above equations, and when $m_1 = m_2 = K = 0$ the factor $1/2$ should be replaced by $1/4$.

$$
\begin{aligned}
|E_{3a}\rangle &= (1/\sqrt{2})\left[|m_1, m_2\rangle|J, K\rangle + (-1)^J|m_2, m_1\rangle|J, -K\rangle\right] \\
|E_{3b}\rangle &= (14)(26)(35)(78)^*|E_{3a}\rangle \\
&= (1/\sqrt{2})(-1)^K\left[|-m_2, -m_1\rangle|J, K\rangle + (-1)^J|-m_1, -m_2\rangle|J, -K\rangle\right] \\
|E_{4a}\rangle &= (1/\sqrt{2})\left[|m_1, m_2\rangle|J, K\rangle - (-1)^J|m_2, m_1\rangle|J, -K\rangle\right] \\
|E_{4b}\rangle &= (14)(26)(35)(78)^*|E_{4a}\rangle \\
&= (1/\sqrt{2})(-1)^K\left[|-m_2, -m_1\rangle|J, K\rangle - (-1)^J|-m_1, -m_2\rangle|J, -K\rangle\right],
\end{aligned}
\tag{3.4.192}
$$

where $m_1 = 3n + 1$ $(n = 0, \pm1, \pm2, \ldots), m_2 = 3n' + 1$ $(n' = 0, \pm1, \pm2, \ldots)$, and $0 \leq K \leq J$. When $m_1 = m_2$ and $K = 0$, the factor $1/\sqrt{2}$ should be replaced by $1/2$ in the above equations.

Hamiltonian Matrix Elements

It is easy to obtain expressions of Hamiltonian matrix elements $\langle m_1, m_2; J, K|H|m_1', m_2'; J, K'\rangle$, corresponding to Eqs. 3.4.78–3.4.81 for one-top problem. The Hamiltonian matrices for each symmetry species of $\boldsymbol{G}_{18}$ and $\boldsymbol{G}_{36}$ are constructed by combining basis set functions given by Eqs. 3.4.186–3.4.192 with the matrix elements $\langle m_1, m_2; J, K|H|m_1', m_2'; J, K'\rangle$.

3.4.4 Tunneling Matrix Formulation for Molecules with Two Methyl Internal Rotors

We describe the tunneling matrix formulation in the case of two methyl internal rotors. As mentioned in the one-top problem, the tunneling matrix formulation is effective in the case of a high potential barrier to internal rotation. The description is somewhat different depending on geometrical symmetry of a molecule. Case $\boldsymbol{C}_1(\boldsymbol{G}_9)$ of a molecule with inequivalent two methyl tops and case $\boldsymbol{C}_s(\boldsymbol{G}_{18})$ of a molecule with equivalent two methyl tops will be treated below.

3.4.4.1 Case $\boldsymbol{C}_1(\boldsymbol{G}_9)$ of a Molecule with Inequivalent Two Methyl Tops

Considering 2-butanol as an example, we will describe the formulation.

Vibrational Framework Functions and Basis Functions Belonging to Each Symmetry Species

When $|1\rangle$ represents the vibrational framework function at framework 1, nine vibrational framework functions $|n\rangle(n = 1, 2, 3, \ldots, 9)$ are defined as

$$|n\rangle = O_n|1\rangle, \tag{3.4.193}$$

where operations $O_n(n = 1, 2, 3, \ldots, 9)$ are as follows:

$$\begin{aligned} &O_1 = E, \\ &O_2 = (123),\ O_3 = (132),\ O_4 = (456),\ O_5 = (465), \\ &O_6 = (123)(456),\ O_7 = (123)(465), O_8 = (132)(456),\ O_9 = (132)(465). \end{aligned} \tag{3.4.194}$$

We note again that the concept of framework function is effective in a high barrier case. Basis functions belonging to each of symmetry species of $\boldsymbol{G}_9$, constructed from framework functions, are given as follows using the theorem well known in the group theory

$$|\Gamma(\text{torsion})\rangle = \frac{1}{N(\Gamma)} \sum_{n=1}^{9} \left[\chi^{\Gamma}(O_n)\right]^* |n\rangle, \tag{3.4.195}$$

where $\chi^{\Gamma}(O_n)(n = 1, 2, \ldots, 9)$ are characters given in Table 3.11, and

$$\begin{aligned} N(A) &= \sqrt{9(1 + 2S_2 + 2S_4 + 2S_6 + 2S_7)}, \\ N(E_{1+}) = N(E_{1-}) &= \sqrt{9(1 - S_2 + 2S_4 - S_6 - S_7)}, \\ N(E_{2+}) = N(E_{2-}) &= \sqrt{9(1 + 2S_2 - S_4 - S_6 - S_7)}, \\ N(E_{3+}) = N(E_{3-}) &= \sqrt{9(1 - S_2 - S_4 - S_6 + 2S_7)}, \\ N(E_{4+}) = N(E_{4-}) &= \sqrt{9(1 - S_2 - S_4 + 2S_6 - S_7)}, \end{aligned} \tag{3.4.196}$$

where $S_n = \langle 1|n\rangle (n = 1, 2, \ldots, 9)$; note $S_1 = 1$.

Phenomenological Hamiltonian Operator and Hamiltonian Matrix Element Expressions

Since rotational functions $|J, K\rangle$ $(-J \leq K \leq J)$ are invariant under symmetry operations of the PI group $\boldsymbol{G}_9$, torsional–rotational basis functions belonging to each symmetry species are given by

$$|\Gamma; J, K\rangle = |\Gamma(\text{torsion})\rangle |J, K\rangle. \tag{3.4.197}$$

We adopt the following phenomenological Hamiltonian operator

$$H = h_v + AJ_z^2 + BJ_x^2 + CJ_y^2 + iqJ_z + irJ_x + isJ_y. \tag{3.4.198}$$

The last three terms in Eq. 3.4.198 represent the Coriolis interaction between the overall rotation and the methyl internal rotation. All the coefficients, h_v, A, B, C, q, r, and s, are of A-symmetry. The following transformation properties of the coefficients under the combined operation of Hermitian conjugation and time reversal (indicated by ‡) are also useful:

Table 3.17 Numerical factors f_n and g_n in Eq. 3.4.200

	$n=1$		$n=2$		$n=4$		$n=6$		$n=7$	
	f_n	g_n	f_n	g_n	f_n	g_n	f_n	g_n	f_n	g_n
A	1	0	2	0	2	0	2	0	2	0
E_{1+}	1	0	−1	1	2	0	−1	1	−1	1
E_{2+}	1	0	2	0	−1	1	−1	1	−1	−1
E_{3+}	1	0	−1	1	−1	1	−1	−1	2	0
E_{4+}	1	0	−1	1	−1	−1	2	0	−1	−1

$$\begin{aligned} h^{\ddagger} &= +h \quad \text{for } h_v, A, B \text{ and } C, \\ h^{\ddagger} &= -h \quad \text{for } q, r \text{ and } s. \end{aligned} \tag{3.4.199}$$

Based on the description given above, parameterized expressions for the torsional–rotational Hamiltonian matrix elements are given as

$$\begin{aligned} \langle \Gamma; J, K|H|\Gamma; J, K'\rangle = \frac{9}{N(\Gamma)^2} \Bigg\{ & \sum_{n=1,2,4,6,7} f(\Gamma)_n \big[\langle 1|h_v|n\rangle \delta_{KK'} + \langle 1|A|n\rangle K^2 \delta_{KK'} \\ & + \langle 1|B|n\rangle \langle J, K|J_x^2|J, K'\rangle + \langle 1|C|n\rangle \langle J, K|J_y^2|J, K'\rangle \big] \\ & + \sum_{n=1,2,4,6,7} \sqrt{3} g(\Gamma)_n [\langle 1|q|n\rangle K \delta_{KK'} + \langle 1|r|n\rangle \langle J, K|J_x|J, K'\rangle \\ & + \langle 1|s|n\rangle \langle J, K|J_y|J, K'\rangle \big] \Bigg\} \end{aligned} \tag{3.4.200}$$

where $f(\Gamma)_n$ and $g(\Gamma)_n$ are numerical factors given in Table 3.17. In Eq. 3.4.200, the symmetry species Γ takes A and $E_{i+}(i = 1, 2, 3, 4)$. The Hamiltonian matrix for $E_{i-}(i = 1, 2, 3, 4)$ produces the same eigenvalues as that for E_{i+} does since we have a relation

$$\begin{aligned} \langle E_{i-}; J, K|H|E_{i-}; J, K'\rangle &= \left(\langle E_{i-}; J, K'|H^{\dagger}|E_{i-}; J, K\rangle\right)^* \\ &= \langle E_{i+}; J, -K'|H|E_{i+}; J, -K\rangle. \end{aligned} \tag{3.4.201}$$

When obtaining numerical factors f_n and g_n in Table 3.17 the following equalities are used:

$$\begin{aligned} &\langle 1|h|2\rangle = \langle 1|h|3\rangle, \langle 1|h|4\rangle = \langle 1|h|5\rangle, \\ &\langle 1|h|6\rangle = \langle 1|h|9\rangle, \langle 1|h|7\rangle = \langle 1|h|8\rangle, \end{aligned} \tag{3.4.202}$$

for $h = h_v, A, B$, and C, and

$$\begin{aligned} &\langle 1|h|1\rangle = 0, \\ &\langle 1|h|2\rangle = -\langle 1|h|3\rangle, \langle 1|h|4\rangle = -\langle 1|h|5\rangle, \\ &\langle 1|h|6\rangle = -\langle 1|h|9\rangle, \langle 1|h|7\rangle = -\langle 1|h|8\rangle, \end{aligned} \tag{3.4.203}$$

for $h = q, r$, and s.

The description given above is also available for case $\boldsymbol{C}_s(\boldsymbol{G}_{18})$ of inequivalent-two-top molecules except for that the term is J_y in Eq. 3.4.198 does not contribute to any Hamiltonian matrix element and that symmetry species A for case $\boldsymbol{C}_1(\boldsymbol{G}_9)$ corresponds to A_1 and A_2 for case $\boldsymbol{C}_s(\boldsymbol{G}_{18})$, which distinguish the two K-type doubling levels (the $J = K = 0$ level belongs to either A_1 or A_2 symmetry species depending on the symmetry property of the torsional state under the symmetry operation $(23)(56)(78)^*$, the reflection in the plane of symmetry in point group).

3.4.4.2 Case $\boldsymbol{C}_s(\boldsymbol{G}_{18})$ of a Molecule with Equivalent Two Methyl Tops

We treat the tunneling matrix formulation for a dimethylamine-like molecule. We obtain the formulation for this case by making suitable changes in some of Eqs. 3.4.193–3.4.203 and Table 3.17. Using the character table of $\boldsymbol{G}_{18}$ for a dimethylamine-like molecule shown in Table 3.14, it is shown that nine vibrational framework functions, given by Eq. 3.4.193 with Eq. 3.4.194, produce symmetrized torsional functions with the following symmetry species:

$$\begin{array}{ll} A_1 + E + E_{1\text{sep}} + G_{\text{sep}} & \text{for } (14)(26)(35)(78)^*|1\rangle = +|1\rangle, \\ \text{or } A_2 + E + E_{2\text{sep}} + G_{\text{sep}} & \text{for } (14)(26)(35)(78)^*|1\rangle = -|1\rangle. \end{array} \tag{3.4.204}$$

For simplicity, we will discuss the former case of Eq. 3.4.204 in detail. The *symmetrized torsional basis functions* belonging to each of symmetry species are given by

$$\begin{aligned} A_1 &: |A_1(\text{torsion})\rangle = N(A_1)[1,1,1,1,1,1,1,1,1], \\ E &: |E_a(\text{torsion})\rangle = N(E)[1,\omega^*,\omega,\omega^*,\omega,\omega,1,1,\omega^*], \\ &\quad |E_b(\text{torsion})\rangle = N(E)[1,\omega,\omega^*,\omega,\omega^*,\omega^*,1,1,\omega], \\ E_{1\text{sep}} &: |E_{1\text{sep},a}(\text{torsion})\rangle \equiv |A_{1+}(\text{torsion})\rangle = N(E_{1\text{sep}})[1,\omega^*,\omega,\omega,\omega^*,1,\omega,\omega^*,1], \\ &: |E_{1\text{sep},b}(\text{torsion})\rangle \equiv |A_{1-}(\text{torsion})\rangle = N(E_{1\text{sep}})[1,\omega,\omega^*,\omega^*,\omega,1,\omega^*,\omega,1], \\ G_{\text{sep}} &: |G_{\text{sep},a}(\text{torsion})\rangle \equiv |E_{+a}(\text{torsion})\rangle = N(G_{\text{sep}})[1,\omega,\omega^*,1,1,\omega,\omega,\omega^*,\omega^*], \\ &: |G_{\text{sep},b}(\text{torsion})\rangle \equiv |E_{+b}(\text{torsion})\rangle = N(G_{\text{sep}})[1,1,1,\omega^*,\omega,\omega^*,\omega,\omega^*,\omega], \\ &: |G_{\text{sep},c}(\text{torsion})\rangle \equiv |E_{-a}(\text{torsion})\rangle = N(G_{\text{sep}})[1,\omega^*,\omega,1,1,\omega^*,\omega^*,\omega,\omega], \\ &: |G_{\text{sep},d}(\text{torsion})\rangle \equiv |E_{-b}(\text{torsion})\rangle = N(G_{\text{sep}})[1,1,1,\omega,\omega^*,\omega,\omega^*,\omega,\omega^*], \end{aligned} \tag{3.4.205}$$

where $[a_1, a_2, \ldots, a_9] = \sum_{n=1}^{9} a_n|n\rangle$, and

$$\begin{array}{ll} N(A_1) = 1/\sqrt{9(1+4S_2+2S_6+2S_7)}, & N(E) = 1/\sqrt{9(1-2S_2-S_6+2S_7)}, \\ N(E_{1\text{sep}}) = 1/\sqrt{9(1-2S_2+2S_6-S_7)}, & N(G_{\text{sep}}) = 1/\sqrt{9(1+S_2-S_6-S_7)}, \end{array} \tag{3.4.206}$$

Since transformation properties of rotational functions under generating operations of $\boldsymbol{G}_{18}$ are given as

$$\begin{aligned}(123)|J,K\rangle &= |J,K\rangle,\\ (456)|J,K\rangle &= |J,K\rangle,\\ (14)(26)(35)(78)^{*}|J,K\rangle &= (-1)^{K}|J,K\rangle,\end{aligned} \tag{3.4.207}$$

torsional–rotational basis functions belonging to each symmetry species are given as

$$\begin{aligned}|A_1(\text{overall});J,K\rangle &= |A_1(\text{torsion})\rangle|J,K=\text{even}\rangle,\\ |A_2(\text{overall});J,K\rangle &= |A_1(\text{torsion})\rangle|J,K=\text{odd}\rangle,\\ |E_\alpha(\text{overall});J,K\rangle &= |E_\alpha(\text{torsion})\rangle|J,K\rangle,\ (\alpha=a,b)\\ |E_{1\text{sep}\,\alpha}(\text{overall});J,K\rangle &= |E_{1\text{sep}\,\alpha}(\text{torsion})\rangle|J,K=\text{even}\rangle,\ (\alpha=a,b)\\ |E_{2\text{sep}\,\alpha}(\text{overall});J,K\rangle &= |E_{1\text{sep}\,\alpha}(\text{torsion})\rangle|J,K=\text{odd}\rangle,\ (\alpha=a,b)\\ |G_{\text{sep}\,\alpha}(\text{overall});J,K\rangle &= |G_{\text{sep}\,\alpha}(\text{torsion})\rangle|J,K\rangle\ (\alpha=a,b,c,d).\end{aligned} \tag{3.4.208}$$

In the *phenomenological Hamiltonian operator* given also by Eq. 3.4.198, coefficients h_v, A, B, C and q are of A_1 symmetry, and r and s are of A_2 symmetry since J_z, J_x, and J_y are of A_1, A_2 and A_2 symmetry, respectively (see Table 3.16). Using these symmetry properties of the coefficients and their transformation properties under the combined operation ($\ddagger$) of Hermitian conjugation and time reversal shown in Eq. 3.4.199, we have the following relations:

$$\begin{aligned}\langle 1|h|2\rangle &= \langle 1|h|3\rangle = \langle 1|h|4\rangle = \langle 1|h|5\rangle,\\ \langle 1|h|6\rangle &= \langle 1|h|9\rangle,\\ \langle 1|h|7\rangle &= \langle 1|h|8\rangle,\end{aligned} \tag{3.4.209}$$

for $h = h_v, A, B$, and C,

$$\begin{aligned}\langle 1|q|1\rangle &= 0,\\ \langle 1|q|2\rangle &= -\langle 1|q|3\rangle = -\langle 1|q|4\rangle = \langle 1|q|5\rangle,\\ \langle 1|q|6\rangle &= \langle 1|q|9\rangle = 0,\\ \langle 1|q|7\rangle &= -\langle 1|q|8\rangle,\end{aligned} \tag{3.4.210}$$

and

$$\begin{aligned}\langle 1|h|1\rangle &= 0,\\ \langle 1|h|2\rangle &= -\langle 1|h|3\rangle = \langle 1|h|4\rangle = -\langle 1|h|5\rangle,\\ \langle 1|h|6\rangle &= -\langle 1|h|9\rangle,\\ \langle 1|h|7\rangle &= \langle 1|h|8\rangle = 0,\end{aligned} \tag{3.4.211}$$

for $h = r$ and s. From Eqs. 3.4.209–3.4.211, we obtain the following parameterized expressions of Hamiltonian matrix elements for each of symmetry species:

$$
\begin{aligned}
&\langle A(\text{overall}); J, K|H|A(\text{overall}); J, K'\rangle \\
&\quad = 9N(A_1)^2 \sum_{n=1,2,6,7} \sum_{k=1,2,3,4} a(A)_n \langle 1|h_k|n\rangle \langle J, K|R_k|J, K'\rangle, \\
&\langle E_a(\text{overall}); J, K|H|E_a(\text{overall}); J, K'\rangle \\
&\quad = 9N(E)^2 \Bigg[\sum_{n=1,2,6,7} \sum_{k=1,2,3,4} a(E)_n \langle 1|h_k|n\rangle \langle J, K|R_k|J, K'\rangle \\
&\qquad + \sqrt{3}(2\langle 1|r|2\rangle - \langle 1|r|6\rangle)\langle J, K|J_x|J, K'\rangle \\
&\qquad + \sqrt{3}(2\langle 1|s|2\rangle - \langle 1|s|6\rangle)\langle J, K|J_y|J, K'\rangle \Bigg], \\
&\langle E_{\text{sep}\,a}(\text{overall}); J, K|H|E_{\text{sep}\,a}(\text{overall}); J, K'\rangle \\
&\quad = 9N(E_{\text{sep}})^2 \Bigg[\sum_{n=1,2,6,7} \sum_{k=1,2,3,4} a(E_{\text{sep}})_n \langle 1|h_k|n\rangle \langle J, K|R_k|J, K'\rangle \\
&\qquad + \sqrt{3}(2\langle 1|q|2\rangle - \langle 1|q|7\rangle) K\delta_{KK'} \Bigg] \\
&\langle G_{\text{sep}\,a}(\text{overall}); J, K|H|G_{\text{sep}\,a}(\text{overall}); J, K'\rangle \\
&\quad = 9N(G_{\text{sep}})^2 \Bigg[\sum_{n=1,2,6,7} \sum_{k=1,2,3,4} a(G_{\text{sep}})_n \langle 1|h_k|n\rangle \langle J, K|R_k|J, K'\rangle \\
&\qquad - \sqrt{3}(\langle 1|q|2\rangle + \langle 1|q|7\rangle) K\delta_{KK'} \\
&\qquad - \sqrt{3}(\langle 1|r|2\rangle + \langle 1|r|6\rangle)\langle J, K|J_x|J, K'\rangle \\
&\qquad - \sqrt{3}(\langle 1|s|2\rangle + \langle 1|s|6\rangle)\langle J, K|J_y|J, K'\rangle \Bigg]
\end{aligned}
\tag{3.4.212}
$$

where

$$
\begin{aligned}
&\sum_{k=1,2,3,4} h_k R_k = h_v + AJ_z^2 + BJ_x^2 + CJ_y^2, \\
&\big(a(A)_1, a(A)_2, a(A)_6, a(A)_7\big) = (1, 4, 2, 2), \\
&\big(a(E)_1, a(E)_2, a(E)_6, a(E)_7\big) = (1, -2, -1, 2), \\
&\big(a(E_{\text{sep}})_1, a(E_{\text{sep}})_2, a(E_{\text{sep}})_6, a(E_{\text{sep}})_7\big) = (1, -2, 2, -1), \\
&\text{and } \big(a(G_{\text{sep}})_1, a(G_{\text{sep}})_2, a(G_{\text{sep}})_6, a(G_{\text{sep}})_7\big) = (1, 1, -1, -1).
\end{aligned}
$$

In Eq. 3.4.212, an unsubscripted A is used to indicate either of A_1 or A_2 since A_1 and A_2 discriminate merely between $K =$ even and $K =$ odd levels, and E_{sep} is similarly used for either of $E_{1\text{sep}}(K = \text{even})$ or $E_{2\text{sep}}(K = \text{odd})$.

We will mention briefly changes occurring in the treatment of the tunneling matrix formulation for acetone-like molecule of case $\boldsymbol{C}_{2v}(\boldsymbol{G}_{36})$. When we assume

$$
(14)(26)(35)(78)^*|1\rangle = +|1\rangle \quad \text{and} \quad (23)(56)^*|1\rangle = +|1\rangle, \tag{3.4.213}
$$

the symmetrized torsional functions, $|A_1(\text{torsion})\rangle$, $|E(\text{torsion})\rangle$, $|E_{1\text{sep}}(\text{torsion})\rangle$ and $|G(\text{torsion})\rangle$, shown for the case of a dimethylamine-like molecule in Eq. 3.4.205 corresponds to $|A_1(\text{torsion})\rangle$, $|E_3(\text{torsion})\rangle$, $|E_1(\text{torsion})\rangle$ and $|G(\text{torsion})\rangle$,

respectively, for an acetone-like molecule of case $\boldsymbol{C}_{2v}(\boldsymbol{G}_{36})$. Rotational functions are classified in the case of an acetone-like molecule as follows:

$$\begin{aligned}
|A_1(\text{rotation}); J, K\rangle &= (1/\sqrt{2})\left[|J, K\rangle + (-1)^{J-K}|J, -K\rangle\right], (K = \text{even}, K \geq 0)\\
|A_2(\text{rotation}); J, K\rangle &= (1/\sqrt{2})\left[|J, K\rangle - (-1)^{J-K}|J, -K\rangle\right], (K = \text{even}, K \geq 0)\\
|A_3(\text{rotation}); J, K\rangle &= (1/\sqrt{2})\left[|J, K\rangle - (-1)^{J-K}|J, -K\rangle\right], (K = \text{odd}, K > 0)\\
|A_4(\text{rotation}); J, K\rangle &= (1/\sqrt{2})\left[|J, K\rangle + (-1)^{J-K}|J, -K\rangle\right], (K = \text{odd}, K > 0).
\end{aligned} \tag{3.4.214}$$

When $K = 0$, the factor $1/\sqrt{2}$ should be replaced by $1/2$ in the above equations.

Another change is that contributions from the term isJ_y should be removed in the parameterized expressions Eq. 3.4.212 of Hamiltonian matrix elements.

3.4.5 Appendix to 3.4

3.4.5.1 Mathematical Relation 1

$$\begin{aligned}
e^{-i\chi_{\text{RAM}}J_z/\hbar}\left(J_x \pm iJ_y\right)e^{i\chi_{\text{RAM}}J_z/\hbar} &= e^{\pm i\chi_{\text{RAM}}}\left(J_x \pm iJ_y\right),\\
e^{-i\theta_{\text{RAM}}J_y/\hbar}\left(J_z \pm iJ_x\right)e^{i\theta_{\text{RAM}}J_y/\hbar} &= e^{\pm i\theta_{\text{RAM}}}\left(J_z \pm iJ_x\right),\\
e^{-i\phi_{\text{RAM}}J_z/\hbar}\left(J_x \pm iJ_y\right)e^{i\phi_{\text{RAM}}J_z/\hbar} &= e^{\pm i\phi_{\text{RAM}}}\left(J_x \pm iJ_y\right).
\end{aligned} \tag{3.4.215}$$

Proof By putting

$$U = e^{-i\alpha J_z/\hbar}\left(J_x \pm iJ_y\right)e^{i\alpha J_z/\hbar}, \tag{3.4.216}$$

we have

$$\begin{aligned}
\frac{\partial U}{\partial \alpha} &= -\frac{i}{\hbar}J_z U + \frac{i}{\hbar}UJ_z\\
&= -\frac{i}{\hbar}\left(J_z U - UJ_z\right)\\
&= -\frac{i}{\hbar}e^{-i\alpha J_z/\hbar}\left[J_z, J_x \pm iJ_y\right]e^{i\alpha J_z/\hbar}\\
&= -\frac{i}{\hbar}e^{-i\alpha J_z/\hbar}\left(-i\hbar J_y \pm i^2\hbar J_x\right)e^{i\alpha J_z/\hbar}\\
&= \pm ie^{-i\alpha J_z/\hbar}\left(J_x \pm iJ_y\right)e^{i\alpha J_z/\hbar}\\
&= \pm iU.
\end{aligned} \tag{3.4.217}$$

That is

$$\frac{\partial U}{\partial \alpha} = \pm iU. \tag{3.4.218}$$

Solving this differential equation, we have $U = u\exp(\pm i\alpha)$. Since $U = J_x \pm J_y$ at $\alpha = 0$, we obtain

$$U = e^{\pm i\alpha}\left(J_x \pm iJ_y\right). \tag{3.4.219}$$

The first relation of (3.4.215) is thus derived. □

Similarly, the second and the third relations of (3.4.215) can be derived.

3.4.5.2 Mathematical Relation 2

$$\begin{aligned} &e^{-i\phi_{\mathrm{RAM}}J_z/\hbar}e^{-i\theta_{\mathrm{RAM}}J_y/\hbar}e^{-i\chi_{\mathrm{RAM}}J_z/\hbar}\begin{bmatrix} J_x \\ J_y \\ J_z \end{bmatrix}e^{i\chi_{\mathrm{RAM}}J_z/\hbar}e^{i\theta_{\mathrm{RAM}}J_y/\hbar}e^{i\phi_{\mathrm{RAM}}J_z/\hbar} \\ &= S^{+1}(-\theta_{\mathrm{RAM}}, -\phi_{\mathrm{RAM}}, -\chi_{\mathrm{RAM}})\begin{bmatrix} J_x \\ J_y \\ J_z \end{bmatrix} \end{aligned} \tag{3.4.220}$$

Proof From the first relation of (3.4.215) we have

$$\begin{aligned} e^{-i\chi_{\mathrm{RAM}}J_z/\hbar}J_x e^{i\chi_{\mathrm{RAM}}J_z/\hbar} &= \frac{1}{2}\left(e^{i\chi_{\mathrm{RAM}}} + e^{-i\chi_{\mathrm{RAM}}}\right)J_x + \frac{i}{2}\left(e^{i\chi_{\mathrm{RAM}}} - e^{-i\chi_{\mathrm{RAM}}}\right)J_y \\ &= (\cos\chi_{\mathrm{RAM}})J_x - (\sin\chi_{\mathrm{RAM}})J_y, \\ e^{-i\chi_{\mathrm{RAM}}J_z/\hbar}J_y e^{i\chi_{\mathrm{RAM}}J_z/\hbar} &= \frac{1}{2i}\left(e^{i\chi_{\mathrm{RAM}}} - e^{-i\chi_{\mathrm{RAM}}}\right)J_x + \frac{1}{2}\left(e^{i\chi_{\mathrm{RAM}}} + e^{-i\chi_{\mathrm{RAM}}}\right)J_y \\ &= (\sin\chi_{\mathrm{RAM}})J_x + (\cos\chi_{\mathrm{RAM}})J_y, \end{aligned}$$

Therefore, we have

$$e^{-i\chi_{\mathrm{RAM}}J_z/\hbar}\begin{bmatrix} J_x \\ J_y \\ J_z \end{bmatrix}e^{i\chi_{\mathrm{RAM}}J_z/\hbar} = S^{+1}(0, 0, -\chi_{\mathrm{RAM}})\begin{bmatrix} J_x \\ J_y \\ J_z \end{bmatrix}. \tag{3.4.221}$$

Similarly by using the second and the third relations of (3.4.215), we have

$$
\begin{aligned}
&e^{-i\phi_{\mathrm{RAM}}J_z/\hbar}e^{-i\theta_{\mathrm{RAM}}J_y/\hbar}e^{-i\chi_{\mathrm{RAM}}J_z/\hbar}\begin{bmatrix}J_x\\J_y\\J_z\end{bmatrix}e^{i\chi_{\mathrm{RAM}}J_z/\hbar}e^{i\theta_{\mathrm{RAM}}J_y/\hbar}e^{i\phi_{\mathrm{RAM}}J_z/\hbar}\\
&\quad= e^{-i\phi_{\mathrm{RAM}}J_z/\hbar}e^{-i\theta_{\mathrm{RAM}}J_y/\hbar}S^{+1}(0,0,-\chi_{\mathrm{RAM}})\begin{bmatrix}J_x\\J_y\\J_z\end{bmatrix}e^{i\theta_{\mathrm{RAM}}J_y/\hbar}e^{i\phi_{\mathrm{RAM}}J_z/\hbar}\\
&\quad= S^{+1}(0,0,-\chi_{\mathrm{RAM}})e^{-i\phi_{\mathrm{RAM}}J_z/\hbar}e^{-i\theta_{\mathrm{RAM}}J_y/\hbar}\begin{bmatrix}J_x\\J_y\\J_z\end{bmatrix}e^{i\theta_{\mathrm{RAM}}J_y/\hbar}e^{i\phi_{\mathrm{RAM}}J_z/\hbar}\\
&\quad= S^{+1}(0,0,-\chi_{\mathrm{RAM}})S^{+1}(-\theta_{\mathrm{RAM}},0,0)e^{-i\phi_{\mathrm{RAM}}J_z/\hbar}\begin{bmatrix}J_x\\J_y\\J_z\end{bmatrix}e^{i\phi_{\mathrm{RAM}}J_z/\hbar}\\
&\quad= S^{+1}(0,0,-\chi_{\mathrm{RAM}})S^{+1}(-\theta_{\mathrm{RAM}},0,0)S^{+1}(0,-\phi_{\mathrm{RAM}},0)\begin{bmatrix}J_x\\J_y\\J_z\end{bmatrix}\\
&\quad= S^{+1}(-\theta_{\mathrm{RAM}},-\phi_{\mathrm{RAM}},-\chi_{\mathrm{RAM}})\begin{bmatrix}J_x\\J_y\\J_z\end{bmatrix}.
\end{aligned}
$$

□

3.4.5.3 Mathematical Relation 3

$$
\begin{aligned}
&e^{-i\phi_{\mathrm{RAM}}J_z/\hbar}e^{-i\theta_{\mathrm{RAM}}J_y/\hbar}e^{-i\chi_{\mathrm{RAM}}J_z/\hbar}S^{-1}(\theta,\phi,\chi)e^{i\chi_{\mathrm{RAM}}J_z/\hbar}e^{i\theta_{\mathrm{RAM}}J_y/\hbar}e^{i\phi_{\mathrm{RAM}}J_z/\hbar}\\
&\quad= S^{-1}(\theta,\phi,\chi)S^{-1}(-\theta_{\mathrm{RAM}},-\phi_{\mathrm{RAM}},-\chi_{\mathrm{RAM}})
\end{aligned}
\tag{3.4.222}
$$

Proof Using Eq. 3.4.220 and the relation between the molecule-fixed components J_x, J_y, J_z and the laboratory-fixed components J_X, J_Y, J_Z of the angular momentum operator

$$
\begin{bmatrix}J_x\\J_y\\J_z\end{bmatrix} = S^{+1}(\theta,\phi,\chi)\begin{bmatrix}J_X\\J_Y\\J_Z\end{bmatrix}, \tag{3.4.223}
$$

together with the commutation relations $[J_\alpha, J_i] = 0(\alpha = x, y, z; i = X, Y, Z)$, we have

$$e^{-i\phi_{\mathrm{RAM}}J_z/\hbar}e^{-i\theta_{\mathrm{RAM}}J_y/\hbar}e^{-i\chi_{\mathrm{RAM}}J_z/\hbar}S^{+1}(\theta,\phi,\chi)e^{i\chi_{\mathrm{RAM}}J_z/\hbar}e^{i\theta_{\mathrm{RAM}}J_y/\hbar}e^{i\phi_{\mathrm{RAM}}J_z/\hbar}$$
$$= S^{+1}(-\theta_{\mathrm{RAM}},-\phi_{\mathrm{RAM}},-\chi_{\mathrm{RAM}})S^{+1}(\theta,\phi,\chi),$$

By taking the inverse operation in both sides of the above equation, we obtain the relation (3.4.222). □

3.4.5.4 Permutation–Inversion Group

The permutation–inversion group proposed by Longuet-Higgins [35] will be mentioned below briefly.

In order to introduce the permutation–inversion group, we take an exact copy of some sentences from the paper of Longuet-Higgins [35] with permission from Taylor & Francis.

"Let P be any permutation of positions and spins of identical nuclei, or any product of such permutations. Let E be the identity, E^* the inversion of all particle positions, and P^* the product $PE^* = E^*P$. Then the molecular symmetry group is the set of

1. all feasible P, including E,
2. all feasible P^*, not necessarily including E^*".

The molecular symmetry group used above is equivalent to the permutation–inversion group. In the above description, the word "feasible" involves very important concept. "feasible" transformations are those which can be achieved within the time scale of a given laboratory experiment without passing over an insuperable energy barrier. Although any P and any P^* keep the Hamiltonian operator of a free molecule invariant surely, the molecular symmetry group (permutation–inversion group) is composed of feasible P and feasible P^*. Such an idea will be natural, considering that experimental spectra reflect phenomena occurring only within the time scale of observation.

Let define the group operations in the permutation–inversion group, taking the case of the CH_3OH molecule as a simple example. Let call methyl protons 1, 2 and 3. If the internal rotation is not feasible, the permutation–inversion group elements are E and $(23)^*$. $(23)^*$ corresponds to a plane of symmetry. As shown in Table 3.8, a configuration produced by the operation $(23)^*$ can be achieved by an overall rotation about molecule-fixed y-axis. When the internal rotation is feasible, we have six group operations $E, (123), (132), (23)^*, (13)^*, (12)^*$, which are generated from two elements (123) and $(23)^*$ (such two elements are called generating operations). We call the permutation–inversion for the methanol $\boldsymbol{G}_6$ for a simple reason that it has six elements. When $F(\boldsymbol{R}_1, \boldsymbol{R}_2, \boldsymbol{R}_3; \sigma_\alpha(1), \sigma_\beta(2), \sigma_\gamma(3))$ be a function or an operator regarding to nuclei 1, 2, and 3, the permutation–inversion operations are defined as follows, obeying Hougen's method described in Ref. [48]:

$$
\begin{aligned}
(23)^{*}F\left(\boldsymbol{R}_1,\boldsymbol{R}_2,\boldsymbol{R}_3;\sigma_\alpha(1),\sigma_\beta(2),\sigma_\gamma(3)\right) &= F\left(-\boldsymbol{R}_1,-\boldsymbol{R}_3,-\boldsymbol{R}_2;\sigma_\alpha(1),\sigma_\beta(3),\sigma_\gamma(2)\right),\\
(123)F\left(\boldsymbol{R}_1,\boldsymbol{R}_2,\boldsymbol{R}_3;\sigma_\alpha(1),\sigma_\beta(2),\sigma_\gamma(3)\right) &= F\left(\boldsymbol{R}_2,\boldsymbol{R}_3,\boldsymbol{R}_1;\sigma_\alpha(2),\sigma_\beta(3),\sigma_\gamma(1)\right),\\
(23)^{*}(123)F\left(\boldsymbol{R}_1,\boldsymbol{R}_2,\boldsymbol{R}_3;\sigma_\alpha(1),\sigma_\beta(2),\sigma_\gamma(3)\right) &= (23)^{*}F\left(\boldsymbol{R}_2,\boldsymbol{R}_3,\boldsymbol{R}_1;\sigma_\alpha(2),\sigma_\beta(3),\sigma_\gamma(1)\right)\\
&= F\left(-\boldsymbol{R}_3,-\boldsymbol{R}_2,-\boldsymbol{R}_1;\sigma_\alpha(3),\sigma_\beta(2),\sigma_\gamma(1)\right),\\
&= (13)^{*}F\left(\boldsymbol{R}_1,\boldsymbol{R}_2,\boldsymbol{R}_3;\sigma_\alpha(1),\sigma_\beta(2),\sigma_\gamma(3)\right).
\end{aligned}
\tag{3.4.224}
$$

3.4.5.5 Framework Functions Defined so as to be Orthogonalized with Each Other

Let us put N framework functions localized at each of N potential minima as follows:

$$
|n\rangle = O_n|1\rangle,\ (n=1,2,3,\ldots,N), \tag{3.4.225}
$$

where $O_n(n=1,2,3,\ldots,N)$ stand for permutation–inversion group operations corresponding to feasible large-amplitude vibrations. For the case of a molecule with one methyl top executing internal rotation, $O_1 = E$ (identity transformation), $O_2 = (123)$, and $O_3 = (132)$. The framework functions $|n\rangle(n=1,2,3,\ldots,N)$ as defined above in Eq. 3.4.225 have non-zero overlap integrals $\Delta_{ij}(\Delta_{ij} = \langle i|j\rangle)$ and it is inconvenient in the viewpoint of spectral analysis. For avoiding the inconvenience, we introduce framework functions defined newly as follows:

$$
|i:\mathrm{new}\rangle = \sum_{m=1}^{N}\left(\Delta^{-1/2}\right)_{mi}|m\rangle,\quad (i=1,2,3,\ldots,N) \tag{3.4.226}
$$

where $\Delta^{-1/2} \equiv Sd^{-1/2}S^{\dagger}$, and $d \equiv S^{\dagger}\Delta S$ is the diagonal matrix of positive eigenvalues obtained by applying the unitary transformation S to Δ (Δ is a matrix composed of elements $\Delta_{ij}(i,j=1,2,3,\ldots,N)$). For the new framework functions $|i:\mathrm{new}\rangle(i=1,2,3,\ldots,N)$, it can be shown that

$$
\begin{aligned}
\langle i:\mathrm{new}|j:\mathrm{new}\rangle &= \delta_{ij},\\
|i:\mathrm{new}\rangle &= O_i|1:\mathrm{new}\rangle,
\end{aligned}
\tag{3.4.227}
$$

assuming $\langle 1|1\rangle = 1$.

For a simple case of a molecule with one methyl top, Eq. 3.4.226 leads to

$$
\begin{pmatrix} |1:\mathrm{new}\rangle \\ |2:\mathrm{new}\rangle \\ |3:\mathrm{new}\rangle \end{pmatrix} = \frac{1}{3}\begin{bmatrix} \frac{1}{\sqrt{1+2S}}+\frac{2}{\sqrt{1-S}} & \frac{1}{\sqrt{1+2S}}-\frac{1}{\sqrt{1-S}} & \frac{1}{\sqrt{1+2S}}-\frac{1}{\sqrt{1-S}} \\ \frac{1}{\sqrt{1+2S}}-\frac{1}{\sqrt{1-S}} & \frac{1}{\sqrt{1+2S}}+\frac{2}{\sqrt{1-S}} & \frac{1}{\sqrt{1+2S}}-\frac{1}{\sqrt{1-S}} \\ \frac{1}{\sqrt{1+2S}}-\frac{1}{\sqrt{1-S}} & \frac{1}{\sqrt{1+2S}}-\frac{1}{\sqrt{1-S}} & \frac{1}{\sqrt{1+2S}}+\frac{2}{\sqrt{1-S}} \end{bmatrix}\begin{pmatrix} |1\rangle \\ |2\rangle \\ |3\rangle \end{pmatrix} \tag{3.4.228}
$$

where $S = \langle 1|2\rangle = \langle 2|1\rangle = \langle 1|3\rangle = \langle 3|1\rangle = \langle 2|3\rangle = \langle 3|2\rangle$.

References

1. L.I. Schiff, *Quantum Mechanics*, 2nd edn. (McGraw-Hill, New York, 1969)
2. G. Herzberg, *Atomic Spectra and Atomic Structure* (Dover Publications, Inc., New York, 1944)
3. S. Yamamoto, S. Saito, Astrophys. J. **370**, L103 (1991)
4. H. Klein, F. Lewen, R. Schieder, J. Stutzki, G. Winnewisser, Astrophys. J. **494**, L125 (1998)
5. C.H. Townes, A.L. Schawlow, *Microwave Spectroscopy* (McGraw- Hill, New York, 1955)
6. M. Born, J.R. Oppenheimer, Ann. Phys. **84**, 457 (1927)
7. T. Oka, J. Chem. Phys. **47**, 5410 (1967)
8. M.R. Aliev, J.K.G. Watson, in Chapter 1 in *Molecular Spectroscopy: Modern Research*, vol. III, ed. by K. Narahari Rao (Academic Press, Orland, 1985)
9. J.L. Dunham, Phys. Rev. **41**, 721 (1932)
10. E. Hirota, J.M. Brown, J.T. Hougen, T. Shida, N. Hirota, Pure Appl. Chem. **66**, 571 (1994)
11. P.R. Bunker, R.E. Moss, J. Mol. Spectrosc. **80**, 217 (1980)
12. W. Gordy, R.L. Cook, *Microwave Molecular Spectra* (Wiley, New York, 1970)
13. B.T. Sutcliffe, J. Tennyson, Int. J. Quantum. Chem. **39**, 183 (1991)
14. P.R. Bunker, *Molecular Symmetry and Spectroscopy* (Academic Press, New York, 1979)
15. E.B. Wilson, J.C. Decius, P. Cross, *Molecular Vibrations* (McGraw-Hill, New York, 1955)
16. D. Papoušek, M.R. Aliev, *Molecular Vibrational–Rotational Spectra* (Elsevier, Amsterdam, 1982)
17. C. Eckart, Phys. Rev. **47**, 552 (1935)
18. E.B. Wilson, J. Chem. Phys. **7**, 1047 (1939)
19. H.H. Nielsen, Rev. Mod. Phys. **23**, 90 (1951)
20. J.K.G. Watson, Mol. Phys. **15**, 479 (1968)
21. A.R. Hoy, I.M. Mills, G. Strey, Mol. Phys. **24**, 1265 (1972)
22. P. Jensen, P.R. Bunker (eds.), *Computational Molecular Spectroscopy* (Wiley, Chichester, 2000)
23. E.B. Wilson, J.B. Howard, J. Chem. Phys. **4**, 260 (1936)
24. B.T. Darling, D.M. Dennison, Phys. Rev. **57**, 128 (1940)
25. P.R. Bunker, P. Jensen, *Molecular Symmetry and Spectroscopy*, 2nd edn. (NRC Press, Ottawa, 1998)
26. S. Maes, G. Amat, Cah. Phys. **11**, 25 (1957)
27. J.K.G. Watson, J. Chem. Phys. **46**, 1935 (1967)
28. J.K.G. Watson, in *Vibrational Spectra and Structure*, vol. 6, ed. by J. Durig (Elsevier, Amsterdam, 1977)
29. K. Sarka, D. Papoušek, J. Demaison, H. Mäder, H. Harder, in *Vibration-Rotational Spectroscopy and Molecular Dynamics*, ed. by D. Papoušek. *Advanced Series in Physical Chemistry*, vol. 9 (World Scientific, Singapore, 1997)
30. K. Sarka, J. Demaison, in *Computational Molecular Spectroscopy*, eds. by P. Jensen, P.R. Bunker (Wiley, Chichester, 2000)
31. P.R. Bunker, P. Jensen, *Fundamentals of Molecular Symmetry* (IOP Publishing, Bristol, 2004)
32. P. Jensen, P.R. Bunker, in *Encyclopedia of Chemical Physics and Physical Chemistry*, eds. by J.H. Moore, N.D. Spencer (IOP Publishing, Bristol, 2001)
33. R.G.A. Bone, T.W. Rowland, N.C. Handy, A.J. Stone, Mol. Phys., **72**, 33 (1991)
34. V. Špirko, S. Civiš, M. Ebert, V. Danielis, J. Mol. Spectrosc. **119**, 426 (1986)
35. H.C. Longuet-Higgins, Mol. Phys. **6**, 445 (1963)
36. V. Špirko, W.P. Kraemer, J. Mol. Spectrosc. **133**, 331 (1989)
37. C.D. Esposti, G. Cazzoli, D. Damlani, P.G. Favero, F. Strumia, Infrared Phys. **28**, 21 (1988)
38. W.J. Lafferty, F.J. Lovas, J. Phys. Chem. Ref. Data **7**, 441 (1978)
39. A.J. Alexander, H.W. Kroto, D.R.M. Walton, J. Mol. Spectrosc. **62**, 175 (1976)

40. M.B. Bell, P.A. Feldman, M.J. Travers, M.C. McCarthy, C.A. Gottlieb, P. Thaddeus, Astrophys. J. **483**, L61 (1997)
41. R. Boquet, J. Demaison, L. Poteau, M. Liedtke, S. Belov, K.M.T. Yamada, G. Winnewisser, C. Gerke, J. Grippm, Th. Koöhler, J. Mol. Spectrosc. **177**, 154 (1996)
42. G. Herzberg, *Molecular Spectra and Molecular Structure*, vol. III (D. van Nostrand Co, Inc., Princeton, 1967)
43. K. Yamada, J. Mol. Spectrosc. **81**, 139 (1980)
44. F.W. Loomis, R.W. Wood, Phys. Rev. **32**, 223 (1928)
45. B.P. Winnewisser, J. Reinstädtler, K.M.T. Yamada, J. Behrend, J. Mol. Spectrosc. **136**, 12 (1989)
46. J.T. Hougen, I. Kleiner, M. Godefroid, J. Mol. Spectrosc. **163**, 559 (1994)
47. D.R. Herschbach, J. Chem. Phys. **31**, 91 (1959)
48. J.T. Hougen, J. Mol. Spectrosc. **89**, 296 (1981)
49. N. Ohashi, J.T. Hougen, R.D. Suenram, F.J. Lovas, Y. Kawashima, M. Fujitake, J. Pyka, J. Mol. Spectrosc. **227**, 28 (2004)

Chapter 4
Laboratory Experimental Methods

Thomas F. Giesen and Karl Jacobs

4.1 Introduction

The vast majority of molecules detected in space has been identified by rotational and ro-vibrational spectra in the millimeter- and sub-millimeter wavelength region. Laboratory studies at sub-millimeter wavelengths or terahertz frequencies require sophisticated spectroscopic techniques, which have been developed over the last few decades by worldwide leading spectroscopy groups. In this section spectroscopic tools for high resolution Terahertz spectroscopy of gas phase molecules are presented and illustrated by examples from the Cologne laboratories.

4.1.1 Molecules Relevant to Laboratory Astrophysics

The class of molecules relevant to astronomy is quite extensive and it contains well known stable molecules like carbon monoxide, water, and ammonia, as well as highly reactive, unstable species, e.g., unsaturated carbon hydrides and a number of molecular ions. Hydrogen is by far the prevailing element of gas phase interstellar matter, and molecular and protonated molecular hydrogen are the first molecules to be formed in interstellar space. In reactions with more heavy atoms, e.g., carbon, oxygen, nitrogen, sulfur, fluorine and chlorine, light molecular hydrides and their cations are formed. Up to date CH^+, CH, CH_2, NH, NH_2, NH_3, OH, OH^+, H_2O, H_2O^+, H_3O^+, HCl, H_2Cl^+, HF, SH^+, and H_2S have been detected in diffuse clouds and cold environments of the interstellar medium. With the center

T. F. Giesen (✉) and K. Jacobs
Universität zu Köln, I. Physikalisches Institut, Zülpicher Str. 77, 50937 Köln, Germany
e-mail: giesen@ph1.uni-koeln.de

K. M. T. Yamada and G. Winnewisser (eds.), *Interstellar Molecules*,
Springer Tracts in Modern Physics 241, DOI: 10.1007/978-3-642-16268-8_4,

of mass almost at the central heavy atom, light hydrides have small momenta of inertia and accordingly large rotational constants. As a consequence their rotational spectra are predominantly found in the THz region. For example, the ground state rotational constant of methylidynium, CH^+, is $B = 418$ GHz. Only recently accurate laboratory data of the lowest rotational transition $J = 1 \leftarrow 0$ at 835 GHz were reported by Amano in 2010 [1], and following this CH^+ was astronomically detected in the direction of massive star forming regions by Falgarone et al. [2] using the Heterodyne Instrument for the Far Infrared (HIFI) onboard the Herschel satellite [3].

Due to the lack of a permanent electrical dipole moment, molecular and protonated molecular hydrogen, H_2, and H_3^+, have no pure rotational spectra to be observed in the millimeter- and sub-millimeter-wavelength region, but their deuterated isotopologues HD, H_2D^+, D_2H^+ posses rotational transitions in the Terahertz region thanks to a dipole moment pointing along the axis of symmetry. Because of their relevance to astronomy they are prime targets for laboratory investigations. The lowest rotational transitions of *para*-H_2D^+ at 1.370 THz and of *ortho*-D_2H^+ at 1.477 THz were recently revisited by Asvany et al. [4] applying most accurate laser induced reaction spectroscopy at sub-millimeter wavelengths.

From the list of molecules detected in space, see tables in Chap. 5, it becomes evident that carbon containing species contribute mostly to the diversity of interstellar chemistry. Carbon chain molecules terminated by nitrogen, oxygen or hydrogen groups are present as well as pure carbon chains and carbon hydrogen rings. Most of them are highly reactive and unstable under terrestrial conditions. Laboratory studies of carbon species therefore rely on advanced preparatory methods such as electrical discharge cells and supersonic jet laser ablation sources. Provided a permanent electrical dipole moment their rotational spectra spread over the frequency range of a few Terahertz, but at low temperatures, as predominate in cold interstellar clouds, the maximum of line intensities is shifted to lower frequencies of tens to hundreds of GHz. Pure carbon chain molecules have no permanent dipole moment and thus no pure rotational spectra, but thanks to their low lying vibrational modes they can be identified by ro-vibrational spectra in the 1–5 THz region.

Figure 4.1 shows the stick spectra of a few example molecules relevant to astrophysics. It is clearly to be seen that H_2D^+ and H_2O have only few rotational transitions in the Terahertz region. In opposite, pure rotational spectra of heavier molecules, e.g., the C_3H carbon chain molecule, are more dense and mostly below 1 THz whereas ro-vibrational transitions of lowest bending modes of carbon chain molecules occur in the Terahertz region, as for example in case of the $v = 1 \leftarrow 0$ transitions of C_3H. Figure 4.1 also shows that spectra of larger, asymmetric top molecules such as dimethyl ether (DME) are rather complex with spectral line densities often close to the confusion limit. Beside DME, other organic molecules have been found mostly in warm regions of the interstellar medium with consequently complicated and dense spectra. It is one of the challenges of laboratory astrophysics to record and analyze spectra of complex molecules in the Terahertz

region and to give highly accurate frequency positions for a clear assignment of spectra from astrophysical observations.

So far laboratory studies led to the large amount of spectroscopic data currently available in molecular data bases, such as the Jet Propulsion Laboratories (JPL) data base [5] and the Cologne Data Base for Molecular Spectroscopy [6]. The number of molecules under laboratory investigation is still growing and hence the number of entrances in data bases do as well. Especially the demand for Terahertz spectroscopic data is tremendous due to the advent of observatories operating at high frequencies, such as the APEX telescope [7] or the HIFI instrument onboard the Herschel satellite [3]. No doubt, we currently live in a very exciting and challenging time for both laboratory astrophysics and astronomical observations.

4.1.2 Spectral Line Widths and Intensities

Absorption spectroscopy is widely used to study spectra of gas phase molecules at highest spectral resolution. The general setup of an absorption spectrometer consists of a monochromatic tunable radiation source, a sample of molecules under investigation, and a sensitive detection system. As has been pointed out above, the Terahertz spectral region is most relevant for astrophysical observations and, therefore, appropriate tunable radiation sources with highest spectral resolution for

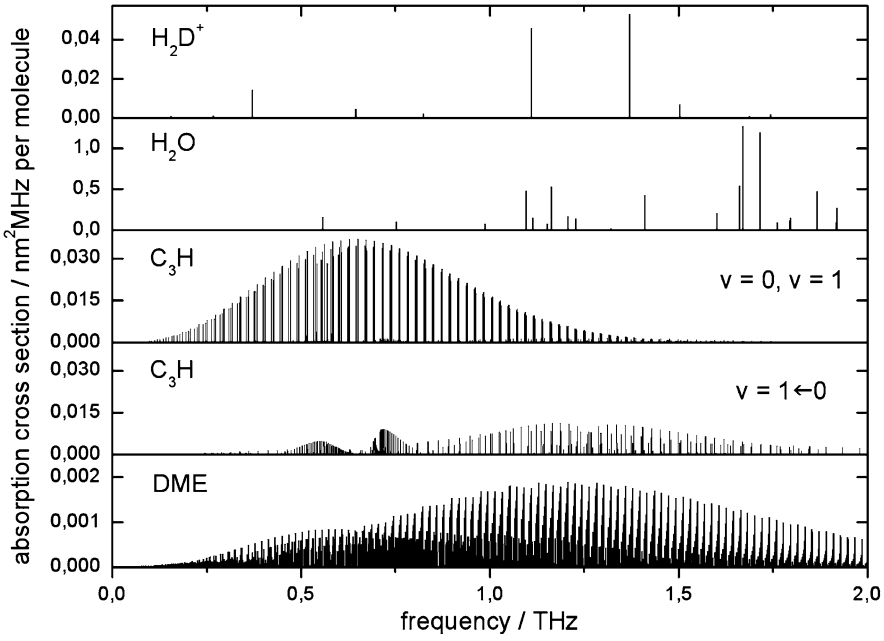

Fig. 4.1 Calculated stick spectra of specific molecules in the Terahertz region

laboratory investigations are a prerequisite. At low sample pressures the spectral line width is given by the molecules velocity distribution, which leads to Doppler line profiles with full width at half maximum $\Delta\nu_D$,

$$\Delta\nu_D = \nu \cdot 7.1 \times 10^{-7} \cdot \sqrt{\frac{T}{M}}. \tag{4.1.1}$$

Here ν denotes the transition frequency, T the temperature in Kelvin (K) and M the mass of the molecule in atomic mass units (amu). At 1 THz and room temperature the Doppler width of a molecule like C_3H, with $M = 37$ amu, is $\Delta\nu_D = 2$ MHz, which requires a spectrometer with a spectral resolution $\Delta\nu$ of better than 10^{-6}. Radiation sources with monochromaticity $\Delta\nu$ of typically 10^{-7} to 10^{-8} are needed to measure molecular line contours and, in sophisticated sub-Doppler experiments, the underlying substructure of hyperfine lines.

4.2 Monochromatic Radiation Sources for High Resolution Absorption Spectroscopy

4.2.1 Overview

Until recently a major constraint in high resolution Terahertz spectroscopy was the lack of appropriate monochromatic radiation sources. High frequency electronic devices, such as Klystrons, Gunn diodes and electron tubes [8] have been used to generate monochromatic radiation up to roughly 100 GHz and subsequent frequency multiplication techniques by Schottky multiplier devices generate radiation in the THz region, although with a significant drop in output power. In the 1980th backward wave oscillators (BWOs) were developed for Terahertz spectroscopy. They produce radiation from a guided electron beam traveling along a high voltage periodic structure placed in a resonator tube. BWOs above 1 THz, which are tunable over a spectral range of a few hundred GHz, and with output powers of several mW, were developed and successfully applied to spectroscopy. For two decades, BWOs became workhorse radiation sources in many laboratories until recently, when multiplier based all solid state sources became more favorable. For several reasons BWOs did not prevail in the spectroscopic community, major ones being constraints in handiness, lifetime, and commercial availability. Instead, commercially available cascaded Schottky multiplier chains fed by highly monochromatic radiation of a synthesizer at typically 10–30 GHz are nowadays widely in use to cover the spectral range up to 2 THz. Although the optical quality of their radiation is better in comparison to BWO tubes, the low output power at the end of the multiplication process is still of concern. Amplifiers for frequencies above 100 GHz and multipliers with smaller losses may ease this constraint and allow to further extend the spectral range above 2 THz. A promising approach to frequency multiplication are superlattice devices and first results have been reported recently

by Endres et al. [9]. Because they generate only odd numbered harmonics the power-drop at higher harmonics is less drastically compared to Schottky type multipliers, although at 3.1 THz the output does not exceed a few 10^{-9} W. While for frequencies in the mid-infrared region and above quite powerful high resolution sources are available, the range from 2 to 10 THz is still a technical challenge. Efforts to bridge the Terahertz gap from the high frequency side have been reviewed by Siegel [10] and new solutions, such as quantum cascade lasers for Terahertz radiation, became commercially available recently.[1]

Lasers have also been used for both frequency down- and up-conversion to generate Terahertz radiation. Far-infrared gas lasers at fixed frequencies are mixed with radiation from tunable sources on appropriate mixing devices. By this manner, tunable laser-sideband radiation is generated at Terahertz frequencies, which can be used for high resolution spectroscopy. Finally, laser-mixing of far-infrared and near infrared lasers were used for difference frequency generation in the Terahertz range. First commercially available systems are offered by Toptica Photonics AG.[2]

In cases when less spectral resolution is sufficient, Fourier Transform spectroscopy proofs to be a useful tool to record broad scan spectra. The constraint of commonly used black body radiation sources (globars)—emitting only few photons in the Terahertz region with low optical beam quality—has recently been overcome by collimated synchrotron radiation sources for the far infrared, which emit 2–3 orders of magnitudes more photons than globars do. The French SOLEIL and the Canadian Light Source synchrotron facilities both have far infrared beam lines combined with high resolution Fourier-Transform spectrometers. Although Fourier Transform spectroscopy is of relevance to Terahertz spectroscopy, in the following section the focus is on spectrometers which make use of monochromatic radiation sources.

4.2.2 Terahertz Backward-Wave Oscillators

4.2.2.1 Principle and Performance of BWOs

One of the most successfully used sources for monochromatic THz radiation is the BWO. The device consists of a periodic metallic structure placed inside a resonator tube. Electrons leaving a heated filament are accelerated in a strong electrical field of several kV. An axial homogenous magnetic field of order of 1 T confines the electrons to a narrow beam with current densities as high as 300 A/cm^2. By passing the low voltage periodic structure (typically at 20 V) the electron phase

[1] Alpes Lasers, http://www.alpeslasers.ch/.

[2] http://www.toptica.com/.

velocity is modulated and energy is transferred to eigenmodes of the resonator, thereby stimulating electromagnetic modes to oscillate.

The oscillation frequency depends on the electron velocity and the dimension of the periodic structure. Higher electron velocities or reduced grid spacings both lead to higher frequencies. Figure 4.2 shows a schematic drawing of the BWO tube and a typically frequency–voltage curve. At −5 kV cathode voltage the electron velocity reaches 10% of the speed of light. A detailed theoretical description of BWOs can be found in articles by Levush [11, 12] and references therein. Tubes with different periodic structures have been designed and fabricated by the Russian company ISTOK Research and Production in Fryazino. They cover the spectral range from 36 GHz to 1.4 THz (see [13]) with output powers of some tens of mW at low and medium frequencies (300–600 GHz) and one to a few mW at the high frequency end. The line width of BWO radiation is of the order of few MHz. As an example the upper trace of Fig. 4.3 shows the ${}^rQ_3$ branch spectrum of H_2S_2 at 978 GHz which has been recorded with a BWO spectrometer [14, 15]. For comparison the lower trace shows the same spectrum measured with the high-resolution Fourier-Transform Spectrometer at Giessen university [16]. The full Doppler width at half maximum of H_2S_2 lines at room temperature and at 1 THz is 1.5 MHz, which is easily resolved by a BWO spectrometer. On the other hand an FT-spectrometer with two meter optical path length has a spectral resolution of only 2.5×10^{-3} cm^{-1} or 75 MHz. The line width of BWOs is mainly attributed to phase noise, instabilities of the voltage supply and inhomogeneity of the magnetic field. The frequency accuracy and stability of BWOs can significantly be improved by at least three orders of magnitude when the output radiation is phase-locked to a highly accurate frequency standard. Rubidium standards with frequency accuracy of $\Delta\nu/\nu = 10^{-11}$ or the GPS time standard are well suited to stabilize the BWO frequency in a phase-locking loop (PLL) mode.

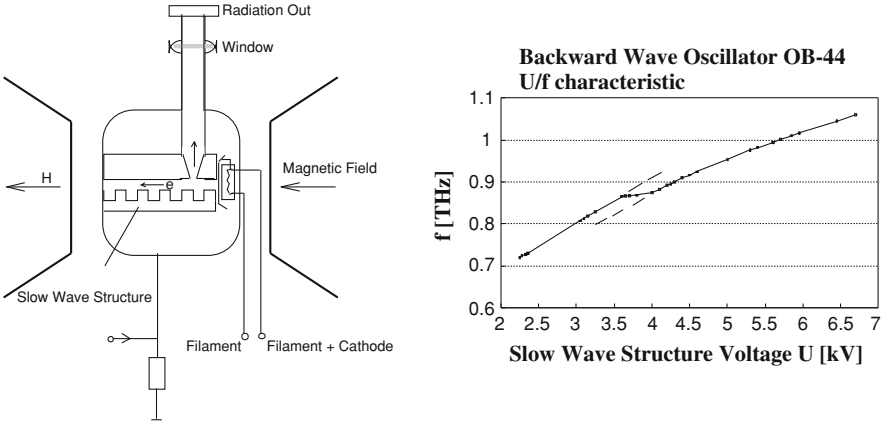

Fig. 4.2 Schematic drawing of a backward wave oscillator (BWO) and typical frequency versus voltage curve

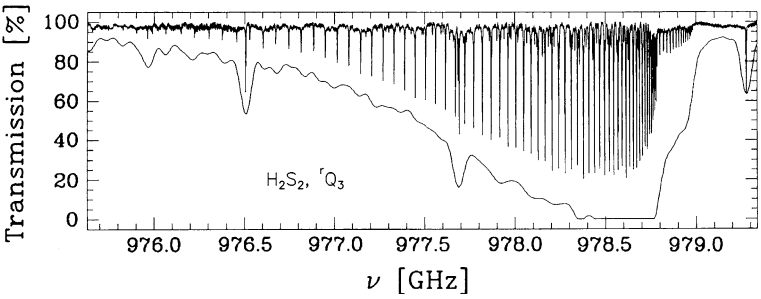

Fig. 4.3 $^rQ_3$ branch of H_2S_2 recorded with a BWO spectrometer (*upper trace*) and with a high resolution FT-Spectrometer (*lower trace*). (Modified version of Fig. 4.2 with permission from [14], © 1993, Elsevier)

4.2.2.2 Principle of Phase-Lock Loops

The technique of phase-locking is widely used to reduce and stabilize radiation in the cm- and mm-wavelength region (see, e.g., Bester et al. [17]). Phase-locking applied to a BWO at 170 GHz has been reported as early as 1970 [18]. Later Goy et al. used a phase-lock loop to stabilize the output of a carcinotron, which is a West-European type of a BWO [19]. In 1982 van Vliet reported on a frequency doubled 230 GHz PLL-BWO which was used as accurate local oscillator in a heterodyne receiver setup at 460–500 GHz [20]. Goy et al. and Bogey et al. used phase-locked Thomson-CSF carcinotrons up to 480 GHz [21], and Bava et al. a 600 GHz PLL-BWO [22]. In 1993 the Cologne spectroscopy group reported the first PLL-BWO at 1 THz (see [15, 23, 24]). Later Bogey used Russian PLL-BWOs up to 900 GHz [25]. PLL-BWOs were also used in laboratory groups in Japan, namely by Yamada at 1 THz [26] and Amano at 600 GHz [27]. Thanks to Terahertz BWOs an extensively large number of molecules has been measured and most reliable spectroscopic data in the submm-wavelength region were achieved.

A PLL compares the frequency of a monochromatic radiation source with a most accurate frequency standard. Deviation from the reference standard generates an error signal in the PLL which is fed back to the monochromatic radiation source to correct the output frequency. Frequency accuracies of $\Delta\nu/\nu = 10^{-9}$ and better are feasible which corresponds to an absolute frequency accuracy of 1 kHz at 1 THz.

To phase-lock the frequency (ν_{BWO}) of a BWO to the frequency (ν_{REF}) of a reference standard the BWO frequency is superimposed on a fast harmonic mixer with the mth harmonics of a phase locked synthesizer signal ($m \cdot \nu_{MW}$). The generated intermediate frequencies $\nu_{IF} = \nu_{BWO} - m \cdot \nu_{MW}$ is amplified and used in a feed back loop to control the voltage supply of the BWO. A schematic diagram of a PLL unit is shown in Fig. 4.4. An IF matching unit separates the intermediate frequency (IF), which is typically in the order of a few 10–350 MHz, from other products of the mixer unit and the IF signal is amplified by a low noise HEMT amplifier (For details see [28]). The low frequency intermediate signal enters a

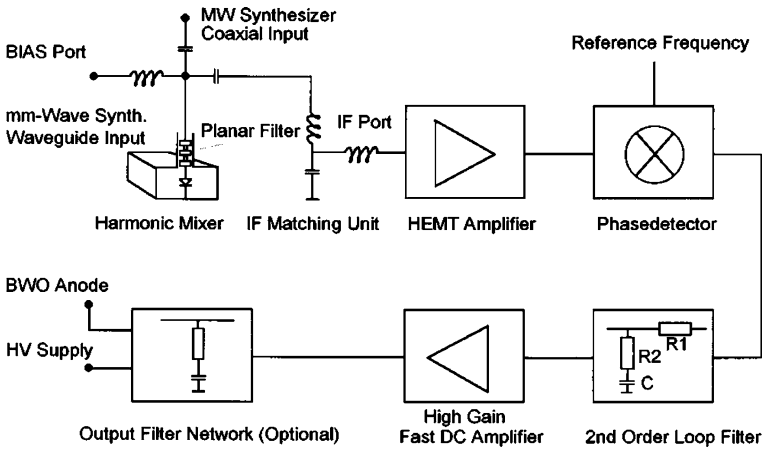

Fig. 4.4 Schematic diagram of a PLL unit for locking the frequency of a BWO to a reference frequency. (Reproduction of Fig. 4.3 with permission from [28]. © 1998, American Institute of Physics)

phase detector and is compared to the precise phase of a reference signal (ν_{REF}), which can be either a rubidium time standard, the GPS time reference signal, or a signal of comparable accuracy. The Cologne spectrometers are synchronized to rubidium standards of either 5 or 10 MHz. The phase comparator detects slightest deviations of the intermediate signal from the reference and generates an error signal voltage which is amplified in a high gain fast DC amplifier and fed to the anode of the BWO to correct the BWO frequency. A review on phase locked BWO has been published by Krupnov [29].

The phase lock is monitored by a frequency analyzer, which displays the IF signal (see Fig. 4.5). The quality of the PLL depends on the stability and sufficient radiation power of the BWO and the synthesizer signal as well. For stable operation the peak maximum of the IF signal has to be at least 30 dB above the side lobes. Additional filters can partly reduce the levels of side lobes.

4.2.3 BWO Terahertz Spectrometers

Phase locked BWOs have been implemented in high resolution spectrometers to record spectra of gas phase molecules in simple absorption cells, electrical discharge cells and in supersonically cooled molecular jets.

One of the successfully operating instruments is the Cologne Terahertz spectrometer which uses several BWO tubes to cover the spectral range from 200 GHz to 1.2 THz. Figure 4.6 shows the experimental setup with a standard absorption cell 2–3 m long. To avoid collisional line broadening the pressure in the sample cell is kept typically at a few tens to hundreds μbar. The signal is detected on a

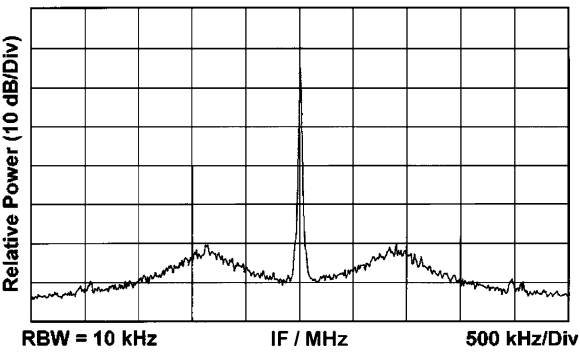

Fig. 4.5 Intermediate frequency (IF) signal of a phase locked BWO monitored by a frequency analyzer (logarithmic plot). The noise sidebands are approximately 48 dB at 10 kHz resolution bandwidth below the carrier. (Reproduction of Fig. 4.6 with permission [28]. © 1998, American Institute of Physics)

4 K liquid helium cooled InSb hot electron bolometer (QMC Instruments, Cardiff) with sensitivity of $10^{-11}\mathrm{W}/\sqrt{\mathrm{Hz}}$. The detector peak sensitivity can be tuned from typically 600 GHz up to 2 THz with an inhomogeneous magnetic field. This allows sensitive detection from 100 GHz up to 2.3 THz. To increase the sensitivity of the spectrometer the BWO output is frequency modulated at typically 50 kHz to record signals in second derivative using a fast Lock-In amplifier. A PC records the output signal of the Lock-In and controls the frequency tuning of the BWO by continuously stepping the output frequencies of a synthesizer. For the setup shown in Fig. 4.6 a 110 GHz and alternatively a 18 GHz synthesizer was used. Tuning the synthesizer frequency the PLL error signal corrects the BWO input voltage until the error signal is zero. For example, to record spectra at 1 THz the 9th harmonic of a 110 GHz synthesizer signal is used to generate an IF signal of 350 MHz and slowly scanned to record spectra. By this manner a number of stable molecules, such as carbon monoxyde (CO), water (H_2O), methanol (CH_3OH), hydrogen cyanide (HCN), methyl cyanide (CH_3CN), formic acid (HCOOH), dimethyl ether (CH_3OCH_3), ethylmethylether($C_2H_5OCH_3$), and many others, including isotopologues, have been recorded with the Cologne THz spectrometer. Beside stable molecular species a large number of radicals and unstable molecules, produced in discharge cells, have been studied with the aid of BWO spectrometers such as light hydrides, SH, PH, NH, CH_2, chain molecules like C_3, HC_3, HC_3N and HC_5N, the sulfur containing species HSOH and HSSH, and molecular ions, for example, CO^+ and HCO^+. A list of recently investigated molecules at Cologne is given in [30]. Figure 4.7 shows as an example the ${}^rQ_4$ branch spectrum of HSSH at 1.258 THz.

4.2.4 Sub-Doppler Spectroscopy

At pressures low enough that collisional broadening of spectral lines is negligible molecular line shapes are Gaussian and the line width is determined by the molecular mass, the center frequency, and the temperature of the gas (see Eq. 4.1.1). The Gaussian profile results from an ensemble of molecules with

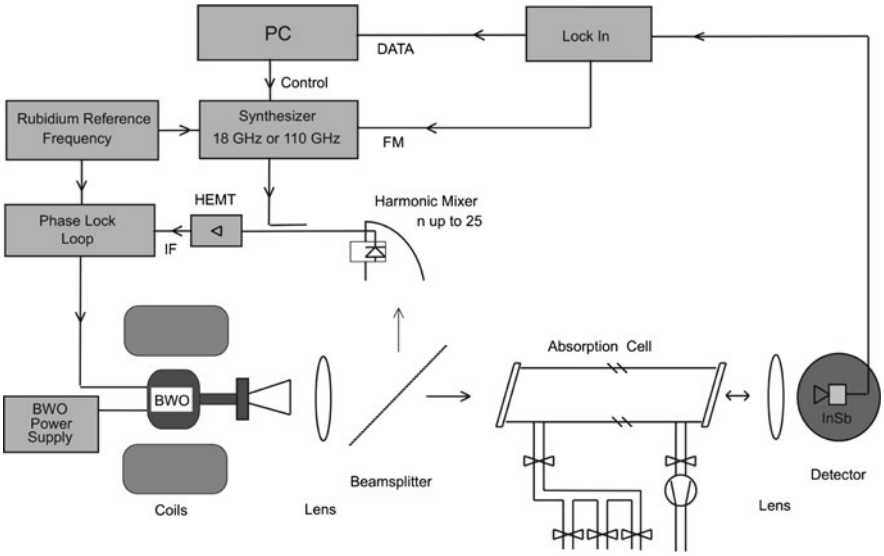

Fig. 4.6 Schematic diagram of the Cologne terahertz spectrometer. (Reproduction of Fig. 4.1 with permission from [28]. © 1998 American Institute of Physics)

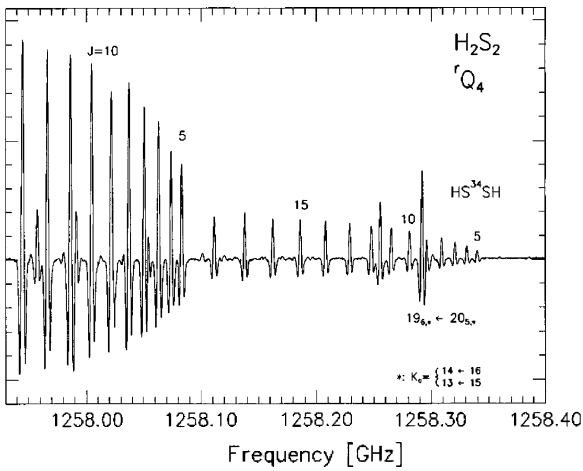

Fig. 4.7 Doppler limited spectrum of HSSH at 1.258 THz recorded in second derivative. In comparison to the main isotopomer, the bandhead of the ^{34}S isotopomer is displaced toward higher frequencies. (Reproduction of Fig. 4.4 of [85], © 1995 with permission from Elsevier)

Maxwell–Boltzmann velocity distribution which absorb electromagnetic radiation at Doppler shifted frequencies $\nu = \nu_0 + \Delta\nu_D$. Here $\Delta\nu_D = -\nu_z \cdot \nu_0/c$ denotes the frequency shift due to the Doppler effect for molecules with velocity ν_z propagating parallel to the incident beam. For $\nu_z > 0, \Delta\nu_D$ is negative and the absorption frequency ν is shifted to lower frequencies. ν_0 is the rest frequency at $\nu_z = 0$, and c is the speed of light.

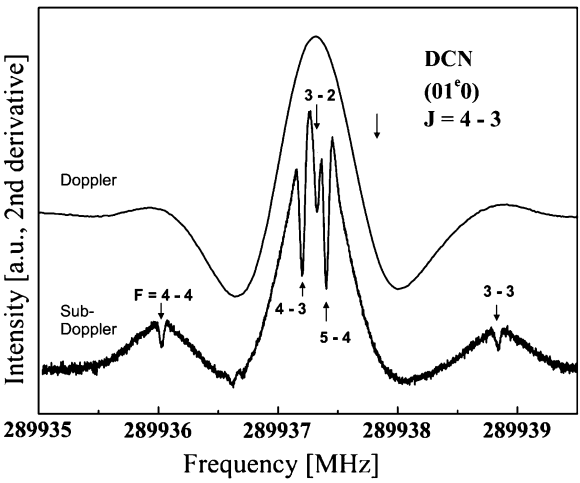

Fig. 4.8 Sub-Doppler spectrum of the $J = 4 \leftarrow 3$ transition of DCN in its first excited v_2 bending state at 290 GHz including hyperfine components (*lower trace*). For comparison the Doppler limited spectrum is shown in the *upper trace*. (Reproduced from [34], © 2004, with permission from Elsevier)

To record sub-Doppler line profiles part of the incident beam is reflected back by a mirror or at the detector surface and passes the gas cell a second time but in opposite direction, thereby depopulating the lower states of molecules with velocity component $-v_z$. When the spectrometer is tuned to the rest frequency $v = v_0$, radiation of both incident and back reflected beam is absorbed by the same group of molecules with velocity $v_z = 0$. Radiation of the back reflected beam now depopulates the lower state of molecules with $v_z = 0$ and thus less radiation of the incident beam gets absorbed. As a consequence a narrow dip at rest frequency v_0 occurs and in favorable cases underlying hyperfine structure transitions can be resolved. The high-resolution possibilities of BWO applications have been demonstrated by sub-Doppler spectra of $C^{17}O$ at 449 GHz [31], DCN up to 942 GHz [32], $H^{13}CN$ at 604 GHz and $D^{13}C^{15}N$ at 764 GHz [33, 34]. Figure 4.8 shows the sub-Doppler spectrum of the $J = 4 \leftarrow 3$ transition of DCN in its first excited v_2 bending state at 290 GHz. The line width of hyperfine components is 30 kHz with a corresponding accuracy of 1–5 kHz.

4.2.5 Multiplier-Spectrometer

Above 1 THz the output power of BWOs drops drastically. Electrical and mechanical constraints restrict the operational range of BWOs for spectroscopic applications to slightly above 1 THz. To reach frequencies above 1 THz multipliers are nowadays widely in use to generate higher harmonic output frequencies from low fundamental input frequencies. The development of multiplier configurations is subject of current research [10, 35–39]. Multiplier devices make use of the nonlinear current–voltage response of semiconductor materials to generate higher harmonic frequencies. Today multiplier devices and cascaded multiplier chains are

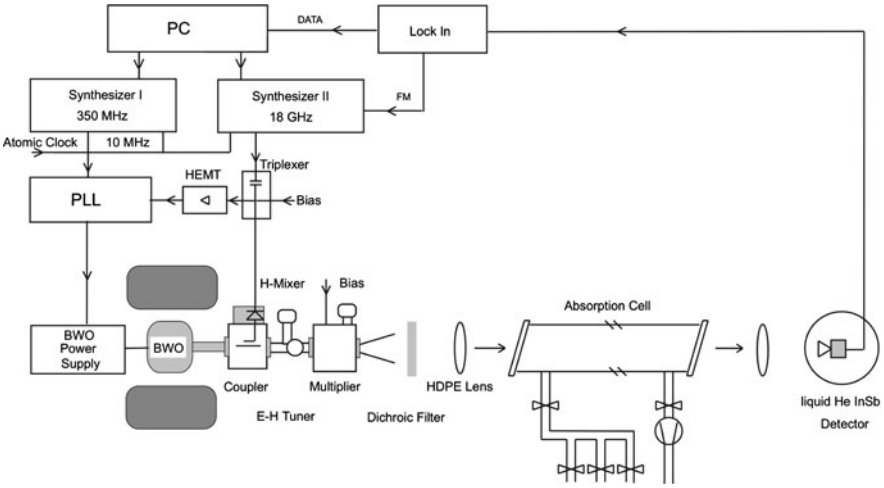

Fig. 4.9 Schematic drawing of a multiplier spectrometer. The setup uses a planar Schottky multiplier. (Reproduced from [44], © 2000, with permission from Elsevier)

commercially available for frequencies up to 2 THz with μW output power [40].[3] The use of multiplier chains up to frequencies above 2 THz in molecular spectroscopy has recently been described thoroughly by Drouin et al. [41].

Often planar Schottky diodes based on GaAs semiconductors are used for frequency multiplication. Semiconductor doping concentrations, break down voltage, heat conductivity, anode diameter size and the epitaxial layer thickness are parameters which need to be optimized to allow for high-conversion efficiencies. The diodes are placed in state-of-the art cross guide or inline waveguide blocks which are either mechanically milled or electro-formed. The mechanical and electrical design of the multiplier device is crucial to achieve broadband response, low standing wave ratios, and good idler matching within the operation band. For an extension to higher frequencies low series resistances, low parasitic capacities and high cut-off frequencies of the semiconductor material is prerequisite. For details on solid state multipliers see for example [40, 42]. As fundamental frequency sources for input of multiplier devices BWOs, Gunn diodes, and commercial synthesizers with sufficient output are used. Figure 4.9 shows the Cololgne spectrometer setup with a phase-locked BWO as radiation source and a planar Schottky multiplier device to produce 1.4 [43] and 1.6 THz [44] radiation. Different types of multipliers such as superlattice devices [45] and monolithic membrane diodes (MOMEDs) [39] have been developed and tested in recent years to generate frequencies up to 3 THz.

[3] Virginia Diodes, Inc., 979 Second Street SE, Suite 309, Charlottesville, VA 22902; Radiometer Physics GmbH, http://www.radiometer-physics.de/rpg/html/home.html

4.2.6 Planar Schottky Multipliers

Figure 4.10 shows a planar Schottky frequency multiplier designed for broad-band spectroscopy at 1.38 THz. The multiplier generates harmonics of a fundamental frequency of 110–240 GHz. A planar low-capacitance resistive mixer diode is adapted to broad-band impedance matching. The planar Schottky diode provides a junction capacitance of 3 fF, a series resistance of 11 Ω, an ideality factor of 1.3, a breakdown voltage of 8.4 V, and additionally a small parasitic capacitance (less than 1 fF). With these specifications the calculated cutoff frequency is 4 THz. The anode size of the diode is less than $2 \times 1\,\mu m^2$. The anode beam lead is made of gold and is about 300 µm in length. This offers a very low ohmic resistance at Terahertz frequencies and a mechanically flexible anode. To minimize the parasitic capacitance of the anode, an air bridge approx. 20 µm in length was etched below an Au-anode finger. To achieve a mechanically stable contact, the volume of the air bridge is filled with polyimide ($\epsilon_r = 2.7$) and a part of the finger structure is additionally fixed with a polyimide layer on the top. The GaAs chip is etched down to a size of $170 \times 100\,\mu m^2$. A GaAs-substrate (doping concentration, $n = 2 - 3 \times 10^{18}\,cm^{-3}$) with a 2 µm buffer layer ($n = 5 \times 10^{18}\,cm^{-3}$) and a 50 nm-thin epilayer ($n = 5 \times 10^{17}\,cm^{-3}$) was employed. The ohmic contact is made on the surface of the GaAs crystal and spaced 8 µm from the junction area, thus reducing effectively the ohmic resistance of the device. The diode definition and its fabrication were carried out in the Laboratory of Semiconductor Devices, State University of Nishnii Novgorod, Russia [42]. The polyimide reinforced film-diode is quite rugged and reliable, with enhanced power handling capability compared to whisker-contacted diodes. The input waveguide (WR 10) of the multiplier is linearly tapered from a full-size rectangular waveguide to a single-ridge waveguide, which forms a small gap of 300 µm.

Figure 4.11 shows the multiplier block with the planar Schottky diode incorporated. The planar diode is mounted across the gap, with the cathode connected to the planar filter structure. An $E - H$ tuner is mounted on the input waveguide

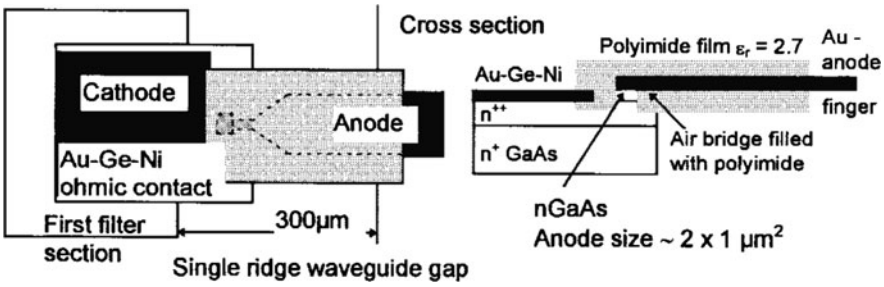

Fig. 4.10 Design of a GaAs Schottky planar film diode. The overall size of the diode is 500 µm × 150 µm; the anode size is less than 2 µm × 1 µm. (Reproduced with permission from [43], © 1999, IEEE)

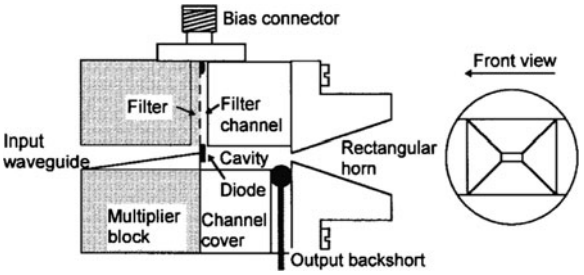

Fig. 4.11 Schematic diagram of the multiplier block, the channel cover, and the rectangular horn antenna. The drawing is not to scale. (Reproduced with permission from [43]. © 1999, IEEE)

flange of the multiplier to improve the input power matching. The planar filter and the channel cover forms a suspended substrate transmission line. The horn antenna is a scaled version of a standard-gain rectangular horn antenna and was milled in four single-plane triangular parts. For a particular backshort setting, a bandwidth of 1 GHz at the second harmonic is achieved. Sufficient power for molecular spectroscopy beyond 1 THz can be produced. Compared to whisker contacted devices planar diodes are easy to handle.

4.2.7 Monolithic Membrane Diodes

For frequencies above 50 GHz GaAs is the III–V semiconductor material of choice to fabricate solid state multipliers with response times of sub-picoseconds, corresponding to Terahertz frequencies. However, short response times require fabrication of rather thin semiconductor microstrip circuits, which are difficult to machine. An alternative option for low capacity devices is the production of MOMED, which are made of ultra thin layers. MOMEDs are used as mixers in various applications up to 2.5 THz. One such device fabricated at the JPL in Passadena has been used as frequency tripler with adjustable backshorts. The device has been tested with a high power (10 mW) BWO at 780 GHz as input radiation source to generate output frequencies of 2.3–2.7 THz. Figure 4.12 shows a D_2O transition at 2.33 THz recorded in Cologne.

4.2.8 COSSTA: Cologne Sideband Spectrometer for THz Applications

An alternative approach to generate Terahertz radiation is the FIR-laser sideband technique. Radiation from an optically pumped FIR gas laser is superimposed with radiation of a tunable monochromatic microwave source on a fast, non-linear mixing device to generate sidebands at the sum and difference frequencies of the two input frequencies. FIR gas lasers, when operated with different gain media, such as CH_3F, CH_3OH, and HCOOH have thousands of laser lines in the range of

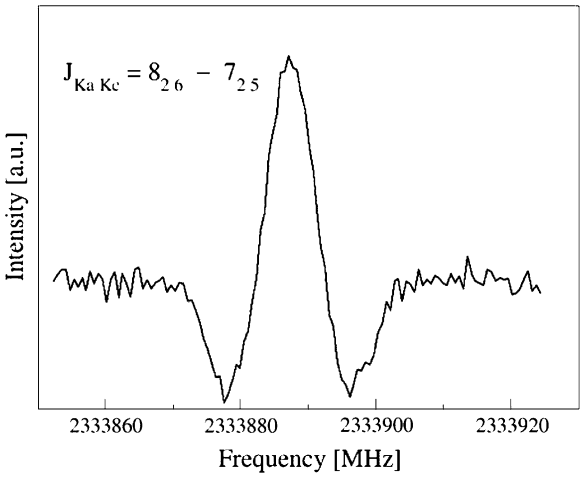

Fig. 4.12 A 2.3 THz spectrum of D_2O recorded with a MOMED multiplier spectrometer

0.2 to over 10 THz. Strong THz laser lines at a few tens mW mixed with microwave radiation from either a YIG oscillator (2–4 GHz) [46], a frequency multiplied synthesizer (up to 75 GHz) [47], or a klystron (22–114 GHz) [48] have been used to generate tunable laser sideband signals up to 3 THz on a GaAs-Schottky barrier diode. The microwave is either coupled to the mixer coaxially or via waveguides. The separation of sidebands from the fundamental laser radiation is achieved by a diplexer in combination with a Farbry–Perot interferometer or by a grating monochromator. Frequency tuning of the laser sidebands is achieved by tuning the frequency of the microwave radiation source.

In 1997 the Cologne group presented a FIR sideband laser system using a PLL locked BWO (280–380 GHz) as tunable microwave source [49]. The high frequency of the BWO leads to sidebands well separated from the carrier frequency which can easily be extracted by a grating monochromator. Both the optical coupling of BWO radiation onto the mixer as well as the clearly separated sidebands have substantially simplified the use of laser sideband techniques for Terahertz applications. A schematic overview of the layout of the Cologne sideband spectrometer for Terahertz applications (COSSTA) is presented in Fig. 4.13.

Aside from the traditional absorption cell and the hot carrier liquid-He-cooled magnetically tuned InSb detector COSSTA consists of three essential units: (a) the frequency-stabilized FIR laser system, (b) the evacuated optics and mixer arrangement, which serves to superimpose the BWO and FIR beams, and (c) the BWO phase-lock assembly. The radiation of a frequency-stabilized FIR ring-laser system is mixed on an open-structure Schottky barrier diode pumped with phase-stabilized power output from a BWO for generating the sidebands. The tunability of the system is basically determined by the frequency coverage of the BWOs, which is about 100 GHz at 330 GHz center frequency. An example of the wide tuning range and the high frequencies accessible with COSSTA is shown in Fig. 4.14. The $J = 16 \leftarrow 15$ rotational transitions of CO in different excited vibrational states

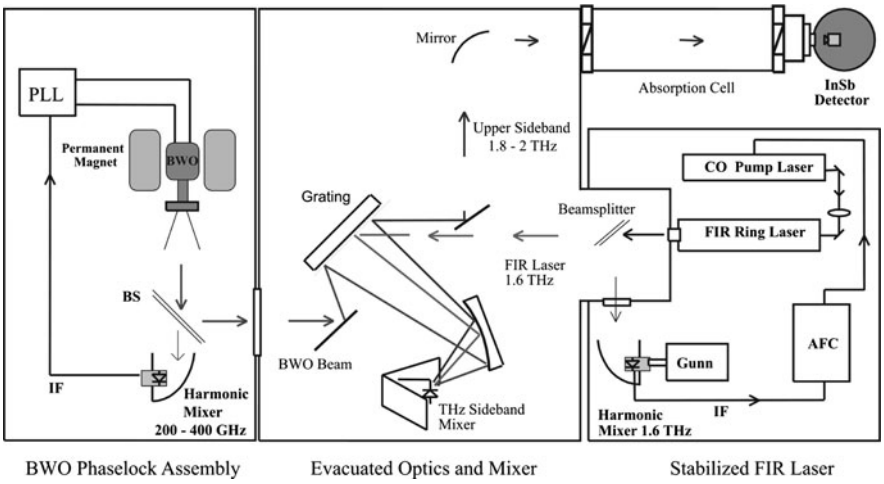

Fig. 4.13 Cologne sideband spectrometer for Terahertz applications—COSSTA. (Reproduction of Fig. 4.1 of [51], © 2000, with permission from Elsevier)

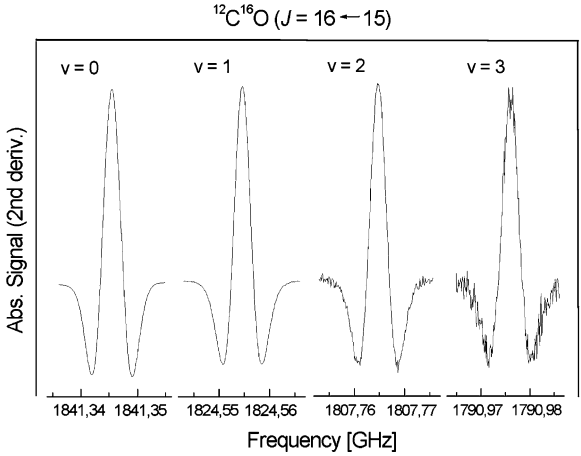

Fig. 4.14 The $J = 16 \leftarrow 15$ transitions are shown for $v = 0$–3. The lines appear as second derivatives of a Gaussian line-shape because of the 2*f*-modulation. Reproduced from Fig. 4.2 of [86] with permission © 2009, ESO

of quantum numbers $v = 0$, 1, 2, and 3 in the range from 1791 to 1841 GHz is depicted.

The frequency stability of this sideband spectrometer is limited solely by the instability of the FIR laser frequency, which is typically in the range of 15 MHz. To overcome this limitation, an analog automatic frequency control (AFC) loop was developed to synchronize the FIR laser frequency of 1.626 THz with the 15th harmonic of a Gunn oscillator (InP Gunn, 108 GHz), which is phase-locked to a stable reference frequency [50]. The IF of the harmonic mixer is amplified by an ultralow noise HEMT operating at 350 MHz. The frequency error signal drives a

piezo actuator to move the grating of the CO_2 pump laser whose frequency is corrected within the gain profile of a CO_2 laser line. By this manner long term frequency stability (AFC loop error) of 2 kHz and absolute frequency calibration of the FIR laser was achieved. The BWO submillimeter and FIR laser radiation are coupled quasi-optically onto a whisker-contacted Schottky diode for generating laser sidebands. Separation of laser frequency and tunable sidebands are achieved with a low-loss blazed grating (see Fig. 4.13). Finally the tunable sideband beam passes the absorption cell and is focused onto a liquid-helium-cooled InSb bolometer. With a 1T6 Schottky diode (University of Virginia), sideband power levels of 1.6 μW were reached. To avoid power losses introduced by water vapor absorption, a vacuum box for the optical system is used to cover the entire sideband beam and the main part of the laser beam. Various applications of COSSTA to molecular spectroscopy have been published (see, e.g., [32, 51–55].

4.3 Spectroscopy in Supersonic Jets

4.3.1 General Remarks

Supersonic jets are nowadays widely used for spectroscopic investigations of reactive, short-lived molecules such as molecular radicals and ions [56], weakly bound van der Waals complexes [57], and large bio-molecules [58]. In the adiabatic expansion of a buffer gas the rotational temperature of seeded molecules drops to a few K and the molecular partition function is strongly reduced compared to standard gas cell experiments at room temperature. Adiabatically cooled molecules have significantly simplified rotational spectra with strongly enhanced line intensities which compensate for the usually short path lengths of the probing beam through a jet.

4.3.2 SuJeSTA

A Supersonic Jet Spectrometer for Terahertz Applications (SuJeSTA) has been developed at the Cologne laboratories to study reactive molecules by means of high resolution mm- and submm-wavelength spectroscopy at lowest temperatures (see Fig. 4.15). For this purpose a supersonic jet apparatus has been combined with a phase stabilized sub-millimetre-wave spectrometer. Highly reactive molecules are produced either in an electrical discharge, which is placed in the throat of the nozzle, or by laser ablation of solid targets such as graphite and silicon. Both techniques are well established and have been described in the literature (see, e.g., [59, 60]).

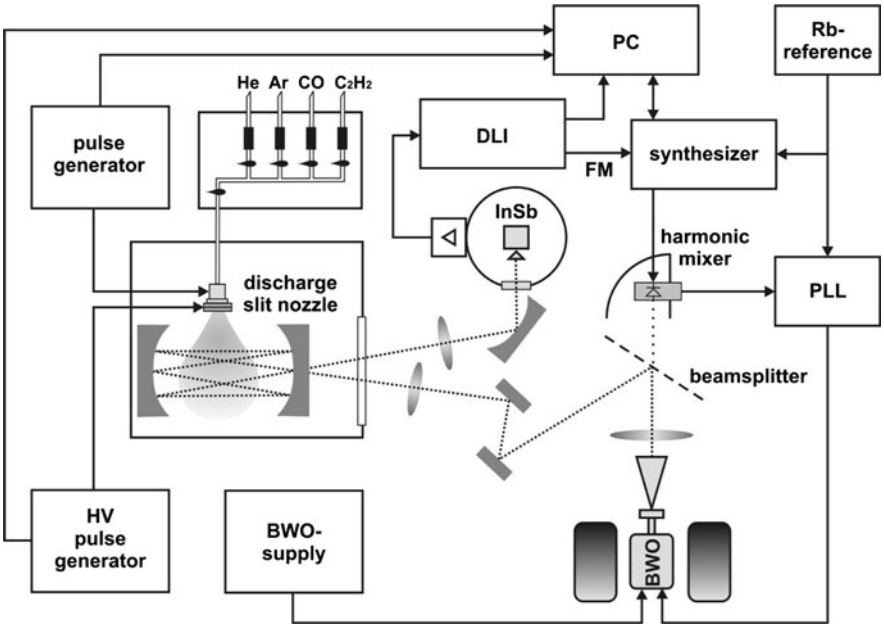

Fig. 4.15 SuJeSTA Spectrometer is presented as a block diagram. (Reproduction of Fig. 4.1 of [87], © 2009, with permission from Elsevier)

4.3.2.1 Electrical Discharge Sources

A pulsed jet discharge source at typically 20–50 Hz repetition rate and pulse duration times of a few hundreds of μs is used to produce reactive molecules from a mixture of precursor gases (see Fig. 4.15). Flow controller units allow for stable and reproducible gas flow conditions and constant mixing ratios during the measurements. Fast background subtraction during the off-times of the jet leads to a substantial reduction of the noise level and allows for corrections of baseline instabilities due to etalon effects. The amount of radicals and ions strongly depends on the source conditions such as the length of the discharge pulse compared to the length of the precursor gas pulse and the time delay between them. A pumping unit with a two stage roots blower keeps the pressure in the chamber at about 5×10^{-2} mbar.

The jet is probed by radiation of tunable BWOs operating between 300 and 1200 GHz. The BWO spectrometer can be used in two different modes, a phase stabilized mode for highly precise measurements over a small range of about 500 MHz, and in a free running fast scanning mode, which covers a large frequency range of several GHz but with less accuracy. The fast scanning mode is used for searching absorption lines of little or even completely unknown species, whereas the phase stabilized mode is used for highly precise measurements (10 kHz accuracy) on selected, identified lines and for long integration times to

record spectra of weak lines. Instead of BWOs, a synthesizer combined with frequency multiplier chains can be used to cover most of the frequency range from 100 to 2000 GHz.

The probing THz beam (see Fig. 4.15) is oriented perpendicular to the jet. Multipass optics increase the path length through the jet by an order of magnitude. Alternatively, the radiation can be oriented in line with the supersonic jet propagating in a double pass configuration. Figure 4.16 shows the $^{13}C^{16}O J = 4 \leftarrow 3$ transition at 440.8 GHz recorded with a probing beam parallel to the propagation of the jet. Two Doppler shifted components appear at ± 1.25 MHz off the center frequency. From these data the CO velocity has been calculated to be 850 m/s. The line width of the CO transition is reduced by a factor of 3 compared to CO measured in a stagnation cell at 300 K. For phase sensitive detection the BWO output frequency was modulated with 57 kHz and demodulated by a lock-In amplifier to record absorption spectra in second derivative.

4.3.2.2 Laser Ablation Sources

An alternative way of producing short-lived molecules in supersonic jets is the ablation of solid targets by pulsed lasers. A schematic drawing of a laser ablation source is shown in Fig. 4.17. In our setup light of a *Q*-switched Nd:YAG laser operating at either the fundamental mode (1064 nm) or at the 2nd, 3rd, or 4th harmonic, is focused by a 30-cm focal length CaF_2 lens onto the surface of a solid rod of graphite, silicon, or other target materials. The vaporized products are diluted in a pulse of helium and collisionally cooled in a supersonic expansion. Highest yields and stable conditions are usually achieved at Nd:YAG laser power of 10–40 mJ per pulse at 10 ns pulse duration. Molecules are preferably formed in the

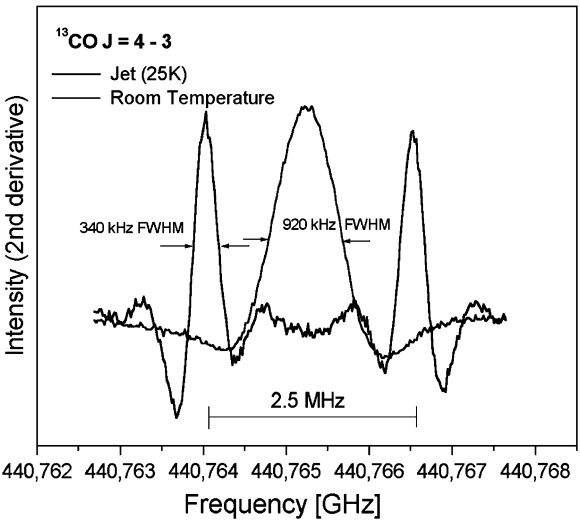

Fig. 4.16 ^{13}CO in a supersonic jet expansion. The two 340 kHz wide Doppler components are shifted by ± 1.25 MHz. For comparison a three times broader line at the center has been measured in a cell at room temperature

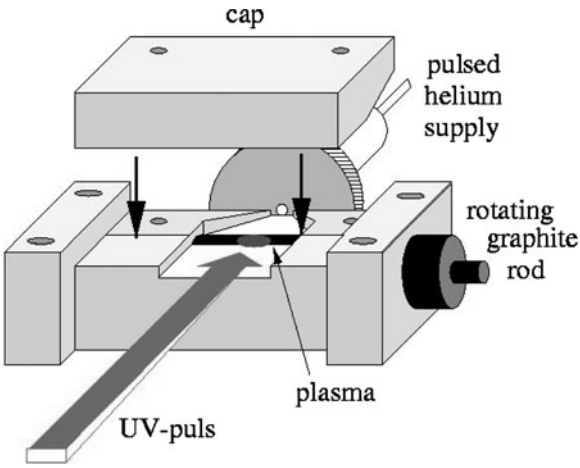

Fig. 4.17 The laser ablation source used for producing C_3, TiO, TiO_2, and AlO in Cologne

high pressure regime of a 6 mm-long reaction channel before adiabatically expanding in supersonic jet propagation into the vacuum chamber. Largest yields are usually obtained for helium backing pressures of 2 bar at a background pressure of 50 μbar in the vacuum chamber. Operation of the pulsed gas valve, timing of the ablation laser, and signal recording is controlled and synchronized by a TTL timer unit at 30 Hz repetition rate. Laser ablation sources have been successfully used in our laboratory to study gas phase spectra of C_3, TiO, TiO_2, and AlO.

4.3.3 OROTRON

The absorption of electromagnetic radiation in a gas probe is significantly enhanced when resonant cavities are used instead of single pass absorption cells. The gain in effective optical path length is of the order $Q \cdot \lambda/2\pi$, where Q is the cavity quality factor and λ is the free-space wavelength. Since Q can be quite large, cavity spectrometers are very sensitive, which is advantageous for measurements in molecular jets or beams where absorption lengths are rather short. The major constraints in the application of an *external* resonant cavity absorption cell is that the long effective path length occurs only when the microwave source frequency and the cavity resonant frequency are exactly synchronized. Furthermore, application of source frequency modulation, normally used to increase the sensitivity, gives rise to baseline fluctuations, which are substantially stronger compared to those of a simple spectrometer operated with a free space absorption cell. These technical problems are principally avoided in an *intracavity* resonator with a tunable coherent source incorporated [61, 62].

A sensitive intracavity spectrometer was developed for investigation of generally very weak absorption lines in the millimeter-wavelength region. Key element

of the spectrometer is a tunable oscillator, called OROTRON, which generates millimeter-wave radiation through the interaction of an electron beam with the electromagnetic field of a high quality ($Q \approx 10^4$) Fabry–Pérot resonator cavity. The cavity consists of a movable spherical mirror and a fixed planar mirror with a periodic structure imprinted on its surface. Focused by the field of strong permanent magnets the electron beam travels along the periodic structure of the plane mirror, thus stimulating cavity modes to oscillate. A typical value for the anode voltage is in the range of 500–1200 V with current of the electron beam of 15–40 mA. A thin mica foil separates this ultra high vacuum region of the OROTRON from the probing region. A molecular jet is injected by a pulsed valve into the probing region perpendicular to the resonator axis. Absorption in the jet attenuates the electromagnetic field of the resonator which is sensitively detected by measuring the electric current of the electron beam. The movable spherical mirror is furnished with mechanical screws for adjustment of the cavity length and with piezoceramic transducer units for fine tuning of the resonator in the process of line search and recording. A small portion of the resonator radiation leaks out through an orifice in the center of the spherical mirror and is used to determine the resonance frequency during the measurements. Figure 4.18 shows the setup of the OROTRON.

The OROTRON is a very stable intracavity radiation source which is tunable in a wide spectral range. The frequency stability $\delta\nu/\nu$ is proportional to the voltage

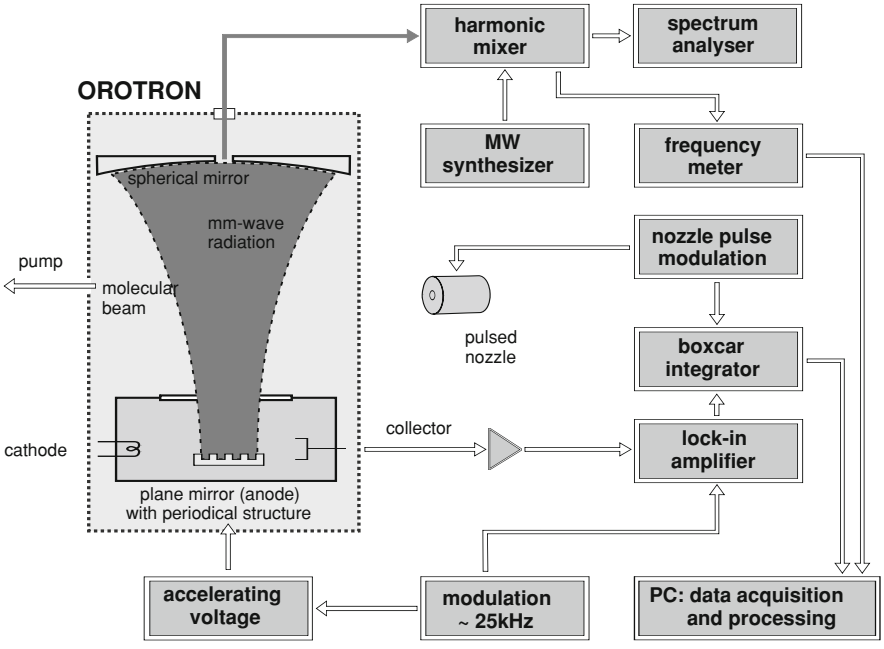

Fig. 4.18 Block diagram of an OROTRON spectrometer: a highly sensitive intracavity spectrometer. (Reproduced from [69], © 2003, with permission from Elsevier)

stability $\delta U/U$ applied to the periodic structure (anode) and scales with the inverse of the cavity quality factor Q:

$$\frac{\delta v}{v} \approx 2 \cdot \frac{\delta U}{U} \cdot \frac{k}{Q}, \tag{4.3.1}$$

where $k \simeq 100$ is the number of ridges in the periodic structure. The high quality of the Fabry–Pérot resonant cavity (typically about 10^4) leads to high frequency stability.

At a reasonable voltage stability of 10^{-5} the frequency stability is $\delta v / v \approx 10^{-7}$ which corresponds to a radiation line width of 10–15 kHz at 100–150 GHz. Thanks to high Q values the stability of the frequency is not seriously affected by the instability of the voltage U and therefore active frequency stabilization is not necessary. In addition simple tunability of the OROTRON spectrometer makes it a very efficient tool to search for weak transitions of molecules or for highly diluted trace gases. Initially designed for studies of weakly absorbing stable molecules [63] and trace gases at concentrations of 0.01–1 ppm in air and water vapor [64], a most promising new application of the OROTRON is the application to molecular jet spectroscopy [65]. The potential of the new technique for observation of very weakly bound van-der-Waals complexes of type R–CO, with R = Ar, Ne, He, H_2, D_2, N_2, and CO have been investigated by Surin and co-workers (see [66] and references therein). As an example, which demonstrates the sensitivity of the OROTRON spectrometer, the 107 GHz $J = 1 \leftarrow 0$ transition of $^{13}C^{17}O$ in natural abundance (4×10^{-6}) is shown in Fig. 4.19a. The observed linewidth of the hyperfine structure components of 300–400 kHz is caused by Doppler broadening in a free expanding supersonic jet. The effect of Doppler broadening can partly be reduced in cases of power saturation. Figure 4.19b shows three saturation dips of

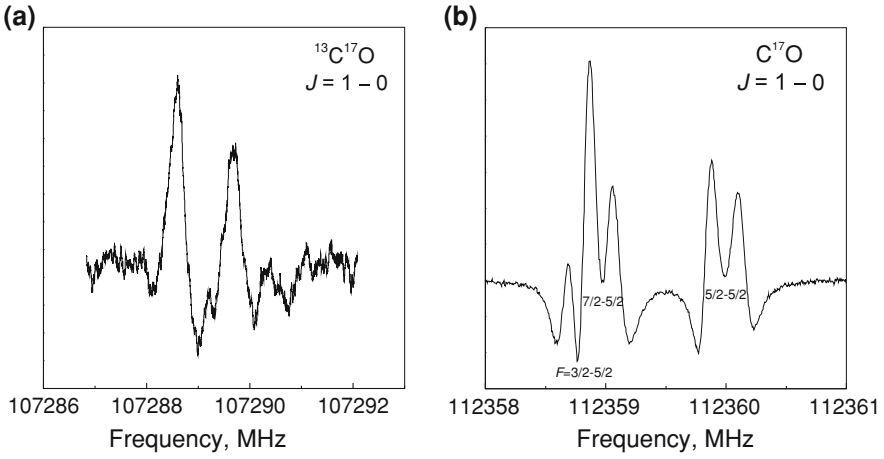

Fig. 4.19 Spectra of $^{13}C^{17}O$ and sub-Doppler spectra of $^{12}C^{17}O$. (Reproduction with permission from [65], © 2001, American Institute of Physics)

the $J = 1 \leftarrow 0$ transition of $^{12}C^{17}O$. The hyperfine structure is caused by the ^{17}O nuclear quadrupole moment [31, 65]. The dips exhibit line-widths of about 100 kHz.

At present three OROTRON tubes operating at 90–130, 110–160, and 130–180 GHz at anode voltages of 350–700, 550–1100, and 700–1300 V, respectively, are available at Cologne, which have been designed and constructed in Russia. OROTRONs with higher anode voltages and higher output frequencies are feasible but the increase of dissipative heat in the periodic structure is a major concern. The heat load can be reduced when operating the OROTRON in a pulsed current mode. As a first approach to sub-millimeter wavelengths a pulsed OROTRON with current of 50–100 mA for frequencies up to 380 GHz was developed in Russia in close collaboration with the Institute of Spectroscopy (Troitsk, Moscow region) and the Institute for Metrology and Space (Mendeleevo, Moscow region). Switching the power on and off was accomplished by tuning the low potential on a grid placed between emitting cathode and periodical structure and the output pulse power was found to be 20–40 mW [67, 68].

4.3.3.1 Two-Photon-Pump-Probe Experiments

To extend the accessible frequency range of OROTRON jet spectrometers beyond the millimeter wavelength region and into the microwave range a new double resonance technique has been developed and successfully applied. The setup utilizes the 90–160 GHz OROTRON as probe beam for signal detection, and an amplified 18–43 GHz beam of a microwave synthesizer (HP 86350) as pump beam. The pump beam radiation is emitted from a broadband horn-antenna and focused by two lenses into the sample region inside the OROTRON cavity. The molecular jet is oriented perpendicular to both pump beam and probe beam which intersects the radiation in the middle of the OROTRON cavity. In a first application this technique has been used to measure new transitions of the CO dimer in the microwave frequency range at 18–43 GHz [69]. As an example Fig. 4.20 shows the $P(5)$ transition of the $f \leftarrow d$ subband of the CO-dimer at 38.275 GHz which is indicated as heavy single ended arrow in the inlet. To detect this new transition the OROTRON probe beam is set to the previously known $Q(4)$ transition of the $f \leftarrow a$ subband at 153890.572 MHz (double ended arrow). The microwave pump radiation is slowly scanned while the OROTRON frequency is fixed to the $Q(4)$ center frequency. For phase sensitive detection the microwave output power is amplitude modulated at 50 kHz (square-wave modulation) and the double resonance signal was recorded in the OROTRON collector circuit by a lock-in amplifier at 50 kHz reference frequency. Because the jet is pulsed the output signal of the lock-in has to be recorded with a boxcar integrator synchronized to the pulse of the jet.

From these experiments it becomes evident that this OROTRON-detected double resonance technique can be extended to higher frequencies provided high

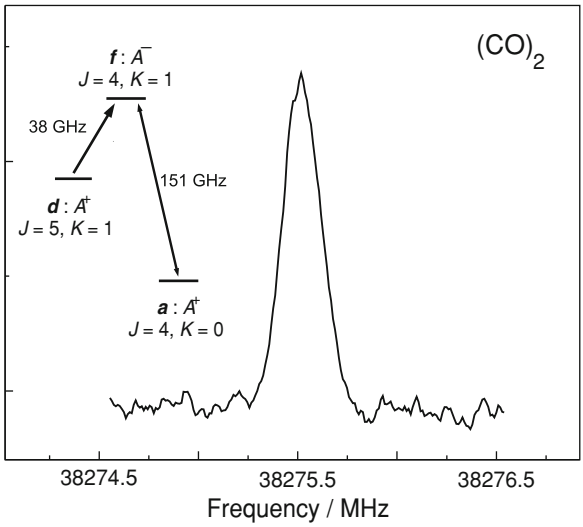

Fig. 4.20 ^{12}CO double resonance experiment. (Reproduction from [69], © 2004, with permission from Elsevier)

power radiation sources as pumps in the submillimeter wave region (200–1000 GHz) are available. In case of weak output powers of the pump, multipass optics or cavity arrangements can be introduced to ensure more effective coupling to the molecular sample.

4.3.3.2 Two-Photon Absorption Spectroscopy

The possibility of using two-photon absorption in a standing electromagnetic wave by molecular or atomic gases for removing Doppler broadening of the absorption lines was first discussed by Vasilenko et al. [70]. The idea of the method is that, for a particular velocity group of the absorbing particles in a gas, the first order Doppler shift has an opposite sign for two counterpropagating electromagnetic waves. Therefore, if one quantum of radiation is absorbed from each of the two counter-propagating waves, the resulting frequency of the two-photon transition does not depend on the velocity of the particle; i.e., the Doppler effect will not influence the absorption linewidth. This effect has been used for Doppler-free laser spectroscopy in the infrared or optical regions, involving electronic or vibrational transitions of atoms or molecules (see, for example [71]). Observations of Doppler-free two-photon absorption lines in the microwave or millimeter wave regions on pure rotational molecular transitions became possible using highly sensitive intracavity OROTRON spectrometer. As an example two-photon absorption on rotational transitions of OCS molecules was measured [72]. A recording of the $J = 12 \leftarrow 10$ transition is shown in Fig. 4.21. The width FWHM of the central peak is about 40 kHz, 7–8 times smaller than the normal Doppler width of a single-photon absorption line. The center frequencies of the recorded transitions coincide within

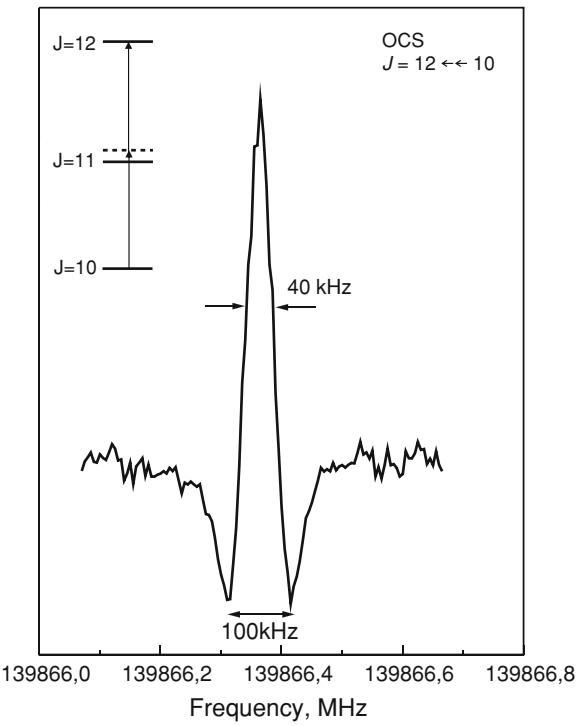

Fig. 4.21 OCS two photon transition with sub-Doppler line width. (Reproduced with permission from [72], © 2001 by the American Physical Society)

the estimated uncertainty to the values obtained in the previous Lamb dip and molecular beam studies.

4.4 Heterodyne Mixers for High Resolution Spectroscopy of Interstellar Molecules

4.4.1 Heterodyne Detection

To measure doppler shifts and line profiles of interstellar molecular lines, sometimes resolutions as high as 10^6 are needed. Whereas moderate resolution spectroscopy can use direct detectors behind grating- or Fabry–Pérot spectrometers, instruments with resolutions of 10^3 or higher typically use the heterodyne principle. Heterodyne receivers take the RF signal at v_{RF} picked up by an antenna and combine it with a, usually much stronger, sinusoidal "local oscillator" signal at v_{LO}. In a nonlinear device known as mixer, the two frequencies are multiplied, resulting in, among others, the difference frequency $v_{IF} = v_{sig} - v_{LO}$ which is called the intermediate frequency or IF. The IF frequency is an exact replica of the RF frequency. Because $v_{IF} \ll v_{RF}$, it is easy to achieve high frequency resolution

at the IF with multichannel spectrum analyzers such as a filter bank, an acousto-optical spectrometer or a digital Fast Fourier Transform spectrometer.

The frequency- and phase conservation of the heterodyne principle also allows aperture synthesis interferometry, where the IF output of several receivers can be cross-correlated, thus allowing a much higher spatial resolution than would be achievable with a single dish telescope. This is exploited, e.g., in the Atacama Large Millimeter Array (ALMA).

At frequencies up to the 100 GHz range, it is possible to use a low noise amplifier behind the antenna, so that simple nonlinear mixing elements such as semiconductor Schottky diodes can be used. Their rather large noise and low conversion efficiency thus does not determine the input noise performance of the system.

However, at frequencies in the mm-wave band up to the FIR, low noise amplifiers are nonexistent. The mixing element is the first element in the signal chain, so that its noise performance and conversion efficiency determine the system performance. The extreme sensitivity requirements of radio astronomy can only be achieved using superconducting devices as mixers. Superconductor–Isolator–Superconductor (SIS) tunnel junctions for frequencies in the mm-bands up to about 1.5 THz and superconducting Hot Electron Bolometer mixers are the workhorses of astronomical receiver systems today. With their outstanding sensitivities they are the building blocks of cornerstone instruments for submm/THz spectroscopy such as the HIFI on the Herschel Space Observatory, the ALMA or the Stratospheric Observatory for the Far-Infrared (SOFIA).

After an early phase using Schottky diode mixer receivers at the KOSMA Gornergrat observatory in the mm-wavelength bands, KOSMA has started to develop and fabricate superconducting mixers in the late 1980s and has used them subsequently in all receivers operated in the observatory, including a 490/880 GHz dual color multi-pixel receiver, now in operation at the NANTEN2 observatory (Atacama).Building on this expertise, we were selected to contribute one of the mixer channels for HIFI on the Herschel Space Observatory. We also developed SIS and Hot-Electron Bolometer (HEB) mixers for several other projects, such as AST/RO at South Pole Station, the GREAT instrument for SOFIA, the SMA interferometer, the Stratospheric Terahertz Observatory and atmospheric physics projects.

A good overview over the field of superconducting detectors can also be found in [73].

4.4.2 SIS Mixers

4.4.2.1 Physical Principles and Frequency Limits

The characteristic energy scale of (low-temperature) superconductivity is in the few meV range, corresponding to frequencies in the submillimeter-wave or

Terahertz range (at 1 THz, $h\nu = 4$ meV). It can therefore be expected that superconductors can be used for detection of photons in this energy range. Superconductor–Insulator–Superconductor mixers use the sharp current nonlinearity of quasiparticle excitations (approximately equivalent to normal conduction electrons) tunneling across an insulating barrier between the two superconductors (Fig. 4.22).

Biasing one side of the tunnel junction to the "gap voltage" $2\Delta/e$ results in a current flow across the barrier. Due to the singularity in the density of states at the energy gap of the superconductor, the nonlinearity is almost as sharp as a switch, which would be the ideal frequency mixer. Under irradiation with photons, quasiparticles can gain enough energy to enable tunneling even at bias voltages below the gap voltage. This process is called photon assisted tunneling and leads to the characteristic "photon steps" in the DC *I*/*V* curve. Figure 4.23 shows a typical example of the irradiated or "pumped" DC-*I*/*V* curve of an SIS tunnel junction mixer at 630 GHz together with the IF output power response to hot (296 K) and cold (77 K) blackbody radiation.

The fact that photon quanta become visible in a simple DC tunneling *I*/*V* is a remarkable feature. Mixers showing this behaviour, i.e., where $h\nu/e$ is larger than the voltage scale of their DC nonlinearity, are called quantum mixers. As it turns out, such a mixer can reach the quantum limit of heterodyne detection sensitivity given by the Heisenberg uncertainty relation between amplitude and phase.

An additional advantage of SIS mixers is their rather low local oscillator power requirement. This is especially true for the submillimeter/Terahertz range where local oscillator power is very scarce. The required LO power can be roughly estimated by $P_{LO} = (h\nu/e)^2/R_N$, with R_N as the normal resistance of the tunnel junction at bias voltages beyond the gap. With R_N of 10–50 Ω, typical LO powers are in the few hundred nanowatt range. Note that the required power scales with ν^2. The gap energy 2Δ, which is the binding energy of the Cooper pairs, is about

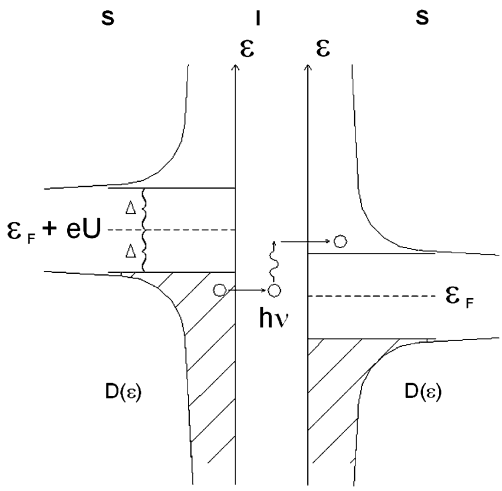

Fig. 4.22 "Semiconductor" model of the density of states in SIS

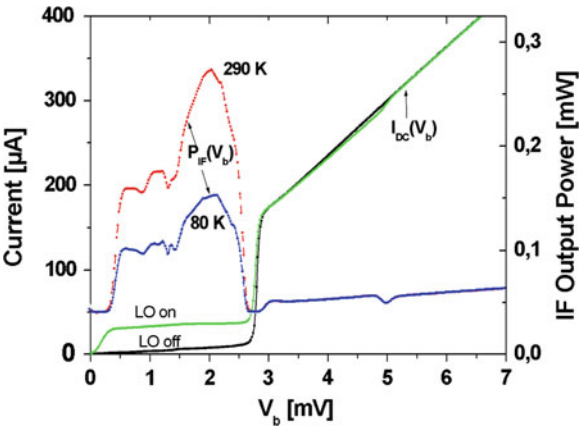

Fig. 4.23 SIS junction under photon irradiation and mixer output power

2.8 meV for Niobium, a standard superconductor for SIS mixers, corresponding to a "gap frequency" of $2\Delta/h = 700$ GHz. A fundamental frequency limit for the tunneling process, and therefore for frequency mixing with SIS elements, occurs at frequencies above twice the gap frequency at $4\Delta/h$, 1400 GHz for Niobium. At this frequency, the photon energy is high enough to produce equal tunneling currents in both directions of the barrier for all DC bias voltages, effectively canceling each other. It turns out in practice that above 1200 GHz the DC-bias range for mixer operation is getting too small for practical mixers. This frequency limit can only be surpassed with tunnel junctions made of superconductors other than Niobium with higher energy gaps, corresponding to higher critical temperatures.

The intrinsic mixing properties of an SIS mixer are described by the Quantum Theory of Mixing introduced by John Tucker in 1979 [74, 75]. This theory in its three-frequency approximation turns out to be a very powerful instrument for the practical design of SIS mixers because it only needs the DC I/V characteristic and the embedding impedance of the junction at the signal-, local oscillator- and IF to completely predict its RF properties. All higher harmonics can usually be safely ignored due to the high shunting capacitance of the junction. The theory takes the non-classical response of the tunnel currents to external fields into account, predicting the mixer gain and input noise. The non-classical effects include negative differential resistance with non-classical mixer gain >1 and the possibility of zero added mixer noise, thus achieving quantum limited heterodyne detection with a minimum noise temperature of the order of $h\nu/k$, corresponding to 4.8 K/100 GHz. The theory does not address any effects from the tunneling of the Cooper pairs (Josephson effects), effectively expecting their complete suppression by an external magnetic field.

As will be shown below, practical SIS mixers have to use high-Q integrated RF transmission line matching circuits to exploit their full sensitivity. Up to frequencies close to the gap frequency, the same superconductors as for the tunnel junctions can be used as lossless conductors for these transmission lines.

Above, the photon energy is high enough to destroy the superconductivity, giving rise to large losses in the now normal-conducting lines. The loss in the junction electrodes themselves can become important if the junction area cannot be assumed to be small against the wavelength in the junction so that the junction itself is a lossy transmission line. These phenomena lead to the fact that Niobium-based SIS mixers have a strong decrease in sensitivity above about 750 GHz and other materials have to be used for the circuits above this frequency.

4.4.3 SIS Mixer Device Design and Fabrication

4.4.3.1 SIS Tunnel Junctions

After the first experience with Pb–Oxide–Pb (lead) based SIS junctions (a spin-off of the IBM superconducting computer project) in the early 1980s [76], Nb junctions were developed to solve the problems of the mechanically and chemically unstable lead junctions. The initially achieved tunnel characteristics however were disappointingly rounded and leaky due to the unfavorable characteristics of Niobium oxide as the insulating barrier. The discovery of Gurvitch et al. [77] that a very thin layer of aluminum perfectly wets the Niobium surface and can serve as an artificial tunneling barrier after oxidation was a breakthrough and resulted in nearly ideal Nb–Al–Al_2O_3–Nb–SIS junctions with extremely low leakage currents and high current densities. Figure 4.24 shows a cross section of a typical SIS tunnel junction.

High quality Nb thin film layers are fabricated by sputtering from a high purity target. The background pressure must be in the low 10^{-8} mbar range to avoid the incorporation of oxygen which reduces the critical temperature. This dictates the need for a load-locked vacuum system. Care has also to be taken that the Nb surface has to cool down before sputtering the thin barrier aluminum layer to avoid diffusion into the grain boundaries of the Nb film. Thermal oxidation produces a tunnel barrier of Al_2O_3. The thickness and therefore the tunnel current density is approximately proportional to the product of oxygen pressure and exposure time. After blanket-depositing the tunnel layers onto the substrate, the (sub)-micron sized tunnel junctions are defined by either photolithography or direct electron beam writing, followed by an anisotropic Reactive Ion Etching process using reactive gases such as SF_6 in a plasma discharge. Silicon monoxide or silicon

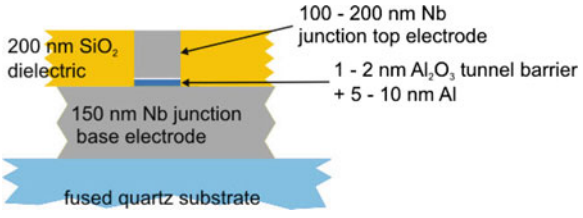

Fig. 4.24 Cross section of an SIS tunnel junction

dioxide layers are evaporated or sputtered to insulate the top wiring layer connecting the tunnel junctions to the circuit. The insulation layer also serves as the dielectric layer for integrated RF circuits described below.

4.4.3.2 RF Properties of SIS Junctions

To exploit the quantum limited sensitivity of the tunnel junctions, they have to be very effectively coupled to the radiation of the telescope. As the typical tunnel junction size is $\approx$1 μm, which is much smaller than the wavelength being received, an antenna is needed. One approach is the conversion of the free space wave from, e.g., a telescope to a guided wave using a horn connected to a single-mode waveguide. A probe then couples the waveguide mode into a thin-film transmission line on the detector substrate. At sub-millimeter wavelengths, the challenge is that the device substrate has to be ultra-thin, and only a few groups have the technology available. The second widely used approach is to integrate the detector into a planar antenna on the same chip and use a dielectric lens to focus the radiation onto the antenna. The advantage is that the device substrate can now be thick, but the coupling to a Gaussian beam is limited in efficiency, whereas corrugated horns can reach 98%.

A major complication to the impedance match of an SIS tunnel junction to either the waveguide probe or the planar antenna impedance is their large intrinsic capacitance due to the very thin barrier acting as a dielectric between the two superconductors. Typical values for Nb-based junctions are 80–90 fF/μm^2, effectively shorting out the tunnel resistance even for micron-sized junctions. The capacitance has to be compensated at the operating frequency by an external circuit. This limits the intrinsic RF bandwidth of the detector to about $B = 2/\omega R_N C_J$, with R_N the tunnel junction normal resistance, ω the operating angular frequency, and C_J the junction capacitance. Note that the $R_N C$ product is independent of junction size but is inverse proportional to the current density of the junction, i.e., for large bandwidths one needs high current density devices. As R_N is approximately the RF impedance of the nonlinear junction characteristic, the requirement to have R_N in a range of 10–50 Ω for easy matching to waveguides or other transmission lines leads to junction sizes of microns or submicrons. The present state of the art allows producing junctions of 0.6 μm^2 to 0.25 μm^2 with current densities up to 15 kA/cm^2 with Aluminum Oxide as the barrier. At 1 THz, this translates into a fractional bandwidth of 25% with R_N = 20–60 Ω. Higher current densities can be achieved with Aluminum Nitride (AlN) barriers.

4.4.3.3 Integrated Matching Circuits

Early experiments with SIS mixers used waveguide circuits with tunable backshorts to compensate the capacitance. This approach leads to low coupling efficiencies at

submm wavelengths due to the waveguide and backshort losses, which are severe due to the high-Q of the circuit. The breakthrough for SIS junctions at submm wavelengths came with the integration of superconducting transmission lines, mostly as microstrip lines, as resonant and/or impedance-transforming elements together with the tunnel junctions. To meet the desired impedance match conditions between junction and waveguide of course requires detailed knowledge about the superconducting transmission lines [78]. The determining parameter is the complex surface impedance of the superconductor, which can be calculated with the Mattis–Bardeen theory [79, 80]. The imaginary part of the surface impedance contains a "kinetic" inductance part (caused by the pair current component), the real part corresponds to power loss. Below the gap frequency of the superconductor, the losses are extremely small, allowing to design the necessary high-Q circuits with negligible loss. This is the main reason for the very low noise performance of SIS receivers up to about 700 GHz. Figure 4.25 shows a microscope photograph of a typical junction circuit with an integrated tuning structure developed at KOSMA [81], consisting of a series inductive line next to the junction followed by two $\lambda/4$ impedance transformer sections.

The SiO_2 dielectric layer for the Nb–SiO_2–Nb microstrip line can be the same as the junction isolation layer, adding no processing steps.

Above the gap frequency of the superconductor, the surface resistance and subsequently the RF loss increases dramatically, so that even conventional normal conductors are less lossy than the superconductor. The crossover point is slightly higher than the gap frequency due to the higher phase velocity in normal metal microstrip line, leading to longer line lengths. Figure 4.26 shows calculations of the power loss in a quarter wavelength microstrip transmission line for several combinations of Nb, NbTiN and Al as studied for the Herschel HIFI band-2 mixer. It can be seen that Niobium deteriorates above 650 GHz and has a crossover with

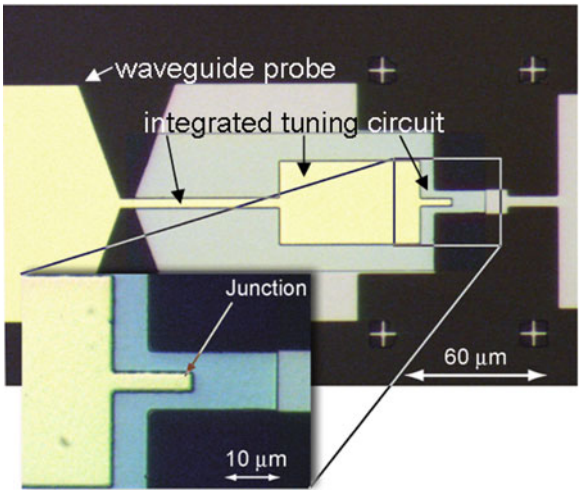

Fig. 4.25 Microphotograph of SIS mixer circuit

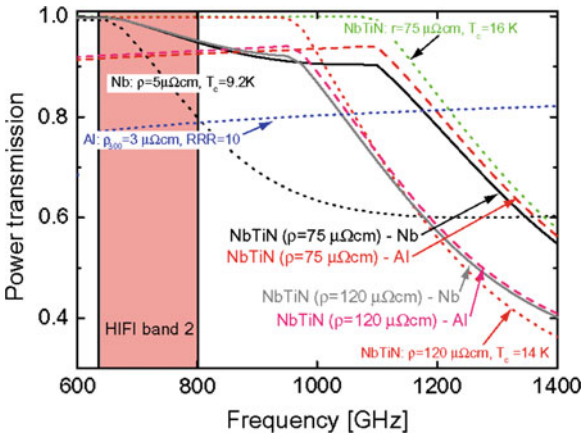

Fig. 4.26 Transmission loss in superconducting microstrip lines

the normal metal Aluminum at about 800 GHz. In principle, NbTiN films of practical quality would allow lossless tuning structures up to 1150 GHz. Above, a good normal conductor (at 4.2 K) such as Aluminum has to be used.

Very important for low-noise operation of SIS mixers is the complete suppression of the AC-Josephson effects with a (preferably superconducting) magnet producing a flux of at least one flux quantum in the barrier (0.014 T for a 1 μm^2 Nb junction). The AC-Josephson effect produces noise in the vicinity of the Shapiro steps, occurring at bias voltages of $nh\nu/2e$ corresponding to harmonics of the local oscillator frequency. Especially at submillimeter wavelengths, the first order step is within the bias voltage range of the first photon step, where optimum mixer performance is usually achieved. Incomplete suppression leads to a smaller range of available bias voltages and/or additional noise. Trapping of external flux can be a source of instability.

4.4.3.4 Waveguide Mixers

In the early attempts to match to the small impedance of the capacitively shunted junctions, waveguide mixers with two adjustable mechanical backshorts had to be used. For applications in radio astronomy, especially for remote observing or space instruments, this is very inconvenient, and mechanical elements operating at 4 K tend to be unreliable. With the incorporation of the junctions into integrated impedance matching structures, it became possible to use only one backshort, and with the modern three-dimensional electromagnetic simulation software, it is possible to design mixers with a fixed backshort for instantaneous RF bandwidths of 35%. Figure 4.27 shows a rendered drawing of the inside of a typical waveguide mixer block used at KOSMA.

The backshort cavity behind the mixer device is stamped into a copper block using a steel stencil. The junction is mounted in a channel across the waveguide, and the horn antenna is flanged to the front surface. The mixer also incorporates

the superconducting magnets to suppress the unwanted Josephson current. As a further example, the mixer developed at KOSMA for the Herschel space observatory is shown in Fig. 4.28. Several versions of such fixed-tuned broadband mixers with excellent noise performance in the 345, 490, 660 and 800 GHz bands have been built and have been successfully used as mixers in receivers for ground-based astronomical telescopes such as the Gornergrat Observatory or AST/RO at the Amundsen–Scott South Pole Station.

The integration of matching circuits with the SIS tunnel junction resulted in a breakthrough in performance over the entire mm- and submm wavelength range. The receivers in today's instruments (Herschel, ALMA, NANTEN, APEX, etc.) typically achieve noise temperatures between 3 and 5 hv/k up to the Niobium gap frequency, increasing to 10–15 hv/k at 1200 K.

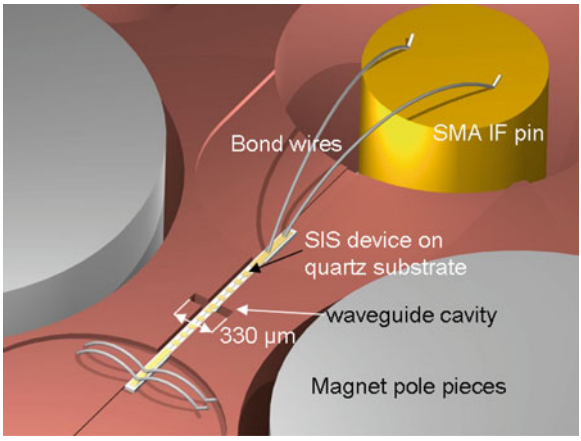

Fig. 4.27 SIS waveguide mixer

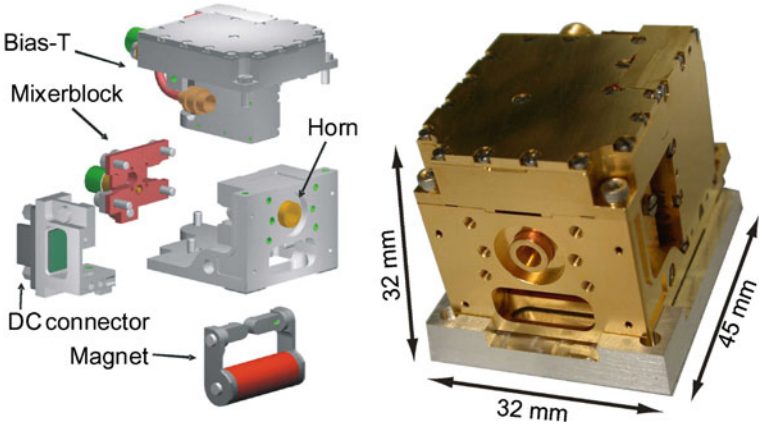

Fig. 4.28 SIS waveguide mixer for Band 2 on HIFI/Herschel

Typical local oscillator sources are Schottky diode frequency multiplier chains, multiplying either a Gunn oscillator source signal at around 100 GHz or the power of a 10–20 GHz synthesizer multiplied to about 100 GHz, where power amplifiers are recently available. These chains now operate up to 1900 GHz with output powers in the few hundred microwatts at low submillimeter wavelengths to less than 10 μW at THz frequencies. THz sources under development are laser photomixers and quantum cascade lasers.

With single pixel mixers operating close to their theoretical noise limit, an effective increase in sensitivity can only be achieved with a combination of multipixel "array" receivers, an increase of the instantaneous IF bandwidth, and adding more functionality to the mixer circuit, such as balanced mixers or sideband separating mixers. Smaller arrays such as the KOSMA/NANTEN dual color receiver for 490/880 GHz (Sub-Mm Array Receiver for Two frequencies) can be built by essentially stacking the available single pixel detectors. Present developments concentrate on introducing new concepts such as SIS mixers on Silicon membranes with integrated beam lead contacts, making the assembly of mixers substantially easier. Figure 4.29 shows a micrograph of such a novel SIS mixer fabricated at KOSMA.

Achieving larger instantaneous IF bandwidth than the present 4 or 8 GHz is especially desirable at THz frequency because of the increased linewidths, and certainly for the large Doppler linewidth of extragalactic sources. Matching between the SIS mixer and the first cryogenic amplifier is the main obstacle here. A solution needs low-inductance contacting (beam leads) and possibly the integration of mixer and first amplifier stage.

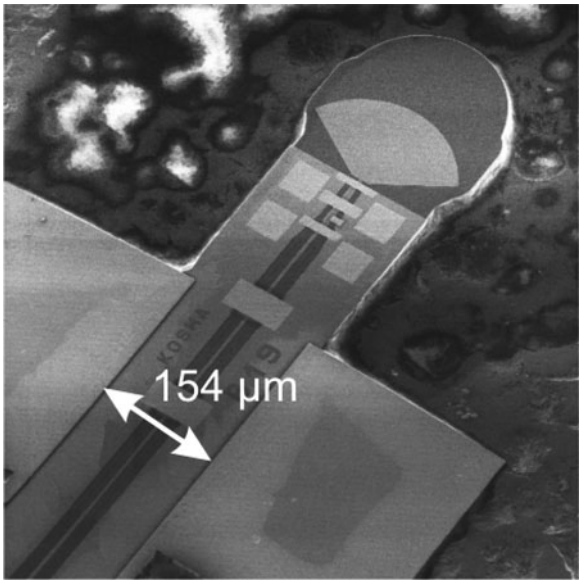

Fig. 4.29 SIS mixer device on Silicon membrane with beam lead contacts

Another field of present research is pushing the limit of SIS mixers to at least 2 THz, beyond the demonstrated present limit of 1200 GHz. SIS mixers at THz have the advantage of better sensitivity, wider instantaneous IF bandwidth and better power stability over their only available alternative at the low THz frequency band: superconducting Hot Electron Bolometers (see below). This development mainly needs good quality high-current density SIS tunnel junctions where at least one of the Nb electrodes is replaced by a compatible material with higher critical temperature, such as NbN or NbTiN. There is little hope that materials can be found that could push the limit higher. The high-T_c superconductors found until today cannot be used to make good hysteretic tunnel barrier junctions, and also their RF properties at THz are not favourable.

4.4.4 Superconducting Hot-Electron Bolometers

Superconducting HEBs rely on the electron heating and the resulting phase transition to normal conductor of a small superconducting bridge. With the device biased at the transition temperature, the local oscillator and signal power heat up the device. The beat frequency between the two signals consequently causes a large resistance variation which causes a current at the difference frequency at constant bias. The HEB mixer is therefore an example of a "square law" mixer, responding to the square (i.e., power) of the sum of the incident fields but unable to follow the instantaneous field. The speed or maximum IF of a bolometer is determined by the heat capacitance and the thermal conductance of the cooling mechanism. Superconducting bolometers can be very fast, as the radiation power is directly absorbed by the electrons in the superconductor rather than in a separate absorber. Using very thin (< 10 nm) films with the superconductor in the "dirty limit", only the electron gas is heated up and the heat capacitance is low. Also, the devices are very small with a device length in the 100 nm range.

In the initial proposals by Gershenzon et al. [82] cooling by phonons (i.e., via the substrate to the thermal bath) was assumed as the cooling mechanism. For Nb, the electron–phonon relaxation time is in the nanosecond (100 MHz) range, which is not fast enough for astronomical applications. However, materials such as Niobium Nitride (NbN) have small enough electron–phonon and phonon escape time constants, so that IF's up to several GHz became possible. In 1993, D. Prober proposed a new type of hot-electron bolometer [83], which uses the diffusion of the hot electrons into a large (normal conducting) heat sink at the ends of the microbridge as cooling mechanism. This avoids the slow electron–phonon relaxation time and leads to very fast bolometers if the bridge is short enough. The IF frequency scales as $(\text{length})^{-2}$ and is about 2 GHz for a 200 nm long bridge. IF bandwidths up to 8 GHz have been demonstrated at 20 GHz LO frequency, but practical difficulties in biasing the devices stably made the phonon-cooled variant more successful up to date.

Using only the heating of the electron gas in the bridge, the mixing response is not limited by the superconductor gap frequency, so that HEB mixers can be used

far into the THz range. An enormous advantage from the RF engineering viewpoint is that the device is almost purely resistive, thus not requiring any high-Q (lossy) tuning circuit. Also, there is no need for a magnetic field. The local oscillator power requirement is below 1 μW coupled power and is not frequency dependent. At these power levels, solid state local oscillator sources become feasible even at THz frequencies.

The dominant noise source of the device is the thermal fluctuation noise, a smaller contribution is from Johnson noise of the device resistance. As the thermal fluctuation noise has the same roll-off frequency as the mixer gain (thermal response time), the noise bandwidth is actually larger than the gain bandwidth. The input noise temperature of the device is frequency independent except for the quantum limit.

Practical mixers have reached a noise temperature of less than 1000 K at 1.9 THz with an IF bandwidth of over 3 GHz. This can be regarded as a breakthrough for high-resolution spectroscopy in the Far Infrared region which came just in time for the new observatories such as SOFIA or Herschel. Although most groups have to rely on the technologically less demanding quasioptical techniques for coupling the radiation to the bolometer, waveguide technology with its advantages in coupling to a Gaussian beam can even be used at 1.9 THz, if micromachining technology is available. Figure 4.30 shows a photograph of a 1.9 THz mixer using a NbTiN Hot Electron Bolometer on a Silicon Nitride membrane fabricated at KOSMA [84].

The waveguide dimension is only 60 × 120 μm. The device is mounted in "flip-chip" technique with the device facing the waveguide, so that it is seen through the almost transparent Silicon Nitride substrate. The bolometer size is 0.4 × 4 μm and is fabricated with electron-beam lithography. A similar mixer for 1.4 THz was successfully used at the APEX telescope (MPIfR Bonn, Atacama) to take astronomical spectra. Similar mixers for 1.4 and 1.9 THz were delivered to the German receiver at terahertz frequencies (GREAT), which is waiting to be flown on the SOFIA aircraft starting in 2011.

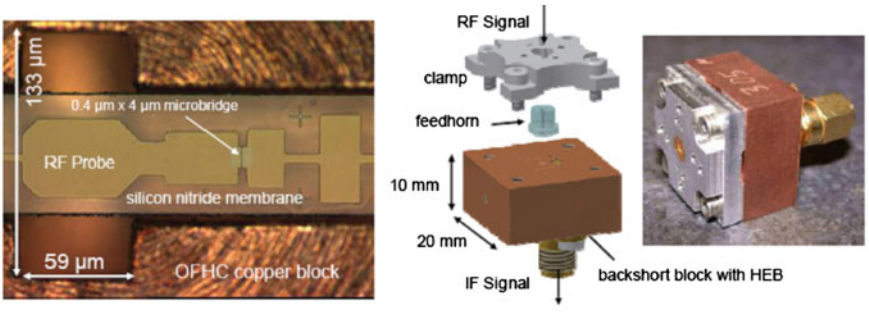

Fig. 4.30 1.9 THz HEB mixer for SOFIA

References

1. T. Amano, Astrophys. J. **716**, L1 (2010)
2. E. Falgarone, V. Ossenkopf, M. Gerin, P. Lesaffre, B. Godard, J. Pearson, S. Cabrit, Ch. Joblin, A.O. Benz, F. Boulanger, A. Fuente, R. Güsten, A. Harris, T. Klein, C. Kramer, S. Lord, P. Martin, J. Martin-Pintado, D. Neufeld, T.G. Phillips, M. Röllig, R. Simon, J. Stutzki, F. van der Tak, D. Tryssier, M. Yorke, N. Erickson, M. Fich, W. Jellema, A. Marston, C. Risacher, M. Salez, F. Schmülling, Astron. Astrophys. **518**, L118 (2010)
3. T. de Graauw et al. (with 165 authors), Astron. Astrophys. **518**, L6 (2010)
4. O. Asvany, O. Ricken, H.S.P. Müller, M.C. Wiedner, T.F. Giesen, S. Schlemmer, Phys. Rev. Lett. **100**, 233004 (2008)
5. H.M. Pickett, R.L. Poynter, E.A. Cohen, M.L. Delitsky, J.C. Pearson, H.S.P. Müller, J. Quant. Spectrosc. Radiat. Transf. **60**, 883 (1998)
6. H.S.P. Müller, F. Schlöder, J. Stutzki, G. Winnewisser, J. Mol. Struct. **742**, 215 (2005)
7. R. Güsten, L.Å. Nyman, P. Schilke, K. Menten, C. Cesarsky, R. Booth, Astron. Astrophys. **454**, L13 (2006)
8. A. Staprans, E.W. McCune, J.A. Ruetz, Proc. IEEE **61**, 299 (1973)
9. C.P. Endres, B.J. Drouin, J.C. Pearson, H.S.P. Müller, F. Lewen, S. Schlemmer, T.F. Giesen, Astron. Astrophys. **504**, 635 (2009)
10. P.H. Siegel, IEEE Trans. Microw. Theory Tech. **50**, 910 (2002)
11. B. Levush, T. Antonsen Jr., A. Bromborsky, W.R. Lou, D. Abe, S. Miller, Y. Carmel, J. Rodgers, V. Granatstein, W. Destler, in *Electron Devices Meeting 1991, Technical Digest* (1991), p. 775
12. B. Levush, T.M. Anonsen, A. Bromborsky, W.R. Lou, Y. Carmel, IEEE Trans. Plasma Sci. **20**, 263 (1992)
13. A.N. Korolev, S.A. Zaitsev, I.I. Golenitskij, Y.V. Zhary, A.D. Zarkurdayev, M.I. Lopin, P.M. Meleshkevich, E.A. Gelvich, A.A. Negirev, A.S. Podedonostsev, V.I. Poognin, V.B. Homich, A.N. Gargin, IEEE Trans. Electron. Devices **48**, 2929 (2001)
14. M. Liedtke, R. Schieder, K.M.T. Yamada, G. Winnewisser, S.P. Belov, A.F. Krupnov, J. Mol. Spectrosc. **161**, 317 (1993)
15. S.P. Below, M. Liedtke, T. Klaus, R. Schieder, A.H. Saleck, J. Behrend, K.M.T. Yamada, G. Winnewisser, A.F. Krupnov, J. Mol. Spectrosc. **166**, 489 (1994)
16. G.M. Plummer, G. Winnewisser, M. Winnewisser, J. Hahn, K. Reinartz, J. Mol. Spectrosc. **126**, 255 (1987)
17. M. Bester, K. Jacobs, B. Vowinkel, in *Proceedings of 13th European Microwave Conference, Nürnberg* (1983), p. 308
18. A.F. Krupnov, L.I. Gershtein, Prib. Tekh. Eksp. **6**, 143 (1970)
19. P. Goy, C. Fabre, M. Gross, S. Haroche, J. Phys. B **13**, L83–L91 (1980)
20. A.H.F. van Vliet, T. de Graauw, S. Lindholm, H. van de Stadt, Int. J. Infrared Millimeter Wave **3**, 817 (1982)
21. P. Goy, J.M. Raimond, G. Vitrant, S. Haroshe, Phys. Rev. A **26**, 2733 (1982)
22. E. Bava, A. Godone, G.D. Rovera, Infrared Phys. **23**, 157 (1983)
23. G. Winnewisser, A.F. Krupnov, M.Yu. Tretyakov, M. Liedtke, F. Lewen, A.H. Saleck, R. Schieder, A.P. Shkaev, S.V. Volokhov, J. Mol. Spectrosc. **165**, 294 (1994)
24. G. Winnewisser, Vib. Spectrosc. **8**, 241 (1995)
25. M. Bogey, S. Civi, B. Delcroix, C. Demuynck, A.F. Krupnov, J. Quiguer, M.Yu. Tretyakov, A. Walters, J. Mol. Spectrosc. **182**, 85 (1997)
26. I. Morino, M. Fabian, H. Takeo, K.M.T. Yamada, J. Mol. Spectrosc. **185**, 142 (1997)
27. T. Amano, Astrophys. J. **531**, L161 (2000)
28. F. Lewen, R. Gendriesch, I. Pak, D.G. Paveliev, M. Hepp, R. Schieder, G. Winnewisser, Rev. Sci. Instrum. **69**, 32 (1998)
29. A.F. Krupnov, Int. J. Infrared Millimeter Waves **22**, 1 (2001)

30. S. Schlemmer, T. Giesen, F. Lewen, G. Winnewisser, in *Frontiers of Molecular Spectroscopy*, ed. by J. Laane (Elsevier, Amsterdam, 2009), p. 241
31. G. Klapper, L. Surin, F. Lewen, H.S.P. Müller, I. Pak, G. Winnewisser, Astrophys. J. **582**, 262 (2003)
32. S. Brünken, E.A. Michael, F. Lewen, T. Giesen, H. Ozeki, G. Winnewisser, P. Jensen, E. Herbst, Can. J. Chem. **82**, 676 (2004)
33. U. Fuchs, S. Brünken, G.W. Fuchs, S. Thorwirth, V. Ahrens, F. Lewen, S. Urban, T. Giesen, G. Winnewisser, Z. Naturforsch. **59**, 861 (2004)
34. S. Brünken, U. Fuchs, F. Lewen, S. Urban, T. Giesen, G. Winnewisser, J. Mol. Spectrosc. **225**, 152 (2004)
35. P. Siegel, R. Smith, M. Graidis, S. Martin, IEEE Trans. Microw. Theory Tech. **47**, 59 (1999)
36. J. Bruston, E. Schlecht, A. Maestrini, F. Maiwald, S. Martin, R. Smith, I. Mehdi, P. Siegel, J. Pearson, in *Proceedings of the SPIE-International Symposium on Astronomical Telescope and Instrumentation* (2000), p. 22
37. G. Chattopadhyay, E. Schlecht, J. Ward, J. Gill, H. Javadi, F. Maiwald, I. Medhi, IEEE Trans. Microw. Theory Tech. **52**, 1538 (2004)
38. A. Maestrini, J. Ward, J. Gill, H. Javadi, E. Schlecht, G. Chattopadhyay, F. Maiwald, N. Erickson, I. Mehdi, IEEE Microw. Wirel. Compon. Lett. **14**, 253 (2004)
39. F. Maiwald, S. Martin, J. Bruston, A. Maestrini, T. Crawford, P.H. Siegel, in *Microwave Symposium Digest, 2001 IEEE MTT-S International*, vol. 3 (2001), p. 1637
40. H. Xu, G.S. Schoenthal, J.L. Hesler, T.W. Crowe, R.M. Weikle, IEEE Trans. Microw. Theory Tech. **55**, 648 (2007)
41. B.J. Drouin, F.W. Maiwald, J.C. Pearson, Rev. Sci. Inst. **76**, 093113 (2005)
42. F. Lewen, D.G. Paveljev, B. Vowinkel, J. Freyer, H. Grothe, G. Winnewisser, in *Proceedings of 4th International Workshop on Terahertz Electronics*, Erlangen (1996)
43. F. Maiwald, F. Lewen, B. Vowinkel, W. Jabs, D.G. Paveljev, M. Winnewisser, G. Winnewisser, IEEE Microw. Guided Wave Lett. **9**, 198 (1999)
44. F. Maiwald, F. Lewen, V. Ahrens, M. Beaky, R. Gendriesch, A.N. Koroliev, A.A. Negirev, D.G. Paveljev, B. Vowinkel, G. Winnewisser, J. Mol. Spectrosc. **202**, 166 (2000)
45. C.P. Endres, F. Lewen, T.F. Giesen, S. Schlemmer, D.G. Paveliev, Y.I. Koschurinov, V.M. Ustinov, A.E. Zhucov, Rev. Sci. Instrum. **78**, 043106 (2007)
46. G. Piau, F.X. Brown, D. Dangoisse, P. Glorieux, IEEE J. Quantum Electron. **QE-23**, 1388 (1987)
47. G.A. Blake, K.B. Laughlin, R.C. Cohen, K.L. Busarow, D.H. Gwo, C.A. Schmuttenmaer, D.W. Steyert, R.J. Saykally, Rev. Sci. Inst. **62**, 1701 (1991)
48. P. Verhoeve, E. Zwart, M. Versluis, M. Drabbels, J.J. ter Meulen, W.L. Meerts, A. Dymanus, D.B. Mclay, Rev. Sci. Inst. **61**, 1612 (1990)
49. F. Lewen, E. Michael, J. Stutzki, G. Winnewisser, J. Mol. Spectrosc. **183**, 207 (1997)
50. E. Michael, F. Lewen, R. Gendriesch, J. Stutzki, G. Winnewisser, Int. J. Infrared Millimeter Waves **20**, 1073 (1999)
51. R. Gendriesch, F. Lewen, G. Winnewisser, J. Hahn, J. Mol. Spectrosc. **203**, 205 (2000)
52. R. Gendriesch, F. Lewen, G. Winnewisser, H.S.P. Müller, J. Mol. Struct. **599**, 293 (2001)
53. R. Gendriesch, K. Pehl, T. Giesen, G. Winnewisser, F. Lewen, Z. Naturforsch. **58**, 129 (2003)
54. S. Brünken, H.S.P. Müller, F. Lewen, G. Winnewisser, Phys. Chem. Chem. Phys. **5**, 1515 (2003)
55. S. Brünken, H.S.P. Müller, S. Thorwirth, F. Lewen, G. Winnewisser, J. Mol. Struct. **780**(81), 3 (2006)
56. H. Linnartz, T. Motylewski, F. Maiwald, D.A. Roth, F. Lewen, I. Pak, G. Winnewisser, Chem. Phys. Lett. **292**, 188 (1998)
57. M. Hepp, R. Gendriesch, I. Pak, Y.A. Kuritsyn, F. Lewen, G. Winnewisser, M. Brookes, A.R.W. McKellar, J.K.G. Watson, T. Amano, Mol. Phys. **92**, 229 (1997)
58. T. Imasaka, D.S. Moore, T. Vo-Dinh, Pure Appl. Chem. **75**, 975 (2003)
59. T. Motylewski, O. Vaizert, T.F. Giesen, H. Linnartz, J.P. Maier, J. Chem. Phys. **111**, 6161 (1999)

60. T.F. Giesen, A. Van Orden, H.J. Hwang, R.S. Fellers, R.A. Provencal, R.J. Saykally, Science **265**, 756 (1994)
61. B.S. Dumesh, V.P. Kostromin, F.S. Rusin, L.A. Surin, Meas. Sci. Technol. **3**, 873 (1992)
62. B.S. Dumesh, L.A. Surin, Rev. Sci. Instrum. **67**, 3458 (1996)
63. L.A. Surin, Vib. Spectrosc. **24**, 147 (2000)
64. B.S. Dumesh, V.D. Gorbatenkov, V.G. Koloshnikov, V.A. Panfilov, L.A. Surin, Spectrochim. Acta A **53**, 835 (1997)
65. L.A. Surin, B.S. Dumesh, F. Lewen, D.A. Roth, V.P. Kostromin, F.S. Rusin, G. Winnewisser, I. Pak, Rev. Sci. Instrum. **72**, 2535 (2001)
66. A.V. Potapov, L. Surin, V.A. Panfilov, B.S. Dumesh, Opt. Spectrosc. **106**, 183 (2009)
67. V.L. Bratman, B.S. Dumesh, A.E. Fedotov, Yu.A. Grishin, F.S. Rusin, Int. J. Infrared Millimeter Waves **23**, 1595 (2002)
68. Yu. Grishin, M. Fuchs, A. Schnegg, A. Dubinski, B. Dumesh, F. Rusin, V. Bratman, K. Mobius, Rev. Sci. Instrum. **75**, 2928 (2004)
69. L.A. Surin, D.N. Fourzikov, F. Lewen, B.S. Dumesh, G. Winnewisser, A.R.W. McKellar, J. Mol. Spectrosc. **222**, 93 (2003)
70. L.S. Vasilenko, V.P. Chebotaev, A.V. Shishaev, Pis'ma, Zh. Eksp. Teor. Fis **12**, 161 (1970)
71. V.S. Letokhov, V.P. Chebotaev, *Springer Series in Optical Sciences*, vol. 4 (Springer, Berlin, 1970)
72. L.A. Surin, B.S. Dumesh, F.S. Rusin, G. Winnewisser, I. Pak, Phys. Rev. Lett. **86**, 2002 (2001)
73. J. Zmuidzinas, P.L. Richards, Proc. IEEE **92**, 1597 (2004)
74. J.R. Tucker, IEEE J. Quantum Electron. **QE-15**(11), 1234 (1979)
75. J.R. Tucker, M.J. Feldman, Rev. Mod. Phys. **57**(4), 1055 (1985)
76. K.-H. Gundlach, S. Takada, M. Zahn, H.J. Hartfuss, Appl. Phys. Lett. **41**, 294 (1982)
77. M. Gurvitch, M.A. Washington, H.A. Huggins, Appl. Phys. Lett. **42**, 472 (1983)
78. R.L. Kautz, J. Appl. Phys **49**(1), 308 (1978)
79. D.C. Mattis, J. Bardeen, Phys. Rev. **111**, 412 (1958)
80. R. Pöpel, J. Appl. Phys. **66**, 5950 (1989)
81. K. Jacobs, U. Kotthaus, B. Vowinkel, Int. J. Infrared Millimeter Waves **13**, 15 (1992)
82. E.M. Gershenzon, M.E. Gershenzon, G.N. Goltsman, A.D. Semenov, A.V. Sergeev, IEEE Trans. Magn. **27**, 1317 (1991)
83. D.E. Prober, Appl. Phys. Lett. **62**, 2119 (1993)
84. P.P. Munoz, S. Bedorf, M. Brandt, T. Tils, N. Honingh, K. Jacobs, IEEE MWCL **16**(11), 606 (2006)
85. S.P. Belov, F. Lewen, T. Klaus, G. Winnewisser, J. Mol. Spectrosc. **174**, 606 (1995)
86. R. Gendriesch, F. Lewen, G. Klapper, K.M. Menten, G. Winnewisser, J.A. Coxon, H.S.P. Müller, Astron. Astrophys. **497**, 927 (2009)
87. M. Caris, T.F. Giesen, C. Duan, H.S.P. Müller, S. Schlemmer, K.M.T. Yamada, J. Mol. Spectrosc. **253**, 99 (2009)

Chapter 5
List of Molecules Observed in Interstellar Space

Koichi M. T. Yamada and Gisbert Winnewisser

By the end of July 2010, the number of observed interstellar molecules listed in CDMS (Cologne Database for Molecular Spectra)[1] has reached 163.

Many of them are *organic* molecules. Among them 27 molecules are composed only of carbon and hydrogen, which are listed in Table 5.1. Table 5.2 lists 51 organic molecules, which contain one hetero atom. Although the populations of hetero-atoms are much less than that of the carbon atom in the universe, organic molecules which contain two hetero-atoms have been detected (14 molecules) in the interstellar space as listed in Table 5.3.

In addition to those *organic* molecules, fairly many *inorganic* molecules have been detected in the interstellar space (Tables 5.4, 5.5, 5.6). Among them 30 molecules contain one or more carbon atoms, as listed in Table 5.4. Table 5.5 lists 23 inorganic molecules which contain one or more hydrogen atoms so far detected. The rest 18 molecules contain neither a carbon nor a hydrogen atom.

K. M. T. Yamada (✉)
National Institute of Advanced industrial Science and Technology (AIST), EMTech, Onogawa 16-1, Tsukuba, Ibaraki 305-8569, Japan
e-mail: kmt.yamada@aist.go.jp

G. Winnewisser
Alte Str. 8A, 79249, Merzhausen, Germany

[1] http://www.astro.uni-koeln.de/cdms/.

K. M. T. Yamada and G. Winnewisser (eds.), *Interstellar Molecules*,
Springer Tracts in Modern Physics 241, DOI: 10.1007/978-3-642-16268-8_5,

Table 5.1 Organic molecule composed of carbon and hydrogen[†]

2 atoms	3 atoms	4 atoms	5 atoms	6 atoms	7 atoms	8 atoms	9 atoms	10 atoms	11 atoms	12 atoms
CH	CH_2	CH_3 *	CH_4 *							
	C_2H	*l*-C_3H	C_4H	C_5H	C_6H	C_7H	C_8H			
		c-C_3H	C_4H^-		C_6H^-		C_8H^-			
			l-C_3H_2	*l*-C_4H_2		C_6H_2				
			c-C_3H_2							C_6H_6 *
				C_2H_4*						
		HCCH*		HC_4H *	HC_6H *?					
					CH_3C_2H		CH_3C_4H		CH_3C_6H	
							CH_2CHCH_3			
CH^+										

[†]The mark "*" is used for vibration-rotation transitions and "?" for tentative assignments. The symbols "*l*" and "*c*" indicates *linear* and *cyclic* isomers, respectively

Table 5.2 Organic molecules containing one hetero atom[†]

3 atoms	4 atoms	5 atoms	6 atoms	7 atoms	8 atoms	9 atoms	10 atoms	11 atoms	12 atoms	13 atoms
HCO	H_2CO	H_2CCO	*c*-H_2C_3O							
			CH_3OH							
	H_2CS		CH_3SH							
	H_2CN	H_2CCN	CH_3CN		CH_3C_2CN	C_2H_5CN	CH_3C_5N		*n*-C_3H_7CN	
			CH_3NC			C_2H_5OH			H_2CNH	H_2CCNH?
		H_2NCN								
HCN	HCCN	HCCCN	HC_4N	HC_5N		HC_7N		HC_9N		$HC_{11}N$
		HCCNC		CH_2CHCN						
			HC_2CHO	CH_3CHO	CH_2CHCHO?		C_2H_5CHO	C_2H_5OCHO	$C_2H_5OCH_3$	
				c-C_2H_4O						
				CH_2CHOH	CH_2CCHCN		$(CH_2OH)_2$			
				CH_3NH_2		$(CH_3)_2O$	$(CH_3)_2CO$			
HNC		HNC_3								
HCP										
	$HCNH^+$		HC_3NH^+							
HCO^+		H_2COH^+								
HCS^+										
HOC^+										

[†]The symbol "*n*" is used for the *normal* isomer

Table 5.3 Organic molecules containing two hetero atoms

4 atoms	5 atoms	6 atoms	7 atoms	8 atoms	9 atoms
HNCO		NH_2CHO		CH_3OCHO	
HCNO				CH_3COOH	CH_3CONH_2
HOCN				CH_2OHCHO	
HNCS				H_2NCH_2CN	
HSCN					
	HC(O)CN				
$HOCO^+$	HCOOH				

Table 5.4 Inorganic molecules containing one or more carbon atoms†

2 atoms	3 atoms	4 atoms	5 atoms	6 atoms
C_2 **	C_3 *		C_5 *	
		C_3N		C_5N
		C_3N^-		C_5N^-
CO	CO_2 *			
	OCS			
	C_2O	C_3O		
	C_2P	C_3S		
CO^+				
CN	AlNC			
	MgCN			
	MgNC			
	NaCN			
	SiCN			
	SiNC			
CP				
CS	C_2S			
CSi	*c*-C_2Si	*c*-C_3Si	C_4Si	
CF^+				

†The mark "*" is used for rovibrational transitions, and "**" for rovibronic transitions. The symbol "*c*" is used for cyclic isomers.

Table 5.5 Inorganic molecules containing one or more hydrogen atoms

2 atoms	3 atoms	4 atoms	5 atoms
H_2	H_3^+ *	H_3O^+	
HD	H_2D^+		
	HD_2^+		
	H_2O		
	H_2O^+		
	H_2S		
NH	NH_2	NH_3	
		PH_3 ?	
	HNO		
	HN_2^+		
OH			
OH^+			
	AlOH		
SH *			
SH^+			
SiH ?			SiH_4 *
HCl			
HF			

†The mark "*" is used for vibration-rotation transitions, and "?" for tentative assignments.

Table 5.6 Inorganic molecules without a carbon and a hydrogen atom

2 atoms	3 atoms
AlF	
AlCl	
AlO	
ClK	
ClNa	
FeO	
NO	N_2O
NS	
NSi	
NP	
O2	
PO	
SO	SO_2
SO^+	
SiO	
SiS	

Index